

# THESE

présentée par

**Matthew Juniper**

pour l'obtention du

**GRADE de DOCTEUR**

Formation doctorale : Energétique

Laboratoire d'accueil : Laboratoire d'Energétique Moléculaire et Macroscopique,  
Combustion (EM2C) du CNRS et de l'ECP

## Structure et stabilisation des flammes cryotechniques

(Structure and stabilization of cryogenic spray flames)

Soutenue le 26 novembre 2001

Composition du jury : MM. Candel S.  
Darabiha N.  
Hopfinger E.  
Searby G. Rapporteur  
Thomas J-L.  
Vuillermoz P.  
Yang V.  
Zaleski S. Rapporteur





# Acknowledgements

I would like to thank Geoff Searby and Stephane Zaleski for reviewing this manuscript in detail. I would also like to thank Emil Hopfinger, Stéphane Zurbach, Patrick Vuillermoz and Vigor Yang for kindly agreeing to be members of the jury.

Particular thanks go to Sébastien Candel, who provided the main motivation for this work. His ideas and phenomenal knowledge of the domain were inspirational. An hour spent in discussion with him would often save several weeks' work alone. Juan-Carlos Rolon and Daniel Durox helped greatly with ideas for the experimental work and the keenness of Philippe Scoufflaire was priceless on practical issues. A great deal of work was performed with Amita Tripathi, both on experimental and theoretical points. I greatly appreciated discussions with her about flame structure, as well as her diplomacy and patience in dealing with the frustrations of a tongue-tied Englishman.

The team at ONERA, Palaiseau deserves special thanks. The complex experimental facility is handled with extraordinary competence by Lucien Vingert and Mohammed Habiballah. Maintenance is carried out with commendable speed by Jean Champy and Alain Mouthon, who always made us feel at home.

At this laboratory, I would particularly like to thank Nasser Darabiha and Olivier Gicquel for help regarding counterflow diffusion flames and numerical schemes in general. The experimental work performed in conjunction with Bertrand Leroux, François Lacas and two sets of masters' students was very fruitful and relied heavily on their excellent experimental expertise. Aside from these specific contributions, many other Ph.D students contributed important comments and criticism.

From further afield, two short discussions with Patrick Huerre concerning absolute instabilities were invaluable. I would also like to thank Peter Monkewitz and Thomas Loiseleux for their technical help and encouragement via e-mail.

Finally, it is important to acknowledge the efficient running of the laboratory in the capable hands of Jean-Pierre Martin, Caroline Angeli and Michèle Messica. Without such a solid base, research would be slow and painful. The support, both moral and technical, of the technical staff has also been essential.



# Abstract

The success of a satellite launcher depends to a great extent on its efficiency and reliability. Engines using cryogenic fuels, such as liquid oxygen and hydrogen, are used for most missions since they combine high performance with a relatively light structure. The design of such motors has, until recently, been based on empirical results from systematic tests. Future design will rely on numerical simulations and will envisage alternative reactant combinations, such as methane and oxygen. The definition of entry conditions to these numerical simulations requires a knowledge of the flame structure, particularly of the region near the fuel injectors. These practical considerations motivate this investigation.

As well as discussion on the overall flame shape under subcritical and supercritical conditions, two aspects are given special attention: (1) the injector geometry, (2) stabilization of the flame. The latter question is critical for the system's reliability and is particularly important when considering fuels which are less reactive than hydrogen and oxygen.

Systematic experiments are performed at up to 70 bar pressure on a coaxial fuel injector similar to those used in current motors. Optical diagnostics combined with image processing yield the flame structure. Models are then developed regarding the effect of injector geometry and tested against experimental results from this and other coaxial injectors. In this manner the physical mechanisms controlling flame shape are deduced. A result of scientific interest is that a wake flow, consisting of a slow stream within a faster stream, is more unstable when enclosed within a duct. This provides one possible mechanism for the effect of recess on the cryogenic flame.

The question of stabilization is approached in carefully-defined stages so that model problems from the field of combustion science can be applied. First the base of the flame is divided into two parts and one is treated as a counterflow diffusion flame above a condensed surface. Numerical simulations performed here add new results to the study of this configuration. The second part of the base is treated initially as a corner flame, a model problem which has been investigated only recently. Two parameters controlling the shape of the flame are defined and the relationship between them is deduced from numerical simulations. This approach permits a simple progression to more complex geometries. The flames above a porous plate with fuel injection and then above a vaporizing reactant are considered. Finally, the situation of a flame behind a step over a vaporizing reactant is analysed. This is a realistic model of the base of a cryogenic spray flame. Through this progression the non-dimensional parameters governing behaviour are introduced successively and the most influential parameters are identified. The final result will aid design both of the engine and the control sequences of ignition, leading to enhanced reliability.



# Resumé

La réussite d'un lanceur dépend, pour une grande part, de son efficacité et de sa fiabilité. Les moteurs à ergols cryotechniques, par exemple à l'oxygène liquide et à l'hydrogène, sont utilisés pour la plupart des missions car ils combinent une performance élevée et une structure relativement légère. La mise au point de ces moteurs a été très largement fondée sur l'utilisation d'essais systématiques. Un des objectifs actuels est le développement de méthodes de conception fondées sur des simulations numériques fiables. L'utilisation d'autres réactifs est aussi envisagée. Le développement de méthodes numériques doit s'appuyer sur une connaissance détaillée des structures de flamme et des conditions d'entrée bien définies. Ce projet de recherche est motivée par ces considérations pratiques. Il concerne la région proche des injecteurs d'ergols.

Au delà d'une discussion sur la structure générale de la flamme aux pressions subcritiques et supercritiques, on traite ici: (1) l'effet de la géométrie de l'injecteur, (2) la stabilisation de la flamme. Ce dernier point a une forte influence sur la fiabilité des moteurs. Il est d'une importance primordiale dans le cadre d'un changement d'ergols dans lequel l'hydrogène pourrait être remplacé par une substance moins réactive (par exemple du méthane).

Des essais systématiques sont effectués, à des pressions jusqu'à 70 bar, sur un injecteur comparable à ceux des moteurs réels. La structure de la flamme est obtenue au moyen de diagnostics optiques avec un traitement d'images adapté. Les modèles sont développés et leurs résultats comparés avec les résultats expérimentaux afin d'étudier l'effet de la géométrie de l'injecteur. Un nouveau résultat d'intérêt scientifique est qu'un sillage, formé par un écoulement lent à l'intérieur d'un écoulement rapide, est plus instable quand l'écoulement extérieur est confiné dans un conduit. Ce mécanisme pourrait expliquer l'effet du retrait sur la flamme cryotechnique.

Les connaissances scientifique développées dans le domaine de la combustion peuvent s'appliquer au problème de la stabilisation. Dans un premier temps, la zone initiale de la flamme est divisée en deux parties et une analyse de flamme à contre-courant est appliqué à la zone située en aval du point de stabilisation. De nouveaux résultats numériques sont obtenus ici. La seconde partie est traitée d'abord comme une flamme dans un coin, un problème qui a fait l'objet d'études récentes. Deux paramètres qui pilotent la forme de la flamme sont définis et leur relation est déduite des résultats numériques. Cette approche permet une progression vers les géométries plus complexes. La flamme au dessus d'une plaque poreuse avec injection de comburant est étudiée et on envisage dans un deuxième temps une flamme au dessus d'un comburant en cours de vaporisation. Finalement la flamme derrière une marche au dessus d'une nappe liquide est envisagée. Grâce à cette progression, les paramètres sans dimensions qui pilotent le comportement sont introduits progressivement et les paramètres ayant le plus d'influence sont identifiés. Le résultat final aidera la conception du moteur et doit permettre

une meilleure maîtrise des séquences d'allumage, ce qui pourrait augmenter la fiabilité du système.



# Contents

<b>Introduction</b>	<b>vii</b>
<b>1 Experimental technique and results († denotes work performed with A.Tripathi)</b>	<b>1</b>
1.1 Introduction . . . . .	3
1.2 Objectives of the Experiments . . . . .	3
1.3 Optical Diagnostics . . . . .	6
1.3.1 Introduction † . . . . .	6
1.3.2 Imaging of chemiluminescence of OH* and H <sub>2</sub> O † . . . . .	6
1.3.2.1 Chemiluminescence of OH* and H <sub>2</sub> O † . . . . .	6
1.3.2.2 Absorption of OH* spontaneous emission within the combustion chamber † . . . . .	7
1.3.2.3 The Abel Inversion † . . . . .	7
1.3.2.4 Absorption and Scattering by the Oxygen Jet . . . . .	9
1.3.2.5 Image processing procedure † . . . . .	10
1.3.3 Backlighting . . . . .	10
1.3.3.1 Introduction . . . . .	10
1.3.3.2 Shadowgraphy . . . . .	11
1.3.3.3 Schlieren . . . . .	11
1.3.3.4 Three dimensional refractive index fields . . . . .	11
1.3.3.5 Appropriate techniques for the cryogenic combustion facility	11
1.3.4 Summary . . . . .	12
1.4 First test series, 10 bar . . . . .	15
1.4.1 Experimental configuration † . . . . .	15
1.4.1.1 Spectroscopy † . . . . .	15
1.4.1.2 OH* and H <sub>2</sub> O emission † . . . . .	15
1.4.1.3 Backlighting . . . . .	15
1.4.2 Results . . . . .	15
1.4.2.1 Spectroscopy † . . . . .	16
1.4.2.2 OH* and H <sub>2</sub> O Emission † . . . . .	16
1.4.2.3 Backlighting . . . . .	17
1.5 Second test series; high pressure . . . . .	21
1.5.1 Experimental configuration † . . . . .	21
1.5.1.1 Spectroscopy † . . . . .	21
1.5.1.2 OH and H <sub>2</sub> O average emission images † . . . . .	21



1.5.1.3	Backlighting and instantaneous emission images . . . . .	21
1.5.1.4	Pressure drop within the recessed injector . . . . .	22
1.5.2	Operating conditions † . . . . .	25
1.5.3	Results . . . . .	25
1.5.3.1	Spectroscopy † . . . . .	25
1.5.3.2	Average Emission from OH* and H <sub>2</sub> O † . . . . .	25
1.5.3.3	Backlighting and Instantaneous Emission Results . . . . .	26
1.5.3.4	Pressure drop across injector . . . . .	35
1.6	Third test series; low hydrogen temperature . . . . .	38
1.6.1	Experimental configuration . . . . .	38
1.6.1.1	Spontaneous OH* emission . . . . .	38
1.6.1.2	Backlighting . . . . .	39
1.6.1.3	Simultaneous OH* emission and backlighting images . . . . .	39
1.6.1.4	Natural emission . . . . .	39
1.6.2	Results . . . . .	40
1.6.2.1	OH* Emission and Backlighting images . . . . .	40
1.6.2.2	Effect of reducing the hydrogen temperature . . . . .	40
1.6.2.3	Estimation of velocities in the chamber . . . . .	40
<b>2</b>	<b>Flame Structure</b> . . . . .	<b>47</b>
2.1	Introduction . . . . .	49
2.2	General structure . . . . .	49
2.3	Structure near the injector . . . . .	50
2.4	Flame expansion angle . . . . .	52
2.4.1	A quantitative result . . . . .	52
2.4.2	Measurement of flame expansion angle . . . . .	53
2.4.3	Parameters affecting the flame expansion angle . . . . .	53
2.4.3.1	Balance equations . . . . .	56
2.4.3.2	Numerical results . . . . .	57
2.4.4	Experimental results . . . . .	59
2.4.4.1	Effect of hydrogen velocity and gasification rate . . . . .	59
2.4.4.2	Effect of pressure . . . . .	60
2.5	Balance between vaporization and turbulent mixing . . . . .	61
2.5.1	Characteristic mixing time . . . . .	61
2.5.2	Characteristic vaporization time . . . . .	62
2.5.3	Characteristic chemical time . . . . .	63
2.5.4	The Damköhler number . . . . .	63
2.6	Conclusion . . . . .	64
<b>3</b>	<b>Effect of Recess</b> . . . . .	<b>65</b>
3.1	Introduction . . . . .	68
3.2	Experimental evidence of the effect of recess . . . . .	68
3.3	Break-up and mixing of coaxial jets . . . . .	68
3.3.1	Introduction . . . . .	68
3.3.2	Break-up regimes of coaxial injectors . . . . .	69
3.3.2.1	Rayleigh regime . . . . .	69



3.3.2.2	Membrane regime . . . . .	70
3.3.2.3	Fibrous regime . . . . .	70
3.3.2.4	Superpulsating fibrous regime . . . . .	71
3.3.3	Primary atomization in the fibrous regime . . . . .	71
3.3.4	Analysis in the linear range of primary atomization . . . . .	72
3.3.5	Global mixing layer models . . . . .	75
3.3.6	Experimental determination of jet break-up length . . . . .	76
3.3.7	Summary - Break-up and mixing of coaxial jets . . . . .	76
3.4	Proposed mechanisms - Introduction . . . . .	79
3.5	Interaction of inner and outer mixing layers . . . . .	79
3.6	Blockage and heating by combustion products . . . . .	81
3.7	Acoustic feedback in recessed portion . . . . .	84
3.8	Stability of a bounded wake flow . . . . .	87
3.8.1	Introduction . . . . .	87
3.8.2	Global Stability of Wakes . . . . .	87
3.8.3	Two-dimensional bounded wake flow . . . . .	90
3.8.4	Temporal Instability Analysis . . . . .	91
3.8.5	Space-time Instability analysis . . . . .	93
3.8.5.1	Introduction . . . . .	93
3.8.5.2	Convective/absolute transition in the unbounded wake . . . . .	94
3.8.5.3	Convective/absolute transition in the bounded wake . . . . .	97
3.8.6	Experiments . . . . .	103
3.8.7	Development of an improved model . . . . .	110
3.8.8	Conclusions - stability of a bounded wake flow . . . . .	110
3.9	Conclusion - effect of recess . . . . .	111
<b>4</b>	<b>Extinction limits of a counterflow flame fed by a condensed reactant</b>	<b>115</b>
4.1	Introduction . . . . .	117
4.2	One-dimensional test case . . . . .	117
4.3	Boundary conditions and governing equations . . . . .	119
4.3.1	Formulation of subcritical vs. supercritical problems . . . . .	119
4.3.2	Governing equations . . . . .	119
4.3.3	Boundary conditions . . . . .	121
4.4	Results . . . . .	122
4.4.1	Species profiles in the flame . . . . .	122
4.4.2	Effect of strain rate . . . . .	123
4.4.3	Effect of inlet hydrogen temperature on extinction strain rate . . . . .	125
4.4.4	Effect of a temperature gradient in the liquid oxygen . . . . .	127
4.4.5	Effect of pressure . . . . .	127
4.5	Conclusions . . . . .	128
<b>5</b>	<b>Selection of a suitable H<sub>2</sub>/O<sub>2</sub> reaction mechanism</b>	<b>133</b>
5.1	Introduction . . . . .	135
5.2	Modelling Requirements . . . . .	135
5.3	Approaches to simple reaction and transport models . . . . .	136
5.3.1	Flame prolongation of ILDM . . . . .	136

5.3.2	The global reaction concept . . . . .	136
5.4	Reduction to a global reaction model with complex thermodynamics and transport . . . . .	137
5.4.1	Analytical correlations for flame properties . . . . .	137
5.4.2	Procedure for reduction to a global reaction model . . . . .	138
5.5	Reduction to simple transport and thermodynamic properties . . . . .	140
5.6	Conclusions . . . . .	143
<b>6</b>	<b>Corner flames</b>	<b>145</b>
6.1	Introduction . . . . .	147
6.2	Edge flames . . . . .	147
6.3	Corner flames - Introduction . . . . .	150
6.4	Corner flames - Dimensional analysis . . . . .	153
6.4.1	Damköhler number based on characteristic times . . . . .	153
6.4.2	Damköhler number based on characteristic velocities . . . . .	154
6.4.3	Other dimensionless parameters . . . . .	154
6.5	Numerical study of a corner flame . . . . .	155
6.5.1	Introduction . . . . .	155
6.5.2	Validation of the numerical model . . . . .	155
6.5.3	Results - strain rate-controlled corner flame . . . . .	159
6.5.4	Results - convection-controlled corner flame . . . . .	166
6.6	Corner flames - conclusion . . . . .	173
<b>7</b>	<b>Flame over a condensed reactant</b>	<b>175</b>
7.1	Introduction . . . . .	177
7.2	Flame over a porous plate . . . . .	177
7.3	Dimensional analysis . . . . .	178
7.4	Analysis of a flame above a condensed fuel . . . . .	179
7.4.1	Stability of a flame over condensed fuel . . . . .	182
7.4.2	Numerical study of a flame over a condensed surface . . . . .	183
7.5	Conclusions . . . . .	183
<b>8</b>	<b>Flame stabilization behind a step over a liquid fuel</b>	<b>189</b>
8.1	Introduction . . . . .	191
8.2	Premixed flame stabilization behind a bluff body . . . . .	191
8.3	Non-premixed flame stabilization behind a splitter plate . . . . .	191
8.4	Flame stabilization behind a step over a porous plate . . . . .	193
8.5	Dimensional analysis . . . . .	195
8.6	Numerical platform . . . . .	195
8.7	Tests and results . . . . .	198
8.7.1	Non-dimensional step height, $\Psi$ . . . . .	198
8.7.2	Exposed flame . . . . .	199
8.7.3	Tucked flame - effect of Spalding transfer coefficient . . . . .	201
8.7.4	Tucked flame - effect of Damköhler number via changing hydrogen velocity . . . . .	201



8.7.5	Tucked flame - effect of Damköhler number - varying hydrogen temperature . . . . .	203
8.7.6	Heat transfer to the step . . . . .	204
8.8	Conclusion . . . . .	206
<b>9</b>	<b>Conclusions</b>	<b>213</b>
9.1	Flame structure and effect of recess . . . . .	216
9.2	Flame stabilization . . . . .	217
9.3	Ignition . . . . .	217
<b>A</b>	<b>Shadowgraphy and Schlieren techniques</b>	<b>219</b>
A.1	Introduction . . . . .	219
A.2	Ray deviation by a refractive index field . . . . .	220
A.2.1	General Formula . . . . .	220
A.2.2	Limit for Small Deviations . . . . .	222
A.3	Shadowgraphy . . . . .	223
A.3.1	Introduction . . . . .	223
A.3.2	Parallel ray shadowgraphy . . . . .	223
A.3.3	Diffused ray shadowgraphy . . . . .	227
A.4	Schlieren . . . . .	227
A.5	Three Dimensional Refractive Index Fields . . . . .	228
<b>B</b>	<b>Dispersion relation of a two-dimensional bounded wake flow</b>	<b>229</b>
<b>C</b>	<b>Conditions at a liquid/vapour interface</b>	<b>233</b>
C.1	Single component system . . . . .	233
C.1.1	Criteria for existance of a liquid/vapour interface. . . . .	233
C.1.2	Equilibrium at a liquid/vapour interface in a pure species. . . . .	234
C.1.3	Transport Properties and Heat Capacity. . . . .	234
C.2	Binary mixture . . . . .	234
C.2.1	Criteria for existance of a liquid/vapour interface. . . . .	235
C.2.2	Equilibrium at a liquid/vapour interface in a binary mixture. . . . .	235
C.2.3	Transport properties and heat capacity of the mixture. . . . .	236
C.3	Multi Component Mixtures . . . . .	237
C.4	Conclusion . . . . .	237
<b>D</b>	<b>Consumption rates in strained laminar diffusion flames</b>	<b>239</b>



# Introduction

Ce projet de recherche traite des problèmes d'écoulement dans les chambres de combustion des moteurs fusées à ergols liquides. On s'intéresse au cas spécifique où les ergols sont cryotechniques et on envisage essentiellement le couple oxygène liquide et hydrogène gazeux. Ces réactifs sont utilisés dans les moteurs à haute performance comme HM7, le moteur du troisième étage d'Ariane 4 ou Vulcain, le moteur de l'étage principal d'Ariane 5.

Parmi les nombreux problèmes qu'il faut envisager dans le développement d'un lanceur, deux points sont particulièrement importants: (1) La performance mesurée par le rapport de la charge utile à la masse d'ergols nécessaire et (2) La fiabilité du système.

La performance dépend pour une grande part des caractéristiques thermodynamiques des ergols et de l'efficacité de combustion dans le moteur. Le rendement de combustion est fonction de la forme des injecteurs et du dimensionnement général de la chambre. La performance globale du lanceur dépend aussi de la masse à vide. Pour augmenter l'efficacité structurale on peut s'orienter vers des ergols plus denses, par exemple  $\text{CH}_4$ , qui nécessite un réservoir moins volumineux que celui pour  $\text{H}_2$ .

L'amélioration des méthodes de conception de la chambre et des injecteurs passe par une meilleure connaissance des phénomènes et par le développement de méthodes de simulation numérique. Les modèles internes des codes numériques déterminent la qualité des simulations et leur amélioration passe par la connaissance détaillée de la structure de la flamme. Les conditions d'entrée du code doivent être aussi correctement formulées, ce qui souligne l'importance d'une étude de la région proche de l'injecteur. La première partie de ce mémoire traite des expériences réalisées sur un banc de combustion cryotechnique. Les paramètres qui affectent la structure de flamme sont déduits d'expériences systématiques réalisées sur une large gamme de pression, dans des conditions subcritiques et supercritiques. Une étude approfondie a été notamment développée pour comprendre l'effet du retrait du conduit d'oxygène par rapport au conduit d'hydrogène.

La deuxième partie de ce mémoire traite des problèmes de stabilisation de flamme. L'accrochage de la flamme est un sujet particulièrement important, bien maîtrisé en pratique mais encore insuffisamment étudié sur le plan théorique et numérique. Les conditions nécessaires à la stabilisation de la flamme sont étudiées soigneusement dans cette deuxième partie. L'analyse est développée en considérant des problèmes modèles successifs et en dégagant les paramètres sans dimension importants.

## Nomenclature

$C_F$	Thrust coefficient
$C^*$	Characteristic velocity
$F$	Force
$m$	Mass
$p$	Pressure
$r$	Gas constant
$t$	Time
$T$	Temperature
$\Delta V$	Velocity gain for a mission
<hr/>	
$\eta$	Combustion efficiency
$\gamma$	Ratio of specific heats
$\Gamma$	Reduced ratio of specific heats
<hr/>	
$\cdot_c$	at throat
$\cdot_e$	at exit plane
$\cdot_f$	final
$\cdot_i$	initial
$\cdot_0$	stagnation



## Rocket propulsion development and combustion science

The science of liquid rocket propulsion has progressed remarkably in the last sixty years. There is now a burgeoning commercial market, particularly for telecommunications satellites operating in geostationary orbits. This progression is possible due to accumulated engineering experience and, more recently, the application of results from the field of combustion science.

A typical launch system is shown in figure 1. It combines solid propellant boosters with liquid fuelled rocket engines. This research project is concerned with liquid fuelled motors, although some of the fundamental physics can also be applied to solid propellant boosters. In a typical motor, shown in figure 2, fuel and oxidizer are pumped through a number of injectors into a combustion chamber. These reactants can either be hypergolic, which ignite on contact, or they can require an ignition source. After reaction, the combustion products escape through a sonic throat into a divergent nozzle. The fluids accelerate in this element and are expelled into space, providing thrust. This research project is concerned uniquely with physical processes occurring in the combustion chamber. The main focus is on cryogenic fuels, which are stored at low temperatures and which require ignition. These fuels, usually liquid oxygen and hydrogen, are used in the Vulcain motor of Ariane 5 and in the Space Shuttle Main Engine. Certain aspects of this study are relevant to hypergolic and storable fuels.

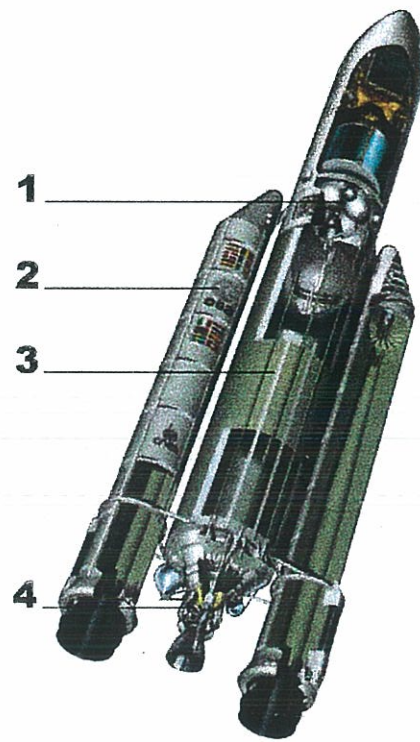
Early research into combustion in liquid rocket motors relied heavily on experiments. An important text book by Barrère et al. (1960) gives an idea of the state of the art some forty years ago. Tests on many injector designs led to rapid adoption of certain configurations. These include coaxial injectors like those in figure 3, which are the subject of this research project. A considerable amount of know-how has been accumulated in this manner with most effort being spent on resolving technical problems. There are, however, some fundamental scientific questions relating to the physical processes at work in the combustion chamber. These mainly concern ignition, flame stabilization, heat transfer to the walls of the chamber, sensitivity to perturbations and combustion instabilities.

Most of these questions require an understanding of the flame structure. This has always been difficult to obtain due to the harsh conditions prevailing in the chamber. The power of an average rocket combustion chamber is several gigawatts - the equivalent of a large nuclear power station - in a volume not much bigger than a kitchen sink. Consequently, even small scale testing is highly energetic and most experiments carried out in the early days of propulsion were limited by the available sensors, data acquisition methods and processing devices. The scientific analysis of cryogenic combustion has been envisaged only recently. This has benefitted from major advances in diagnostics, instrumentation and digital data acquisition. In addition, progress on the theoretical and numerical level has allowed detailed studies of the difficult problems raised in these investigations. The flame structures below and above the critical pressure of oxygen (50.5 bar) are shown in figure 4

## Technological motivation for this study

In recent years, the launch of space vehicles has moved away from its scientific and military roots to become a fully commercial activity. The primary source of revenue is communi-

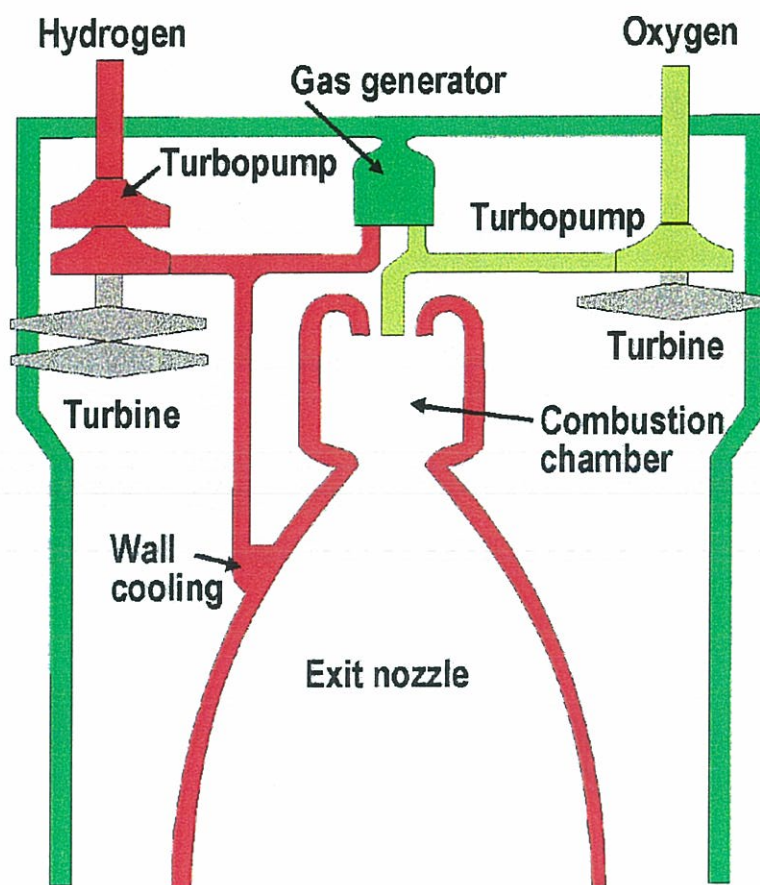




**Figure 1:** *The Ariane 5 rocket at take off. This launch platform consists of three types of motor, indicated in the cut-away image.*

1. *The third stage, which is lit once the second stage has been jettisoned, is fed by storable propellants. These liquid reactants require no ignition since they react on contact. In addition, they are forced into the reaction chamber under pressure from a helium reservoir. These factors greatly increase reliability but reduce efficiency because the fuels have a relatively high molecular mass and must be stored in heavy pressure vessels. A cryogenic third stage would be considerably more efficient if reliability problems could be resolved.*
2. *The solid propellant boosters provide 90% of the thrust at take-off. The solid propellant coats the inside walls of the boosters and also serves as a channel for the hot combustion products. The solid propellant boosters together with the main engine comprise the first and second stage.*
3. *The largest part of the launch platform is this large liquid hydrogen fuel tank. The spherical liquid oxygen tank can be seen above it.*
4. *The main engine, named Vulcain, burns liquid oxygen and gaseous hydrogen. This cryogenic stage is the most efficient but the least reliable. It is lit seven seconds before take-off in order to ensure that stable operating conditions are attained. Efficiency of the entire platform would be improved if this motor could be lit at the end of the solid propellant booster sequence. This motor is shown schematically in figure 2.*



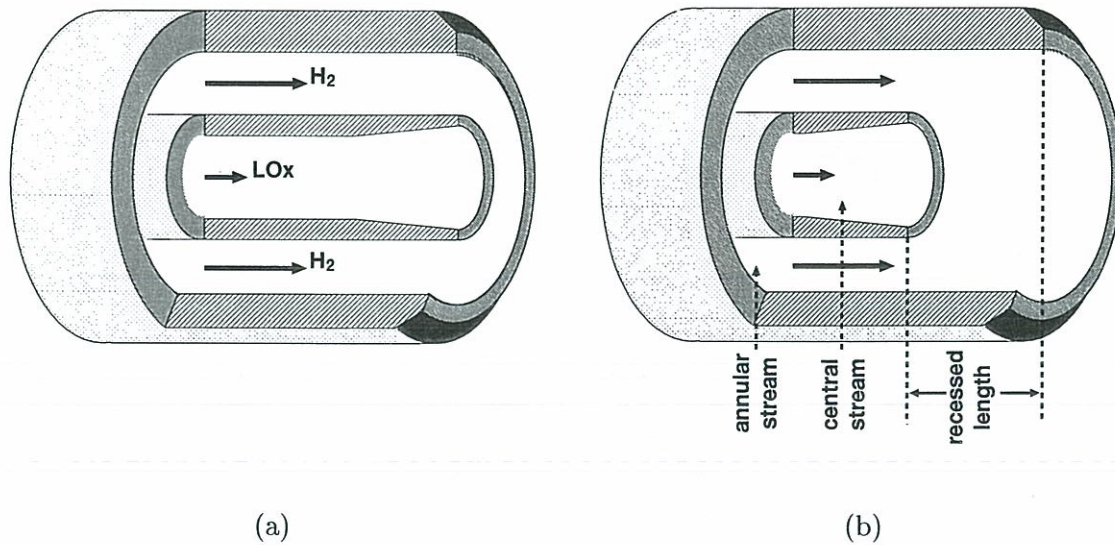


**Figure 2:** Schematic diagram of a cryogenic rocket motor. Oxygen is pumped directly from the reservoir to the chamber and enters as a liquid. Energy to drive the pumps is provided by a smaller cryogenic engine called the gas generator. Hydrogen is pumped through passages in the exit nozzle of the main engine before entering the combustion chamber. This cools the main engine and also ensures that the hydrogen is injected as a relatively light supercritical fluid, rather than a dense fluid. For convenience, in this research project, the hydrogen is said to be gaseous.

cations satellites, which are usually placed in geostationary orbit. Because these payloads have similar masses, launch vehicles can be specifically optimized for such missions. This is the rationale behind Europe's Ariane family of rockets, which has won a large share of the commercial market for geostationary satellite launch.

In the last decade, competition in this market has increased sharply. The new launchers are often based on technology developed in the 1960's, such as the Atlas family from Lockheed-Martin, Protons from Khrounitchev and Deltas from Boeing. Although not originally designed for geostationary missions, their proven reliability and relatively low capital investment could make these launch platforms commercially competitive.

In the fierce competition for the commercial market, the system which excels in both operational reliability and propellant efficiency will have a considerable advantage. These



**Figure 3:** Coaxial injectors of the type used in rocket motors. Liquid oxygen flows through the central tube and gaseous hydrogen through the annular passage. In figure (a) the oxygen tube is set flush with the hydrogen channel. In figure (b) the oxygen tube is recessed

two factors can be explained relatively simply.

### Operational reliability

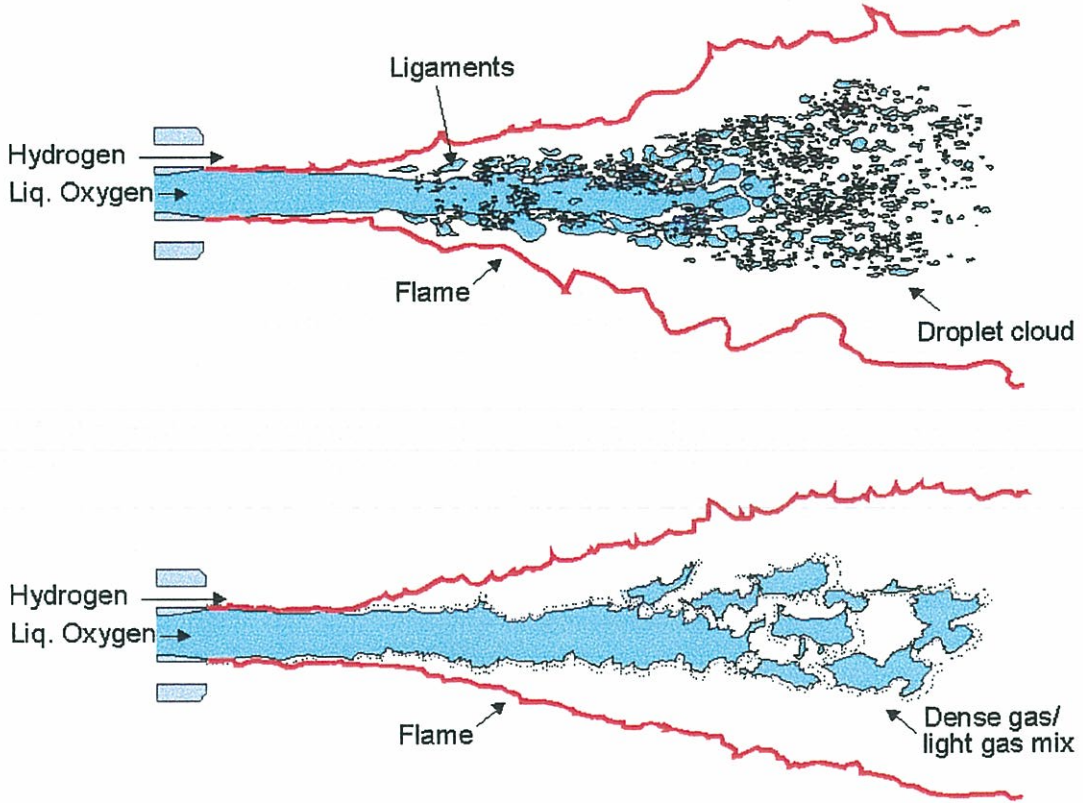
If a multi-billion dollar business plan depends on the operation of a given satellite by a certain date, the cost of a failed launch is much greater than the cost of the payload alone. When insurance is included, an expensive but reliable rocket may well be the most economic option.

The development of reliable engines has always been a difficult task, which has relied in the past on systematic full scale testing. One critical aspect is to ensure a smooth ignition transient before stable nominal operation is attained. Another aspect is to avoid instabilities associated with the resonant coupling of combustion and acoustic eigenmodes of the chamber. These lead to chamber burn-out by increasing heat transfer to the walls or cause vibrations which can destroy the payload. Combustion instability is intimately linked to flame holding within the combustion chamber, a subject which is tackled in detail here.

### Propellant efficiency

As an example of a typical launch system, the Ariane 5 rocket weighs 746 tonnes at take-off for a payload of 6.8 tonnes. The vast majority of the initial mass is fuel and oxidizer. To demonstrate the factors affecting performance, an expression for the take-off mass of a single stage rocket is developed here in terms of the final mass, the desired velocity increase





**Figure 4:** Diagrams of the structure of a cryogenic LOx/H<sub>2</sub> flame fed by a coaxial injector. Top: Below the critical pressure of oxygen (at 50.5 bar). Bottom: Above the critical pressure of oxygen.

and the thrust of the motor. The final mass comprises the payload and the empty mass of the stage.

The velocity increase for a rocket of mass  $m$  subject to force  $F$  between times  $t_i$  and  $t_f$  is obtained by integrating Newton's second law of motion:

$$\Delta V = \int_{t_i}^{t_f} \frac{F}{m} dt \quad (1)$$

In general, the velocity increase is determined by the desired orbit. For example, to reach a geosynchronous orbit one has to increase the velocity by at least  $12 \text{ kms}^{-1}$ . The force  $F$  is given by  $F = \dot{m}C_F C^* - gm$ , where the thrust coefficient,  $C_F$ , and the characteristic velocity,  $C^*$ , are defined as:

$$C_F = \Gamma(\gamma) \left( \frac{2\gamma}{\gamma-1} \left[ 1 - \left( \frac{p_e}{p_0} \right)^{\frac{\gamma-1}{\gamma}} \right] \right)^{1/2} + \frac{A_e}{A_c} \left( \frac{p_e}{P_0} - \frac{p_a}{p_0} \right) \quad (2)$$

$$C^* = \eta C_0^* = \eta \frac{(rT_0)^{1/2}}{\Gamma(\gamma)} \quad (3)$$

where:

$$\Gamma(\gamma) \equiv \sqrt{\gamma} \left( \frac{2}{\gamma+1} \right)^{\frac{\gamma+1}{2(\gamma-1)}}$$

Subscripts '0', 'e' and 'a' denote stagnation, nozzle exit and atmospheric conditions respectively. The factor  $\eta$  is the motor's efficiency, determined by the proportion of reactants which burn completely within the chamber.  $C_0^*$  is a property of the fuel only and is maximized for propellants with small molecular masses.  $\text{H}_2\text{O}$  has one of the lowest molecular masses for any combustion products, which is one reason why hydrogen and oxygen are particularly suitable for rocket propulsion.  $C_F$  depends on the chamber pressure and nozzle diameters and is generally determined by mechanical constraints. By substituting for  $F$  in equation (1), an expression for the take-off mass,  $m_i$  is obtained in terms of the final mass,  $m_f$ :

$$m_i = m_f \exp \left( \frac{\Delta V}{\eta C_f C_0^*} \right) \quad (4)$$

The gravitational acceleration integrated over the flight has been absorbed into  $\Delta V$ , which is the velocity change required for a particular mission.

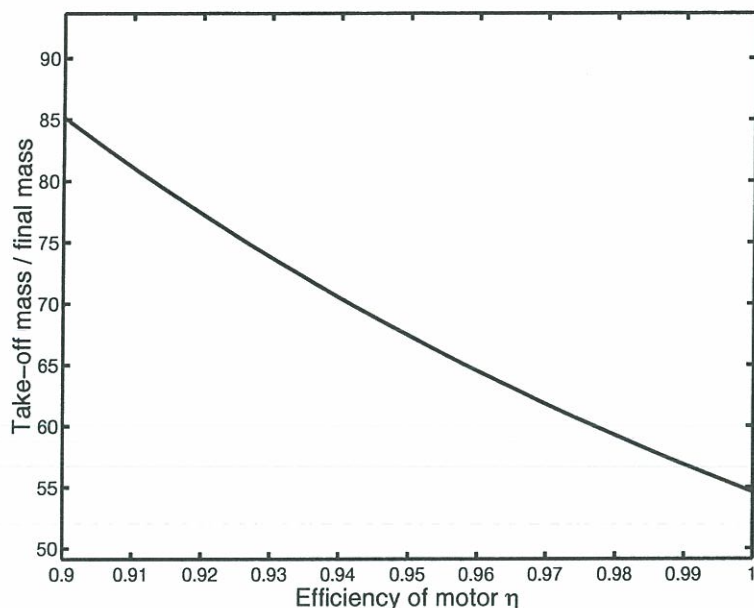
The graph in figure 5 shows how the take-off weight varies with  $\eta$  for a typical mission where  $\Delta V/(C_F C_0^*) = 4$ . Even a small efficiency gain leads to a significant reduction in take-off weight. However, the efficiency factor  $\eta$  is already between 0.98 and 0.99 in current rocket motors. There is little scope for improving it, although it is important to ensure that design changes in the motor do not lead to a reduction of this factor.

It can be inferred from equation (4) that a reduction in the empty mass of the rocket, which is a large proportion of  $m_f$ , will greatly reduce the amount of fuel required. This is particularly true of the third stage engine, since, unlike the other stages, it cannot be jettisoned before the final destination. In order to achieve a lighter structure, methane is being considered as a replacement of the hydrogen fuel. Liquid methane is much denser than liquid hydrogen and requires a smaller reservoir. On the other hand, the combustion products, which contain  $\text{CO}_2$ , have a higher molecular mass (lower gas constant  $r$ ) and therefore, by equation (3), a lower value of  $C^*$ . An optimization of these factors is beyond the scope of this study. However, the methodology developed in this research project is suitable for checking that using methane instead of hydrogen will not compromise reliability of the motor.

Current fuel injectors in cryogenic rocket motors are coaxial, as shown in figure 3. This project examines mainly this type of injector. Further methods of reducing manufacturing costs have been proposed, such as to reduce the number of fuel injectors by moving to a tri-coaxial design. Again, this must not compromise the efficiency or reliability of the motor. The work on the flame structure presented here will help in designing the tri-coaxial injector.

The lack of theoretical understanding already mentioned was highlighted to the Ariane community in 1985 and 1986 when the third stage motor, which at the time was cryogenic, twice failed to ignite. At that time the flame structure and ignition mechanism were not





**Figure 5:** *The efficiency,  $\eta$ , of a rocket motor has a strong effect on the performance of the entire stage. The performance for a typical mission is expressed here as the ratio of the mass at take-off to the final mass. In current motors, the factor  $\eta$  is 0.98 to 0.99 and any alterations to the design must not reduce this. Since the final mass comprises the payload and the empty stage, decreasing the mass of the empty stage can greatly enhance performance.*

well known. Consequently no model or numerical code existed which could reproduce the complexity of the physical situation. In 1989 a scientific research program was launched in order to understand the structure and physical processes in a cryogenic spray flame. In 1993 this was extended to the “GDR Combustion dans les Moteurs Fusées”, which comprised the following five topics:

- Physical processes involved in mixing and atomization
- Physical processes involved in combustion of sprays
- Development of experimental diagnostics applicable to cryogenic combustion
- Experimental measurements on an experimental cryogenic combustion facility (Mascotte)
- Development of numerical models

This research project deals with aspects of the first four of these questions. The first part, chapters 1 to 3, concerns the flame structure. This is studied under subcritical and supercritical conditions, relative to the critical pressure of oxygen at 50.5 bar. The effect of recessing the oxygen tube inside the hydrogen channel is also examined since this corresponds to most practical applications. The second part, chapters 4 to 8 concerns

the flame holding mechanism. This topic is approached by analyzing a series of generic problems which reveal the controlling parameters in carefully defined steps.

# Part I

## Structure of Cryogenic Spray Flames and Effect of Recess

Dans le domaine de la propulsion par fusée, la mise au point des moteurs a été très largement fondée sur l'utilisation d'essais systématiques. Un savoir-faire important a été ainsi accumulé et des succès remarquables ont été obtenus. Cependant, cette approche a des limites et on souhaite de plus en plus comprendre les phénomènes pour assurer leur maîtrise et améliorer les méthodes de conception. Un des objectifs actuels est le développement de méthodes de simulation fiables.

La connaissance des structures des flammes cryotechniques constitue un point central dans l'élaboration des modèles et l'optimisation de la chambre de combustion. Trois campagnes expérimentales sur un banc cryotechnique sont résumées chapitre 1. Les essais correspondent à des pressions de 10 à 70 bar. Des diagnostics optiques sont employés après une vérification de leur validité. La structure de la flamme est mise en évidence et on s'intéresse en particulier à la zone proche. Ces résultats sont combinés à ceux obtenus antérieurement (chapitre 2). Les résultats expérimentaux sont aussi comparés avec des calculs effectués au moyen d'un modèle simplifié de la flamme. Les paramètres qui pilotent la structure de la flamme peuvent être déduits. Il est remarqué qu'il y a un changement de comportement autour de la pression critique de l'oxygène ( $p_{crit} = 50.5$  bar). L'effet de la géométrie de l'injecteur sur le mélange et l'atomisation est examiné. On envisage, en particulier, l'effet du retrait du conduit d'oxygène liquide. Ce problème est analysé au chapitre 3 et plusieurs mécanismes sont proposés pour expliquer l'influence du retrait sur la structure de la flamme.

In high performance rocket propulsion, the engine design has largely been based on systematic testing. A considerable knowledge base has been accumulated, with impressive results, but the scope of this approach is limited. A greater understanding of the physical phenomena is desired in order to improve design methods. One current objective is the development of reliable methods of numerical simulation.

Knowledge of the cryogenic spray flame structure is essential for the development of numerical models and for optimization of the combustion chamber. Three experimental series on a cryogenic combustion facility are summarized in chapter 1 at pressures from 10 to 70 bar. Optical diagnostics are used and their validity is examined carefully in the text. The flame structure is observed very clearly and particular attention is paid to the region near the injector. In chapter 2, these results are merged with those obtained in previous projects. By comparing the experimental data with the results of a simple model, the factors affecting flame structure can be deduced. An interesting feature is the change around the critical pressure of oxygen ( $p_{crit} = 50.5$  bar). The effect of injector geometry on mixing and atomization is also reviewed. Recessing the LOx tube inside the hydrogen tube is known to improve combustion efficiency. This problem is analyzed in chapter 3 and likely mechanisms are proposed for the effect of recess on the flame structure.



## Chapter 1

# Experimental technique and results

Trois campagnes d'essais ont été menées sur le banc cryotechnique Mascotte, à l'Onera. L' étude des structures de flamme a été réalisée au moyen de diagnostics optiques: imagerie de l'émission naturelle des espèces présentes dans la flamme, spectroscopie de la flamme et prise d'images en rétroéclairage (nom générique pour désigner l'ombroscopie et la strioscopie). Des mesures de pression ont aussi été effectuées pour déterminer la perte de charge supplémentaire associée au retrait. Les diagnostics sont décrits dans la première partie de ce chapitre. On traite notamment du rétroéclairage pour comprendre la signification des images obtenues par cette méthode. Les points de fonctionnement, choisis pour les essais à basse pression, correspondent aux points déjà étudiés à 10 bar. Des expériences ont ensuite été réalisées à 70 bar et avec une température d'alimentation d'hydrogène ambiante, puis réduite.

Quelques images, notamment les images de synthèse, sont présentées ici mais les données sont consignées dans trois rapports de contrat de recherche: Tripathi et al. (1998), Tripathi et al. (1999) et Juniper et al. (2000)

## Nomenclature

$A$	Cross-sectional area
$C$	Head loss coefficient
$d$	Diameter
$E$	Mass flux ratio
$G$	Gradient: $\Delta p/(\rho U^2)$
$h$	Length in radial / vertical direction
$i$ or $I$	Intensity
$J$	Momentum flux ratio
$k$	Gladstone coefficient for refractive index calculations
$k_\lambda$	Absorption coefficient
$l$	Length in axial / horizontal direction
$\dot{m}$	Mass flowrate
$M$	Mach number
$n$	Refractive index
$p$	Pressure
$r$	Gas constant
$R$	Outer radius of flame
$S$	Signal received by camera
$U$	Velocity in axial / horizontal direction
$V$	Velocity ratio
$x$	Distance in axial / horizontal direction
$X$	Mole fraction
$y$	Distance in radial / vertical direction
$Z$	Parameter to quantify auto-absorption of OH
$\eta_{opt}$	Optical efficiency
$\gamma$	Ratio of specific heats
$\lambda$	Wavelength
$\rho$	Density
$\cdot_{H_2}$	Hydrogen stream
$\cdot_{LOx}$	Liquid oxygen stream
$\cdot_{O_2}$	Oxygen stream
$\cdot_t$	Throat
$\cdot_1$ to $\cdot_4$	Cross sections in figure 1.22

## 1.1 Introduction

This chapter contains a summary of three test series carried out on a cryogenic spray flame facility at Onera, Palaiseau. Called “Mascotte”, it consists of a single coaxial injector similar to those found in high performance liquid rocket engines such as the Vulcain of Ariane 5. The flame is enclosed within a combustion chamber capable of withstanding pressures of up to 100 bar. The chamber is 50 cm long and has a 5 cm × 5 cm cross-section. A visualization module, with 7 cm long windows on all four sides, can be placed at any point along the chamber. The windows are made from quartz, which does not block near-UV radiation. The power output of this device is around 1.5 MW. It is run by a team of engineers and technicians from Onera.

The third version, V03, of Mascotte is used in these experiments. Previous versions, V01 and V02, performed at similar injection conditions but at lower pressures. A full description of the high pressure experimental facility can be found in Vingert et al. (1997). Laser-induced fluorescence of OH radicals and elastic scattering from the oxygen jet were performed by Snyder et al. (1997) and Herding (1997), results which are also presented in Herding et al. (1997). A full review of the experimental investigations below the critical pressure of oxygen can be found in Candel et al. (1998). Laser-induced fluorescence of oxygen vapour is reported in Guerre et al. (1996) and Cessou et al. (1998). When combined with assumptions about the flame structure, for instance that a coherent flame model can be applied, this work permits an estimation of factors such as the oxygen consumption rate, the average reaction rate and the flame surface density. Atomization of the LOx jet is studied by Giquel (1997) and Vogel (1994). Le Visage (1996) and Carreau et al. (2001) have also studied the effect of recess on the LOx jet in cold flow. Work on similar injectors at high pressure has also been performed by Mayer and Tamura (1996) Mayer et al. (1998) and Ivancic et al. (1999).

The experiments presented in this document were performed in conjunction with Amita Tripathi. Sections marked by a dagger (†) are explained in more detail in her thesis: Tripathi (2001).

This chapter starts with a general overview of the aims of the three experimental series. Optical diagnostics are described in section 1.3. A further diagnostic based on measurement of the pressure drop across the injector is described in section 1.5.1.4. The experimental series are presented separately in sections 1.4, 1.5 and 1.6. These sections describe the configuration, selected results and some analysis. However, most of the discussion is reserved for chapters 2 and 3. In this way the results are grouped by topic rather than by experimental series.

## 1.2 Objectives of the Experiments

The initial aim is to determine the effects of various parameters on the flame structure. In later chapters, mechanisms are proposed for these effects and further experiments, numerical studies and theoretical arguments are developed in order to test these proposals.

Several parameters may affect the flame structure. These include: the Reynolds number, the Weber number, the velocity ratio  $V = U_{H_2}/U_{LOx}$ , the geometry  $d_{H_2}/d_{LOx}$ , the momentum flux ratio  $J = \rho_{H_2}U_{H_2}^2/\rho_{O_2}U_{O_2}^2$ , the mass flux ratio  $E = \dot{m}_{O_2}/\dot{m}_{H_2}$  and the pressure  $p$ . A limited number of variables can be altered on the test facility, such as



	Previous work (VO1/VO2)	New results (VO3)
$p$ (bar)	1, 5, 10	10, 70
$J$	Point C: $J = 6.3 \rightarrow 6.5$ Point D': $J = 9.8 \rightarrow 10.2$ Point A: $J = 13.4 \rightarrow 14.5$	Point C: $J = 3.0 \rightarrow 8.0$  Point A: $J = 9.0 \rightarrow 13.0$
Recess ( $d_{LOx}$ )	0, 1	0, 1, 1.5
$T_{H_2}$ (K)	298 K	298 K $\rightarrow$ 100 K


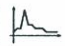

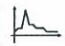









**Table 1.1** : Operating points of the cryogenic test facility

injector geometry, exhaust nozzle throat diameter and mass flowrates. Consequently it is impossible to vary each parameter separately. Instead, it is necessary to study only the parameters judged *a priori* to be the most influential.

Hopfinger and Lasheras (1994) suggest that the momentum flux ratio is the most influential parameter in determining the rupture of the central fluid in a coaxial jet. The pressure is influential when the oxygen jet passes from a subcritical to a supercritical state, which occurs at 50.5 bar. It has been observed that recessing the LOx tube inside the hydrogen tube has a significant effect on jet break-up and a deeper understanding of this is desired. An opportunity also arose to study the effect of the inlet hydrogen temperature, which might affect the stabilization of the flame and the flame structure.

The operating points are summarized in table 1.1. The momentum flux ratio is the hardest parameter to keep constant because it depends on the ratio of the square of the velocities. The desired pressure is also difficult to achieve every time. There is, therefore, some dispersion in the values of these parameters.

The three experimental series presented here are summarized in table 1.2. The first is a repeat of Herding's results at 10 bar using the version V03 of Mascotte. This is to verify that the new chamber does not alter the characteristics of the flame and to check the optical diagnostics. It is described in detail in section 1.4. The second, which contains the most thorough set of results, is at 70 bar. It is described in detail in section 1.5. In the third the hydrogen temperature is reduced from 290K to 110K with either  $J$  or  $E$  constant. The thickness of the hydrogen annulus is also reduced to 7.5mm. This injector geometry is identical to the P8 test facility at the DLR, Lampoldhausen.

	Series 1	Series 2	Series 3
Point	10 bar	70 bar ( $T_{H_2} = 290K$ )	70 bar (recess = 0)
A	recess $0,1,1.5 \times d_{LOx}$  	recess $0,1,1.5 \times d_{LOx}$   	$T_{H_2} = 290K, 110K$  
C	recess $0,1,1.5 \times d_{LOx}$  	recess $0,1,1.5 \times d_{LOx}$   	$T_{H_2} = 292, 224, 211, 136K$ 



OH\* spontaneous emission, H<sub>2</sub>O thermal emission and shadowgraphy.



Spectroscopy.



Pressure measurements across the injector.



Small hydrogen injector.

**Table 1.2 :** Operating conditions of the experimental series

## 1.3 Optical Diagnostics

### 1.3.1 Introduction †

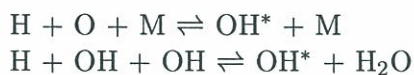
In the early days of combustion research, experiments were limited by the available sensors and the difficulty of obtaining good optical access to a chamber at high temperature and pressure. Great advances have been made since then. For cryogenic flames the introduction of Mascotte, combined with rapid data acquisition, permits optical diagnostics with high spatial and temporal resolution. There are three main groups of optical diagnostics: laser techniques, chemiluminescence (emission) and refractive index visualizations. Previous experimental series on Mascotte between 1 and 10 bar have made use of Laser Induced Fluorescence of OH and elastic scattering of a laser sheet to view the flame front and oxygen jet surface simultaneously. However, at high pressures, collisional quenching overtakes fluorescence as the major de-excitation mechanism of laser-stimulated OH radicals. Furthermore, the large refractive index gradients present in the chamber cause excessive diffusion of the laser sheet. Consequently the signal level at high pressure is decreased and PLIF becomes impractical. Due to the small number of experimental runs on the facility, the more reliable techniques of chemiluminescence and refractive index visualizations are used. Recently Cessou et al. (2001) have demonstrated that Raman imaging of the LOx jet can work at 60 bar. This is because the Raman signal increases with pressure.

Chemiluminescence of excited OH\* radicals and H<sub>2</sub>O molecules is discussed in section 1.3.2. Refractive index visualisations, under the name “Backlighting” are discussed in section 1.3.3 and appendix A.

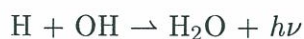
### 1.3.2 Imaging of chemiluminescence of OH\* and H<sub>2</sub>O †

#### 1.3.2.1 Chemiluminescence of OH\* and H<sub>2</sub>O †

At ambient pressure, excited OH\* radicals are created from two reactions, as indicated for example by Dandy and Vosen (1992).



These reactions involve atomic hydrogen, atomic oxygen and OH radicals, species which are only found in the flame front. It is assumed that these, or similar, reactions prevail at high pressure. Once created, OH\* typically releases a photon within 1.5  $\mu\text{s}$  or is de-excited by collision. This time is considerably shorter than typical convection or diffusion times in the chamber, meaning that OH\* emission is a suitable tracer of the flame front. OH\* radiates between 300 nm and 330 nm. The radical OH can also give rise to a background radiation over a range between 300 nm and 700 nm. From the results of Gaydon (1974) most of this background emission comes from the reaction



which is also associated with the flame front.

On the other hand, the combustion product, H<sub>2</sub>O, is thermally excited. Emission from these molecules, which is in the red spectrum, indicates the regions containing hot



products. Filters are used to separate UV emission from red emission and images are recorded with intensified CCD cameras. The flame spectrum is obtained in order to check that this emission corresponds to the expected lines of OH\* and thermally excited H<sub>2</sub>O emission. Certain sequences are averaged and processed with the Abel inversion, described in section 1.3.2.3 in order to reconstruct a slice of the flame.

### 1.3.2.2 Absorption of OH\* spontaneous emission within the combustion chamber †

It is shown in section 1.3.2.3 that absorption has a subtle effect on the image obtained via the Abel inversion. Ground state OH is the only species which appreciably absorbs OH\* emission. See, for example, Pearce and Gaydon (1965) and Davidson et al. (1996). To estimate its magnitude the Bouguer-Lambert relation is used:

$$I/I_0 = \exp\left(-k_\lambda p \int_l X_{OH} dl\right)$$

where  $k_\lambda(\lambda)$  is the OH absorption coefficient,  $p$  is the pressure,  $X_{OH}$  is the molar fraction of ground state OH and  $l$  is the path length. The absorption coefficient,  $k_\lambda$ , is taken to be  $20 \text{ atm}^{-1}\text{cm}^{-1}$ , which is the highest value found by Davidson et al. (1996) and occurs at 306 nm. In the combustion products, where  $X_{OH} \sim 10^{-5}$  and  $l \sim 5 \text{ cm}$ ,  $I/I_0 = 90\%$ , so they cause negligible absorption. In the flame front, however,  $X_{OH}$  can be up to 0.2 and absorption is not negligible. This absorbed radiation is either re-emitted or dissipated thermally.

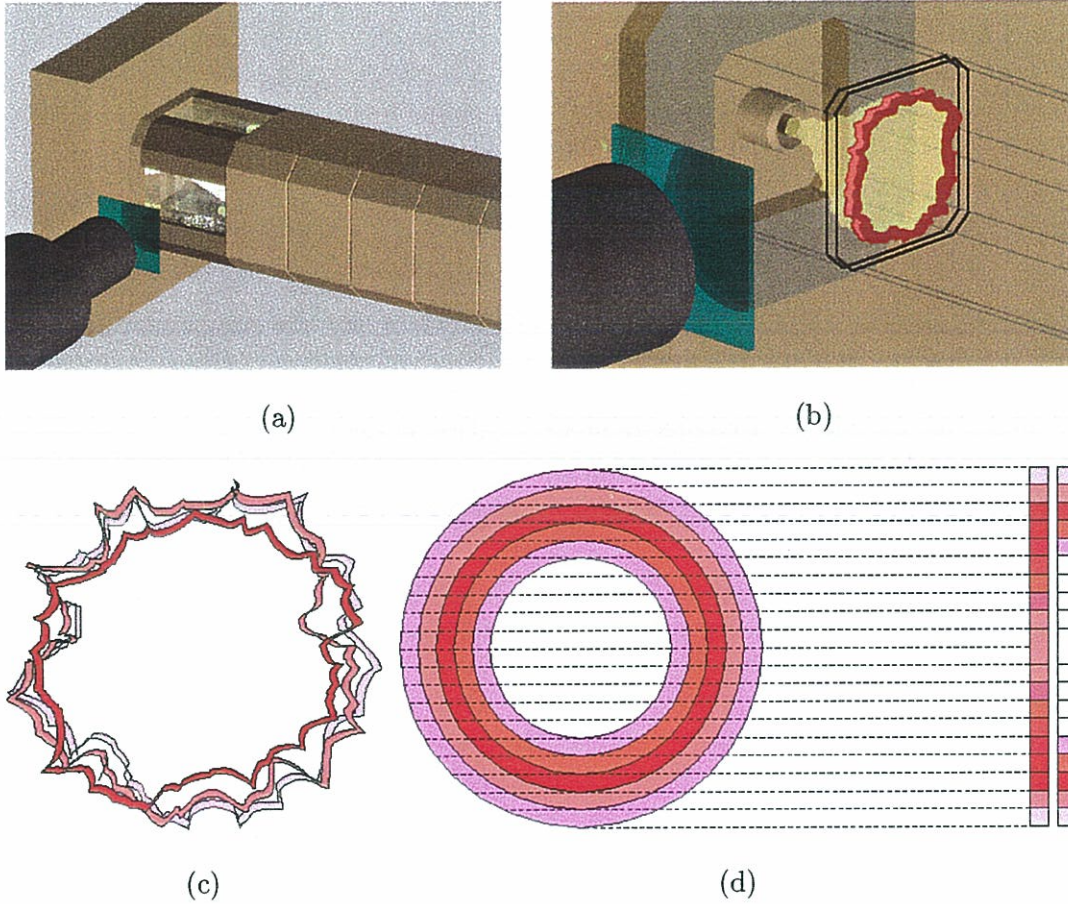
### 1.3.2.3 The Abel Inversion †

The emission intensity distribution (the flame shape) varies in space and time but is axisymmetric in the mean. The image is viewed from the side and emission is accumulated along the line of sight, as shown in figure 1.1. The average radial intensity distribution can be calculated from the average image via the Abel inversion, if there is no absorption. The axisymmetric distribution is assumed to be made up of a series of concentric rings. To calculate the contribution of an inner ring, the contribution of the rings outside it is subtracted from the cumulative image along the line of sight, assuming zero absorption. Working from the outside to the inside, this enables the contribution from each ring to be determined. Around the axis the process is particularly sensitive to error, which accumulates here.

The Abel inversion gives a slice of the mean volumetric OH\* emission distribution. PLIF images, when averaged, give the mean of a slice of the OH distribution. In a distribution which is axisymmetric on average, a slice of the mean is equivalent to the mean of a slice. This has been confirmed by Herding (1997), who compared the Abel inversion with averaged PLIF images at low pressure. The peak of the OH concentration (from PLIF) corresponded exactly with the peak of OH\* emission (from the Abel inversion). Coincidence of the peaks of OH\* and OH is expected at the flame front. This confirms the validity of the Abel inversion when there is little absorption.

At high pressure there is appreciable absorption of OH\* emission by OH radicals. In this section, the effect of selfabsorption on an axisymmetric flame is examined by





**Figure 1.1:** *The principle of the Abel inversion is demonstrated for a section of the flame. The camera is placed next to the side window of the facility (a) and sees the instantaneous intensity distribution integrated along the line of sight, (b). A sequence of these images (c) is averaged over time to give the average intensity distribution (d), which is axisymmetric. The integrated profile which is seen by the camera is the first profile on the right. The Abel inversion consists of calculating the radial intensity distribution, shown on the far right, from the integrated distribution. An “onion peeling” method is used, whereby the intensity of the outer layer is recorded and its contribution then subtracted from the remaining layers.*

simulation. Each simulation calculates the image that a camera would see when viewing a thin cylindrical self-absorbing flame from the side. The signal  $S(y)$  is calculated via equation (1.1), where  $y$  is the vertical distance from the centreline,  $R$  is the outer radius of the flame,  $\eta_{opt}$  is the optical efficiency of the apparatus,  $i_0(x, y)$  is the emission intensity and  $X_{OH}(x, y)$  is the mass fraction of absorbing species at position  $(x, y)$ . Because the OH profile is not known precisely at 70 bar, it is varied in the following simulations, each



being characterized by  $Z \equiv \int X_{OH} dl$  across the entire flame front.

$$S(y) = \eta_{opt} \int_{-\sqrt{R^2-y^2}}^{+\sqrt{R^2-y^2}} i_0(x, y) \exp \left( - \int_x^{+\sqrt{R^2-y^2}} k_{\lambda p} X_{OH}(x', y) dx' \right) dx \quad (1.1)$$

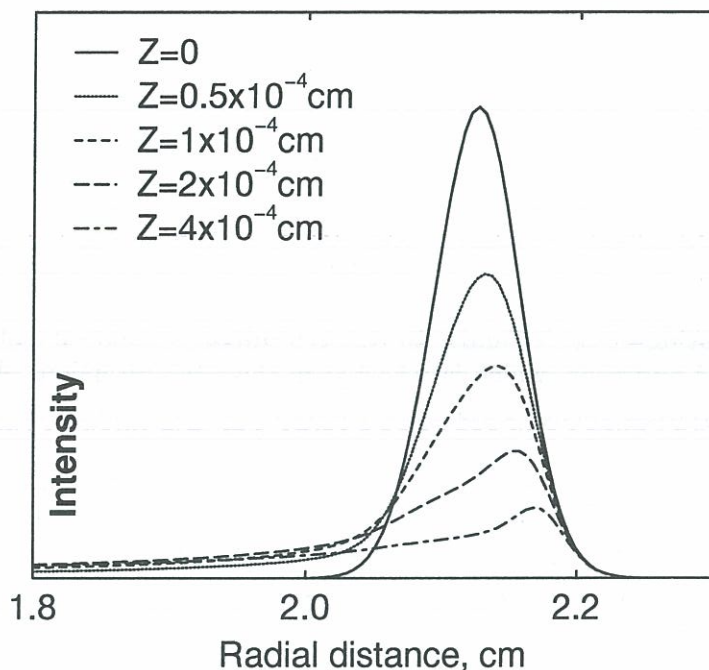
In the simulations, the emission and  $X_{OH}$  profiles are assumed to follow the same Gaussian distribution. For ease of demonstration, the flame thickness and emission intensity are held constant while the maximum  $X_{OH}$  value changes for each simulation, thus representing different values of  $Z$ . Then the Abel inversion of this image is calculated. Results with absorption are shown in Fig. 1.2. With zero absorption this is identical to the radial emission profile. As absorption increases, the apparent flame position shifts to a larger radius. This is because the camera only sees the outer edge of the nearest half of the flame. The resulting image is similar to half the full axisymmetric distribution but with the flame shifted outwards, which is reflected in the Abel inversion. Also, the apparent intensity of the central portion rises slightly because the absorption path length is greater at the top and bottom of the circular flame than at the centre.

The flame is much thinner than the distance over which its radial position fluctuates through turbulence. Even if the camera only sees the outer layer of the flame, on average the effect of this displacement is negligible compared with the effect of the turbulent fluctuation. Thus the position of maximum intensity on the Abel-inverted average image will be the same with or without absorption. However, the intensity level will be different. Also, the Abel inversion of the averaged images will yield higher intensities in the central region than are actually present in the radial intensity profile.

Even with appreciable absorption in the flame front, the Abel inversion gives a good indication of the flame's position, if not its intensity. It should be remembered that the Abel inversion shows the flame's residence time at a point multiplied by its intensity. The highest values are usually seen near the injector, where the residence time is high.

#### 1.3.2.4 Absorption and Scattering by the Oxygen Jet

Absorption by liquid oxygen, which occurs between 327 and 330nm, is weak. However, light is scattered by the strong refractive index gradients at the edge of the jet. At the surface of supercritical oxygen the density changes from  $1100 \text{ kgm}^{-3}$  to  $100 \text{ kgm}^{-3}$  in somewhat less than 1 mm, as can be deduced from the detailed simulations of Oefelein and Yang (1998). The light deviation angle can be estimated as  $\theta = \partial n / \partial y = k \partial \rho / \partial y \approx 10^\circ$  (from Gladstone's law, where  $k = 2 \times 10^{-4} \text{ kg}^{-1} \text{ m}^3$  for oxygen at atmospheric conditions). Additionally, near the critical point appreciable density fluctuations of the same scale as the wavelength of light give rise to critical opalescence. The critical pressure of a mixture of  $\text{O}_2$  with  $\text{H}_2$  or  $\text{H}_2\text{O}$  is greater than the critical pressure of pure  $\text{O}_2$ , at 50.5 bar, so it is possible that parts of the jet are opalescent at 70 bar. The net effect is that the oxygen jet shields emission from the rear portion of the flame, while also scattering some light from other parts of the flame towards the camera. Note that if absorption of OH emission within the flame is high, the jet will not be seen. In any case, its effect is limited to the central portion of the Abel inversion, corresponding to the predominant position of the jet. There is little or no flame surface there so it is permissible to ignore this part of the Abel inversion. In summary, neither critical opalescence nor scattering from the jet will interfere with the relevant parts of the Abel inversion.



**Figure 1.2:** Apparent radial emission profiles calculated via the Abel inversion of a flame with various degrees of self-absorption, which is quantified by  $Z$ . At  $Z = 0$ , which corresponds to zero absorption, the Abel inversion gives the exact emission profile. As absorption increases, the apparent radius of maximum intensity increases, as does the apparent intensity in the central region.

### 1.3.2.5 Image processing procedure †

Sequences of images are recorded with intensified CCD cameras. Exposure times are either short ( $\sim 100$  ns), in order to capture instantaneous phenomena, or long ( $\sim 4$  ms), in order to produce smooth average images. Images at stable operating conditions are averaged and then filtered to remove high frequency noise. The Abel inversion is performed on the top and bottom halves separately. The images are often stained due to deposits which form on the visualisation window and liquid water which recirculates in the cool region near the injector.

## 1.3.3 Backlighting

### 1.3.3.1 Introduction

In shadowgraphy and schlieren techniques, which have the generic name “backlighting”, a fluid flow is examined by recording the way it deflects light. This well established technique has the advantage that the apparatus is relatively simple, is reliable and can be set up and calibrated when the flame is not present. It has been used successfully by Mayer and



Tamura (1996) and Ivancic et al. (1999) in similar cryogenic flame experiments. This is convenient when the number of tests is severely limited, as is the case on the cryogenic test facility. However, the images require careful interpretation. Appendix A contains a detailed description of how shadowgraphy and schlieren images are formed from a refractive index field. It is summarized below.

### 1.3.3.2 Shadowgraphy

A shadowgraph is formed uniquely from the deflection of light. To a first approximation, the intensity at a point on the image is proportional to the second derivative of the refractive index there:  $\partial^2 n / \partial y^2$ . Two configurations can be distinguished. In the first, parallel rays are used. These are formed for example by a point source of light being placed at the focal point of a lens behind the test section, as shown in figure 1.3a. In the second, diffused light is used; figure 1.3b. This is formed by replacing the point light source with a large source, or by placing a piece of frosted glass between the source and the test section. The first configuration is more sensitive than the second.

If light is blocked at any point in the system, for instance by impinging on the aperture of the camera lens or by non-perfect alignment of lenses, the image of that region contains schlieren effects. These can easily pass unnoticed as they occur where the shadowgraphy effect is strongest. A sign of a schlieren effect is a dark region without an adjoining light region. A diffused light configuration is less susceptible to schlieren effects.

### 1.3.3.3 Schlieren

Schlieren images are created by blocking an amount of light which is proportional to its deflection in the test section. A large source of light is generally used to obtain some graduation in this effect. To a first approximation the intensity at a point is proportional to the first derivative of the refractive index:  $\partial n / \partial y$ .

### 1.3.3.4 Three dimensional refractive index fields

The simplistic interpretations of shadowgraphy and schlieren images as providing maps of  $\partial^2 n / \partial y^2$  and  $\partial n / \partial y$  assume that  $n$  is constant along the ray's path. This is not the case in three dimensional refractive index fields.

It can be shown that the deflection due to an axisymmetric field is identical to that from its central plane - the contributions from the far and the near sides cancel out exactly. However, for non-axisymmetric objects, there is not enough information to deduce the refractive index field. Nevertheless, areas of strong contrast indicate that a ray encountered a strong perpendicular refractive index gradient at some point along its path. To a first approximation, the shadowgraphy or schlieren image is that of a slice through the central plane of the object. Superimposed on this are the effects from behind or in front of this plane but these are usually less intense.

### 1.3.3.5 Appropriate techniques for the cryogenic combustion facility

It is more informative to read this section after reviewing the experimental results in the rest of this chapter.



The first priority in any configuration is that the light source for the backlighting apparatus is more intense than the emission of the flame. This can be achieved in many ways. In the first two series, a spark flashlamp is synchronized with the shutter of an ICCD camera. In the third, a diffused continuous source is used in conjunction with filters which block most of the flame's radiation. The details are in sections 1.4.1.3 and 1.5.1.3.

In the combustion chamber of Mascotte there are very high refractive index gradients, which increase linearly with pressure. Consequently, ray deviations are large, typically of the order of  $1^\circ$  in the flame and  $10^\circ$  at the edge of the jet. A small light source leads to a very sensitive schlieren apparatus, which would not be suitable for such high ray deflections. Thus use of the spark flashlamp dictates that shadowgraphy techniques are the most appropriate.

Even then, a careful examination of the results shows that there are significant schlieren effects in the shadowgraphy images at high pressure. These arise because some rays are being blocked by the iris of the camera lens or at other points along the optical path. The iris is circular, so this particular schlieren effect is independent of the direction of the deviation of the rays. It is particularly noticeable in the near-injector region where the refractive index gradients around the flame are strongest. It does not reduce the utility the images but it does make it harder to distinguish the flame from the jet in the near-injector region.

In order to reduce this effect, a diffuse light source was used in the final series. In this way, the rays pass through the chamber over a spread of angles, rather than being parallel. Even at areas of relatively strong refractive index gradient, some of those rays pass through the iris. It is only at the surface of the oxygen jet that the refractive index gradients are strong enough to completely scatter the light. Consequently the jet appears black, while the gaseous regions let some or most of the light pass. This produces clearer images of the jet.

Decker et al. (1998) have compared simultaneous shadowgraphs and Raman images of a supercritical nitrogen jet discharging into a nitrogen atmosphere. These authors demonstrate clearly that packets of light gas, which are entrained within the dense gas, are not seen in the shadowgraphs. This is because the shadowgraphs are integrated along the line of sight, whereas the Raman images show a slice of the jet.

Use of a laser in conjunction with thin band-width filters has been suggested as a convenient light source. Care must be taken to diffuse the laser light so that it is not in phase as it passes through the chamber. This would lead to interference fringes around every deformation on or in the windows, which quickly become stained. This technique has recently been put in place by P. Gicquel at ONERA with good results.

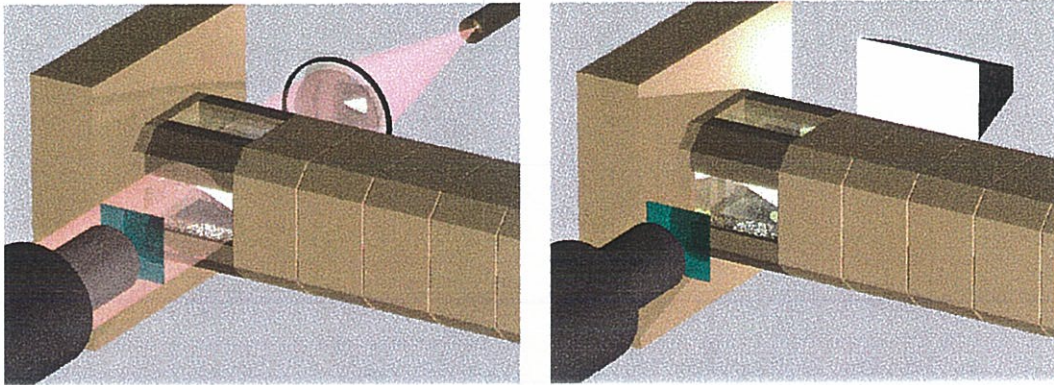
Appendix A demonstrates how a shadowgraph can be inverted to obtain an objects deflection profile. Although this requires cleaner images than can be achieved on the cryogenic combustion facility, the knowledge itself is extremely useful for the design of the apparatus. This work enabled a vast improvement to be made in the backlighting configurations between the first and the second experimental test series.

### 1.3.4 Summary

Emission from  $\text{OH}^*$  radicals provides a good tracer of the flame front. Emission from  $\text{H}_2\text{O}$  molecules should show the position of hot products. The Abel inversion of averaged

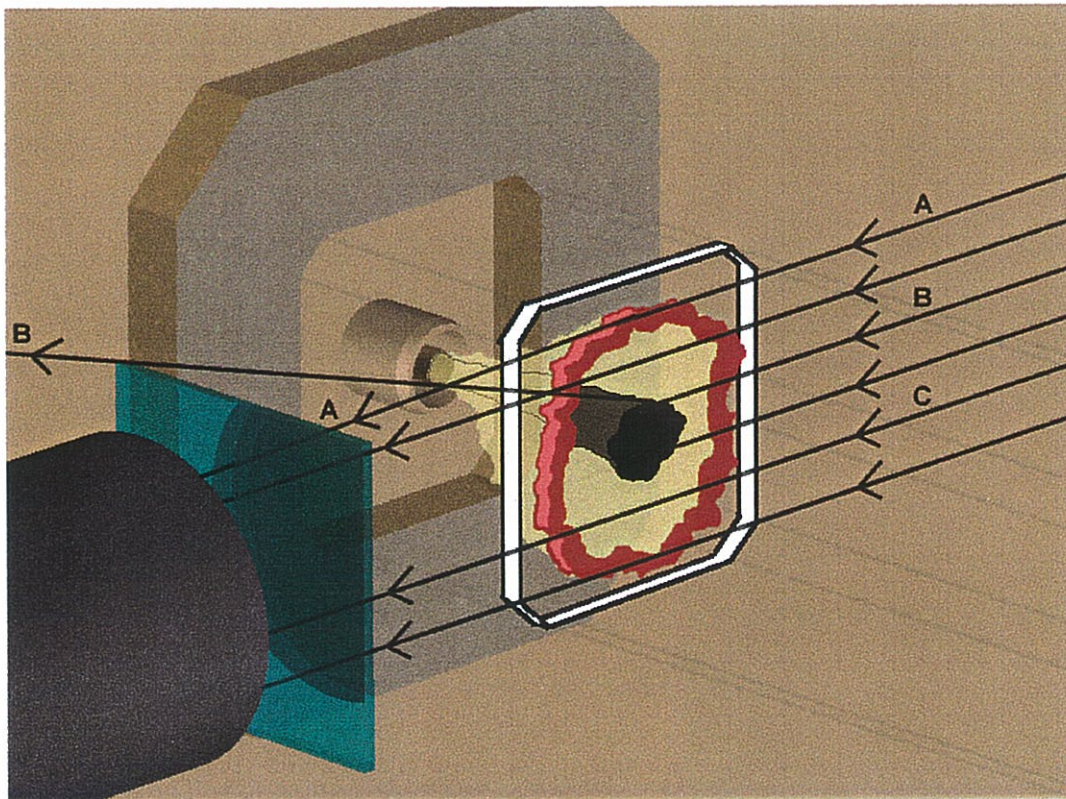
images is equivalent to a slice of the average volumetric intensity distribution. This is qualitatively similar with or without absorption. Backlighting is used to find the position of the dense oxygen jet and strong refractive index gradients in the gas.





(a)

(b)



(c)

**Figure 1.3:** (a) Parallel ray shadowgraphy configuration and (b) Diffused ray shadowgraphy configuration. In (a) a lens placed in front of a point source ensures that parallel rays pass through the test section, where they are deviated. This is shown in figure (c). For example, ray A is slightly deviated by the high refractive index gradient at the flame front. Ray B is strongly deviated by the edge of the condensed jet and misses the camera. Ray C passes with minimal deflection. The diffused ray configuration is less sensitive to slight deviations for the reasons described in appendix A



## 1.4 First test series, 10 bar

### 1.4.1 Experimental configuration †

The first experimental series repeats tests at the operating points studied by Herding (1997) at 10 bar. This is necessary in order to check that the two versions of Mascotte (V02 and V03) are comparable. It also allows the optical diagnostics to be perfected before the second and third series at high pressure. Two values of  $J$  are chosen:  $J=6.2$ , which characterizes a poor atomization of the liquid oxygen jet and  $J=14.5$ , which characterizes good atomization. The LOx tube is recessed to three different positions: zero recess,  $1 \times d_{LOx}$  and  $1.5 \times d_{LOx}$  inside the hydrogen tube. The last value of recess has not been previously examined. The injection conditions are summarized in table 1.3. The configuration of optical diagnostics is shown in figure 1.4.

More detail in sections which are marked with a dagger (†) can be found in Tripathi (2001).

#### 1.4.1.1 Spectroscopy †

A beam-splitter sends a small proportion of the light from the bottom window towards a CCD spectrometer via a mirror and a slit, which isolates emission from 3cm in front of the injector. The resolution,  $\Delta\lambda$ , is 0.15 nm.

#### 1.4.1.2 OH\* and H<sub>2</sub>O emission †

Emission of OH\* radicals in the ultra-violet is viewed directly from the side with an intensified CCD camera (ICCD). Three filters (one UG-5 and two WG-305) are used to let past light only between 300 nm and 400 nm. With an estimation of typical velocities in the chamber, the exposure time of 10  $\mu$ s is chosen to ensure that the images are not blurred. Emission from H<sub>2</sub>O molecules in the red and infra-red is viewed with an ICCD through the bottom window via a mirror. A filter which lets past light only between 550 nm and 720 nm is used in conjunction with a neutral density filter which reduces the intensity reaching the camera. The exposure time of 2 ms is chosen in order to produce smooth average images.

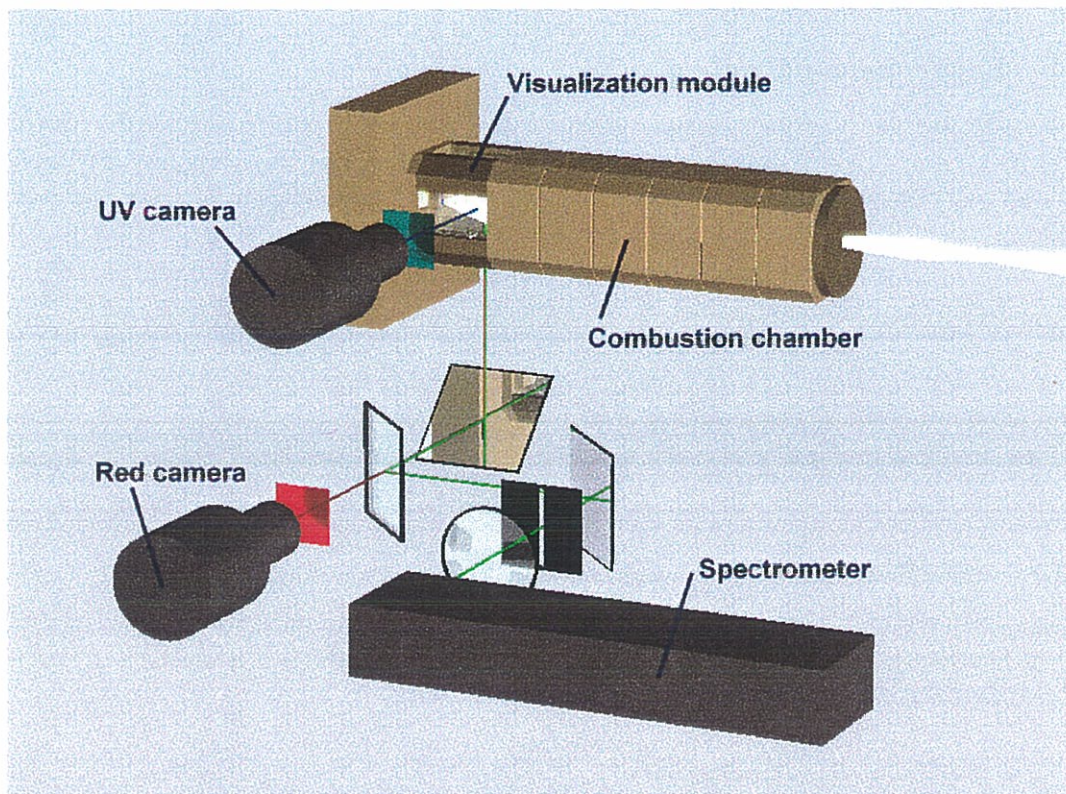
#### 1.4.1.3 Backlighting

The backlighting set-up is shown in figure 1.5. The oxygen jet and sharp refractive index gradients in the gas can be seen with this technique. In the first series, backlighting is evaluated as a possibility for the series at high pressure. For this reason, the configuration is reasonably simple and small lenses are used. Only the first 30mm of the chamber are visible. The configuration is substantially improved for the second and third series.

### 1.4.2 Results

There were around 20 successful experimental runs at 10 bar. Some results are summarized in this section. Other results appear, grouped by topic, in chapters 2 and 3. Complete results can be found in Tripathi et al. (1998), with the technical points and a list of problems which were overcome.





**Figure 1.4:** *Experimental configuration of the first experimental series. The UV camera records  $OH^*$  emission. Emission through the bottom window is shared between the red camera, which views emission of hot products, and the spectrometer.*

#### 1.4.2.1 Spectroscopy †

The spectrum of the flame at 10 bar is shown in figure 1.6 between 300 and 800 nm. The spectral positions of the UV filters and red filter are also shown. The peaks of the emission in the UV range correspond well with the theoretical emission bands of the electronic transition  $A^2\Sigma^+ \rightarrow X^2\Pi$  of OH Gaydon (1974). This suggests that the chosen filter is isolating  $OH^*$  emission. On the other hand, some of the emission in the red range comes from the second order spectrum of the UV emission. Of course, this does not appear in the  $H_2O$  images because it is simply an artefact of the spectrometer. However, it interferes with the signal from thermally excited species and makes it impossible to verify the origin of the emission in this range. The notation “ $H_2O$  emission” is retained for convenience, although emission may actually come from other hot species.

#### 1.4.2.2 $OH^*$ and $H_2O$ Emission †

Figure 1.7 shows instantaneous emission; average emission and a slice of the mean volumetric emission intensity calculated by the Abel-inversion process for both  $OH^*$  and  $H_2O$ . The  $H_2O$  images are smoother because the exposure time is longer. These results are used



Name	$p$ (bar)	$d_{H_2}$ (mm)	$d_{LOx}$ (mm)	$\dot{m}_{GH_2}$ (gs <sup>-1</sup> )	$\dot{m}_{LOx}$ (gs <sup>-1</sup> )	$U_{GH_2}$ (ms <sup>-1</sup> )	$U_{LOx}$ (ms <sup>-1</sup> )	$E$	$J$
A-10	10	10	5	22	47	303	2.1	2.1	14.5
C-10	10	10	5	15	47	198	2.1	3.1	6.2

**Table 1.3:** Operating conditions for the first experimental series. The mass flow ratio is  $E = \dot{m}_{LOx}/\dot{m}_{H_2}$ . The momentum flux ratio is  $J = \rho_{H_2}U_{H_2}^2/\rho_{LOx}U_{LOx}^2$ .

in the discussion on flame structure and flame expansion in chapter 2 and in the discussion on the effect of recess in chapter 3.

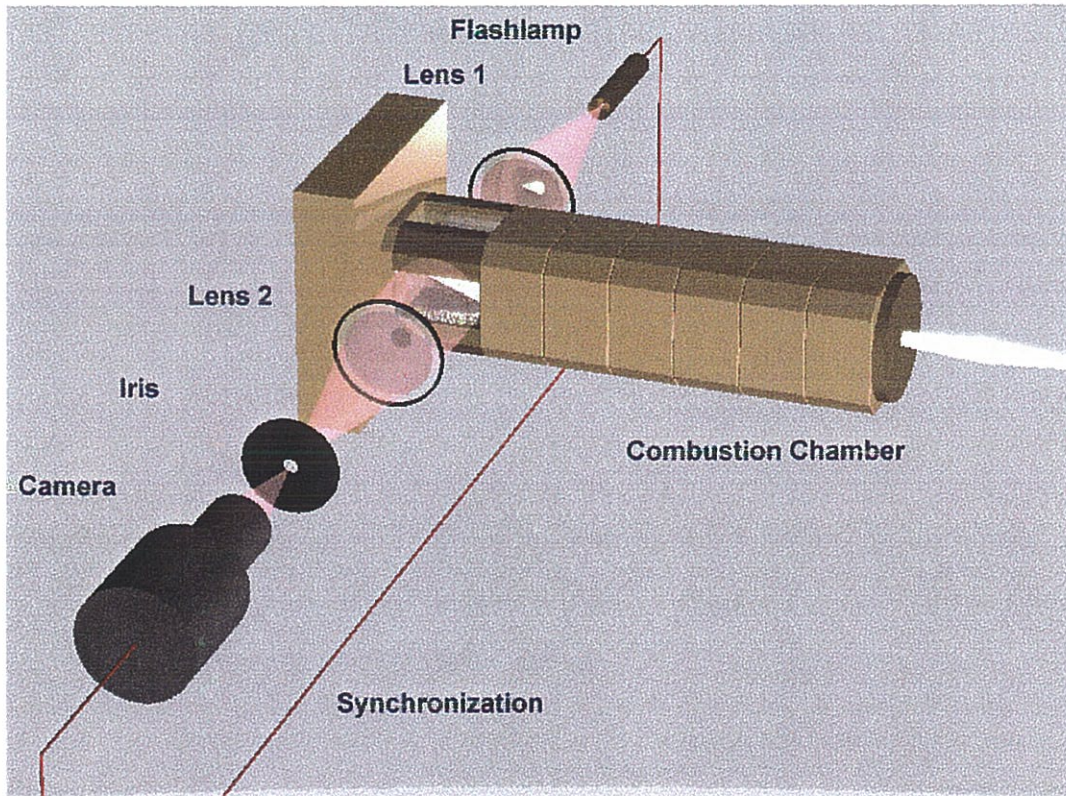
### 1.4.2.3 Backlighting

The backlighting technique works as anticipated, producing useful information about the oxygen jet. The camera is perfectly synchronized with the flashlamp and all natural emission from the flame is cut out. However, there are a number of small points to improve:

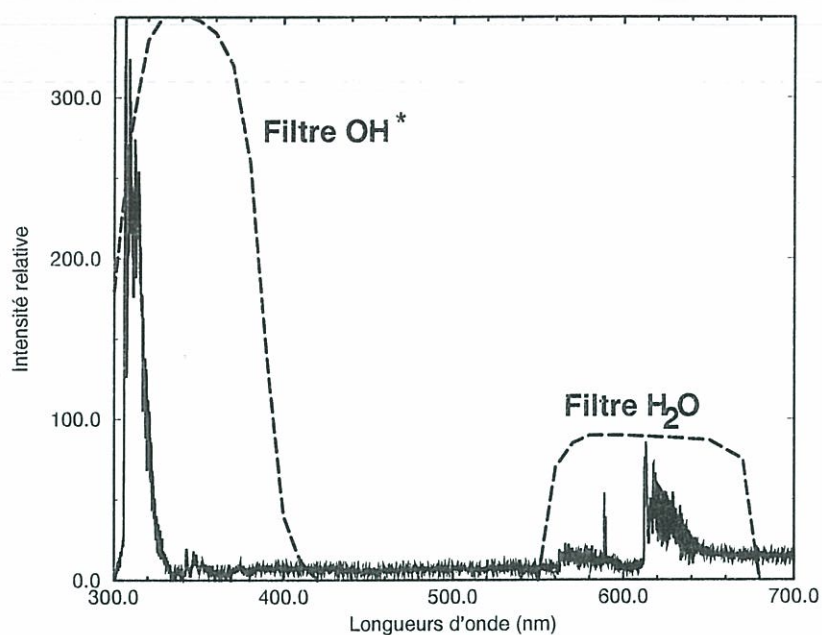
- The focus of the configuration is extremely sensitive. All the images are out of focus, as is required in order to see refractive index gradients in the gas. This is excessive in the first series, although it is progressively improved. For the second and third series, the focus is optimal.
- Similarly, the configuration is very sensitive to stains on the windows and to liquid water recirculating in the chamber. In later series a new technique of preparing the facility for tests is employed in order to eliminate these problems.

Instantaneous images are shown in figure 1.8. The oxygen jet (the black central stream) is unsteady, particularly at recess of 1 and 1.5  $d_{LOx}$ , where long wavelength disturbances can be seen. Around the jet, one can see a turbulent region where the refractive index gradient is very strong. There is a dark/light line at the outer edge of the hydrogen tube which corresponds to the interface between the recirculating combustion products and the hydrogen. Furthermore, on many images, there is a second light/dark line between the hydrogen and the jet, which corresponds to the flame. The presence of light/dark lines indicates a shadowgraphy, rather than schlieren, effect. These results are used in the discussion on flame structure and expansion in chapter 2 and in the discussion on the effect of recess in chapter 3.



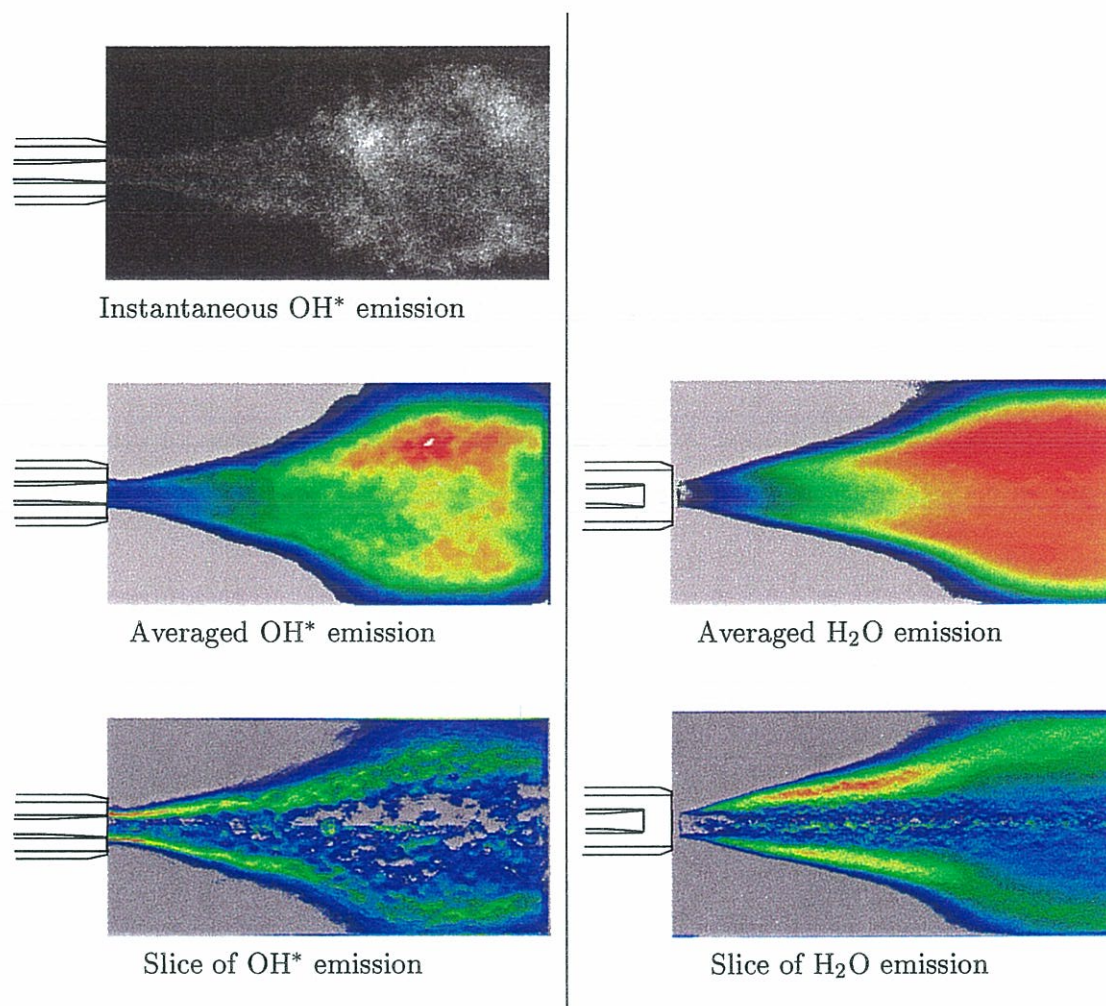


**Figure 1.5:** *Experimental configuration for backlighting. A spark flashlamp is placed at the focal point of a lens behind the flame. This sends parallel rays of light through the test section. These rays are slightly deviated by the flame and, on the other side, are focussed to a point by a second lens. An iris in this plane blocks the vast majority of the flame's natural emission but lets through the emission from the flashlamp, as long as it has not been greatly deviated. This is captured by the camera, after passing through a number of neutral density filters to avoid saturating the CCD. The exposure time of the ICCD (200 ns) is timed to coincide with the spark from the flashlamp, which further reduces emission from the flame. These images, at a video rate of 50 Hz, are stored on magnetic tape and digitized later.*

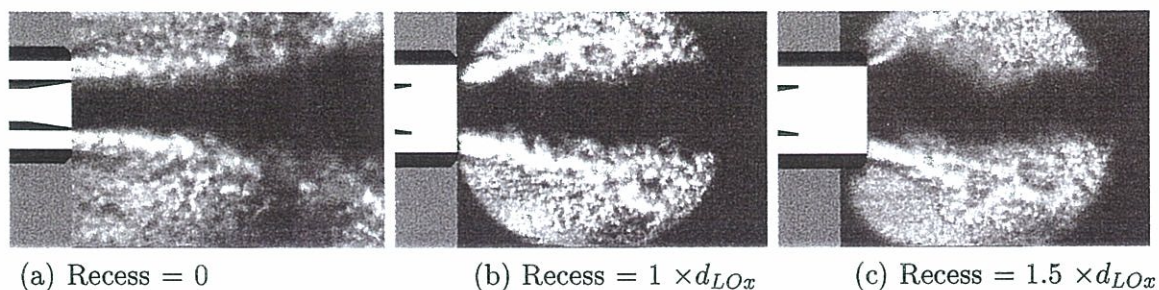


**Figure 1.6:** Emission spectrum of the cryogenic spray flame at 10 bar. The spectral positions of the camera filters are shown as dotted lines. Emission bands within the OH\* filter correspond to theoretical OH\* bands. However, it is impossible to verify the bands within the H<sub>2</sub>O filter due to interference from the 2<sup>nd</sup> order OH\* bands.





**Figure 1.7:** Sample images of OH\* and H<sub>2</sub>O emission for point A at 10 bar. Left: zero recess. Right: recess is  $1 \times d_{LOx}$ . A full catalogue of images can be found in Tripathi et al. (1998).



**Figure 1.8 :** Sample of instantaneous backlighting images, from point C at 10 bar.



Name	$p$ (bar)	$d_{H_2}$ (mm)	$d_{LOx}$ (mm)	$\dot{m}_{GH_2}$ (gs <sup>-1</sup> )	$\dot{m}_{LOx}$ (gs <sup>-1</sup> )	$U_{GH_2}$ (ms <sup>-1</sup> )	$U_{LOx}$ (ms <sup>-1</sup> )	$E$	$J$
A-70	70	10	5	63	90	190	3.9	1.4	14.4
C-70	70	10	5	50	90	150	3.9	1.8	6.8

**Table 1.4** : Nominal operating conditions of the test series at high pressure.

## 1.5 Second test series; high pressure

### 1.5.1 Experimental configuration †

In the second experimental series the chamber pressure is increased to 70 bar. Two values of  $J$  are chosen:  $J=6.2$ , which characterizes a poor atomization of the liquid oxygen jet and  $J=14.5$ , which characterizes good atomization. Three values of recess are examined: zero recess,  $1 \times d_{LOx}$  and  $1.5 \times d_{LOx}$ . The injector geometry and the hydrogen temperature remain constant. The injection conditions are summarized in table 1.4. Certain improvements are made to the diagnostics of the first series but the general principle remains the same. In addition, the pressure drop across the injector is measured using a set of three sensors. Further detail on sections marked with a dagger (†) can be found in Tripathi (2001).

#### 1.5.1.1 Spectroscopy †

The spectroscopy configuration remained unchanged with respect to the first series.

#### 1.5.1.2 OH and H<sub>2</sub>O average emission images †

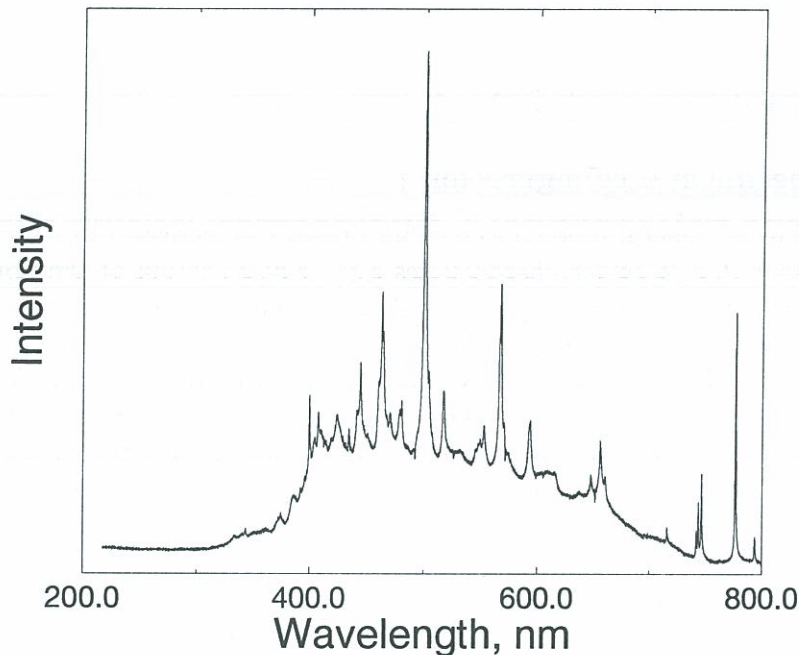
Images of both types of emission are taken from the lateral window of the chamber. An ICCD camera is used, with better resolution than that used in the first series. The exposure time is increased to 3.76 ms in order to obtain smooth averaged images. The same filters are used but neutral density filters are added to adjust for the longer exposure time. The majority of images are taken of the first 70 mm of the chamber. However, for two operating points, the visualization window is moved 50 mm downstream.

#### 1.5.1.3 Backlighting and instantaneous emission images

Two different backlighting configurations are used. The first is similar to that used in the first series, shown in figure 1.5. Having implemented the conclusions of the study in appendix A, the images are much clearer. Larger lenses also ensure a wider field of view. In the second configuration the iris and second lens are replaced by a powerful zoom lens. To block the flame's natural emission, two filters are used which pass light only between 400 and 450 nm. This is chosen taking into account the spectrum of the flashlamp (figure 1.9) and the flame.

Instantaneous emission images are taken afterwards without moving the camera so that the flame and oxygen jet positions can be compared without the need for rescaling.

The zoom lens, made from glass rather than quartz, only passes light of wavelength above 400 nm, which corresponds to broadband emission. This configuration is improved for the 3<sup>rd</sup> series so that simultaneous backlighting and emission images can be taken.



**Figure 1.9** : Emission spectrum of the spark flash lamp

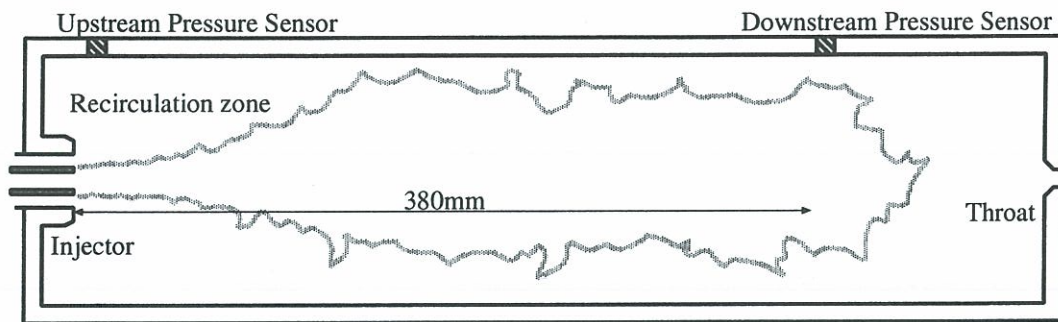
#### 1.5.1.4 Pressure drop within the recessed injector

Calculations presented by Kendrick et al. (1999), Tripathi et al. (1999) and which are developed further in chapter 3 suggest that the pressure drop within the injector will increase with the recess of the LOx tube. Although this drop is small compared with the pressure in the chamber, an attempt is made to measure it using the pressure sensors already on the facility. Figure (1.10) shows the interior of the combustion chamber and the positions of two pressure sensors. They are set flush with the top wall. Figure (1.11) shows a diagram of the injector head, the hydrogen feed line and the position of the third pressure sensor. Upstream of this sensor there is a sonic throat and a baffle. The pressure and temperature at this baffle are taken as the stagnation conditions. A ring with orifices is placed between the feed line and the injector. The flow area in this element is the same as that in the feed line.

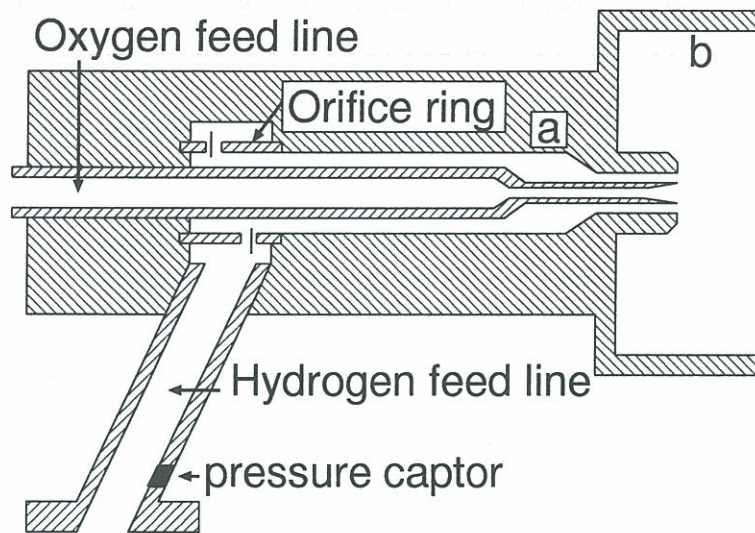
The pressure sensors used in the present experiments have a dynamic range between 1 and 100 bar. Quoted accuracy is  $\pm 1$  bar. They are individually calibrated three times during the series. They are compared with each other a further five times by raising the chamber pressure to 60 bar with nitrogen. These tests demonstrate a difference of less



than 1% between the sensors.



**Figure 1.10:** *Diagram of the interior of the combustion chamber showing the pressure sensor positions. These are set flush with the wall and have an accuracy of  $\pm 1$  bar.*

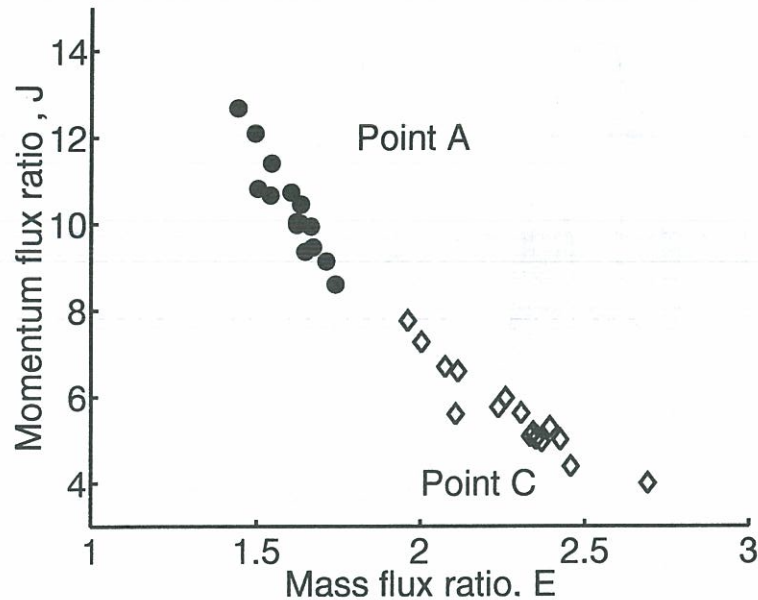


**Figure 1.11:** *Diagram of the injector head and hydrogen feed line. The position of the hydrogen feed line pressure sensor is shown at the bottom left.*



### 1.5.2 Operating conditions †

The desired operating conditions are shown in table 1.4. The operating points achieved during the tests are somewhat different and are shown in figure 1.12. This highlights the difficulty in repeating tests exactly on the cryogenic facility.



**Figure 1.12:** Operating points achieved during the test series at 70 bar. These differ somewhat from the conditions targetted in table 1.4.

### 1.5.3 Results

There are 37 successful experimental runs between 60 and 70 bar. Some results are summarized in this section. Other results appear, grouped by topic, in chapters 2 to 3. Complete results can be found in Tripathi et al. (1999), with the technical points and a list of problems which were overcome.

#### 1.5.3.1 Spectroscopy †

The flame emission spectrum in the near UV region at 70 bar is shown in figure 1.13. This confirms that the UV filter isolates OH\* emission. However, as for the first test series, it is impossible to confirm that the emission transmitted by the red filter comes uniquely from H<sub>2</sub>O.

#### 1.5.3.2 Average Emission from OH\* and H<sub>2</sub>O †

Figure 1.14 shows instantaneous OH\* emission, average OH\* emission and a slice of the mean volumetric emission intensity, calculated by the Abel-inversion process. A long exposure time is used here in order to obtain smooth average images. These results are

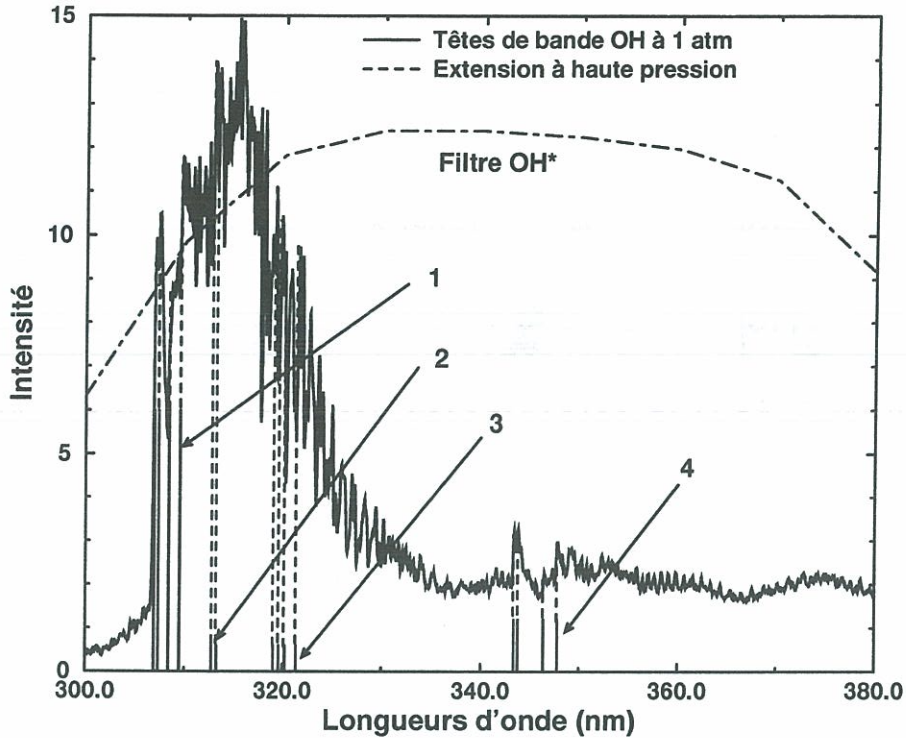


Figure 1.13 : Flame emission spectrum in the near UV range at 70 bar

used in the discussion on flame structure and expansion in chapter 2 and in the discussion on the effect of recess in chapter 3.

### 1.5.3.3 Backlighting and Instantaneous Emission Results

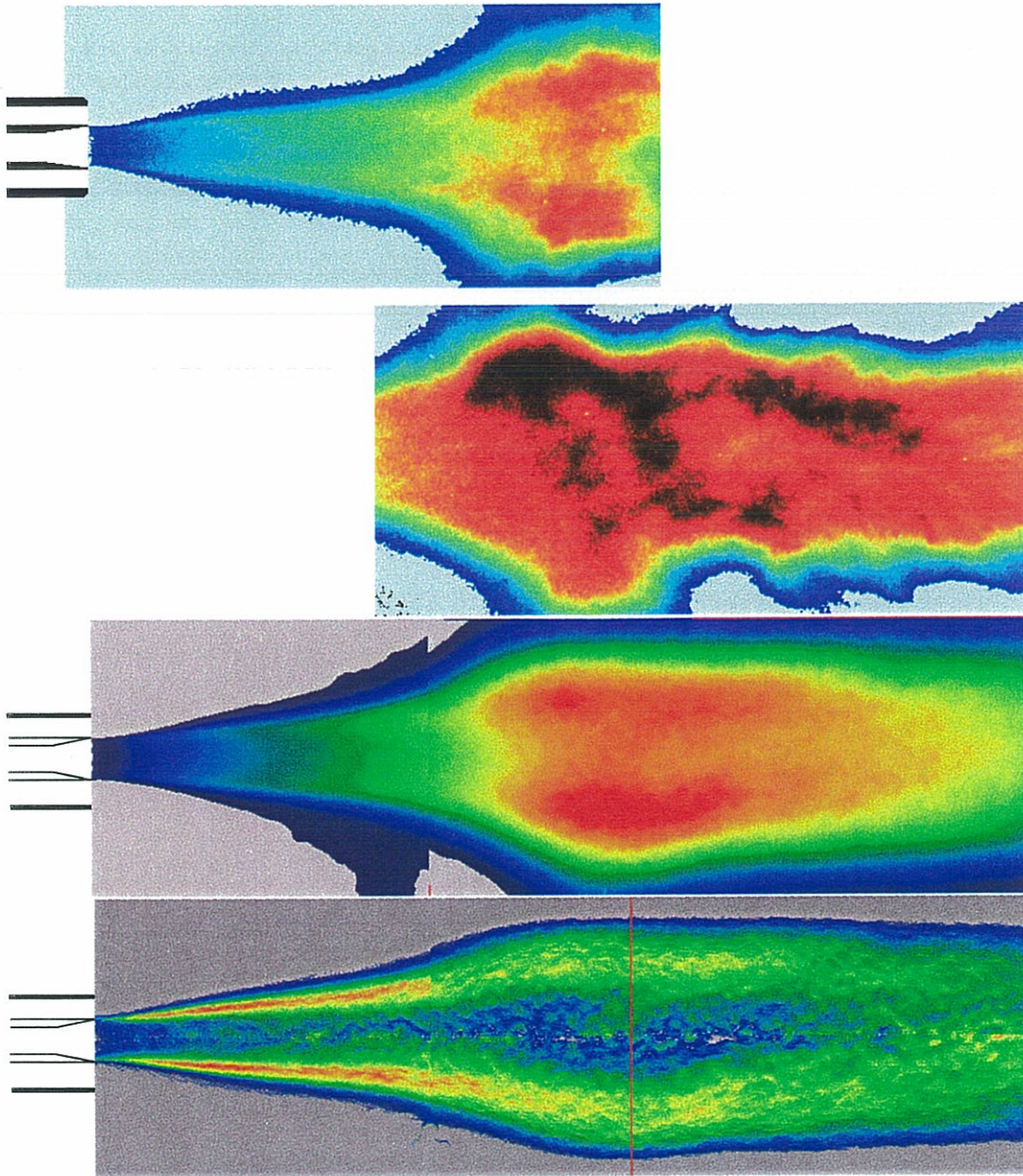
**Broad field results.** A selection of backlighting images is presented in figure 1.15. These show the dense oxygen jet and the regions containing steep refractive index gradients in the gas. The intensity profile of a slice of an image is shown in figure 1.16. The edge of the oxygen jet is taken to be the position where the intensity gradient changes most rapidly. Using this method, the oxygen jet position was found for all images in a sequence. These were then averaged to give a residence time along the line of sight. The shape of this gives a qualitative indication of the rate of expansion of the jet.

A selection of instantaneous  $\text{OH}^*$  emission images is shown in figure 1.15. These images, taken just after the backlighting images, correspond to exactly the same operating point and camera position. These images can also be averaged and processed with the Abel inversion but they are less smooth than the previous images because the exposure time is 50 ns rather than 3.76 ms. The average oxygen jet position can be superimposed, as in figure 1.17.

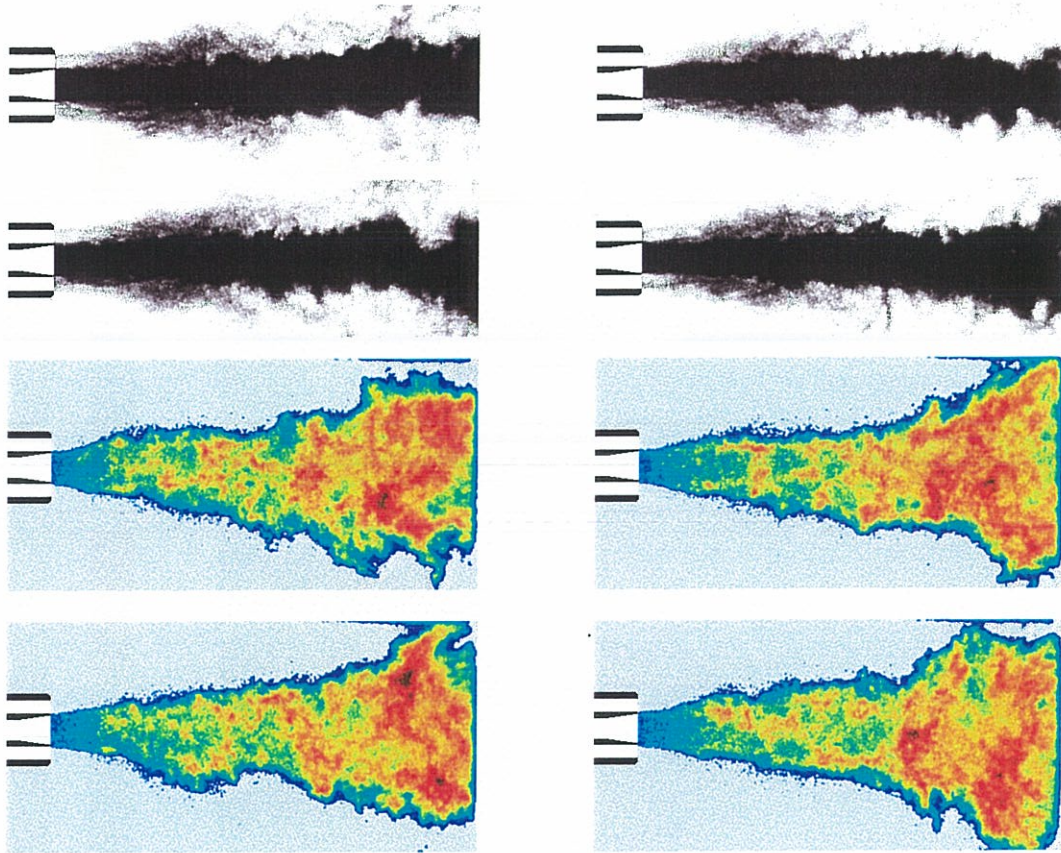
**Near field results.** A selection of backlighting images of the 21 mm field is shown in figure 1.18. As explained in appendix A, these contain schlieren effects because ray deviations are strong enough to deflect light out of the light cone which is captured by the camera. When these images are averaged, the darkness of a pixel corresponds to the average time that a strong gradient has existed at that pixel's position. The strongest deviation occurs where gradients are perpendicular to the ray direction, which is in a slice through the jet's axis. Thus, to a first approximation, the images can be considered to be a slice of this plane and can be compared with the Abel-inverted emission images.

A selection of instantaneous emission images is shown in figure 1.18. These can be averaged and processed with the Abel inversion. They can then be superimposed on the average shadowgraphy images, as shown in figures 1.19, 1.20 and 1.21. This gives much information about the structure of the near-injector region, which shall be discussed in chapter 2 and the chapters on flame stabilization.

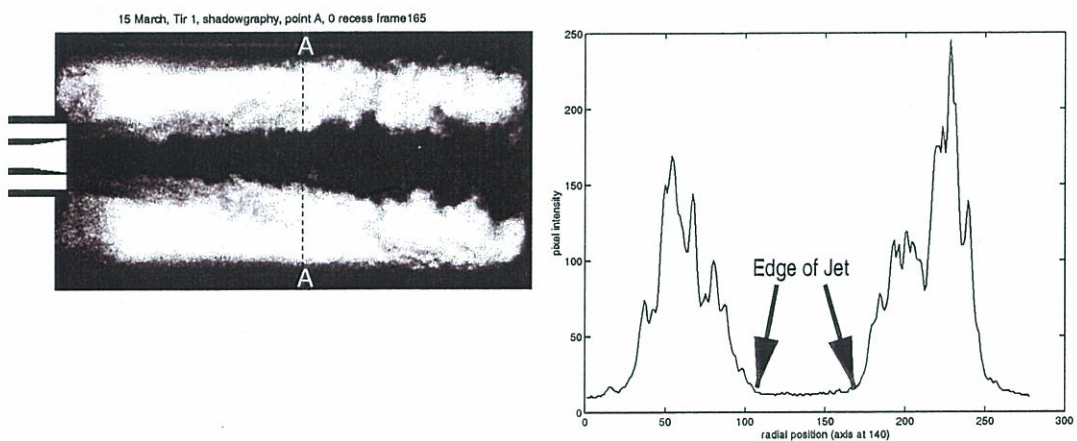




**Figure 1.14:** Sample images of  $OH^*$  emission for point A at 70 bar with zero recess. Top images: Instantaneous ( $\tau_{exp} = 3.7$  ms) near injector. Second image: Instantaneous, further from injector. Third image: Time-averaged image. Bottom image: Abel-inverted image, which reveals a slice through the flame.

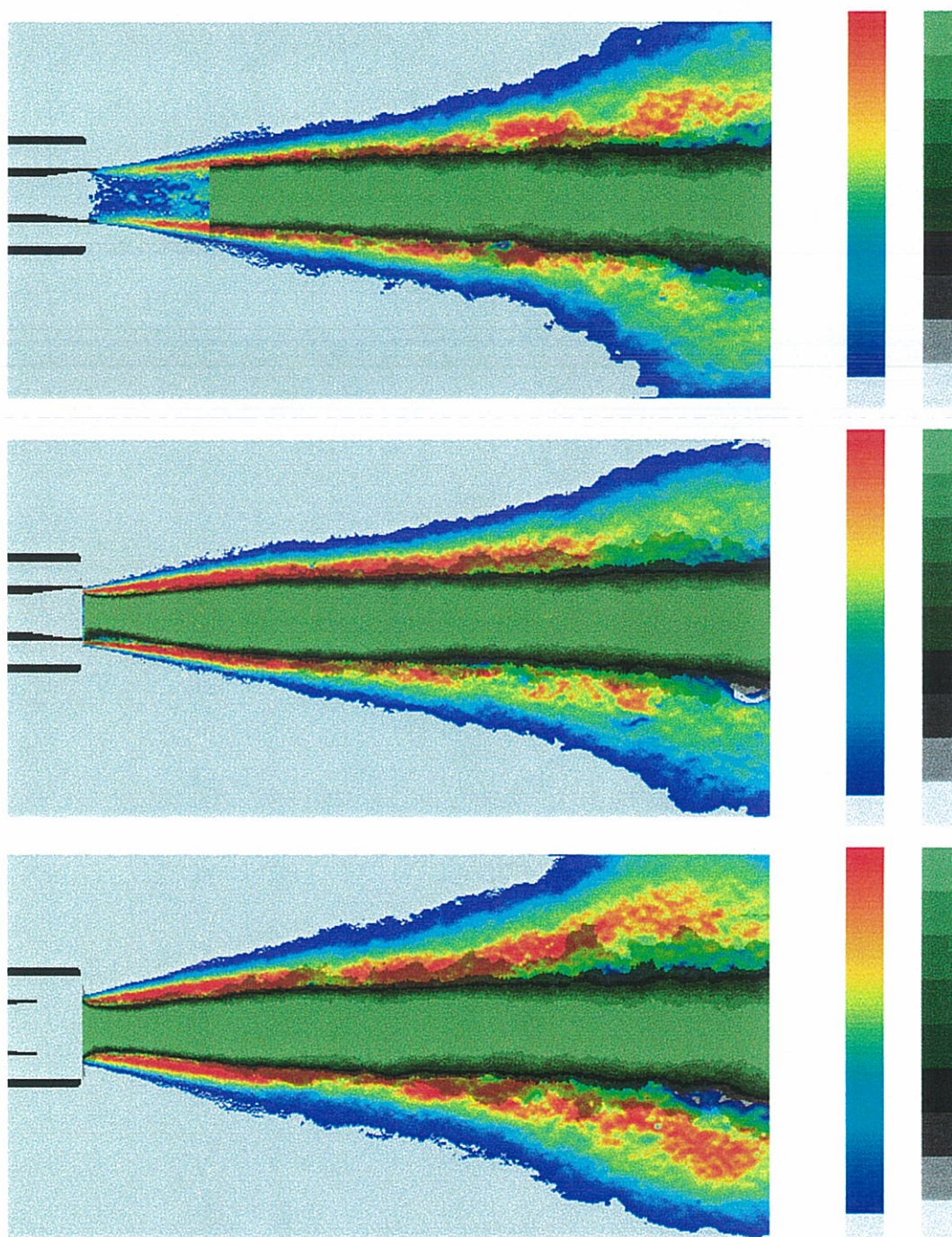


**Figure 1.15:** A sample of instantaneous backlighting images (top) and instantaneous  $OH^*$  images (bottom) for the broad field. The operating points and camera position are identical in both sets of images: Point C,  $p = 70$  bar.



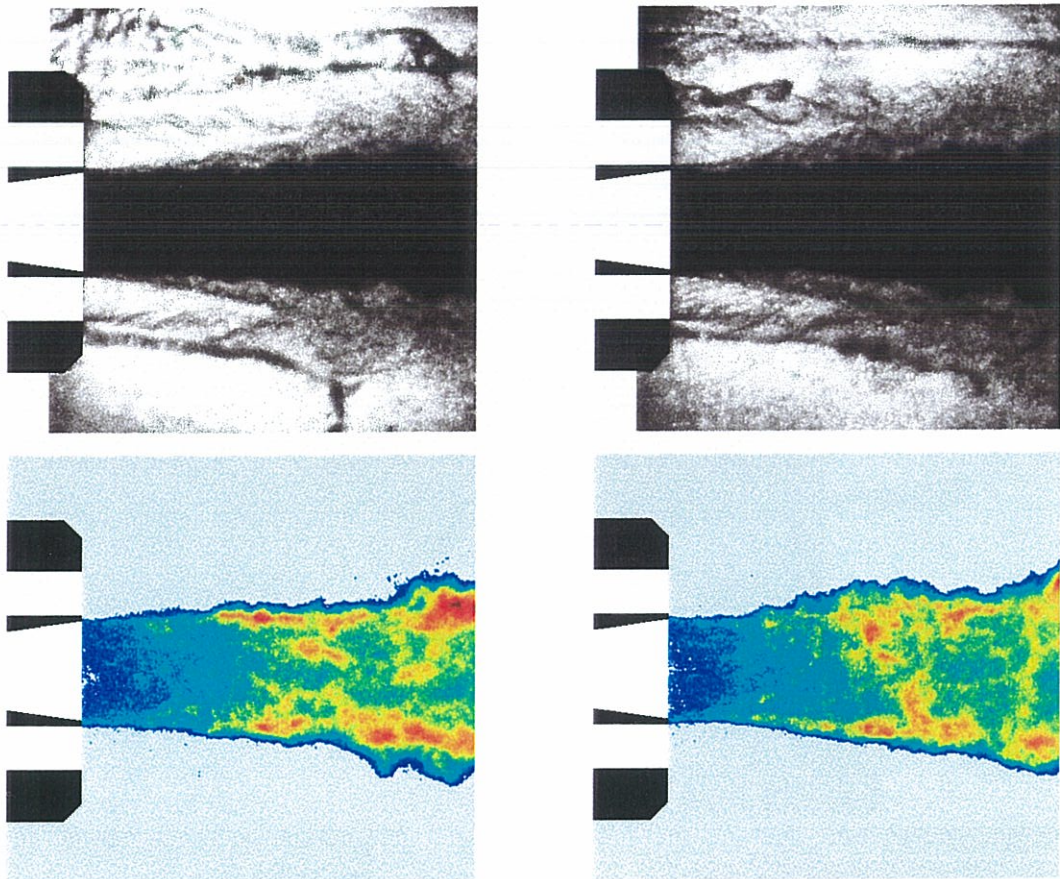
**Figure 1.16:** The edge of the jet is defined from the backlighting images as the point where the intensity gradient changes most rapidly.



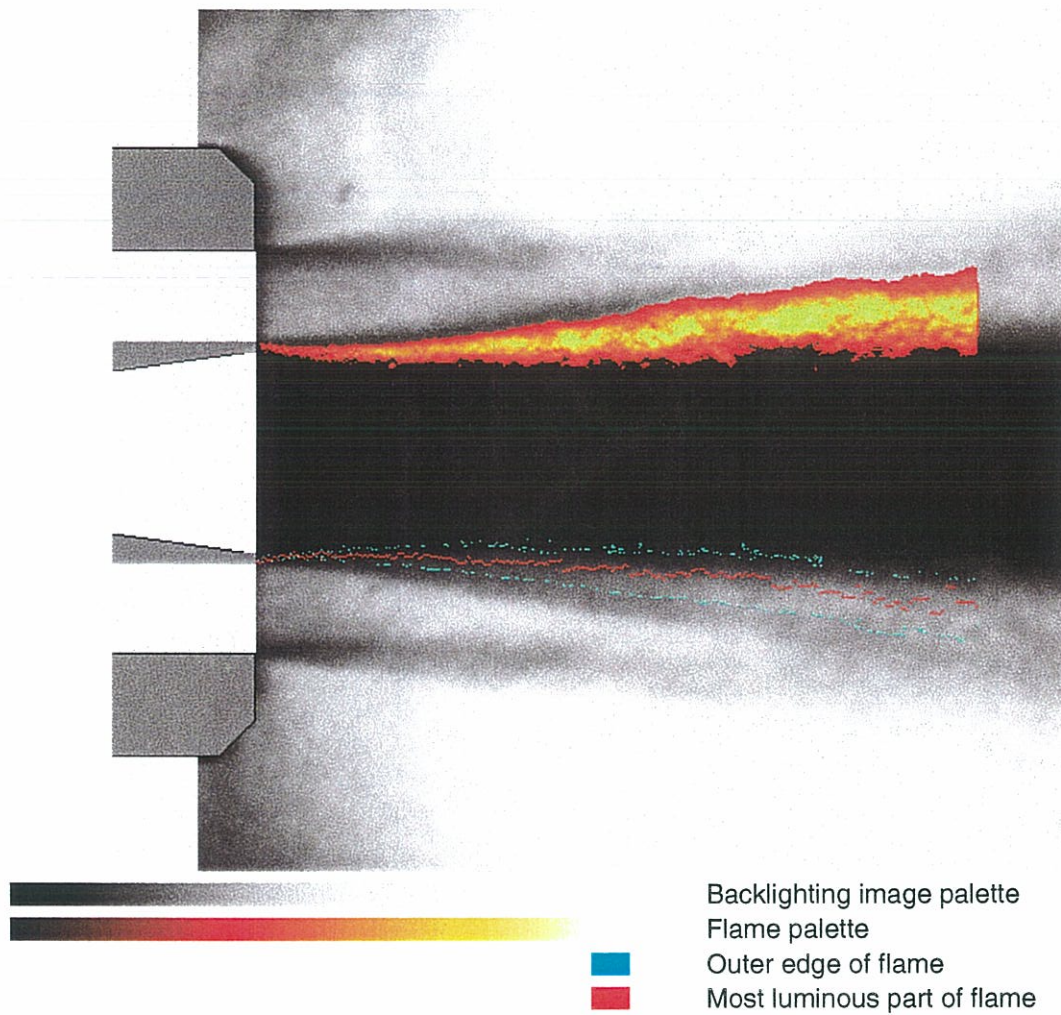


**Figure 1.17:** Combined emission and backlighting images. The colour scale corresponds to a slice of  $OH^*$  emission and the grayscale to the average jet position. Top: Point A, zero recess. Middle: Point C, zero recess. Bottom: Point C, recess of  $1 \times d_{LOx}$ .



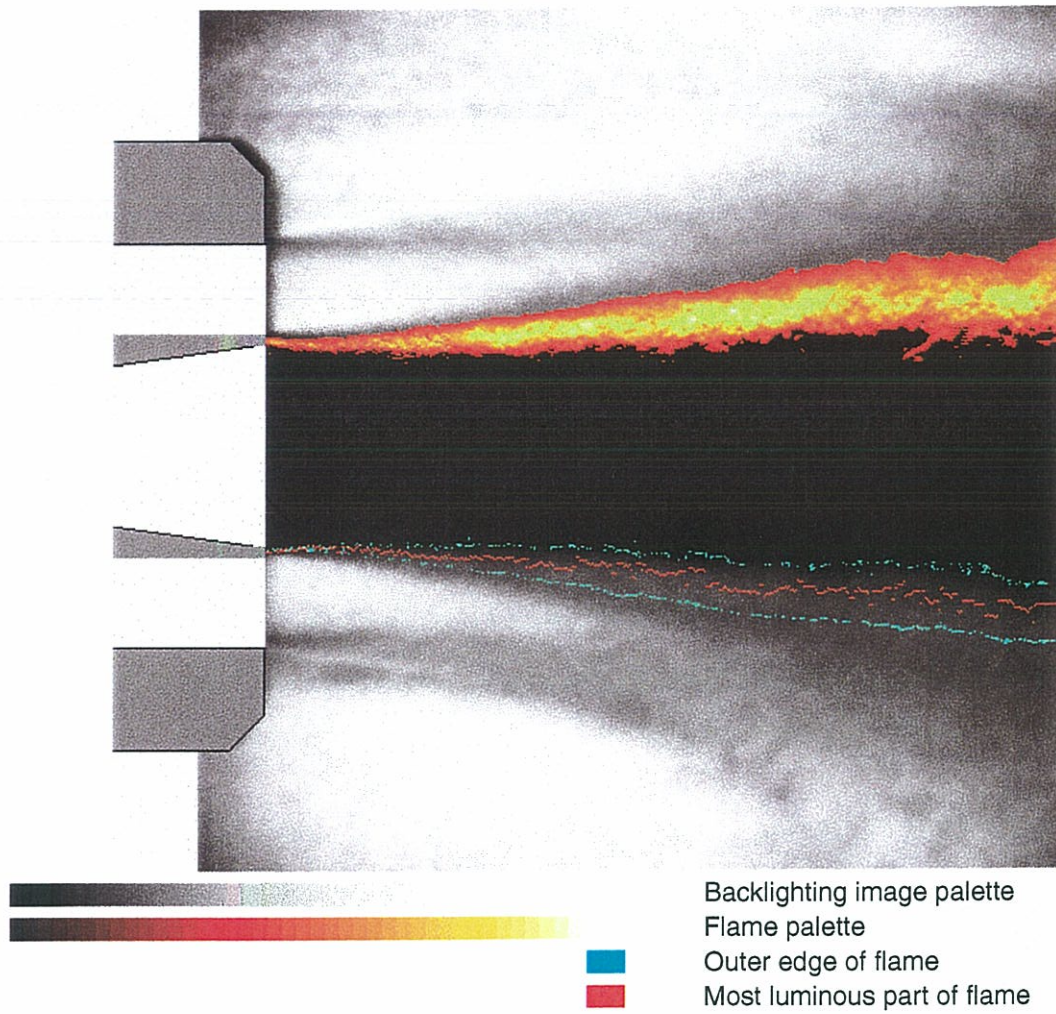


**Figure 1.18:** A sample of instantaneous backlighting images (top) and instantaneous  $OH^*$  images (bottom) for the near field. The operating points and camera position are identical in both sets of images: Point C,  $P = 70$  bar.

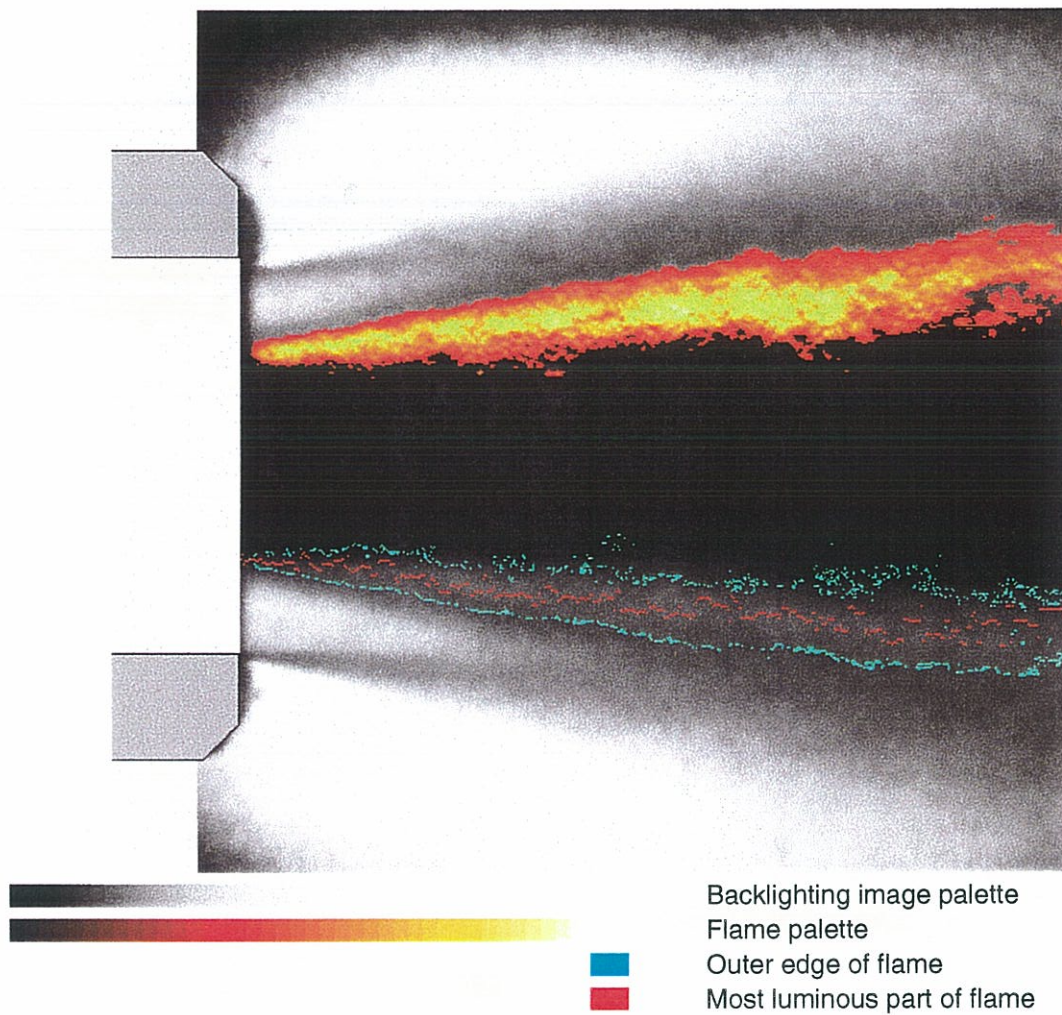


**Figure 1.19:** *Combined emission and backlighting images. The colour scale corresponds to a slice of  $OH^*$  emission and the grayscale to the average backlighting image. Point A, 70 bar, zero recess.*





**Figure 1.20:** *Combined emission and backlighting images. The colour scale corresponds to a slice of  $OH^*$  emission and the grayscale to the average backlighting image. Point C, 70 bar, zero recess.*



**Figure 1.21:** Combined emission and backlighting images. The colour scale corresponds to a slice of  $OH^*$  emission and the grayscale to the average backlighting image. Point C, 70 bar, recess  $1 \times d_{LOx}$ .



### 1.5.3.4 Pressure drop across injector

Measurement of the pressure drop across the injector is important because this may be used to check one of the models for the effect of recess. The pressure drop was measured successfully in 30 experimental runs: 15 with no recess, 10 with recess  $1 \times d_{LOx}$  and 5 with recess  $1.5 \times d_{LOx}$ . In each run, there is a six to ten second period where conditions are stable. The average value of each quantity over this period is calculated and then used in the subsequent analysis.

A schematic diagram of the hydrogen injector and feed line is shown in Figure (1.22). Hydrogen passes from the reservoir into a baffle, which reduces the stagnation pressure in order to obtain the desired flowrate. The static pressure drop between sections 3 and 4 is desired ( $\Delta p_{34}$ ). However, it is not possible to measure this quantity directly. It is assumed that the static pressure is constant in the recirculation zone next to the injector so that the pressure in section 4 is equal to the pressure measured by the upstream sensor. Thus the measured pressure drop is that between section 2 and section 4 ( $\Delta p_{24}$ ), in which the drop between sections 2 and 3 ( $\Delta p_{23}$ ) will be considerably larger than that between 3 and 4.

It is assumed that the pressure drop is proportional to  $\rho U^2/2$ , where  $C_{23}$  and  $C_{34}$  are head loss coefficients.

$$\begin{aligned}\Delta p_{24} &= \Delta p_{23} + \Delta p_{34} \\ &= C_{23} \left( \frac{1}{2} \rho_2 U_2^2 \right) + C_{34} \left( \frac{1}{2} \rho_3 U_3^2 \right)\end{aligned}\quad (1.2)$$

The second term on the right hand side of equation (1.2) can be expressed as a function of  $\rho_2 U_2^2$  by conservation of mass:

$$C_{34} \left( \frac{1}{2} \rho_3 U_3^2 \right) = C_{34} \left( \frac{\rho_2 A_2^2}{\rho_3 A_3^2} \right) \frac{1}{2} \rho_2 U_2^2 = C'_{34} \left( \frac{1}{2} \rho_2 U_2^2 \right) \quad (1.3)$$

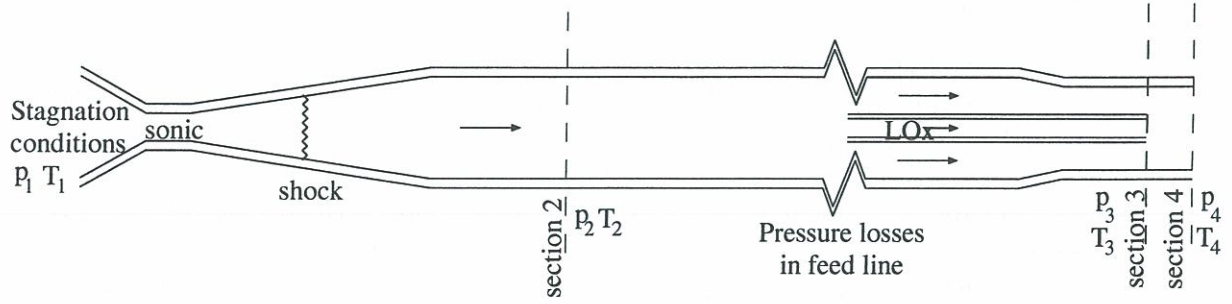
$$\text{thus one obtains} \quad \Delta p_{24} = (C_{23} + C'_{34}) \frac{1}{2} \rho_2 U_2^2$$

A best fit line on a plot of the experimental head loss data:  $\Delta p_{24}$  against  $\rho U^2/2$  has gradient  $G = \Delta(p_{24})/\Delta(\rho U^2) = (C_{23} + C'_{34})$ . One can assume that  $C_{23}$  remains constant as the recess is changed,  $C'_{34}$  can be evaluated from the change in  $G$ .  $C_{34}$  can then be evaluated from equation (1.3).

The hydrogen mass flowrate must be calculated in order to find the quantity  $\rho U^2$ . Assuming isentropic conditions between the baffle and the sonic throat, equation (1.4) expresses the mass flowrate in terms of stagnation conditions:  $p_1$  and  $T_1$  and throat area:  $A_t$ .

$$\dot{m} = p_1 A_t \left( \frac{\gamma}{r T_1} \right)^{\frac{1}{2}} \left( \frac{\gamma + 1}{2} \right)^{-\frac{\gamma+1}{2(\gamma-1)}} \quad (1.4)$$

The dynamic head of hydrogen,  $\rho U^2$ , can be calculated. There is a shock in the divergent portion of the throat, across which the stagnation temperature remains constant. The temperature at section 2 can be deduced from the following set of equations. One



**Figure 1.22:** Schematic diagram of the injector and feed line showing features relevant to the calculation of a pressure drop along the line.

first writes expressions for the Mach number in that section and then one relates  $T_2$  to the stagnation temperature  $T_1$ .

$$M_2 = \frac{U_2}{\sqrt{\gamma r T_2}} \quad (1.5)$$

$$U_2 = \frac{\dot{m}}{\rho_2 A_2} \quad (1.6)$$

$$\rho_2 = \frac{p_2}{r T_2} \quad (1.7)$$

$$T_2 = T_1 \left( 1 + \frac{\gamma - 1}{2} M_2^2 \right)^{-1} \quad (1.8)$$

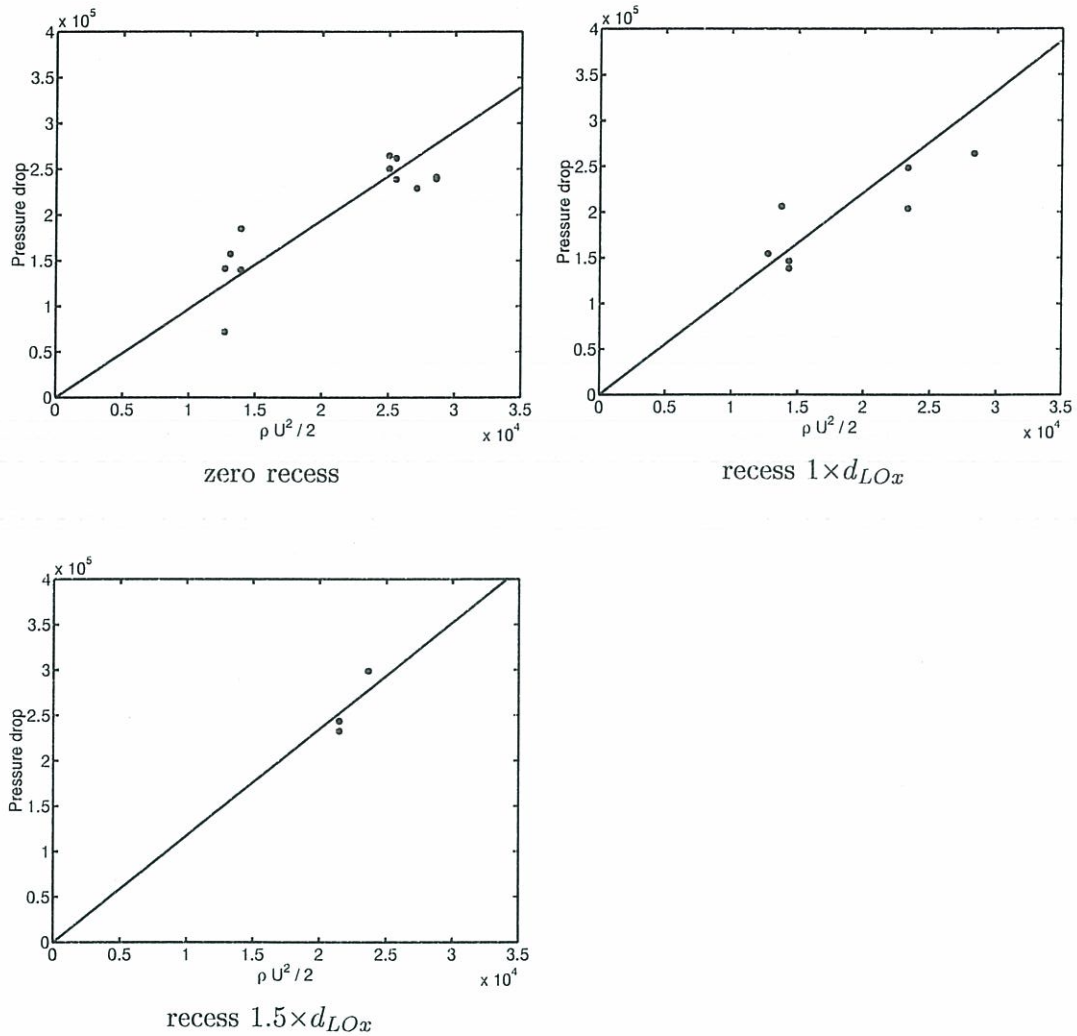
$$T_2 = \frac{\sqrt{1 + 2T_1 \left( \frac{(\gamma - 1)r}{\gamma} \left( \frac{\dot{m}}{p_2 A_2} \right)^2 \right)} - 1}{\frac{(\gamma - 1)r}{\gamma} \left( \frac{\dot{m}}{p_2 A_2} \right)^2} \quad (1.9)$$

After  $T_2$  has been calculated,  $\rho U^2$  is calculated via equations (1.6) and (1.7) with constants:  $\gamma = 1.4$ ,  $r = 4157 \text{ J/Kg/K}$ ,  $A_t = 8.04 \times 10^{-6} \text{ m}^2$ ,  $A_2 = 1.13 \times 10^{-4} \text{ m}^2$

The speed of flame structures in the chamber has been measured by two images taken in quick succession. This quantity is important because it may be used to estimate the pressure drop in the chamber. The flow velocity was estimated from measurements in the second series but only results from the 3rd series shall be presented. It is found that the Mach number in the combustion chamber is not high enough for heat release to cause an appreciable static pressure drop between the two chamber pressure sensors. Therefore, their results are considered to be equivalent.

The results of the previous analysis are plotted in figure 1.23. Lines of best fit which are forced to pass through the origin are also plotted. Their gradients, which correspond to  $C_{23} + C'_{34}$ , are  $G = 9.7$  for zero recess,  $G = 11.1$  for recess  $1 \times d_{LOx}$  and  $G = 11.7$  for recess  $1.5 \times d_{LOx}$ . The general trend is that the pressure drop across the injector increases with increasing recess.  $C_{23}$  is by definition zero when there is no recess, indicating that  $C'_{34}$  is 1.4 for recess  $1 \times d_{LOx}$  and 2.0 for recess  $1.5 \times d_{LOx}$ . Assuming constant hydrogen density in the feed line, the pressure coefficient  $C_{34}$  is equal to  $(A_3/A_2)^2 \times C'_{34}$ . This is





**Figure 1.23:** Graphs of experimentally determined pressure drop (bar) against  $\rho U^2 / 2$  between sections 2 and 4 in figure 1.22. The error in each measurement is a maximum of 1 bar.

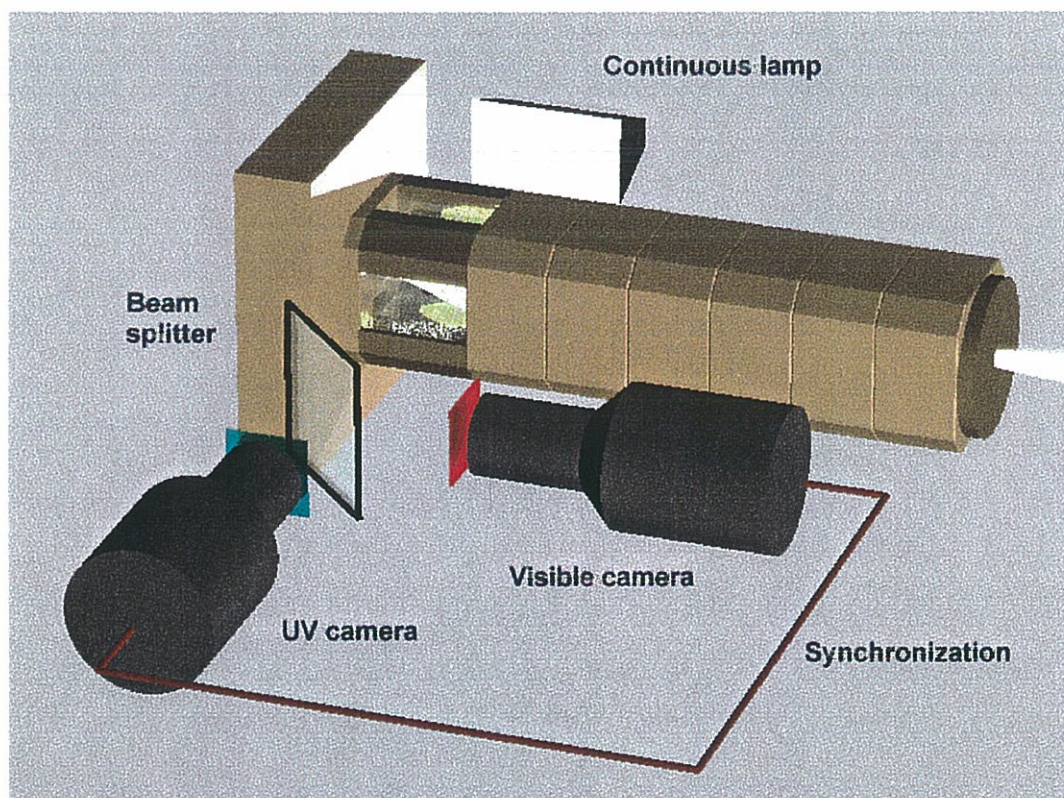
0.31 at recess  $1 \times d_{LOx}$  and 0.46 at recess  $1.5 \times d_{LOx}$ . These results are in agreement with the theoretical predictions in chapter 3.

However, the error in the pressure determination is  $\pm 1$  bar and these results fall within the margin of error. As a consequence, they cannot be considered to be fully conclusive. The measurement technique could be improved by using a differential pressure gauge with one end placed just before the final convergent section of the hydrogen tube and the other end placed somewhere within the recirculation zone in the combustion chamber. These positions, **a** and **b**, are shown in figure 1.11.

## 1.6 Third test series; low hydrogen temperature

### 1.6.1 Experimental configuration

In the third test series, the hydrogen temperature is reduced gradually to 100K. The operating points are shown in table 1.5. One set of points corresponds to  $E \approx 2.5$  and another set to  $J \approx 4.0$ . In addition, two diameters of the hydrogen injector were used: 10 mm, which is the same as that used in the second series and 7.5 mm. The first operating point is similar to point C of the second series, in order to check the consistency of these results. The optical configuration is shown in figure 1.24.



**Figure 1.24:** *Experimental configuration for  $\text{OH}^*$  emission and backlighting in the third experimental series. A beam splitter is employed so that the cameras visualize the same part of the chamber. A diffused light source is used for the backlighting images in order to reduce the visibility of refractive index gradients in the gas.*

#### 1.6.1.1 Spontaneous $\text{OH}^*$ emission

As for the first and second series, UV emission of  $\text{OH}^*$  radicals is recorded with ICCD cameras. Emission in the red part of the spectrum is not recorded. By using a beam-splitter, the two cameras visualize exactly the same position in the chamber, which is either the first 70 mm or the first 21 mm. Short exposure times, below  $1.5 \mu\text{s}$ , ensure



that the images are instantaneous. The cameras can be synchronized so as to produce two images with a certain time delay. In this way the velocity of flame structures can be determined.

### 1.6.1.2 Backlighting

The backlighting set-up differs from that used in the first and second series, where a point source and lens are used to create parallel rays through the chamber. In the new set-up, a powerful lamp illuminates a plate of frosted glass behind the chamber. For the reasons explained in detail in appendix A, the image formed after light has passed through the chamber is less sensitive to refractive index gradients in the gas. However, it remains just as sensitive to diffusion of light by the oxygen jet. Similarly the cameras can be given a certain relative time delay so as to determine the velocity of structures in the jet.

### 1.6.1.3 Simultaneous OH\* emission and backlighting images

With appropriate filters it is possible to obtain simultaneous emission and backlighting images. This is extremely useful for determining the flame structure. The plate of frosted glass cuts out UV light from the lamp and consequently does not interfere with the OH\* radical emission. In the visible range, emission from the lamp is more intense than the flame.

### 1.6.1.4 Natural emission

During runs where the backlighting set-up is not in use, the lamp is replaced with a third camera with a longer exposure time of 63  $\mu$ s. This gives rise to smoother averaged images. No filters are used in front of this camera.

$T_{H_2}$ (K)	$d_{H_2}$ (mm)	$d_{LOx}$ (mm)	$\dot{m}_{GH_2}$ (gs <sup>-1</sup> )	$\dot{m}_{LOx}$ (gs <sup>-1</sup> )	$U_{LOx}$ (ms <sup>-1</sup> )	$U_{GH_2}$ (ms <sup>-1</sup> )	$E$	$J$	$p$ (bar)
292 K	10	5	38.6	105.6	4.53	136.6	2.74	4.02	63.56
224 K	10	5	45.2	99.7	4.32	118.1	2.21	4.53	66.20
211 K	10	5	35.7	106.1	4.53	92.4	2.97	2.51	63.03
136 K	10	5	40.5	103.7	4.39	66.84	2.56	2.17	63.43
123 K	10	5	60.6	105.9	4.45	80.8	1.75	3.79	70.96
118 K	10	5	61.1	105.0	4.40	78.4	1.72	3.78	70.84
113 K	7.5	5	50.70	109.4	4.59	170.84	2.08	17.4	71.52
104 K	7.5	5	51.5	110.8	4.78	157.6	2.16	15.4	72.18
116 K	7.5	5	49.4	116.2	4.88	175.0	2.35	15.3	69.92
91 K	7.5	5	52.7	116.6	4.91	145.3	2.21	13.4	70.58

Table 1.5 : Operating conditions for the third test series.

## 1.6.2 Results

There are 10 successful experimental runs between 60 and 70 bar. Some results are summarized in this section. Complete results can be found in Juniper et al. (2000), with the technical points and a list of problems which were overcome.

### 1.6.2.1 OH\* Emission and Backlighting images

Instantaneous images of OH\* emission are shown in figures 1.25 and 1.27. The images in figure 1.27 are taken 44  $\mu\text{s}$  after those in the same position in figure 1.25. Simultaneous backlighting and OH\* emission images at a hydrogen temperature of 210K are shown in figures 1.26 and 1.28.

### 1.6.2.2 Effect of reducing the hydrogen temperature

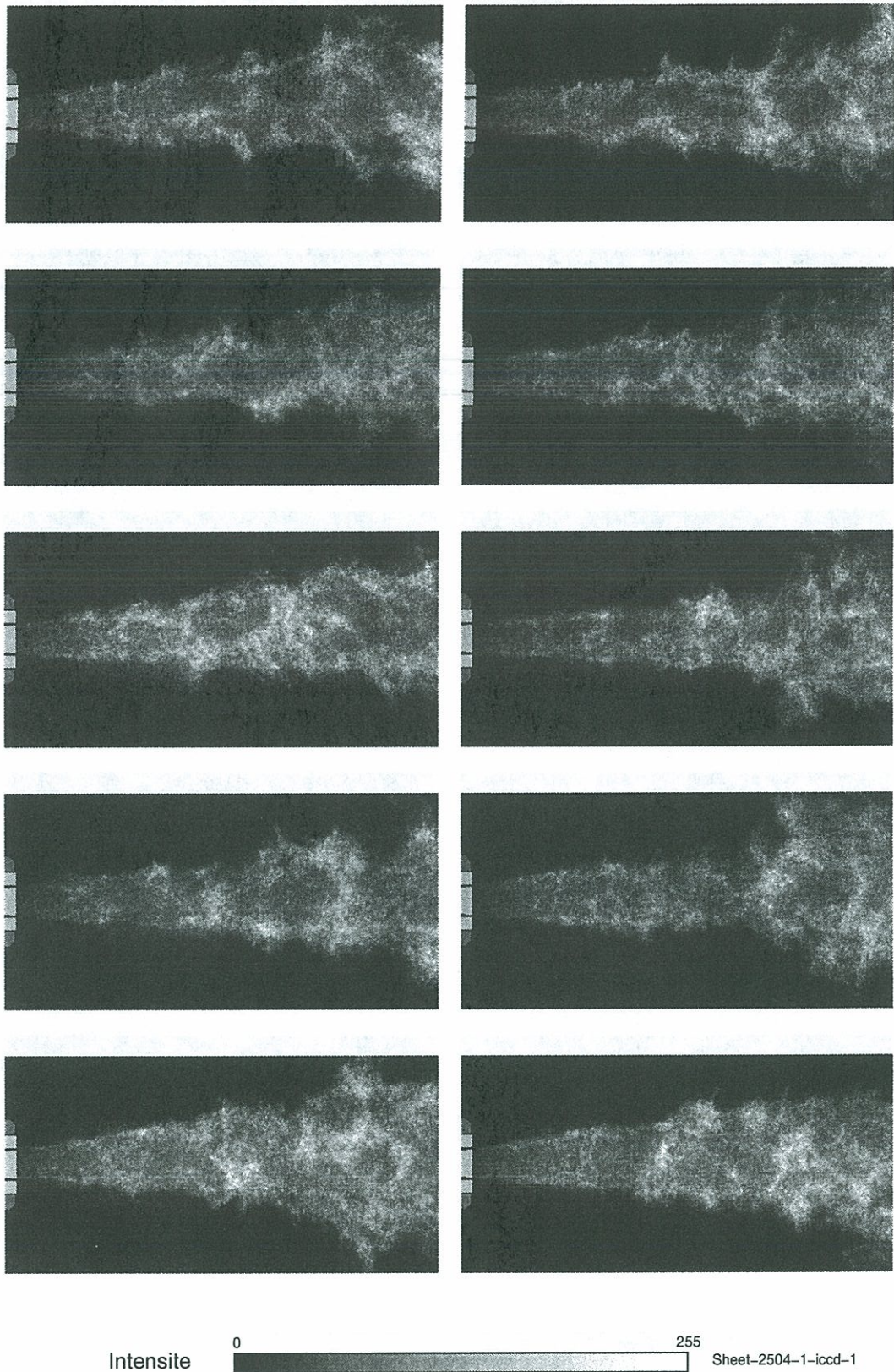
At lower hydrogen temperatures the emission images are fuzzy in the first few centimeters of the chamber. The simultaneous shadowgraphy images show that the natural emission is diffused by a structure which starts at the interface between the recirculating gases ( $\text{H}_2$  and  $\text{H}_2\text{O}$ ) and the outside edge of the hydrogen jet. It is possible that this diffusion is caused by very high refractive index gradients at a flame front or at the boundary of two gases with different density. However, the emission images do not show any emission in this region and the fact that the hydrogen is colder than in the 2nd test series reduces, rather than increases, the density difference. Consequently, one can deduce that this diffusion is not due to strong refractive index gradients. Instead, it is caused by the formation of small particles of condensed water at the outer edge of the cold hydrogen jet. Near the injector, these particles have a high velocity, are widely spaced and are in a thin region. Even further downstream, they have a lower velocity, are closer together and are in a wider region. This leads to increased diffusion of the light downstream. Further downstream they evaporate and the flame can be seen as before. A crown of ice forms on the injector itself. This breaks off periodically, revealing the flame, which is attached to the lip of the oxygen injector. This is shown diagrammatically in figure 1.29.

This effect at low hydrogen temperatures is not seen on the P8 test facility at DLR in Germany, because half the hydrogen is injected as a cooling gas along the sides of the chamber. In this case, if recirculating zones exist, they contain hydrogen rather than water vapour.

### 1.6.2.3 Estimation of velocities in the chamber

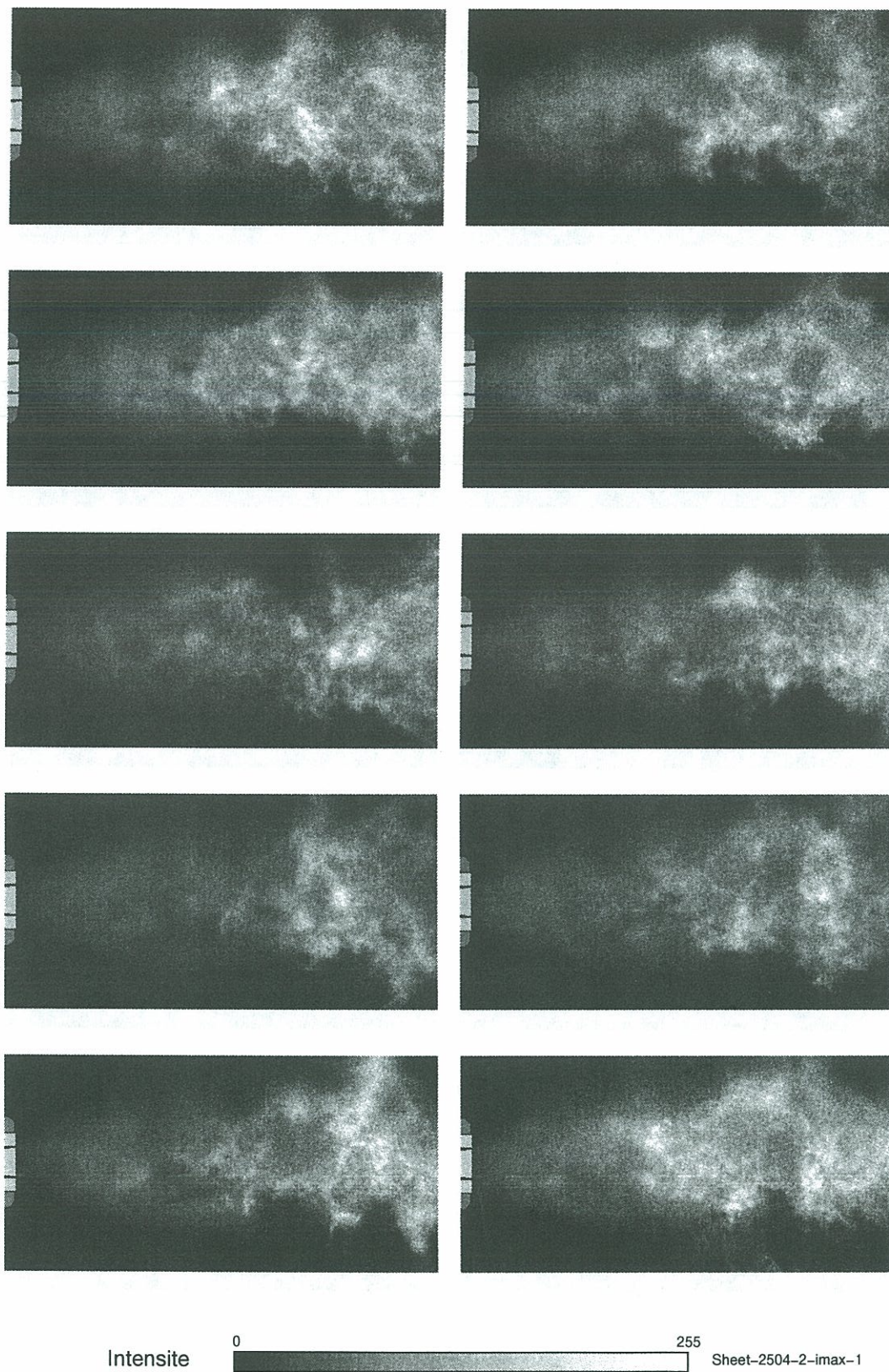
The images in figure 1.25 were taken 44  $\mu\text{s}$  before those in figure 1.27. The coherent structures deform only slightly in this short time, so their convection velocity can be estimated. Only structures which were well defined in both images were followed. There were around 10 such points in each of the thirty pairs of images at the stable operating condition. Figure 1.30 shows the velocity vectors which result from such measurements. The velocity near the injector is around  $50 \text{ ms}^{-1}$  and it decreases as the flame blooms out downstream.





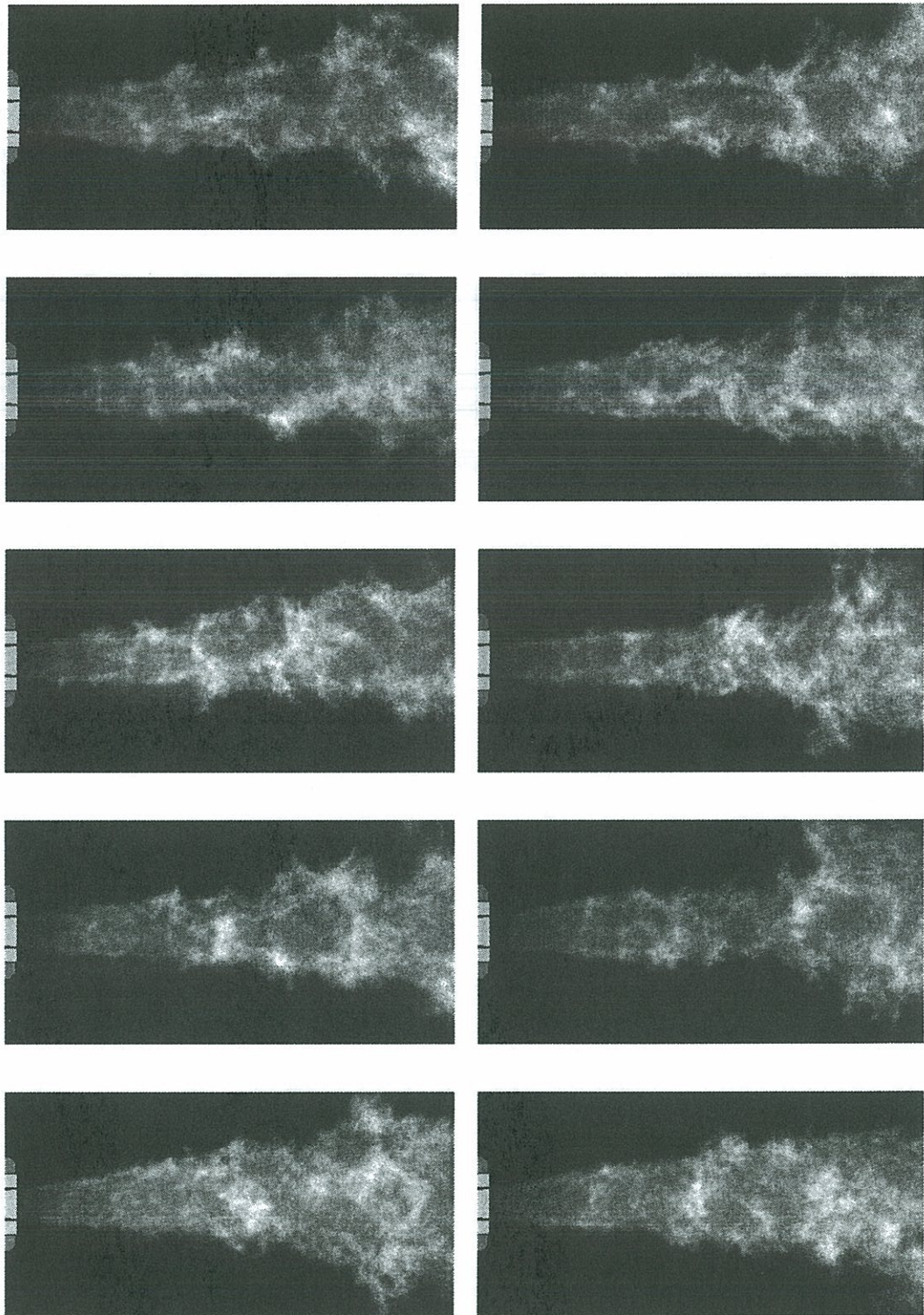
**Figure 1.25:**  $OH^*$  emission images.  $T_{H_2} = 292K$ ,  $J = 4.0$ ,  $E = 2.7$ ,  $p = 64$  bar. Images taken  $44 \mu s$  before those in figure 1.27





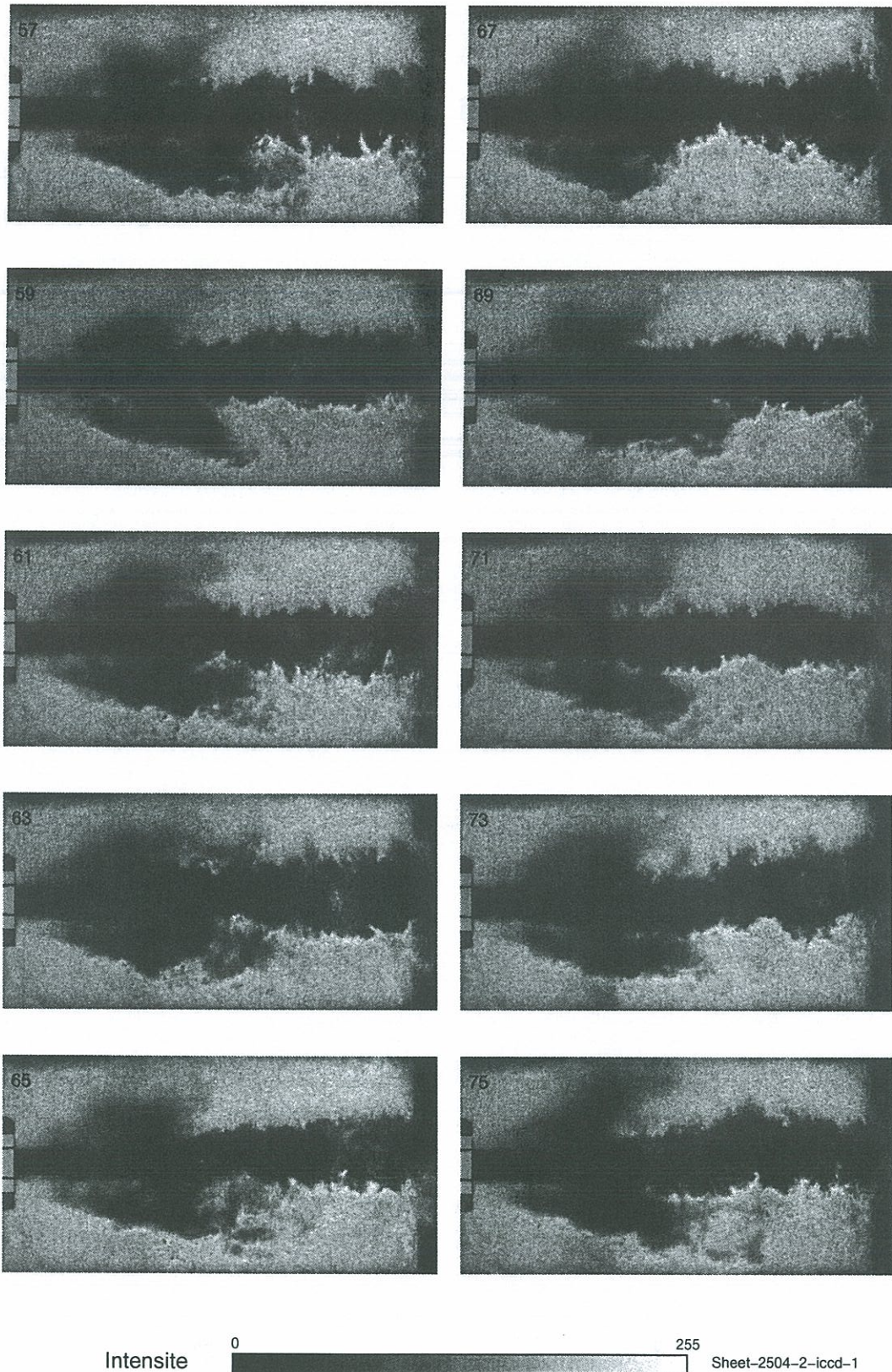
**Figure 1.26:**  $OH^*$  emission images.  $T_{H_2} = 211K$ ,  $J = 2.5$ ,  $E = 3.0$ ,  $p = 63$  bar. Images taken simulatneously with those in figure 1.28





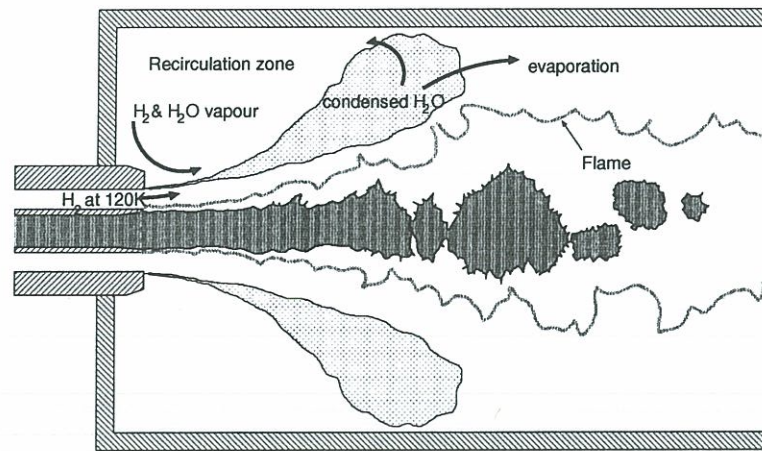
**Figure 1.27:**  $OH^*$  emission images.  $T_{H_2} = 292K$ ,  $J = 4.0$ ,  $E = 2.7$ ,  $p = 64$  bar. Images taken  $44 \mu s$  after those in figure 1.25



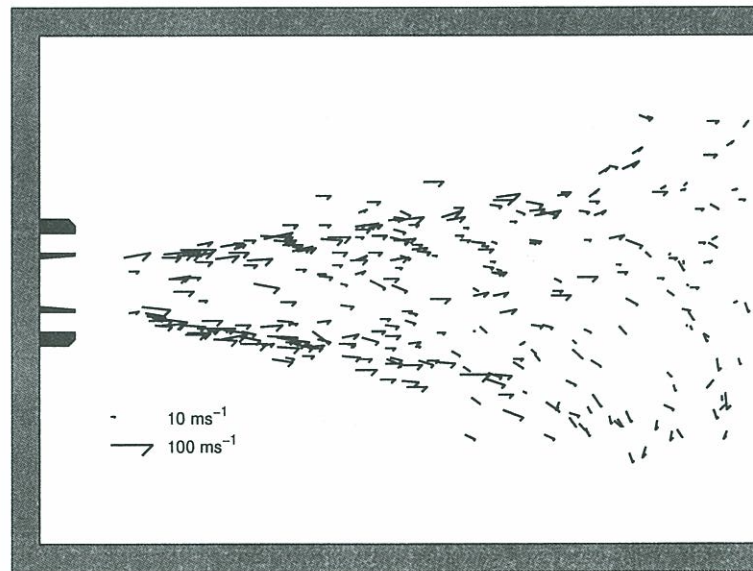


**Figure 1.28:** Backlighting images.  $T_{H_2} = 211K$ ,  $J = 2.5$ ,  $E = 3.0$ ,  $p = 63$  bar. Images taken simulatneously with those in figure 1.26





**Figure 1.29:** Representation of the flame structure with low hydrogen temperature. Low  $T_{H_2}$  has no effect on the flame itself. However, the reaction products which circulate at the upstream edge of the chamber, condense on contact with the incoming hydrogen stream. This forms a cloud which obscures the flame.



**Figure 1.30:** Velocity field in the combustion chamber when  $T_{H_2} = 292\text{K}$ ,  $J = 4.0$ ,  $E = 2.7$ ,  $p = 64 \text{ bar}$ . These are measured by following coherent structures seen in figures 1.25 and 1.27





## Chapter 2

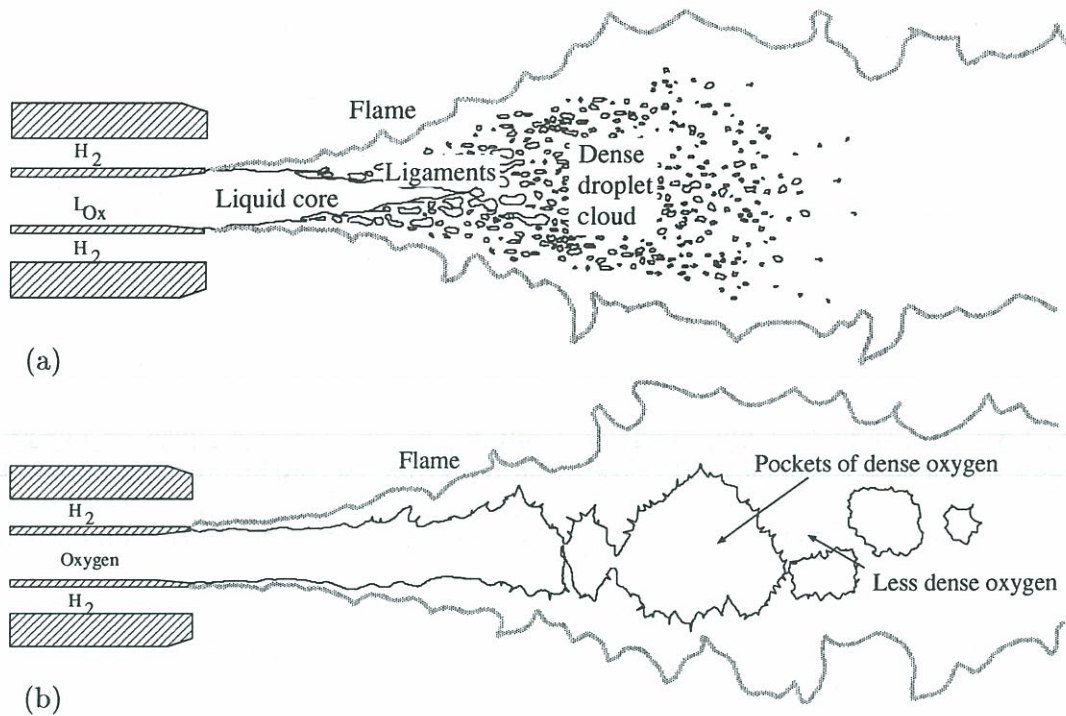
# Flame Structure

La structure générale de la flamme est décrite dans ce chapitre à partir des résultats expérimentaux donnés précédemment. On se concerne ici plutôt de la région proche de l'injecteur où se stabilise la flamme. L'angle d'expansion de la flamme, mesuré à partir des images d'émission d'OH, est comparé à travers tout les campagnes d'essais effectuées depuis 6 ans. Ces résultats sont ensuite comparés aux prévisions d'un modèle simple de flamme, qui met en évidence les paramètres importants qui affectent cet angle. Cette étude permet de rendre compte de la compétition entre les taux de vaporisation, de mélange et de combustion. Un changement de comportement est mis en évidence lorsque la pression passe d'une valeur subcritique à une valeur supercritique (par rapport à la pression critique de l'oxygène). On en déduit que la vaporisation limite le taux de combustion en dessous du point critique et que le mélange limite le taux de combustion au dessus de ce point.

## Nomenclature

$A$	Cross-sectional area
$B_{sp}$	Spalding transfer coefficient
$d$	Diameter
$Da$	Damköhler number
$\mathcal{D}$	Mass diffusivity
$J$	Momentum flux ratio
$L$	Integral eddy scale
$\dot{m}$	Mass flowrate
$p$	Pressure
$q$	Heat release per mass of oxygen burned
$\dot{q}$	Volumetric heat release rate
$Re$	Reynolds number
$T$	Temperature
$u$ or $U$	Axial / horizontal velocity
$V_f$	Volume swept out by flame surface
$\dot{w}$	Consumption rate
$\epsilon$	Mean turbulent energy dissipation rate
$\kappa$	A constant
$\lambda$	Turbulent eddy length scale
$\lambda_k$	Kolmogorov eddy scale
$\nu$	Kinematic viscosity
$\rho$	Density
$\Sigma$	Surface density
$\tau_c$	Characteristic chemical time
$\tau_v$	Characteristic vaporization time
$\tau_m$	Characteristic mixing time





**Figure 2.1:** Diagrams of the flame structure (a) below the critical pressure of oxygen (50.5 bar) (b) above the critical pressure of oxygen.

## 2.1 Introduction

This chapter starts with a general description of the structure of a cryogenic spray flame (section 2.2). More detail can be found in Tripathi (2001). Following this, in section 2.3, is a description of the region near the injector. The flame expansion angle is examined in detail in section 2.4. Experimental data from all series are compared with theoretical results from a simple 1-D model of the flame. This highlights the main factors affecting expansion angle and deductions can be made about the balance between vaporization and mixing. Finally, in section 2.5, a characteristic time argument explains how this balance changes around the critical pressure.

## 2.2 General structure

Within the cryogenic spray flame oxygen evaporates, is transferred by large scale turbulent structures to the flame front and then combusts. The oxygen jet breaks up in a fibrous regime, as defined by Farago and Chigier (1991). The envelope swept out by this jet expands from the injector at a constant angle of around 3°. At subcritical pressures, droplets exist in the combustion chamber (figure 2.1a). However, at supercritical pressures no such droplets can be seen (figure 2.1b). Similar results are reported by Mayer et al. (1998). It should be mentioned that, unlike the results presented here, the momentum flux ratios in their experiments do not match the range found in liquid rocket motors.

Pressure	10 bar	70 bar
Estimated flame volume, $V_f$ (cm <sup>3</sup> )	170	100
LOx mass flowrate, $\dot{m}_{LOx}$ (kgs <sup>-1</sup> )	0.05	0.10
Average oxygen consumption rate, $\dot{w}_{O_2}$ (kgm <sup>-3</sup> s <sup>-1</sup> )	330	1000
Average volumetric heat release, $\bar{q} = q\dot{w}_{O_2}$ (Wm <sup>-3</sup> )	$50 \times 10^8$	$150 \times 10^8$
Mean flame surface density, $\bar{\Sigma}$ (m <sup>-1</sup> ) (m <sup>-1</sup> )	160	260

**Table 2.1:** *The volumetric consumption rate and mean surface density of the flame can be estimated from the experimental measurements in chapter 1.*

Also, their LOx tube, at 1 mm diameter, is much smaller. The Abel-inverted images in chapter 1 show that the flame starts close to the dense oxygen core before expanding to the edges of the combustion chamber. It surrounds the cloud of oxygen droplets or packets, which burn in an external group mode. This general pattern is well described by Tripathi (2001). The flame is turbulent and intense. Pairs of images separated by a very short time interval show that it is convected at around 50 ms<sup>-1</sup> in the near-injector region but slows down considerably once it has expanded to the wall. At low temperatures, water in the recirculation zone condenses on contact with the hydrogen jet, forming a cloud which obscures the flame. The flame is always stabilized on the oxygen injector lip even at low hydrogen temperatures. Above the critical pressure of oxygen ( $p_{crit} = 50.5$  bar), the time-averaged intensity increases rapidly between  $1 \times d_{LOx}$  and  $7 \times d_{LOx}$ . It passes a maximum between 2 and  $4 \times d_{LOx}$ . The width of the time-averaged reacting region, which lies just outside the jet, also increases. At  $7 \times d_{LOx}$ , the reacting region thickens and blooms away from the liquid. The total intensity at a given cross-section increases to a maximum at  $12 \times d_{LOx}$ . After  $12 \times d_{LOx}$ , the reacting region is thick, but extends to smaller and smaller radii, so the total intensity at a given cross-section decreases. Images taken further downstream by Kendrick et al. (1999) show that between 1 and 10 bar the flame is at least 50 cm long. Unfortunately, at 70 bar, images were not taken far enough downstream to see the end of the flame but its length is estimated to be between 20 and 30 cm from the images in chapter 1.

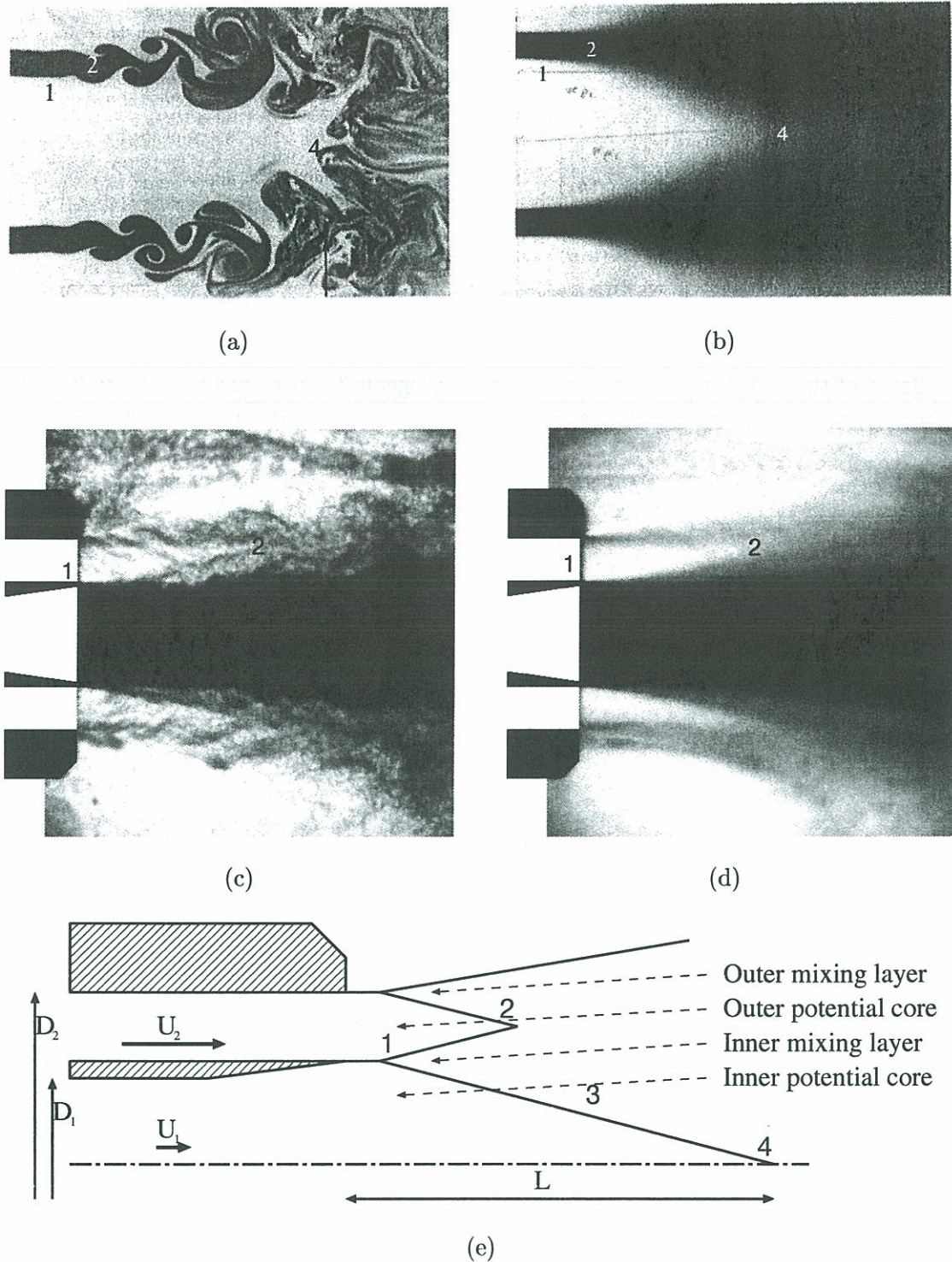
The average heat release rate is estimated in table 2.1. These calculations are based on estimates of the flame's volume and are only accurate to within an order of magnitude.

### 2.3 Structure near the injector

Chapters 4 to 8 are particularly concerned with the region near the injector, where the flame is stabilized. It is worth comparing the shadowgraphy images obtained on the cryogenic facility with images taken by Rehab et al. (1997) on a water/water coaxial injector. This is not equivalent to a gas/liquid configuration but the images, which are reproduced in figure 2.2a and 2.2b, are informative.

The potential cones are characterized by very weak turbulent velocity fluctuations. The mixing layers, on the other hand, contain very strong turbulent fluctuations. Let us consider four positions, indicated in the figures.





**Figure 2.2:** (a) Instantaneous image of a coaxial water jet. The annular flow is shown in black via planar laser induced fluorescence of a non-diffusive dye. From Rehab et al. (1997). (b) An average of 200 instantaneous images of this situation. (c) Instantaneous backlighting image of the cryogenic jet. (d) An average of 30 instantaneous images. (e) Schematic diagram of a homogenous coaxial jet, showing positions of the mixing layers and potential cones.



1. This is where instabilities at the mixing layers can first be seen. If the streams are initially turbulent, this point appears further upstream.
2. The end of outer potential cone. This position depends on the width of the annular channel. Downstream of this point the outer mixing layer interacts with the inner mixing layer and penetrates towards the center. In homogenous jets this combined layer, which contains large turbulent structures, strongly entrains the fluid of the central jet. However, for reasons given later, this is not the case in typical gas/liquid injectors, when the velocity ratio is high.
3. Continued growth of the inner mixing layer. This depends strongly on  $U_2/U_1$ .
4. End of the inner potential cone.

Some of these features can be seen on the cryogenic facility shown in figure 2.2c and 2.2d. The outer mixing layer between the hydrogen annulus and the recirculating gas is similar to that observed by Rehab. The outer potential cone is also similar. However, the inner mixing layer contains many more features in the cryogenic case and cannot be seen as clearly. Essentially two phases are present: dense supercritical oxygen and a less dense gas containing oxygen, water vapour and some hydrogen. The flame, at around 3000K, is also contained in the mixing layer. The concepts introduced in this section will be used in chapters 3 to 8, to analyze the effect of recess and stabilization of the flame.

## 2.4 Flame expansion angle

### 2.4.1 A quantitative result

Sections 2.2 and 2.3 summarize qualitative information about the shape of the flame. This information is useful for the development of models. In order to test these models, it is convenient to have quantitative data. Few quantitative results are available due to the nature of the experiments. For example, emission from OH\* radicals has not been quantitatively linked to the reaction rate. Also, the Abel inversion allows only a qualitative interpretation when self-absorption of OH\* radiation is significant.

The results presented in chapter 1 complement a database which has been built up over 6 years. Images of the flame now exist at operating points from 1 to 70 bar, for momentum flux ratios from  $J = 4$  to  $J = 14$  and recess from 0 to  $1.5 \times d_{LOx}$ . The results from all series should be compared using the same technique in order to determine the factors affecting flame structure. It is essential that this technique is consistent and objective.

The only diagnostic applied systematically at all operating points is OH\* emission. When these images are averaged and processed with the Abel inversion, a slice of the mean volumetric emission is obtained. The line of maximum emission can be traced, which gives the mean position of the flame. This position is determined by the volume of hot products and gaseous oxygen enclosed within the flame. The expansion angle results from the balance between LOx gasification and consumption. It does not simply follow the edge of the LOx spray, as is demonstrated by the blooming of the flame at  $7 \times d_{LOx}$  mentioned in section 2.2. This concept shall be explored more fully in section 2.4.3. The flame's expansion angle can be compared across all experimental runs in the database and gives useful insight into the mechanisms controlling flame structure.



It could be assumed that the flame's degree of fluctuation around its average position is independent of the operating point. In this case, the surface area of the cone of maximum emission is a constant fraction of the actual surface area of the flame. However, this assumption is not made here because it may well not be valid.

### 2.4.2 Measurement of flame expansion angle

The line of maximum mean emission rarely expands in a straight line from the oxygen injector. In previous studies, the flame has been characterized by a set of angles measured by hand, for example in Tripathi (2001) and Herding (1997). However, this is somewhat subjective and does not provide an easy way to compare operating points. More pertinent is the area or volume of the shape of revolution swept out by the line of maximum emission (This is not, of course, the actual surface area of the flame, which is wrinkled). In this study, the area is used, although the results would be very similar if the volume were used. It is better to convert the area back into the angle that would give this surface area if the flame expanded at a straight line from the injector. This is explained in figure 2.3.

This process is automated on computer. However, when trying to find the position of maximum intensity, an automated procedure is frequently misled by noise arising from stains on the windows. These points are found most accurately by hand but it is important not to be swayed by prior knowledge of the operating point in question. For this reason, images were treated four to eight times each in a random order.

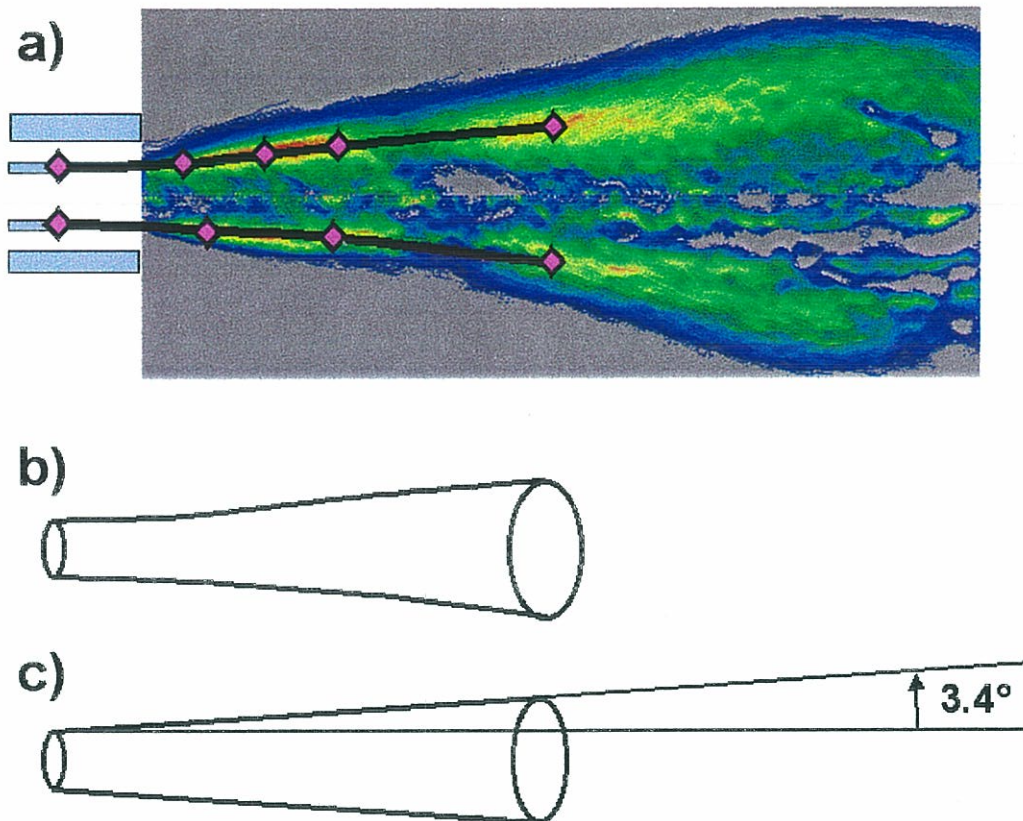
There is often only one measurement for each optical technique at each operating point. A thorough error analysis based on distribution of the results is therefore impossible. However, it is easy to measure the random error in the automated measurement procedure. This procedure was repeated at least four times, until the standard deviation between measurements was below 2.5%. This means that the error is  $\pm 5\%$ .

There are also systematic errors. These arise from the way each image is averaged and processed. For example, the measurement of the size of each image (mm/pixel) is particularly prone to error. These systematic errors are minimized when comparing images taken with the same camera in the same position, processed in the same way. An estimate of the error when different cameras are used can be obtained from a run in the third experimental series, where the two cameras both visualized OH emission simultaneously and from the same position. In this case it is 10%.

The flame expansion angles are shown in tables 2.3, 2.4, and 2.5 in section 2.4.4 for all the points with zero recess. The operating points with recess are discussed in chapter 3.

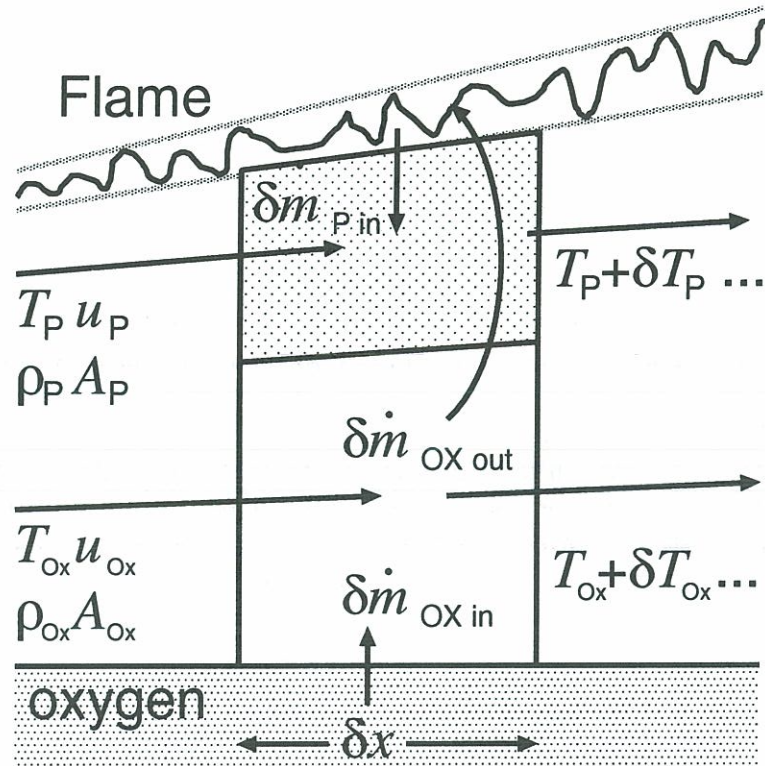
### 2.4.3 Parameters affecting the flame expansion angle

The flame encloses a region of evaporated oxygen and hot products. The volume occupied by these gases determines the flame expansion angle. There is a balance between gasification and consumption of oxygen. A simple 1-D axisymmetric model of the flame is proposed. It uses some of the ideas already exploited by Kendrick et al. (1999) to analyze the effect of recess on cryogenic jet flames. This simplified analysis demonstrates how external parameters such as pressure and hydrogen velocity affect the expansion angle of the flame. The model consists of a central core of dense (liquid) oxygen surrounded by an axisymmetric turbulent flame sheet. These two regions are separated by individual streams of low density (gaseous) oxygen and hot products.



**Figure 2.3:** Procedure for measuring the flame expansion angle. The position of the flame is measured between  $1.5$  and  $7 d_{LOx}$  from the  $LOx$  injector because the first  $1.5 d_{LOx}$  cannot be seen when the injector is recessed. Its position is interpolated between the known injector position and points on the maximum emission line. In order to be consistent, this procedure is adopted for all images. A distance of  $7 \times d_{LOx}$  is chosen because after this position the walls inhibit expansion of the most highly expanded flames.





**Figure 2.4:** A simple 1-D model is used to simulate the flame shape. The control volumes contain product (top) and evaporated oxygen (bottom). The changes in flow variables over an incremental distance  $\delta x$  can be evaluated via mass, momentum and energy balances.

Two control volumes, one containing evaporated oxygen and another containing hot products are considered at distance  $x$  from the injector (figure 2.4). They have axial extent  $\delta x$ , cross-sectional areas  $A_{Ox}$ ,  $A_P$  and properties such as density, velocity and temperature. Density and temperature are related via the equation of state. The recirculating zone which exists outside the expanding flame suggests that the axial pressure drop must be small. This assumption is only valid before the flame has reached the walls. An amount of dense oxygen from the core  $\delta \dot{m}_{Oxin}$  heats up, increases in volume and is injected into the oxygen control volume. At the same time, an amount  $\delta \dot{m}_{Oxout}$  is removed due to combustion. A proportional quantity of hot  $H_2O$  is injected into the products control volume. The speed of the products is found from a momentum balance between the hydrogen and the oxygen. It is also necessary to estimate the amount of products which are ejected to the oxygen side of the flame. For a laminar flame between species of identical diffusivities, the proportion (by mass) of products going to the oxygen side is  $1/(1+s)$ , which is  $1/9$  in this case. It will be different for other fuels, which will affect the sensitivity of flame expansion angle to oxygen consumption rate. Mass, momentum and energy balances in the control volumes lead to changes in density, velocity pressure and temperature across them.

In this model, there is no heat or mass transfer between the oxygen and the products

control volumes. Thus  $u_{Ox} \neq u_P$  and  $T_{Ox} \neq T_P$ . It would be more realistic to introduce a mixing model, such that evaporated oxygen only becomes available for combustion at a later time. However, this requires information from upstream to be stored. When the two streams are separated, the flame shape can be calculated by marching in the positive  $x$ -direction. A similar option, allowing marching, is to imagine that the two streams mix instantaneously. This is arguably more realistic but, given the limited aims of this study, the separated stream option is sufficiently accurate.

Combustion is assumed to take place in a shear layer between the oxygen and hydrogen. In accordance with many studies one may assume that the thickness,  $l$ , of this shear layer grows linearly with axial distance. The radial position of the flame,  $r$ , can be calculated from the combined cross-sectional area of the two flows. The combusting volume is given by  $2\pi r l \delta x$ . The average volumetric consumption rate of oxygen can be estimated from experimental data, as shown in table 2.1. In this table,  $V_f$  is the flame volume estimated from visualizations and  $\dot{m}_{O_2}$  is the mass flowrate of oxygen. Since all the oxygen is consumed,  $\dot{m}_{O_2}/V_f$  gives the average volumetric consumption rate and  $q\dot{m}_{O_2}/V_f$  gives the average heat release rate per unit volume. (Here  $q$  is the heat release per unit mass of oxygen:  $q = 1.5 \times 10^7 \text{ J kg}^{-1}$ ). This method is sufficiently accurate for this application because the oxygen consumption rate per unit volume turns out to have little effect on the flame expansion angle. The oxygen which burns is replaced by hot products, which occupy a similar amount of cross-sectional area. Although not used here, the consumption rate per unit surface can be estimated in order to obtain the flame surface density.

### 2.4.3.1 Balance equations

The procedure used is similar to an integral method of the type used in boundary layer theory. It is somewhat easier, however, since all flow variables are assumed constant in the radial direction. These variables are:  $\rho$ ,  $A$ ,  $u$ ,  $T$  and  $p$ . The pressure is assumed constant and  $T$  is linked to  $\rho$  via the equation of state, so only three variables are independent.

We consider small changes  $\delta\rho$ ,  $\delta A$ ,  $\delta u$  and  $\delta T$  over a distance  $\delta x$ . Mass addition from vaporization and combustion is included. The conservation equations for each control volume are:

- Mass

$$\rho u \delta A + \rho A \delta u + A u \delta \rho = \delta \dot{m}_{in} - \delta \dot{m}_{out}$$

- Momentum projected in the axial direction

$$\rho A u \delta u + \delta p = \delta \dot{m}_{in} (u_{in} - u)$$

- Energy

$$\rho A u (c_p \delta T + u \delta u) = (c_{p_{in}} T_{in} - c_p T + \frac{u_{in}^2 - u^2}{2}) \delta \dot{m}_{in}$$

Equations of state of the form  $p = \rho R T$  are used to describe gaseous oxygen and reaction products.

This results in six equations and six unknowns ( $\delta\rho_{Ox}$ ,  $\delta A_{Ox}$ ,  $\delta u_{Ox}$ ,  $\delta\rho_P$ ,  $\delta A_P$  and  $\delta u_P$ ). Given initial upstream conditions and a LOx evaporation profile, the flame shape can be calculated by marching in the  $x$ -direction. The main parameters of the problem are contained in table 2.2.



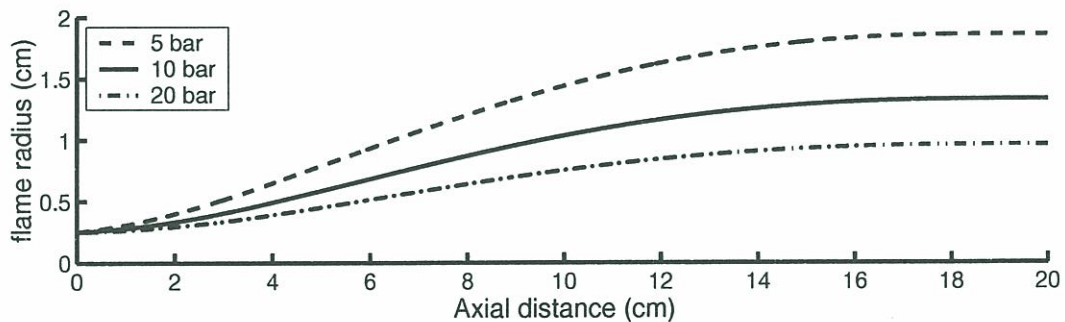
Variable parameters	Base value	Constant parameters	value
hydrogen velocity	100 ms <sup>-1</sup>	liquid oxygen jet diameter	5 mm
pressure	10 bar	liquid oxygen temperature	80 K
vol. consumption of O <sub>2</sub>	100 kgm <sup>-3</sup> s <sup>-1</sup>	liquid oxygen density	1180 kgm <sup>-3</sup>
liquid oxygen velocity	2 ms <sup>-1</sup>	product temperature	2500 K

**Table 2.2:** Values of parameters used to calculate the flame shape using the 1-D axisymmetric model

### 2.4.3.2 Numerical results

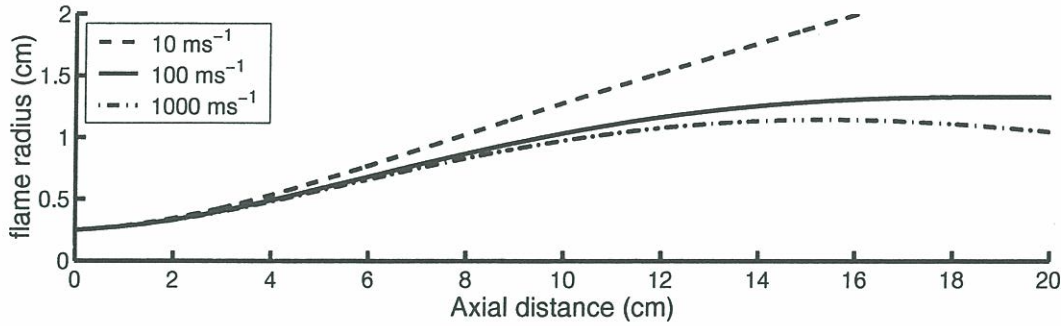
The five particularly important parameters are: pressure, hydrogen velocity, LOx velocity, LOx vaporization profile and oxygen consumption rate. The first three are varied in the experiments and the second two could be influential. An evaporation profile and a set of parameters are defined to produce a base case at  $p = 10$  bar,  $u_{H_2} = 100$  ms<sup>-1</sup>,  $u_{LOx} = 2$  ms<sup>-1</sup>, and volumetric consumption rate  $\bar{w}_{O_2} = 100$  kgm<sup>-3</sup>s<sup>-1</sup>. The parameters are varied one by one, keeping all the others constant. The effect of parameters on each other is ignored. For instance, we ignore the fact that increasing the pressure increases the gasification and consumption rates due to better mixing.

**Effect of Pressure.** In figure 2.5 it can be seen that increasing the pressure leads to a flame which moves closer to the oxygen jet. The gasification rate of oxygen is fixed, so the flame moves closer to the axis because the density of the evaporated oxygen is higher. It therefore takes up less space within the flame. In reality, this effect is compensated by an increase in the rate of oxygen vaporization.



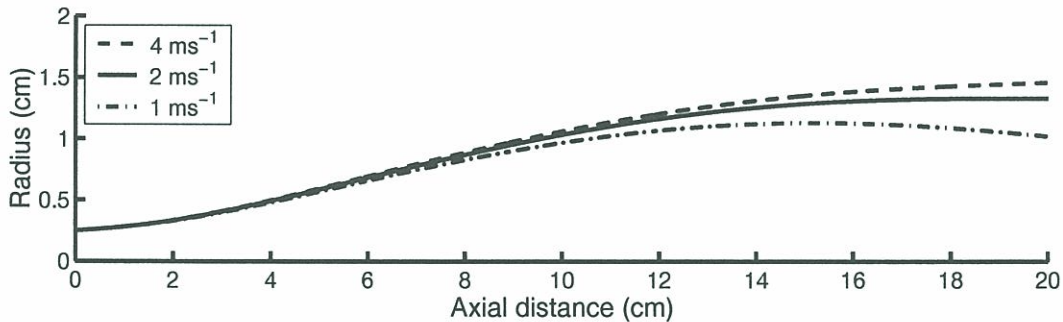
**Figure 2.5:** Flame profile calculated via the 1-D axisymmetric model. Effect of pressure. The values of all other parameters are given in table 2.2.

**Effect of hydrogen velocity.** When the hydrogen velocity increases, the flame moves closer to the oxygen core (figure 2.6). This is because the products inside the flame have a higher velocity and consequently take up less area. The effect is small between 100 ms<sup>-1</sup> and 1000 ms<sup>-1</sup>, which includes the domain in which cryogenic injectors usually operate.



**Figure 2.6:** Flame profile calculated via the 1-D axisymmetric model. Effect of hydrogen velocity. The values of all other parameters are given in table 2.2.

**Effect of the oxygen velocity.** A decrease in the oxygen velocity causes a very slight reduction in the flame expansion angle. This has little effect because, although the mass flowrate rate reduces, the lower velocity means that the area required by the oxygen flow does not change. The slight reduction arises because less area is taken up by the combustion products, whose area depends also on  $u_{H_2}$ .



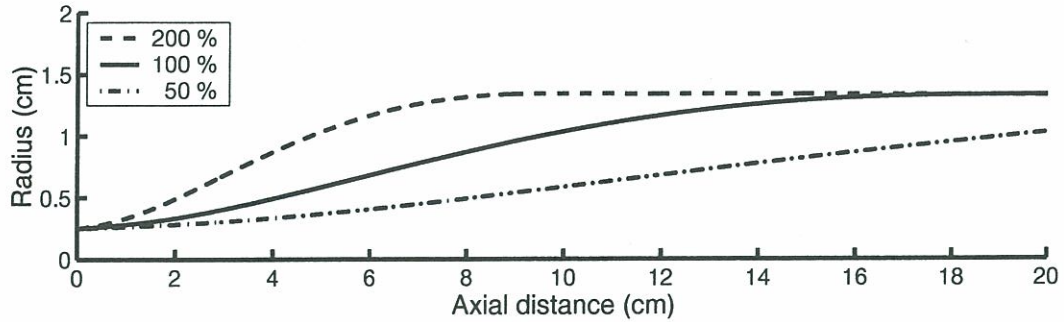
**Figure 2.7:** Flame profile calculated via the 1-D axisymmetric model. Effect of the oxygen velocity. The values of all other parameters are given in table 2.2.

**Effect of the gasification rate of oxygen.** Increasing the rate of dense oxygen gasification means that it is used up sooner. This greatly increases the expansion angle of the flame, as shown in figure 2.8. This is a very important point.

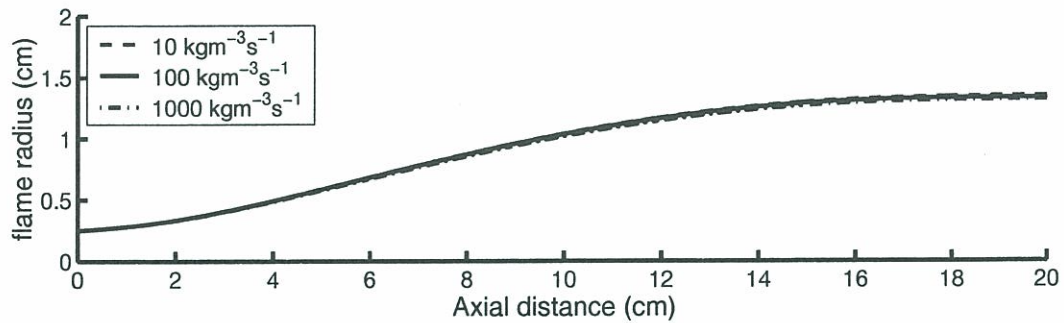
**Effect of the rate of combustion.** Increasing the rate of combustion has a negligible effect on the expansion angle of the flame, as shown in figure 2.9. This is because the combusting oxygen is replaced by 1/9 of the hot products, which take up a similar area. If, instead, all the products are assumed to flow into the oxygen side of the flame, increasing the combustion rate significantly increases the expansion angle of the flame.

These expected trends will be compared with those found from experimental results. The behaviour of the flame can then provide useful information about the crucial balance





**Figure 2.8:** Flame profile calculated via the 1-D axisymmetric model. Effect of gasification rate of oxygen, expressed as a percentage of the base case. The values of all other parameters are given in table 2.2.



**Figure 2.9:** Flame profile calculated via the 1-D axisymmetric model. Effect of the consumption rate of oxygen per unit volume. All other parameters are given in table 2.2.

between vaporization and mixing.

#### 2.4.4 Experimental results

The data from versions V01, V02 and the experiments at 10 bar on V03 are remarkably consistent. They are shown in tables 2.3 to 2.5. The only systematic anomaly is that angles are about  $1^\circ$  lower on version V01. The explanation is simple: in version V01, the oxygen injection line converges smoothly from a large cross-sectional area to the narrow exit plane. The line is also quite short. In version V02, the area contraction is sudden and the line is longer. This leads to higher turbulence in version V02, which enhances jet break-up. This increases the expansion angle of the flame by increasing the gasification rate.

##### 2.4.4.1 Effect of hydrogen velocity and gasification rate

Between 1 and 10 bar, increasing the hydrogen velocity, while keeping the oxygen mass flowrate constant, increases the flame's expansion angle. This is because jet break-up is improved, which increases the surface area and vaporization rate. Jet break-up is well

Pressure	1 bar			5 bar			10 bar		
$U_{H2}(\text{ms}^{-1})$	628	628	893	292	292	432	207	207	308
$U_{LOx}(\text{ms}^{-1})$	2.23	1.78	2.23	2.23	1.78	2.23	2.23	1.78	2.23
$J$	6.3	9.8	13.4	6.5	10.2	14.4	6.5	10.2	14.5
Expansion angle ( $^{\circ}$ )	3.8	3.5	8.4	2.6	3.6	6.8	5.1	5.1	7.2

**Table 2.3:** Operating points and experimentally-derived flame expansion angles of version VO1 of the cryogenic test facility at zero recess. The error in the angle estimation is of the order of 10%.

Pressure	5 bar		10 bar	
$U_{H2}(\text{ms}^{-1})$	292	432	207	308
$U_{LOx}(\text{ms}^{-1})$	2.23	2.23	2.23	2.23
$J$	6.5	14.4	6.5	14.5
Expansion angle ( $^{\circ}$ )	3.7	7.8	6.4	8.3

**Table 2.4:** Operating points and flame expansion angles of version VO2 of the cryogenic test facility. The error in the angle estimation is of the order of 10%.

Pressure	10 bar		70 bar				
$U_{H2}(\text{ms}^{-1})$	207	308	137	130	157	192	208
$U_{LOx}(\text{ms}^{-1})$	2.23	2.23	4.53	4.0	4.3	4.3	4.2
$J$	6.5	14.5	4.0	5.0	6.0	10.0	12.8
Expansion angle ( $^{\circ}$ )	7.1	8.2	4.2	5.0	3.8	3.7	3.6

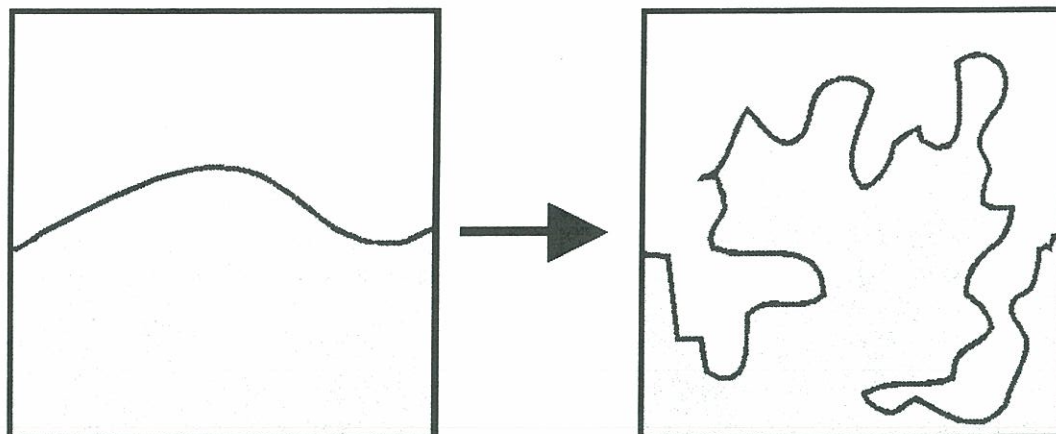
**Table 2.5:** Operating points and flame expansion angles of version VO3 of the cryogenic test facility. The error in the angle estimation is of the order of 10%.

characterized by the momentum flux ratio,  $J$ . On the other hand, at 70 bar, increasing the hydrogen velocity tends to decrease the flame expansion angle slightly. This is in accordance with the 1-D model but is different from the results between 1 and 10 bar. There is no reason to suppose that increasing  $J$  does not enhance jet break-up at this pressure. This leads to the conclusion that increased jet break-up does not affect flame expansion angle at high pressure. The inferences of this shall be discussed in section 2.5.

#### 2.4.4.2 Effect of pressure

There is a general tendency for the expansion angle to reduce with the pressure, as predicted by the 1-D model. Some of the measurements at 10 bar do not quite fit this pattern but this is because, changing the pressure modifies the balance between vaporization and turbulent mixing, which controls the gasification rate.





**Figure 2.10:** *In the model presented here, the degree of mixing is measured by the increase in surface density between two initially unmixed fluids.*

## 2.5 Balance between vaporization and turbulent mixing

The 1-D axisymmetric model in section 2.4.3 highlighted the LOx gasification profile as an important factor affecting flame expansion angle. The experimental results show that increased hydrogen velocity causes better jet break-up which, at subcritical pressures, causes increased oxygen vaporization. However, it seems that better break-up does not cause increased gasification at supercritical pressures. This can be explained by considering the factors affecting gasification rate:

- Heat transfer from the flame to the dense oxygen stream, which is mainly governed by turbulent mixing.
- Heat and mass transfer at small scale across the liquid oxygen surface (vaporization) and its equivalent in the supercritical case.

The slowest of these two rates will be dominant. They can be compared via a Damköhler number  $Da_v = \tau_m/\tau_v$ , where  $\tau_m$  and  $\tau_v$  are characteristic times of mixing and vaporization.

### 2.5.1 Characteristic mixing time

The objective of this section is to derive an expression for the mixing time. The analysis presented here is adapted from Broadwell and Breidenthal (1982), where a mixing layer between gases of similar density is considered. The thickness of the laminar diffusion zone between the two gases must be small with respect to the turbulent layer thickness. This is the case when the Reynolds number,  $Re \equiv \Delta UL/\nu$  is high and when  $\Delta UL/\mathcal{D}$  is high; where  $\mathcal{D}$  is the molecular diffusion coefficient. Equally, the flame must be thin. With these conditions satisfied,  $\Sigma$  is defined as the surface area per unit volume of the interface between the two fluids. Diffusion and combustion will only occur at this interface, so the degree of mixing is measured by the increase of this surface density, shown in figure 2.10

The surface density  $\Sigma$  is followed as the eddies decay to smaller scales. Energy cascades from integral scale eddies of size  $L$  to Kolomogorov scale eddies of size  $\lambda_k$ . The mean energy dissipation rate  $\epsilon$  is assumed to be independent of scale. This is a crude approximation within a mixing layer but is sufficient for this analysis.

The surface density,  $\Sigma$  is inversely proportional to the size of a turbulent scale,  $\lambda$ .  $\Sigma$  grows increasingly rapidly as the eddy size tends to the Kolmogorov scale,  $\lambda_k$ . The following analysis is to find the typical time  $t_k$  that this process takes.

If  $v_\lambda$  is a typical velocity associated with an eddy of scale  $\lambda$ , the mean energy dissipation rate is linked to  $\lambda$  and  $v_\lambda$  by :

$$\epsilon \sim \frac{v_\lambda^3}{\lambda} \sim \frac{\Delta U^3}{L} \quad (\lambda_k < \lambda < L) \quad (2.1)$$

If one assumes that the eddy gives up a large fraction of its energy to smaller scales in the time it takes to revolve once,  $\Delta t_\lambda \sim \lambda/v_\lambda \sim \lambda^{2/3} \epsilon^{-1/3}$ . The requirements of self-similarity suggest that:

$$dt = \kappa \frac{\lambda^{2/3}}{\epsilon^{1/3} \lambda} d\lambda \quad (2.2)$$

where  $\kappa$  is a constant. Integration of (2.1) and (2.2) gives the time to reach a scale  $\lambda$ , starting at  $L$ :

$$t_\lambda = \frac{3}{2} \kappa \frac{L}{\Delta U} \left[ 1 - \left( \frac{\lambda}{L} \right)^{2/3} \right] \quad (2.3)$$

The Kolmogorov scale is related to the large scale  $L$  through:  $\lambda_k \sim L/Re^{3/4}$ . Thus:

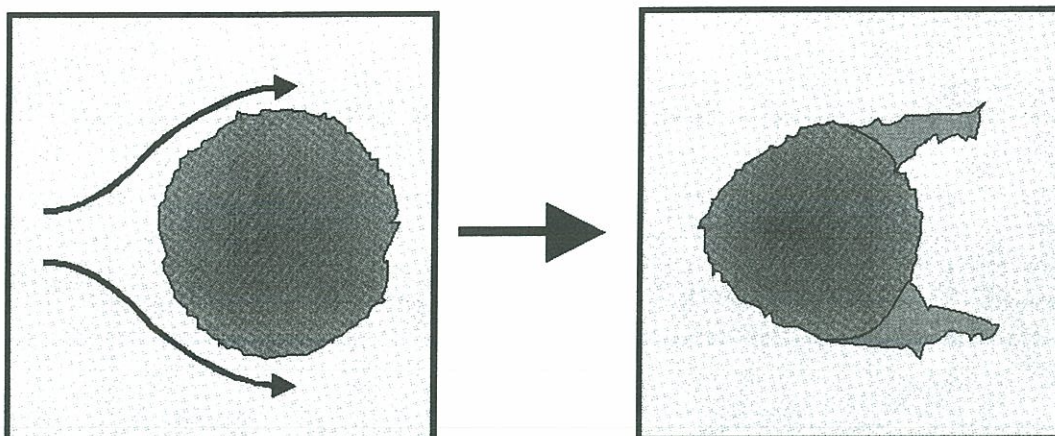
$$t_k = \frac{3}{2} \kappa \frac{L}{\Delta U} \left[ 1 - \frac{1}{Re^{1/2}} \right] \approx \frac{3}{2} \kappa \frac{L}{\Delta U} \quad \text{for } Re \gg 1 \quad (2.4)$$

According to this expression, the time to reach the smallest scales is proportional to  $L/\Delta U$ , virtually independently of the Reynolds number. It is therefore also independent of the pressure. The constant of proportionality,  $\kappa$  is not known *a priori*. It can be estimated by noticing that  $L/\Delta U$  is the time taken for the large eddy to rotate through  $1/\pi$  revolution. Given the assumption used to derive equation (2.2) and noticing that it is the decay of the largest eddies which contribute most to the total time  $t_k$ ,  $\kappa$  is between 1 and 10. For typical  $L$  and  $\Delta U$  in the combustion chamber used in the experiments,  $\tau_m = t_k$  is between 2 and 80  $\mu s$ .

### 2.5.2 Characteristic vaporization time

At subcritical pressures, the vaporization time can be crudely estimated via the model of an isolated droplet in a gas at rest:  $\tau_v = d^2 \rho_l / [8D_{O_2} \rho_g \ln(1 + B_{sp})]$ . The droplet size,  $d$ , is typically 10 to 80  $\mu m$ . The ambient gas is taken to be water vapour at 1000K. The Spalding transfer number,  $B_{sp} = c_p(T_g - T_{LOx})/\Delta h_v = 10$ . Thus at 1 to 10 bar,  $\tau_{vap}$  is from 10  $\mu s$  to 600  $\mu s$ . At 50 bar this decreases to between 1  $\mu s$  and 60  $\mu s$ . However, around and above the critical pressure, surface tension and the latent heat of vaporization





**Figure 2.11:** Above the critical pressure, the surface tension and latent heat of vaporization of a liquid tend to zero. As a consequence, aerodynamic instabilities grow rapidly and the outer layer of droplet is rapidly stripped in a process analogous to vaporization.

diminish. As a result, Delplanque and Sirignano (1994) and Delplanque and Sirignano (1995) propose that aerodynamic instabilities on the surface of a droplet are undamped and grow rapidly. Consequently, the outer layer of the liquid is stripped off and mixes with the surrounding gas in a process analogous to vaporization, shown in figure 2.11. According to their numerical simulations, this rate is larger than the vaporization rate at the same pressure by at least an order of magnitude. This brings the new vaporization time to between  $0.1\mu s$  and  $6\mu s$ .

### 2.5.3 Characteristic chemical time

It is important to check that the rate of reaction will never be limiting and that the flame will be thin. The Chemical time is given by  $\tau_c = D/S_l^2$ . It is typically less than  $2\mu s$  and therefore satisfies both of these criteria.

### 2.5.4 The Damköhler number

The estimates of the characteristic times can be compared as Damköhler numbers. At subcritical pressures ( $p < 50.5$  bar),  $Da_v \sim 10^{-1}$  but at supercritical pressures  $Da_v \sim 10^1$ . This shows that the process determining the rate of gasification changes around the critical pressure. At subcritical pressure it is vaporization-controlled. This rate is affected greatly by the surface area of the liquid jet, which is determined by jet break-up and hence the momentum flux ratio,  $J$ . Above the critical pressure, when there is neither a surface nor a latent heat of vaporization, flame expansion is limited by the rate at which heat can be transferred from the flame to the condensed oxygen, which is determined by turbulent mixing. This rate is no longer affected by the surface area of the condensed jet. In addition, this leads to an enhanced gasification rate at supercritical pressures, which explains why the flame is shorter.

## 2.6 Conclusion

Experimental results from the cryogenic flame show the effect of pressure, gas velocity and gasification rate on its shape. These have been compared with the tendencies deduced from a simplified one-dimensional model. The gasification rate is particularly informative. It is determined by a balance between turbulent mixing and vaporization. The analysis in this section demonstrates that vaporization is the rate-limiting process of oxygen gasification at subcritical pressures and that turbulent mixing is the rate-limiting process at supercritical pressures. This arises because the surface tension and the latent heat of vaporization tend to zero above the critical pressure.



## Chapter 3

# Effect of Recess

Quand le conduit d'oxygène est placé en retrait à l'intérieur de l'injecteur d'hydrogène, l'efficacité de combustion est améliorée. Ceci est dû à une meilleure rupture du jet d'oxygène. Quelques mécanismes sont proposés dans ce chapitre pour rendre compte de cet effet. L'analyse est développée après avoir passé en revue les paramètres qui affectent la rupture d'un jet coaxial. Deux mécanismes doivent être envisagés:

- Les produits de combustion se forment à l'intérieur de l'injecteur d'hydrogène. La section disponible pour l'écoulement d'hydrogène est diminuée car les produits issus de la combustion occupent une partie de la surface disponible pour l'écoulement. En même temps l'écoulement est chauffé par la flamme. La vitesse d'hydrogène est augmentée, ce qui augmente le cisaillement entre le gaz et le liquide et provoque une meilleure rupture du jet.
- L'écoulement d'oxygène se comporte comme un sillage au sein de l'écoulement d'hydrogène. Quand l'écoulement d'hydrogène est borné par les parois du conduit, le sillage a tendance à devenir instable d'une façon absolue, au lieu d'être instable d'une façon convective. Une analogie peut être faite entre le développement d'un sillage derrière un obstacle qui conduit au lâché de tourbillons alternés. Le développement d'une instabilité absolue peut être décrite comme une propagation vers l'amont des perturbations amplifiées. L'instabilité absolue produit une résonance du jet d'oxygène qui entraîne une rupture du jet plus précoce.

## Nomenclature

$a$	Wave amplitude
$A$	Cross-sectional area
$b$	Mixing layer thickness
$B_{sp}$	Spalding transfer coefficient
$c$	Wave phase velocity $\equiv \omega/k$
$c_p$	Specific heat capacity, constant pressure
$C$	Constant
$d$	Diameter
$D$	Dispersion relation
$\mathcal{D}$	Mass diffusivity
$E$	Mass flow ratio
$h_1$	Half-width / radius of central jet
$h_2$	Half-width / radius of annular jet
$h_3$	Width of annular jet; $h_3 = h_2 - h_1$
$\Delta H_{comb}$	Heat release of combustion per unit mass of oxygen
$J$	Momentum flux ratio
$k$	Wavenumber
$l_b$	Break-up length of central jet
$l_r$	Recessed length
$\dot{m}$	Mass flowrate
$M$	Mach number
$n$	An integer
$p$	Pressure
$P$	Set of all control parameters
$r$	Wave growth rate $\equiv a^{-1}dt/da$
$r$	Gas constant
$R$	Universal gas constant
Re	Reynolds number
$s$	Mass stoichiometric ratio
$S$	Density ratio $\rho_1/\rho_2$
$t$	Time
$T$	Temperature
$u$	Axial / horizontal velocity
$u_c$	Convection velocity
$u_p$	Phase velocity
$U$	Free stream axial / horizontal velocity
$V$	Velocity ratio $U_1/U_2$
We	Weber number



$\cdot_2$ or $\cdot_g$	Annular fluid
$\cdot_1$ or $\cdot_l$	Central fluid
$\cdot^*$	Non-dimensional
$\cdot_i$	Imaginary
$\cdot_r$	Real
$\cdot_0$	Absolute wavenumber / frequency
$\beta$	Ratio of radii: $h_2/h_1$
$\beta$	Proportion of LOx which evaporates in recessed portion
$\delta_{sl}$	Shear layer thickness
$\eta$	Corrugation factor ( $\eta > 1$ )
$\gamma$	Ratio of specific heats
$\kappa$	Non-dimensional wavenumber $\equiv k\delta_{sl}$
$\lambda$	Instability wavelength
$\Lambda$	Velocity factor $\equiv (U_1 - U_2)/(U_1 + U_2)$
$\omega$	Angular frequency
$\Omega$	Non-dimensional angular frequency $\equiv \omega/[k(U_2 - U_1)]$
$\varphi$	Gill's expansion factor (equation 3.13)
$\rho$	Density
$\sigma$	surface tension
$\Sigma$	Geometry-weighted density ratio (equation 3.27)
$\tau_c$	Convection time $\equiv l_r/u_c$
$\xi$	Proportion of heat absorbed by hydrogen stream

## 3.1 Introduction

Recessing the liquid oxygen duct inside the hydrogen tube improves the combustion efficiency of cryogenic rocket engines. This is because a larger fraction of the oxygen burns before reaching the chamber exhaust. Experimental data on coaxial injectors, summarized in section 3.2, demonstrates that recess improves break-up of the central jet. Mechanisms of break-up and mixing of coaxial jets are discussed in section 3.3. A number of plausible mechanisms for the effect of recess are proposed and tested experimentally in sections 3.4 to 3.8. The conclusions are presented in section 3.9.

## 3.2 Experimental evidence of the effect of recess

The effect of recess in a coaxial injector can be seen in both reacting flows and cold flows. Le Visage (1996) and Carreau et al. (1997) studied a water/air coaxial injector and found that there is an optimum recessed length which leads to a well pulverized jet and homogenous droplet distribution. At larger recessed length, however, it is found that the spray is channelled by the outer flow, reducing its expansion angle.

A similar water/air coaxial injector has been developed in our laboratory by B. Leroux. It is possible to obtain the same momentum flux ratio,  $J$  and mass flux ratio,  $E$ , as in the cryogenic combustion facility, Mascotte. PDPA and shadowgraphy are used to determine the liquid core length and the distribution of droplet sizes and velocities. Complete details can be found in Leroux (2001) and Blanchère and Defoort (2001). Two particular experimental series are presented in section 3.8.6, both demonstrating that recess affects rupture of the central jet.

Further evidence comes from measurements on the cryogenic combustion facility. Shadowgraphy images indicate that recess improves rupture of the oxygen jet. Furthermore, at low  $J$  and below the oxygen's critical pressure, the flame expansion angle increases strongly with increased recess. This is shown in table 3.1. At subcritical pressures, an increased flame expansion angle indicates increased oxygen gasification, which is caused by better jet break-up. Above the critical pressure, increased jet break-up does not increase the gasification rate near the injector because vaporization, which depends on the jet surface area, is not a rate-limiting process. However, better jet break-up may increase mixing and homogeneity further downstream, which would nevertheless improve combustion efficiency without affecting the initial expansion angle.

## 3.3 Break-up and mixing of coaxial jets

### 3.3.1 Introduction

The experimental evidence indicates that recess acts by improving rupture of the central jet. Since recess only alters the outer boundary of the outer stream, this mechanism must involve interaction of the two flows. In this section, the rupture of the liquid stream in a coaxial injector is reviewed. Two families of models are proposed, one based on an instability analysis, the other based on global properties of mixing layers. These models, which give similar results, are compared with experimental results. The concepts developed in this section provide the basis for the rest of this chapter.



Pressure	5 bar		10 bar (1)		10 bar (2)		70 bar		
Point	C	A	C	A	C	A	C	C	A
$U_{H_2}(\text{ms}^{-1})$	292	432	207	308	207	308	130	157	192
$U_{LOx}(\text{ms}^{-1})$	2.23	2.23	2.23	2.23	2.23	2.23	4.0	4.3	4.3
$J$	6.5	14.4	6.5	14.5	6.5	14.5	5.0	6.0	10.0
Recess ↓	Expansion angle								
$l_r = 0$	<b>3.7°</b>	7.8°	<b>6.4°</b>	8.3°	<b>7.1°</b>	8.2°	5.0°	3.8°	3.7°
$l_r = 1 \times d_{LOx}$	<b>12.7°</b>	7.8°	<b>10.6°</b>	7.4°	<b>12.3°</b>	8.0°	4.3°	3.5°	3.0°
$l_r = 1.5 \times d_{LOx}$	-	-	-	-	<b>10.1°</b>	8.8°	-	3.0°	3.1°

**Table 3.1:** Operating points and expansion angles of the cryogenic spray flame. These are shown as a function of the momentum flux ratio  $J$  and recessed length  $l_r$ . Columns 10 bar(1) and 10 bar(2) refer to different versions of the test facility. Particularly interesting results are in bold type. The error between angle measurements is around 10%. Recess has a significant effect on flame expansion angle only at low  $J$  and pressures below the critical pressure of oxygen. ( $p_{crit}(O_2) = 50.5 \text{ bar}$ )

### 3.3.2 Break-up regimes of coaxial injectors

Atomization in coaxial injectors can be divided into two stages.

- Primary atomization, which refers to the break-up of the central jet into ligaments and large droplets.
- Secondary atomization, which refers to the subsequent disintegration of these structures.

Although the largest amount of the liquid surface area is created via secondary atomization, primary atomization is the rate-limiting process in the regime in which the cryogenic coaxial injector functions.

Farago and Chigier (1991) report extensive visualizations of two phase coaxial jets. Their results are summarized in figure 3.1. These authors conclude that coaxial injectors exhibit three main rupture regimes, introduced below. These are characterized by their modes of primary atomization, which are qualitatively different. Furthermore, increasing the momentum flux ratio (equivalent to increasing the aerodynamic Weber number) within all regimes leads to a mode in which the liquid jet pulsates. Coaxial injectors in rocket motors operate in the fibrous regime and some authors suggest that transition to the “superpulsating” fibrous regime is possible. Consequently these two regimes are studied in particular detail.

#### 3.3.2.1 Rayleigh regime

The Rayleigh mode occurs at low velocities. It is characterized by a varicose instability which is dominated by surface tension. The mean droplet diameter is of the order of the jet diameter. The droplets form without development of membranes or ligaments of fluid. For water/air jets, this mode is active for a Weber number below 25, where  $We = \rho_2(U_2 - U_1)^2/d_1$ .

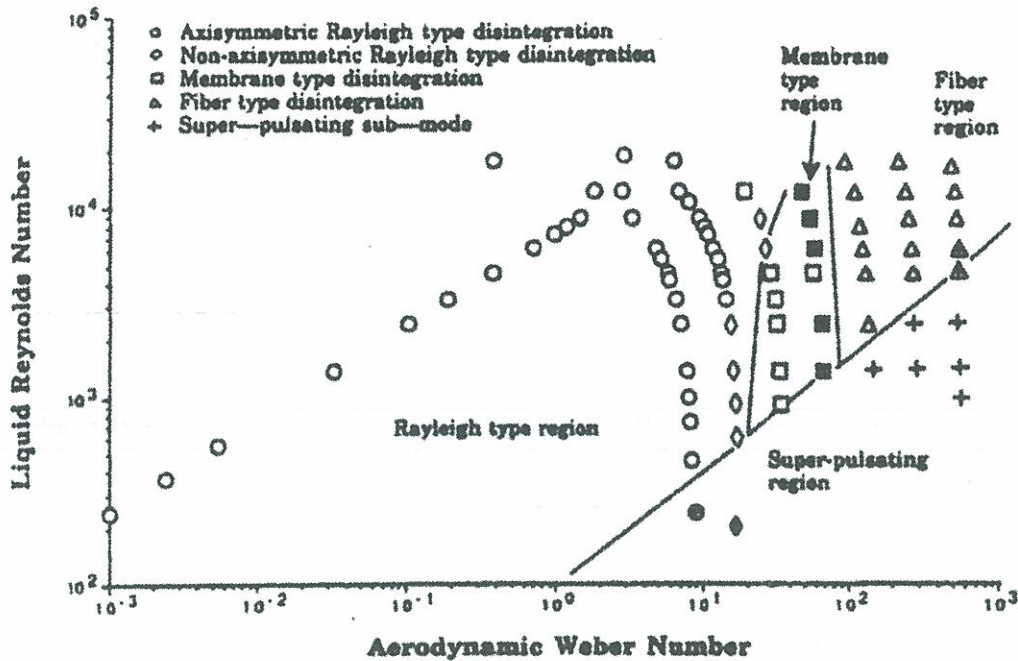


Figure 3.1 : Break-up regimes of coaxial jets, from Farago and Chigier (1991)

### 3.3.2.2 Membrane regime

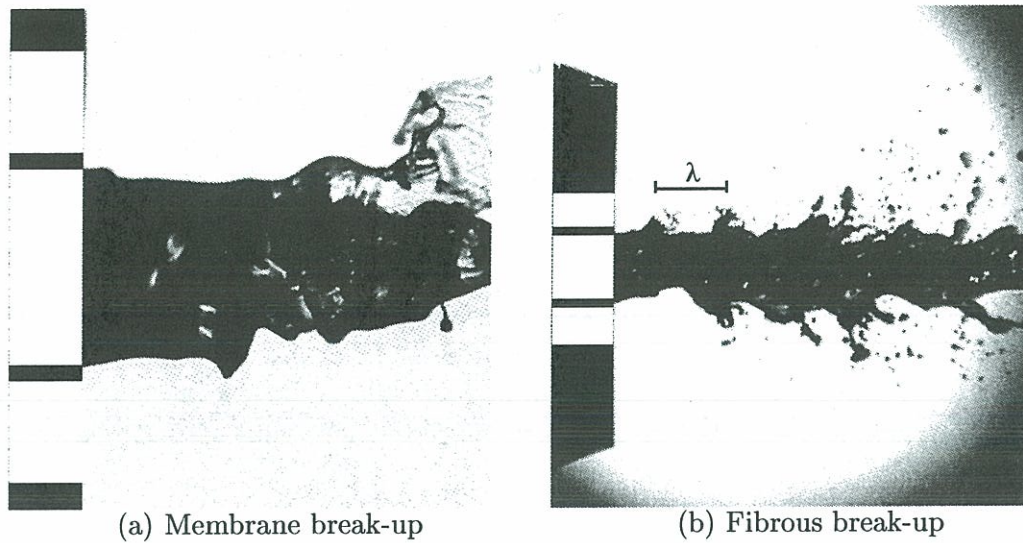
The jet develops into a thin liquid sheet, which then breaks up into droplets. This is shown in figure 3.2a. The droplet diameter is considerably smaller than the diameter of the jet. For water/air jets, this mode is active for  $25 < We < 70$ .

### 3.3.2.3 Fibrous regime

The liquid jet rapidly develops surface waves of wavelength  $\lambda$ , which then deform into ligaments, as in figure 3.2b. This process is well retrieved in the numerical studies of Li et al. (1995), Zaleski (1998) and the experimental images of Lasheras et al. (1998). These ligaments break-up into droplets which are an order of magnitude smaller than the liquid jet diameter. This mode is active for  $70 < We < 500$ .

The parameter  $l_b/d_1$  (length of liquid potential cone divided by liquid jet initial diameter) is often used to quantify the degree of primary atomization. Lower values correspond to better primary atomization. In the fibrous regime,  $l_b/d_1 \gg 1$  and  $\lambda < l_b$ . Consequently, primary atomization can be considered by examining the deformation of waves as they move along the interface. Either temporal or spatial analyses can be employed. The growth of these instabilities is tackled in section 3.3.3





**Figure 3.2:** Images of two jet rupture regimes. In the fibrous regime, the primary instability wavelength is marked.

#### 3.3.2.4 Superpulsating fibrous regime

The superpulsating fibrous regime is attained when  $Re_l/\sqrt{We_g} < 100$ . In this regime the central fluid pulsates. Lasheras et al. (1998) propose that there is a zone of recirculating air just downstream of the liquid core. This can be envisaged as follows: If the liquid velocity were zero, there would be a recirculating zone of air in the wake of the central tube. At low flowrates, the liquid fills some of this zone but is entrained by the gas too quickly to fill all of it. The residual recirculating zone causes pulsation in the entrained flow. When the liquid flowrate is large enough to fill this recirculating region, the conditions correspond to the fibrous regime.

An alternative explanation is that the pulsation is due to the helicoidal instability which will be described in section 3.8. In water/air coaxial jets this seems to occur before the appearance of a recirculating zone. In water/water coaxial jets, Rehab et al. (1997) observe that a helicoidal instability develops after appearance of the recirculating zone.

#### 3.3.3 Primary atomization in the fibrous regime

In this instability analysis primary atomization is divided conceptually into three stages:

1. Creation of tiny perturbations at the interface between the two fluids.
2. Selective amplification of these perturbations while at small amplitudes, where a linear approximation is justified.
3. Non-linear development of these instabilities and the formation of ligaments and droplets. Rupture of these structures is designated as secondary atomization.

When the fluids are initially turbulent, a range of perturbations is imposed immediately at the interface. Their growth in stage (2) is exponential in time, so even the smallest perturbation can rapidly become significant. The combination of initial wavelength distribution and selective amplification gives the distribution of primary instabilities. Unsurprisingly, turbulence has little effect on the predominant primary instability when the most amplified wavelength differs greatly from typical turbulent lengthscales. This has been verified by Raynal (1997).

Numerical simulations such as those by Zaleski (1998) show the structures on the jet's surface during all three stages of primary atomization. The stage which is particularly accessible to analytical analysis is the second, where a linear approximation is justified. This is developed further in section 3.3.4. Furthermore, according to Farago and Chigier (1991) it is likely that the linear stability of the flow also affects the non-linear development in stage (3). However, this is the subject of some debate, particularly regarding the role of surface tension.

### 3.3.4 Analysis in the linear range of primary atomization

The destabilizing mechanism is aerodynamic: Perturbations at the gas/liquid interface alter the fluids' velocities. This creates a pressure differential which amplifies the perturbations further. If the interface is assumed to be infinitely thin, surface tension is the stabilizing mechanism. This acts on small wavelengths with high curvature. This is the pure Kelvin-Helmholtz (pure K-H) mechanism described in Rayleigh (1896) section 365. Assuming disturbances with amplitude proportional to  $e^{i(kx-\omega t)}$ , the dispersion relation is given by equation (3.1).

$$k\sigma + \rho_2(U_2 - c)^2 + \rho_1(U_1 - c)^2 = 0 \quad (3.1)$$

where  $c \equiv \omega/k$ ,  $\sigma$  is the surface tension, subscript 1 denotes the bottom stream and subscript 2 denotes the top stream. Viscosity can be introduced by using the Orr-Sommerfeld analysis but Zaleski (1998) finds that in typical situations this has a negligible effect on the main instability, so it is neglected here. Another stabilizing mechanism, explained later, arises because the shear layer between the two fluids is not infinitely thin.

The growth rate  $r$  for waves of amplitude  $a$  and wavenumber  $k$  is given by equation (3.2).

$$r \equiv \frac{1}{a} \frac{da}{dt} = \omega_i = k \left( \frac{k\sigma}{(\rho_2 + \rho_1)} - \frac{\rho_2\rho_1(u_2 - u_1)^2}{(\rho_2 + \rho_1)^2} \right)^{1/2} \approx ku_2 \left( \frac{\rho_2}{\rho_1} \right)^{1/2} \quad (3.2)$$

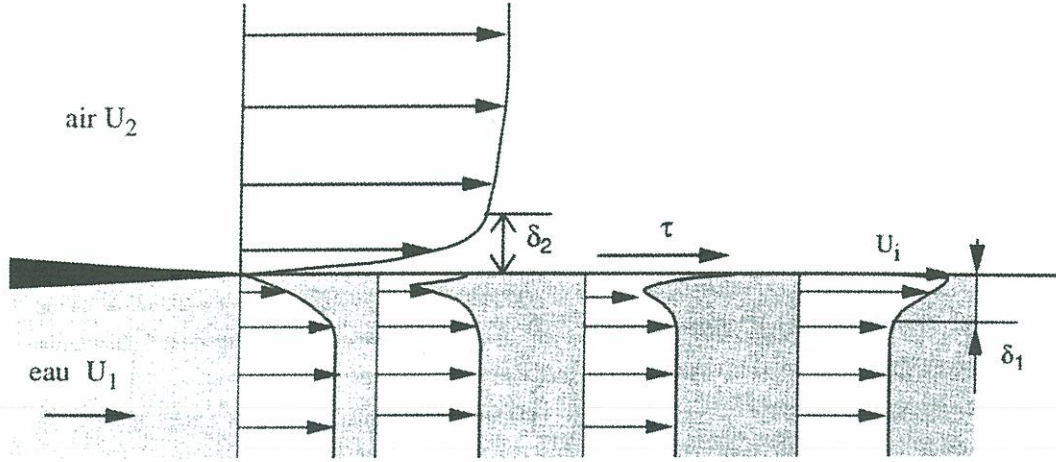
(The approximate expression on the right hand side is in the limit  $\sigma \rightarrow 0$ ,  $\rho_1 \gg \rho_2$  and  $u_2 \gg u_1$ ). With this model, the most amplified wavelength is given by:

$$\lambda = 3\pi \left( \frac{\sigma}{\rho_2 u_2^2} \right) \quad (3.3)$$

although this turns out to be irrelevant.

In reality, the shear layer between the two fluids is not infinitely thin. When the surface tension is small or the velocities high (i.e. at large Weber number), expression (3.3) predicts a wavelength much smaller than the thickness of this shear layer. The pure





**Figure 3.3** : Diagram of the velocity profiles in the shear layers. From Raynal (1997)

K-H model is not valid in this range. This is confirmed by the experimental results of Raynal et al. (1997) and the numerical results of Zaleski (1998) which show that surface tension has no effect on the primary instability wavelength.

Consequently another lengthscale, the shear layer thickness  $\delta_{sl}$ , must be introduced. This approach is explained in Rayleigh (1896), section 367. The velocity profile is assumed to vary linearly between the two free stream values over a distance  $\delta_{sl}$ . The dispersion relation for perturbations in a uniform density fluid is:

$$e^{-2\kappa} = [1 - \kappa(2\Omega + 1)][1 + \kappa(2\Omega - 1)] \quad (3.4)$$

where  $\kappa \equiv k\delta_{sl}$  and  $\Omega \equiv \omega/[k(U_2 - U_1)]$ . In the limit  $\kappa \rightarrow 0$ , which occurs when the wavelength is long compared with the shear layer thickness, this equation necessarily reduces to the dispersion relation (3.1) of the pure K-H model without surface tension. This is easily verified by considering the limit  $\kappa \rightarrow 0$  and expanding (3.4) up to second order terms. The exact shape of the profile turns out not to be very influential; see Esch (1957).

A diagram of the velocity profile at the gas/liquid interface is shown in figure 3.3. Raynal et al. (1997) find that conditions on the gas side dominate because the velocity profile on the liquid side does not have time to develop before the instabilities have grown significantly. Villiermaux (1998) extends Rayleigh's analysis to include a step density increase just outside the piecewise shear profile. This simulates the shear layer on the gaseous side, producing a dispersion relation:

$$e^{-2\kappa} = [1 - \kappa(2\Omega + 1)] \frac{[1 + \kappa(2\Omega - 1) \frac{(\rho_1/\rho_2)+1}{2}]}{[1 + \kappa(2\Omega - 1) \frac{(\rho_1/\rho_2)-1}{2}]} \quad (3.5)$$

By inspection, this reduces to equation (3.4) when  $\rho_1/\rho_2 = 1$ , and therefore reduces to the pure K-H model without surface tension when  $\kappa \rightarrow 0$ . Furthermore, by solving numerically it can be shown that the results of equation (3.5) tend to the pure K-H results

(3.1) when  $\kappa \rightarrow 0$  for any density ratio. This is to be expected and shows that equation (3.5) is simply a refinement of the pure K-H analysis to include a stabilizing mechanism caused by the shear layer thickness rather than by surface tension. It is crucial to note that, for long wavelengths, the two models are equivalent.

After some manipulation, Villermaux (1998) finds that the growth rate of the most amplified instability in the high density ratio limit takes the form:

$$r \sim \frac{\rho_2 u_2}{\rho_1 \delta_{sl}} \quad (3.6)$$

and selected wavelength:

$$\lambda \approx \frac{2\pi}{1.5} \left( \frac{\rho_1}{\rho_2} \right)^{1/2} \delta_{sl} \quad (3.7)$$

For a water/air injector, the density ratio is around 800, which means that the selected wavelength occurs at low values of  $\kappa$  (around 0.05). The stabilizing effect of the shear layer is felt even at this relatively long wavelength. However, results presented in Villermaux (1998) show that as the wavelength increases further the shear layer quickly loses its influence.

The pure K-H mechanism suggests that the speed of wave crests, the phase velocity, is:

$$u_p = \frac{\rho_1 U_1 + \rho_2 U_2}{\rho_1 + \rho_2} \quad (3.8)$$

However, the experimental results of Raynal et al. (1997) show unambiguously that the convection velocity of structures at the interface is:

$$u_c = \frac{\sqrt{\rho_1} U_1 + \sqrt{\rho_2} U_2}{\sqrt{\rho_1} + \sqrt{\rho_2}} \quad (3.9)$$

A convection velocity of this form has been proposed by Bernal and Roshko (1986) for a shear layer in which waves have developed into large amplitude vortex structures. The pure K-H model is valid only at very small amplitude, so it is possible that the convection velocity starts at  $u_p$ , given by equation (3.8), and tends towards  $u_c$ , given by equation (3.9), as the amplitude increases. An alternative explanation is proposed by Villermaux (1998). He states, without a demonstration, that the *group* velocity of equation (3.5) is consistent with equation (3.9). This may be possible in a certain range of  $\kappa$ , but not as  $\kappa \rightarrow 0$ , where pure K-H features are obtained and the group velocity becomes equal to the phase velocity given by equation (3.8). In any case, the group velocity is irrelevant since it designates the speed of the envelope of the waves, not the speed of wave crests. Consequently, it is difficult to believe that the measurement of  $u_c$  by Raynal et al. (1997) can be taken as evidence that the shear layer mechanism is active, although, in fact, this particular evidence is not necessary.

Further evidence for the shear layer mechanism is supplied by the wavelength of the primary instability. Raynal et al. find that this wavelength is proportional to  $U_2^{-1/2}$ . This result is consistent with equation (3.7) if  $\delta_{sl}$  is proportional to  $U_2^{-1/2}$ . This would



be expected since the shear layer thickness will scale in the same manner as a boundary layer thickness. Raynal et al. suggest that the vorticity thickness should be used.

The entrainment velocity is defined as the average velocity at which fluid crosses from the central core to the annular stream. It is given approximately by the product  $r\lambda$  and is proportional to  $u_2(\rho_2/\rho_1)^{1/2}$  for both the shear layer mechanism and the pure K-H mechanism. Assuming an approximately conical liquid core, with a surface area which varies with  $l_b^2$ , this leads to a scaling rule for the length of the potential cone:  $l_b/d_i \propto J^{-1/2}$ . According to this expression, the length  $l_b$  is inversely proportional to the square root of the momentum flux ratio. When  $l_b$  is increased, the length of the cone decreases.

### 3.3.5 Global mixing layer models

Global correlations can be derived for the rate of growth of turbulent mixing layers without considering the structures within the layers. This leads to similar expressions for the break-up length of the central fluid. A result of Abramovich (1963) is applied to a cryogenic coaxial injector by Gill (1978). This model is developed for a mixing layer between two semi-infinite co-flowing streams, as in the previous section. In the following development  $b$  is the mixing layer thickness and  $x$  is the axial distance. It is assumed that  $db/dx$  is a multiple,  $C$ , of the degree of flow turbulence and that momentum change through turbulent mass transfer is proportional to the difference in dynamic heads. The mechanisms of entrainment are implicit in these two assumptions, which lead to equation (3.10).

$$\frac{db}{dx} = C \frac{b}{4} \left| \frac{(\rho_2 U_2^2 - \rho_1 U_1^2) \int_0^b \rho dy}{\left( \int_0^b \rho u dy \right)^2} \right| \quad (3.10)$$

It is possible to estimate the two integrals in this expression:

$$\frac{1}{b} \int_0^b \rho dy = \frac{\rho_2 + \rho_1}{2} \quad (3.11)$$

and

$$\frac{1}{b} \int_0^b \rho u dy = \frac{\rho_2 U_2 + \rho_1 U_1}{2} \quad (3.12)$$

The rate of change of the mixing layer thickness becomes:

$$\frac{db}{dx} = C \left| \frac{b}{4} \frac{(V^2 S - 1)}{(VS + 1)^2 (S + 1)/2} \right| \equiv C |\varphi| \quad (3.13)$$

With the simplifying assumptions (3.11) and (3.12), which allocate average values of  $\rho$  and  $\rho u$  to the mixing layer, equation (3.13) is obtained. The velocity ratio is  $V = U_1/U_2$ . The density ratio  $S = \rho_1/\rho_2$ .  $C = 0.17$  is a constant. This would predict that there is no mixing when the momentum flux ratio  $V^2 S$  is unity. In reality, there will be mixing due to turbulence within the flows, so an extra factor  $\varphi_0$  is added to give:

$$\frac{db}{dx} = C (|\varphi| + \varphi_0) \quad (3.14)$$

Assumptions (3.11) and (3.12) become increasingly invalid as  $V$  and  $S$  depart from unity. In a cryogenic coaxial injector, equation (3.14) provides a qualitative guide only, although it should work well when the density ratio is unity. This model has the advantage of being able to account for the effect of the flame. Leroux (2001) demonstrates that the flame inhibits jet break-up when it separates the streams of liquid and gas. This may act via reducing the turbulence intensity through higher viscosity, an effect which could be modelled by reducing  $C$ . The Stefan flow might also reduce the interface instability but this is beyond the scope of this study.

If it is assumed that the mixing layer is centered on a straight line passing through the injector lip, then  $l_b/d_l \propto 1/\varphi$ . For fluids of equal density, this can be expressed as equation (3.15).

$$\frac{l_b}{d_l} = \frac{V + 1}{V - 1} \quad (3.15)$$

The velocities used in equations (3.10) to (3.15) could be taken in the injection plane. However, Gill (1978) employs a technique to take into account injector geometry, such as recess of the LOx injector. This is described further in section 3.5. This slight change makes no difference to the results of this or the next section.

### 3.3.6 Experimental determination of jet break-up length

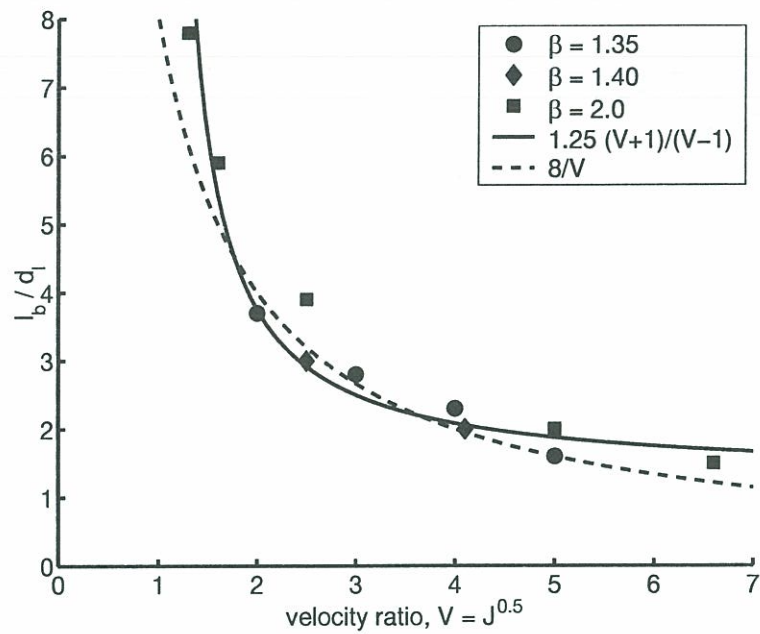
Rehab (1997) summarizes the results of several liquid break-up experiments. He plots the jet break-up length as a function of velocity ratio for a water/water coaxial injector, as shown in figure 3.4.  $\beta$  is the ratio of the annular diameter to the central jet diameter, which seems to have little effect. The velocity ratio  $V$  is equivalent to  $J^{1/2}$ . Rehab proposes a correlation  $l_b/d_l = 8/V$  and Gill's analysis suggests  $l_b/d_l = 5(V + 1)/4(V - 1)$ . Both give similar results for  $1.5 < V < 5$ .

Results obtained on a water/air jet by Leroux (2001) are shown in figure 3.5. These suggest that, if the momentum flux ratio  $J$  is used to correlate the data, the exponent is closer to -0.3, rather than -0.5 predicted by the Kelvin-Helmholtz or the shear layer mechanism. Leroux's results match the experimental data of Carreau et al. (1997) and Eroglu et al. (1991), with some re-arrangement. The latter authors find that  $l_b/d_l \propto We^{-0.4} Re^{0.6}$ . They did not change  $\sigma$  or  $\rho_1$  and  $U_2 \gg U_1$ , so, if the Weber exponent is changed to 0.3, it is acceptable to re-arrange in terms of  $J$ :  $l_b/d_l \propto J^{-0.3}$ . These experiments were performed in the range  $J = 0.2$  to 34. The correlation given by Gill (1978) (equation 3.15) turns out to over-predict the mixing at high momentum flux ratio.

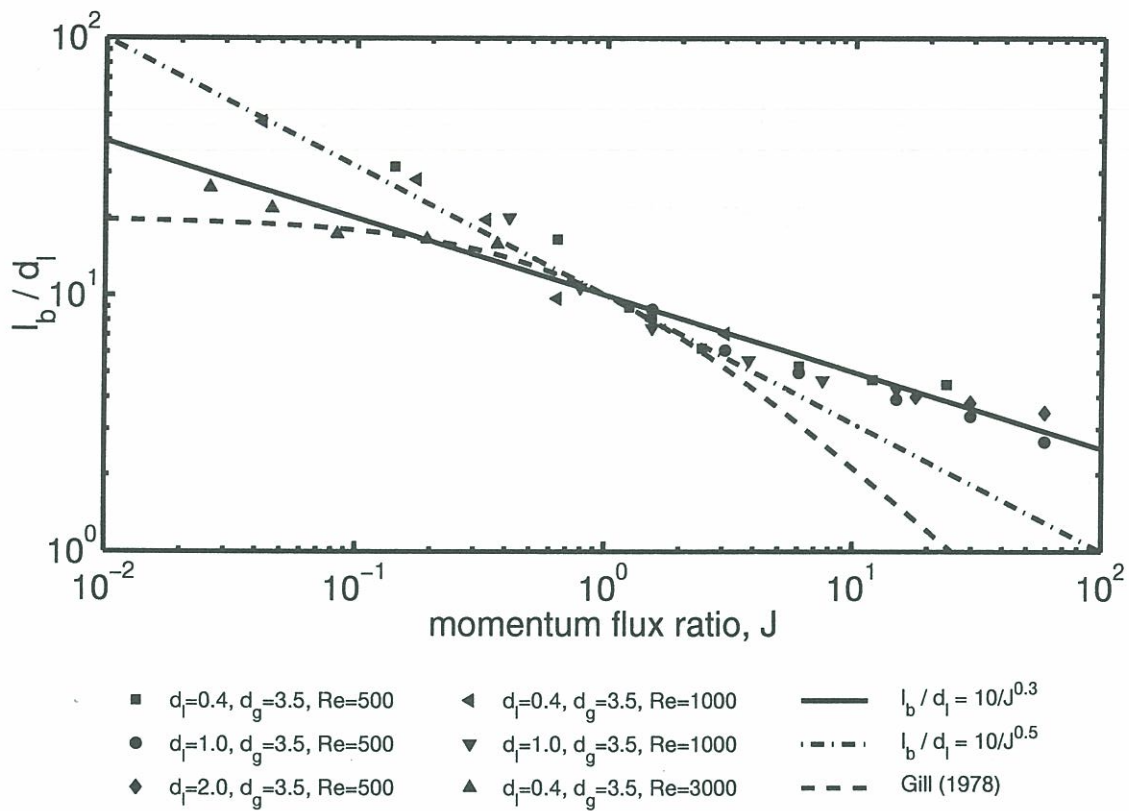
### 3.3.7 Summary - Break-up and mixing of coaxial jets

The key point of this section is that all models predict improved primary atomization when the momentum flux ratio (and hence the velocity ratio) increases. This is confirmed by the experimental data. Furthermore, it is shown that the model in which instabilities develop in the shear layer between the fluids is equivalent to a pure Kelvin-Helmholtz model at long wavelengths.





**Figure 3.4:** Break-up length of the central stream in water/water coaxial injectors as a function of velocity ratio  $V$ , from Rehab et al. (1997).  $\beta$  is the ratio of the annular diameter  $d_2$  to the central jet diameter  $d_1$ , which has little effect. Two correlations are shown:  $l_b/d_l = 5/4(V + 1)(V - 1)$  is generated by Gill (1978) from global correlations for the growth of a turbulent mixing layer.  $l_b/d_l = 8/V$  is generated by Rehab from an instability analysis in a piecewise shear layer.



**Figure 3.5:** . Break up length of the liquid core as a function of momentum flux ratio,  $J$ , for liquid/gas coaxial injectors, from Leroux (2001). The Reynolds number is that of the liquid. At high  $J$ ,  $l_b/d_l = 10/J^{0.3}$  gives the best correlation.



### 3.4 Proposed mechanisms - Introduction

In sections 3.5 to 3.8, four mechanisms for the effect of recess are proposed. They are tested against experimental results and two appear to be active.

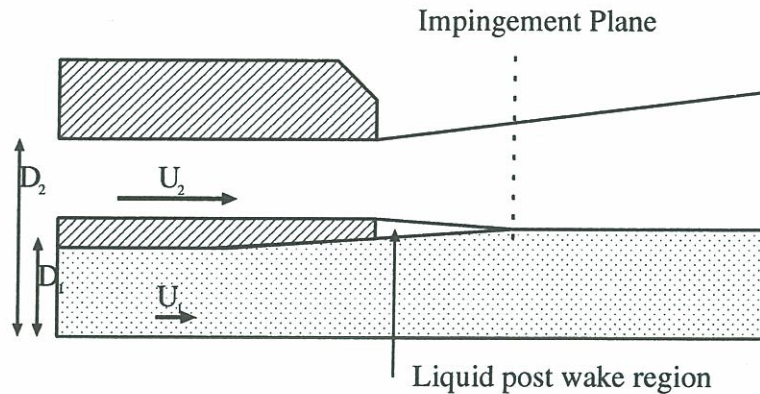
1. Interaction of the mixing layers in a coaxial injector forms the basis of the mechanism presented in section 3.5. This turns out not to be influential in high velocity ratio injectors.
2. The second mechanism, described in section 3.6, occurs when there is combustion. The combustion products, which occupy a certain volume, normally force the annular jet to expand. However, recessing the LOx tube inhibits this expansion. This leads to acceleration and heating of the annular stream, causing improved rupture. Experimental results on the cryogenic injector suggest that this mechanism is active, at least in the low pressure range.
3. The previous two mechanisms act either via increasing the momentum flux ratio or the distance over which a high  $J$  acts. A further mechanism is possible in which acoustic feedback in the recessed portion promotes the initial formation of perturbations. This mechanism is presented in section 3.7 but experimental results suggest that it is not active.
4. The fourth mechanism, in section 3.8 is related to the stability of the flow in the recessed portion. It is shown here that recess has a destabilizing effect which induces a global instability in the flow. This is probably the most influential effect.

### 3.5 Interaction of inner and outer mixing layers

The structure of flame in the the near injector region is described in chapter 2. One mixing layer develops between the central and the annular stream and another between the outer stream and the ambient fluid. When the central tube is recessed, these two mixing layers intersect further downstream relative to the exit plane of the central injector. In his experiments on water/water jets, Rehab (1997) found that entrainment of the central jet is enhanced by the large scale turbulent structures which form when the two mixing layers have intersected. When the velocity ratio  $u_2/u_1$  is close to unity, the break-up of the central core is entirely governed by the outer mixing layer, since the inner mixing layer barely develops at all by itself. Indeed, its behaviour is more like that of a wake. This might suggest that increasing recess will slow down entrainment of the central stream because the outer mixing layer develops later. It also suggests that minimizing the width of the annular stream will improve break-up of the central stream.

Although this may be the case in coaxial injectors with velocity ratios of order unity, it is not the case when there is a large velocity difference between the two fluids. This can be demonstrated by considering the kinetic energy of each flow through the injection plane, which is expressed as  $\dot{m}u^2/2$ , in units of  $\text{Js}^{-1}$ . In Rehab's water/water experiments, the ratio of the energy of the outer stream to the central stream is of order unity. The central stream therefore contains sufficient energy to break up rapidly when exposed to the ambient fluid, even when the annular stream is very thin. However in a typical cryogenic





**Figure 3.6:** Nearfield flow model used by Gill (1978) to examine the effect of momentum flux ratio and recess on mixing in coaxial jets.

injector the energy ratio is of order  $10^4$ , meaning that all energy for rupture comes from the annular fluid. Reducing its size or velocity will reduce the entrainment rate.

This suggests that the high velocity difference between the annular and the central jets has a larger effect on central stream break-up than the turbulent structures created when the two mixing layers join. If this is the case, then recess should enhance break-up of the central tube by lengthening the distance along which this high velocity difference acts. One could imagine calculating the momentum flux ratio across the inner shear layer as a function of axial distance. This would be constant until the end of the annular stream's potential cone. It would then decrease as  $1/x$  due to the effect of mixing with the ambient fluid.

Gill proposes a model which predicts a similar outcome, although it is based on a different physical description, shown in figure 3.6. It was developed before visualizations of the near injector region were available and is not realistic. The annular stream is presumed to expand linearly once it exits the injector, with flow properties changing in a 1-D manner. The factor  $\varphi$  (equation 3.13) is calculated at the end of the liquid post wake region, where the annular stream meets the central stream. The position of this impingement plane depends on the liquid tube recess, the liquid post thickness and the post taper angle. Unlike the analysis proposed in the preceding paragraph, there is very little dependence on the width of the annular flow. If the impingement plane lies within the injector,  $\varphi$  is a maximum. If outside,  $\varphi$  reduces rapidly as the annular jet expands and its velocity falls. Therefore, as the recessed length increases,  $\varphi$  increases to a maximum.

Although the models proposed above are simple, they are not easy to test experimentally. An attempt was made by Blanchère and Defoort (2001). They measured the liquid break-up length as a function of  $J$  (from 1 to 10) and recess (from 0 to  $3.5 \times d_l$ ). Their results suggest that any variation of  $l_b/d_l$  caused by recess is less than 10%, which is of the order of the error in the measurements. They did, however, notice an effect on the droplet mean diameter and velocity distribution, demonstrating that there is an optimum value of recessed length. In this respect, their results are similar to those of Carreau et al. (1997).



### 3.6 Blockage and heating by combustion products

The flame on the cryogenic injector is attached to the LOx tube lip. Reaction products and gaseous oxygen occupy some volume around the central jet and it can be seen from shadowgraphy images that the hydrogen annulus expands outwards accordingly. Recessing the LOx tube simultaneously inhibits this expansion and heats the annular stream. This increases the hydrogen velocity and thus the momentum ratio,  $J$ , at the injector exit. An increase in  $J$  enhances jet break-up and leads to an additional small pressure drop within the injector.

A first attempt to quantify this effect is presented by Kendrick et al. (1999). The calculation is in two parts. First, the fraction of oxygen which combusts before leaving the injector is calculated. This is denoted by  $\beta$ , the rate of oxygen evaporation in the recessed region divided by the total oxygen flowrate. Second, the effect of the resulting quantity of hot products on the hydrogen flow is calculated. It is assumed that the effect on the oxygen flow is negligible. This analysis uses one-dimensional flow concepts to estimate the change in hydrogen flow velocity.

The first part is the more problematic. The model used by Kendrick et al. is that of a flame over a liquid fuel, introduced by Emmons (1956) (see chapter 7). The inherent assumptions are that the gaseous phase is laminar, has a constant  $c_p$ , a constant product of  $\rho\mu$  and that  $Pr = Le = Sc = 1$ . These assumptions are not entirely justified for a gaseous phase containing  $H_2$  and  $O_2$ . However, this model enables a sufficiently accurate value of  $\beta$  to be found by equation (3.16).

$$\beta = \left(\frac{8\eta}{C}\right) \left(\frac{\rho}{\rho_{LOx}}\right) \left[\left(\frac{\mathcal{D}}{d_{LOx}U_{LOx}}\right) \frac{U_{H_2} - U_{LOx}}{U_{LOx}} \frac{l_r}{d_{LOx}}\right]^{1/2} \frac{\ln(1 + B_{sp})}{B_{sp}^{0.15}} \quad (3.16)$$

where  $C \approx 3.7$  (combination of other constants),  $\rho$  = density of the gaseous phase,  $\mathcal{D}$  = diffusivity in the gaseous phase,  $d_{LOx}$  = diameter of the liquid oxygen tube,  $U_{H_2}$  = free stream gas velocity,  $U_{LOx}$  = liquid oxygen velocity,  $l_r$  = distance of LOx tube recess,  $B_{sp}$  = Spalding transfer coefficient (details of which can be found in chapter 7),  $\eta$  = factor to take into account additional interfacial surface due to the wrinkling of the liquid.

From the reasoning in Appendix D, the multiple  $\rho^2\mathcal{D}$  is a function of pressure only:

$$\rho^2\mathcal{D}(p) = \left(\frac{p}{r_{O_2}T_{ref}}\right)^2 \mathcal{D}(T_{ref}, p_{ref}) \frac{p_{ref}}{p} \quad (3.17)$$

Equation (3.16) gives the fraction of oxygen which evaporates and combusts. The second stage is to calculate the subsequent effect of this on the hydrogen flow. The method used by (Kendrick, Herding, Scoufflaire, Rolon, and Candel 1999) has been improved here to take into account density variation and heat addition to the hydrogen flow. For an incremental quantity of oxygen which evaporates,  $\dot{m}_{LOx} d\beta$ , the cross-sectional area of the LOx jet decreases according to equation (3.18) and the area occupied by hot products increases according to equation (3.19).

$$dA_{LOx} = -\frac{\dot{m}_{LOx}}{\rho_{LOx}U_{LOx}}d\beta \quad (3.18)$$

$$dA_{prod} = \frac{s+1}{s} \frac{\dot{m}_{LOx}}{\rho_p U_p} d\beta \quad (3.19)$$

where  $s$  is the mass stoichiometric ratio ( $s = 8$  for hydrogen/oxygen combustion). The sum of (3.18) and (3.19) gives the overall change in area available for the hydrogen flow. Equation (3.20) expresses this as a fraction of the hydrogen area ( $A = \dot{m}_{H_2} / \rho_{H_2} U_{H_2}$ ).

$$\frac{dA}{A} = \left( \frac{\rho_{H_2} U_{H_2}}{\rho_{LOx} U_{LOx}} - \frac{\rho_{H_2} U_{H_2}}{\rho_p U_p} \right) \frac{\dot{m}_{LOx}}{\dot{m}_{H_2}} d\beta \quad (3.20)$$

Assuming ideal gas behaviour, the ratio  $\rho_p / \rho_{H_2} = r_p T_p / r_{H_2} T_{H_2}$ , where  $T_p$  is the product temperature. The product velocity can be estimated via a momentum balance of the reacting species in the axial direction:

$$\dot{m}_p U_p \approx \dot{m}_{GOx} U_{GOx} + \dot{m}_{GH_2} U_{GH_2}$$

The small adverse pressure gradient is neglected so this is an upper bound for the value of  $U_p$ . This yields:

$$(1 + s)U_p = sU_{LOx} + U_{H_2}$$

Since  $U_{H_2} \gg sU_{LOx}$ , one may simply use:

$$U_p \approx U_{H_2} / (1 + s)$$

Thus:

$$\frac{dA}{A}(\rho_{H_2}, U_{H_2}, T_{H_2}) = \left( \frac{\rho_{H_2} U_{H_2}}{\rho_{LOx} U_{LOx}} - \frac{R_p T_p}{R_{H_2} T_{H_2}} \frac{(s+1)^2}{s} \right) E d\beta \quad (3.21)$$

The incremental heat addition divided by the sensible enthalpy of the hydrogen flow is:

$$\frac{dH}{(c_p T)_{H_2}} = \frac{\Delta H_{comb}}{(c_p T)_{H_2}} \frac{E}{s} \xi d\beta \quad (3.22)$$

where  $\Delta H_{comb}$  designates the heat released through chemical reaction per unit mass of oxygen. It is chosen to give an adiabatic combustion temperature of 3000K. The factor  $\xi$  (where  $0 < \xi < 1$ ) is the proportion of the heat of combustion which is absorbed by the hydrogen stream. The Mach number, density and temperature of the hydrogen flow are then calculated using the differential flow relations derived in the standard analysis of one-dimensional flows:

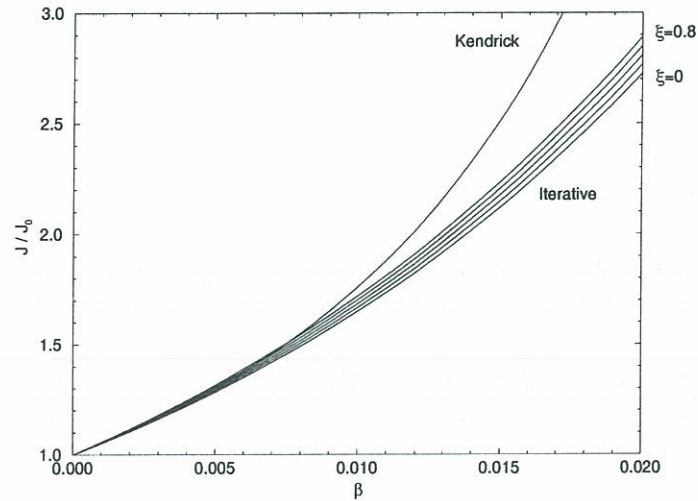
$$\frac{dM}{M} = \left( \frac{1 + \gamma M^2}{2(1 - M^2)} \right) \left( \frac{dH}{c_p T} \right) - \left( \frac{1 + \frac{\gamma-1}{2} M^2}{1 - M^2} \right) \frac{dA}{A} \quad (3.23a)$$

$$\frac{dT}{T} = \left( \frac{1 - \gamma M^2}{1 - M^2} \right) \left( \frac{dH}{c_p T} \right) + \left( \frac{(\gamma - 1) M^2}{1 - M^2} \right) \frac{dA}{A} \quad (3.23b)$$

$$\frac{d\rho}{\rho} = \left( \frac{-1}{1 - M^2} \right) \left( \frac{dH}{c_p T} \right) + \left( \frac{M^2}{1 - M^2} \right) \frac{dA}{A} \quad (3.23c)$$

The changes in hydrogen flow properties are calculated by iteration up to the value of  $\beta$  given by equation (3.16). The results for five different values of  $\xi$  are compared with those of Kendrick et al. in figure 3.7. There is good agreement up to  $\beta \approx 0.01$ . It can be seen





**Figure 3.7:** Predicted effect of recess on momentum flux ratio,  $J$ , using the calculation by Kendrick and the iterative calculation.

that the energy absorbed by the hydrogen flow does not greatly change the momentum flux ratio.

This calculation is applied to the operating points obtained experimentally. It is shown first for points A and C at 10 bar. The following values are used:  $\rho^2 D = 3.25 \times 10^{-4} m^2 s^{-1}$ .  $B_T = 10$ .  $E = 2.1$  for point A and 3.2 for point C,  $\xi = 0.1$ ,  $T_{prod} = 3000K$ .

The values of momentum ratio,  $J$ , and the pressure coefficient  $\Delta p / \rho U^2$  are calculated as functions of the LOx tube recess. The results are shown in figures 3.8 and 3.9. The calculated pressure drop across the recessed portion of the injector,  $\Delta p$ , is very small compared to the absolute chamber pressure. At 70 bar, the head loss coefficient, calculated in the same way, is shown in figure 3.10. It is presented as a function of  $\beta$  in this graph, rather than as a function of recess. This avoids making the assumptions used to derive equation (3.16). The pressure coefficients,  $\Delta p / (\rho U^2)$ , evaluated experimentally in chapter 1 are 0.31 at recess  $1 \times d_{LOx}$  and 0.46 at recess  $1.5 \times d_{LOx}$ . It is not possible to distinguish between points A and C and the error in the results is too large to be conclusive. However, these values fit the hypothesis that the hydrogen flow is accelerated via blockage by products. The fraction of oxygen converted to products within the recessed portion of the injector is of the order of 1%, which corresponds well with initial predictions presented in Kendrick et al. (1999).

These experiments would need to be repeated without combustion in order to confirm that there is no pressure drop without reaction. However, the evidence is reasonably strong that combustion products block the flow and accelerate the hydrogen stream when the LOx injector is recessed. However, it cannot be the only active mechanism because, as was shown in section 3.1, recess also has an effect on non-combusting coaxial injectors.

### 3.7 Acoustic feedback in recessed portion

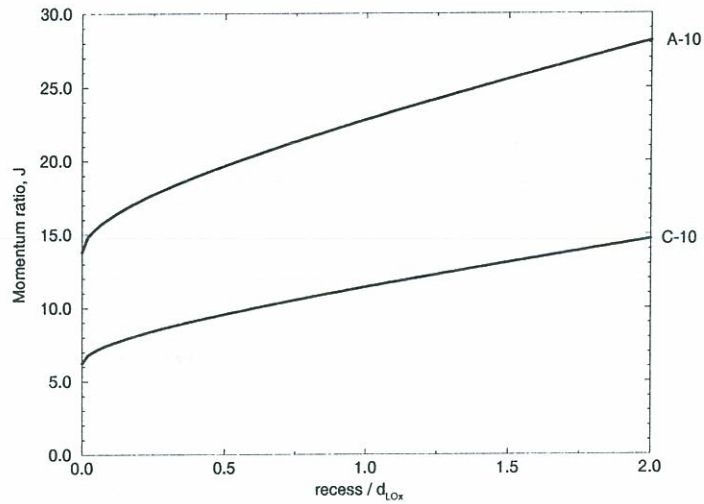
This section deals with the possibility of developing an acoustic feedback in the recessed injector. Consider a small perturbation generated at the upstream injection plane. This grows as it is convected downstream at velocity  $u_c$  and impinges on the downstream injection plane after time  $\tau_c = l_r/u_c$  where  $l_r$  is the recessed length. The interaction with the downstream boundary produces a pressure signal after a delay  $\tau_i$ . This signal propagates in the outer gaseous flow and reaches the upstream injector plane after time  $\tau_a = l_r/(c - u_2)$ , where  $c$  is the speed of sound and  $u_2$  is the flow velocity in the gaseous stream. The pressure signal disturbs the shear layer, producing a new perturbation. This mechanism will produce a resonant oscillation with period  $T$  if  $mT = \tau_c + \tau_a + \tau_i$ , where  $m$  is an integer. In general,  $\tau_a$  is small compared with  $\tau_c$  and may be neglected. One can also assume that  $\tau_i$  is a small fraction of the period:  $\tau_i = \alpha T$  with  $\alpha \ll 1$ . This yields an oscillation frequency  $f$  and a wavelength  $\lambda$ , which scale with the recess dimension  $l_r$ :

$$f = u_c(m - \alpha)/l_r \quad (3.24)$$

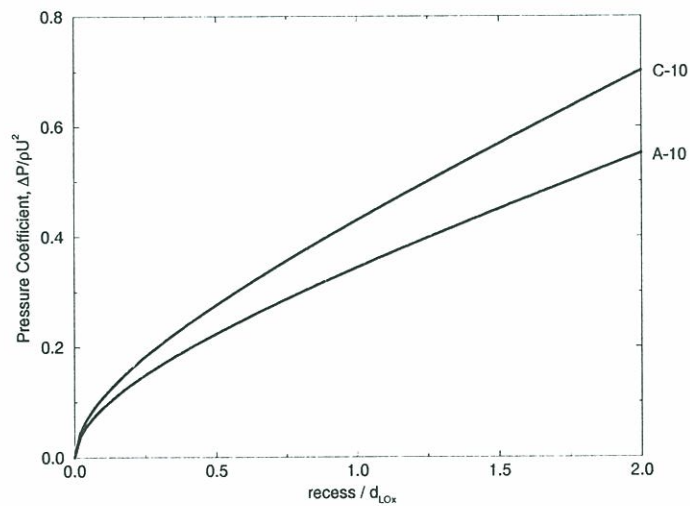
$$\lambda = l_r/(m - \alpha) \quad (3.25)$$

The experiments described later in this chapter (section 3.8.6) show that the long wavelength instabilities enhanced by recess do not scale with the recessed length,  $l_r$ . Consequently they cannot be generated by this mechanism. It remains an open question whether this could be an active mechanism for small wavelength instabilities acting in the shear layer. However, it seems unlikely that small wavelength instabilities, which have a small amplitude relative to the thickness of the annular flow, would generate a very large pressure pulse on leaving the injector.

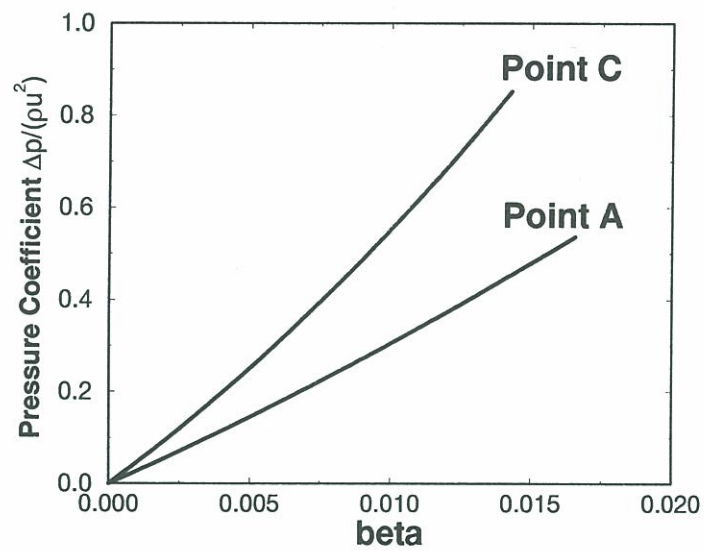




**Figure 3.8:** Predicted effect of recess on momentum ratio for Point A and Point C at 10 bar using the iterative calculation.



**Figure 3.9:** Predicted effect of recess on Pressure Coefficient for Point A and Point C at 10 bar using the iterative calculation



**Figure 3.10:** Head loss coefficient plotted against  $\beta$  (the rate of oxygen evaporation divided by the total mass flow rate of oxygen) for points A and C at 60 bar. Experimental results, which average the results from both point A and point C, suggest a head loss coefficient of 3.1 at recess  $1 \times d_{LOx}$  and 4.6 at recess  $1.5 \times d_{LOx}$ .



## 3.8 Stability of a bounded wake flow

### 3.8.1 Introduction

The mechanisms proposed in sections 3.5 to 3.7 act via increasing instability in the shear layer between the inner and the outer streams. The mechanism proposed in this section concerns instabilities generated by the free stream flows and is qualitatively unaffected by the thickness of the shear layer. There is compelling experimental evidence in section 3.8.6 and in a new interpretation of the results of Rehab et al. (1997) that indicate it is an active mechanism.

Experimental results on the cryogenic coaxial injector, figure 3.30, show that recess causes sinuous or helicoidal instabilities with a wavelength considerably larger than the thickness of the shear layer. This limit is described well by a pure Kelvin-Helmholtz model, as demonstrated in section 3.3. The central fluid behaves like a wake within the annular fluid. The velocity difference between the outer fluid and the ambient gas in the discharge chamber can be ignored when there is recirculation next to the outer flow. Consequently, the unrecessed injector can be modelled by an unbounded wake flow. In the recessed portion of the injector the annular flow is enclosed at a certain radius by a rigid boundary. It is shown in section 3.8.5 that bounding a wake near its base has a destabilizing effect, enhancing the formation of a global instability. Global instabilities correspond to extended wavepackets which reside within the flow and beat at a well defined frequency.

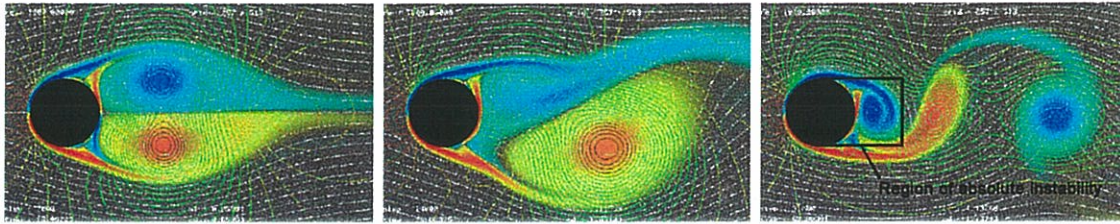
It must be emphasized that the analysis in this section is only intended to be qualitative. Various approximations are made which would render any quantitative results false. Nevertheless, the qualitative understanding is valuable since it highlights a previously unrecognized mode of instability, which can explain why recess has such a strong effect.

Section 3.8.2 contains a brief summary of the literature on global instability of wakes. This demonstrates that a global instability requires a region of local absolute instability to exist in the flow. Section 3.8.3 presents the model used and explains why its conclusions cannot be treated quantitatively. The flow's dispersion relation is derived in Appendix B. A temporal instability analysis is given in section 3.8.4 and in section 3.8.5 a space-time analysis is introduced. The difference between absolute and convective instabilities is explained. The nature of instabilities in the wake is then determined as a function of three parameters: density ratio, velocity ratio and the width of the annular flow relative to the central stream. In section 3.8.6, experimental results are shown which indicate that recess does enhance the type of instability suggested in the previous sections. Finally, section 3.8.7 describes how the model could be made more realistic in order to obtain quantitative results.

### 3.8.2 Global Stability of Wakes

The instability of shear flows and wakes has recently been studied in some depth, for example by Yu and Monkewitz (1990), Huerre and Monkewitz (1990), Loiseleux et al. (1998), Huerre (2000) and references there-in. Koch (1985) showed that a region of local absolute instability exists immediately behind a cylinder in the Kármán vortex street regime, as shown in figure 3.11. Around the same time Mathis et al. (1984) and Strykowski (1986) demonstrated experimentally that Kármán vortex shedding at low Reynolds number is





**Figure 3.11:** *Development of a global instability in the wake behind a cylinder as the Reynolds number increases. The vortex shedding seen here is the non-linear development of a sinuous instability in the wake. In order for the wake to exhibit self-sustained oscillations, a region of absolutely unstable flow must exist at its base, which in this case is just behind the cylinder. The behaviour of the central stream of a coaxial injector has similar characteristics. These numerical simulations were performed by Kunio Kawahara, Institute of Space and Astronautical Science, Kanagawa, Japan*

the result of a global instability. The connection between local and global properties was explored further by Chomaz et al. (1988) and Huerre and Monkewitz (1990) for the Ginzburg-Landau model. Finally, Monkewitz (1988b) showed that the sequence of transitions behind a cylinder wake as the Reynolds number is increased does indeed follow the sequence described in the model of Chomaz et al. (1988):

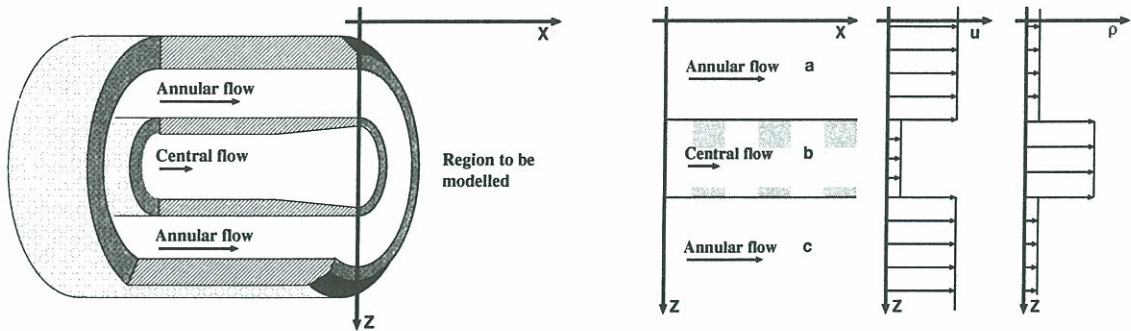
1. Transition from stability to convective instability.
2. Transition from convective to local absolute instability.
3. Transition to a self-sustained global mode when a sufficiently large portion of the flow has become absolutely unstable.

The numerical study of Hannemann and Oertel (1989) demonstrates clearly that only the region directly behind the bluff body is absolutely unstable. This nevertheless can trigger a global mode which affects the entire flow. It then behaves like a self-excited oscillator. The mode of local absolute instability varies with distance from the body and it is not possible to predict exactly which global mode will be favoured. It is most convenient to study the second step: transition from convective to local absolute instability in a locally-parallel flow. This transition is a necessary, although not sufficient, condition for the existence of a globally unstable mode. It yields useful approximations for the critical parameters leading to global instability.

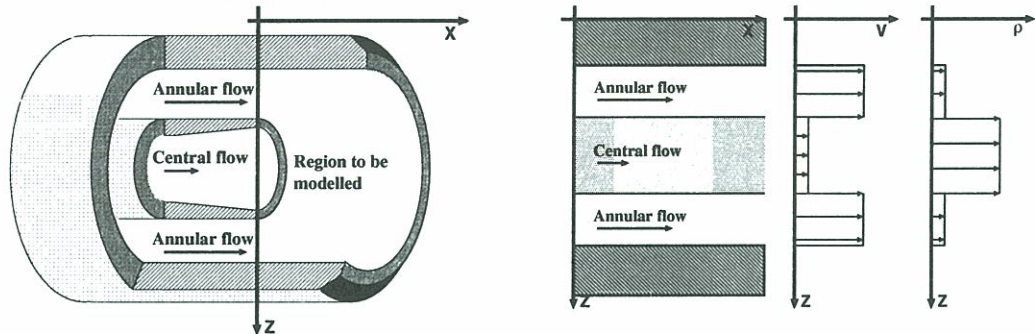
For instance, Monkewitz (1988b) showed that, for a cylinder, transition to convective instability occurs at  $Re = 5$ , and appearance of the first local absolute instability takes place at  $Re = 25$ . The experimentally determined onset of Kármán vortex shedding occurs around  $Re = 45$ . Thus in bluff-body wakes, transition to a globally unstable flow occurs some time after the appearance of the first local absolute instabilities.

Two checks on the validity of this approach are summarized in Huerre and Monkewitz (1990). It is demonstrated in Triantafyllou et al. (1986) that Kármán vortex shedding is not caused by flow separation from the bluff-body surface. Furthermore, the experimental results of Inoue (1985) show that Kármán vortex shedding disappears when the velocity





**Figure 3.12:** Left: Cut-away diagram of a coaxial injector without recess. Right: The two-dimensional model which is used in this analysis for an un-recessed injector. It is an unbounded wake flow with infinite axial extent. Velocity and density profiles are shown.



**Figure 3.13:** Left: Cut-away diagram of a coaxial injector with recess. Right: The two-dimensional model which is used in this analysis for a recessed injector. It is a bounded wake flow with infinite axial extent. Velocity and density profiles are shown.

deficit in the wake is reduced beyond a critical value. Both checks imply that vortex shedding is started by a sinuous global instability mode in the velocity profile of the wake behind the object and not by the object itself.

The above analyses concern vortex shedding behind a cylinder, which is quasi-2-D. The axisymmetric case behind a bluff body of revolution has also been studied. Helical vortex shedding is observed experimentally at a well-defined Strouhal number. In addition, Monkewitz (1988a) demonstrates that a region of absolute instability exists just behind the body. Both these facts strongly imply that a global mode is responsible for this helicoidal instability, which is analogous to the sinuous instability of the 2-D wake. As an aside, it has been noted in jets by Sreenivasan et al. (1989) that the onset of global instability dramatically increases the jet spreading angle.

In summary, the existence of local absolute instability shall be investigated in a 2-D bounded wake flow. This is a useful guide to the behaviour of a bounded axisymmetric flow regarding transition to a global instability.



### 3.8.3 Two-dimensional bounded wake flow

Yu and Monkewitz (1990) propose a simple model of a 2-D wake with infinite axial extent, shown in figure 3.12. The wake and annular flows are both 2-D inviscid fluids with uniform velocity and density. Using a 2-D model removes the azimuthal wavenumber from an instability analysis. A rigorous study of an axisymmetric jet would have to include the azimuthal wavenumber, although a sinuous 2-D mode can be taken to be analogous to a helicoidal mode in an axisymmetric jet. This is one reason why this analysis is only qualitative. A second reason concerns the inviscid approximation, which is equivalent to imposing infinitely-thin shear layers between the fluids. Yu and Monkewitz (1990) find that when viscosity is introduced and the full Orr-Sommerfeld equations solved, results are qualitatively different to the inviscid wake. Nevertheless, they show that absolute instability arises from interaction between the two shear layers, rather than from within each individual layer. Thus the results are qualitatively similar. Indeed, they find that the 2-D inviscid model provides an excellent qualitative guide to the effect of changing density and velocity ratios. In this section the fluids are bounded above and below by solid walls, as shown in figure 3.13. This introduces a third parameter: the ratio of annular flow thickness to wake half-width, which simulates recess. The effect of this parameter on the absolute instability of the wake flow shall be determined. We consider finite surface tension and neglect gravity. This final assumption is valid since the Froude number  $Fr = u^2/(gl)$  is between  $10^2$  and  $10^6$  in a rocket injector. The general formulation here is similar to that in Rayleigh (1896), section 365.

It was mentioned in section 3.8.2 that a global instability in a wake flow is initiated in a region just behind the bluff body. In a coaxial injector, recess is applied precisely in this region, just behind the exit plane of the oxygen jet. Thus it is quite conceivable that recess can effect the entire flow by triggering a global instability in this initial region. In addition, the inviscid analysis is particularly well suited here, since the mixing layers are thin. The dispersion relation (3.26) is derived in Appendix B.

The annular fluid is denoted by subscript 2 and the central flow by subscript 1. The half-width of the central jet  $h_1$  is used as a reference length, a reference velocity is defined as  $u_{ref} = (u_2 + u_1)/2$  and a reference density is  $\rho_2$ . This leads to the following non-dimensional variables:  $k^* = kh_1$ ,  $c^* = c/u_{ref}$ , where  $c = \omega/k$ . Parameters are  $\sigma^* = \sigma/(h_1\rho_2u_{ref}^2)$ , the density ratio  $S = \rho_1/\rho_2$ , the velocity difference  $\Lambda = (u_1 - u_2)/(u_1 + u_2)$  and the ratio of annular flow width  $h_3$  to the half-width of the central jet:  $h_3^* = h_3/h_1$ .

$$-k^*\sigma^* + (1 - \Lambda - c^*)^2 \coth(k^*h_3^*) + S(1 + \Lambda - c^*)^2 \left\{ \begin{array}{l} \tanh(k^*) \quad (\text{sinuous}) \\ \coth(k^*) \quad (\text{varicose}) \end{array} \right\} = 0 \quad (3.26)$$

This dispersion relation is solved numerically in sections 3.8.5 and it is trivially easy to include surface tension. However, under rocket engine conditions surface tension would only be influential at wavelengths smaller than the thickness of the shear layer ( $\lambda \ll \delta_{sl}$ ). This is out of the valid range of this inviscid analysis, so surface tension can be neglected. In fact, even in the water/air case at low velocity, presented in section 3.8.6, the effect of surface tension is negligible on the observed sinuous oscillations with long wavelength.

This assertion can be expressed more formally by comparing typical values of the terms in equation (3.26). For large wavelengths, which have small  $k^*$ ,  $\coth k^*$  is very large and  $\tanh k^*$  tends to  $k^*$ . For water and air,  $\sigma^*$  is typically 0.2 and  $S$  is 800. The  $k^*\sigma^*$  term is



negligible compared with the others, an effect which becomes increasingly pronounced as supercritical conditions are approached.

With surface tension removed, there is no stabilizing mechanism. This violates causality, for reasons described by Huerre (1987). In practice, this does not cause a problem as long as the analysis is restricted to small wavenumbers  $k^*$ .

The dispersion relation with zero surface tension may be cast in the form:

$$\Sigma \frac{(1 + \Lambda - c^*)^2}{(1 - \Lambda - c^*)^2} = -1 \quad (3.27)$$

where  $\Sigma$  is the density ratio  $S$  weighted by the thicknesses of the wake and annulus relative to the instability wavelength.

$$\Sigma = S \frac{\tanh(k^*)}{\coth(k^*h_3^*)} \quad (\text{sinuous}) \quad \Sigma = S \frac{\coth(k^*)}{\coth(k^*h_3^*)} \quad (\text{varicose}) \quad (3.28)$$

In the unbounded wake,  $h_3^* \rightarrow \infty$ . Consequently,  $\coth(k^*h_3^*) \rightarrow 1$  and the dispersion relation is identical to that found in Yu and Monkewitz (1990) for unbounded wake flows. If  $h_3$  is chosen as the reference length instead of  $h_1$ ,  $k^* \equiv kh_3$  and  $h_1^* \equiv h_1/h_3 = 1/h_3^*$ . In the sinuous case, this leads to an identical dispersion relation but with  $h_3^*$  replaced with  $h_1^*$ . Thus, once data has been calculated with  $1 < h_3^* < \infty$ , the same data can be used when  $0 < h_3^* < 1$ , subject to a change in reference length.

### 3.8.4 Temporal Instability Analysis

Before starting a space-time analysis, it is useful to perform a purely temporal study. The dispersion relation is solved with real  $k^*$  and complex  $\omega^*$ . The imaginary part of  $\omega^*$  represents the amplification rate of an instability of wavenumber  $k^*$  with infinite axial extent.

The factor  $\Sigma$  is real when  $k^*$  is real so equation (3.27) can be rearranged to give the following expression:

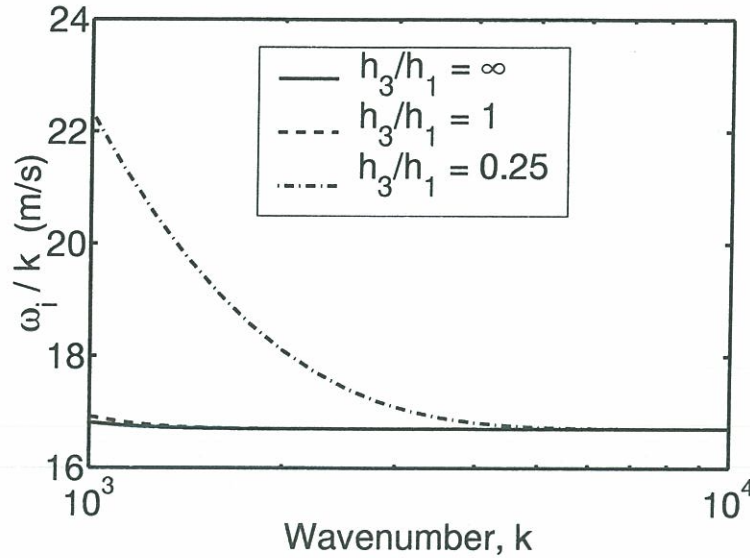
$$c^* = 1 + \Lambda \frac{(\sqrt{\Sigma} \pm i)^2}{\Sigma + 1} \quad (3.29)$$

The positive imaginary part of  $\omega_i$  is, in dimensional form, given by:

$$\frac{\omega_i}{k} = u_{ref} \times \Im\{c^*\} = |\Delta u| \frac{\sqrt{\Sigma}}{\Sigma + 1} \quad (3.30)$$

$$\text{where } \Sigma_{sin} = \frac{\rho_1 \tanh(kh_1)}{\rho_2 \coth(kh_3)} \quad (\text{sinuous}), \quad \Sigma_{var} = \frac{\rho_1 \coth(kh_1)}{\rho_2 \coth(kh_3)} \quad (\text{varicose}) \quad (3.31)$$

The amplification rate is composed of two parts: a linear dependence on the velocity difference  $|\Delta u|$ , which is independent of  $k$ , and a more interesting dependence on the ‘‘geometry-weighted’’ density ratio  $\Sigma$ . The amplification is a maximum when  $\Sigma = 1$  and decreases monotonically on either side of  $\Sigma = 1$ . From equation (3.31), it is easy to observe the effect of  $h_3$  and  $h_1$  on the instability at a given wavenumber  $k$ .



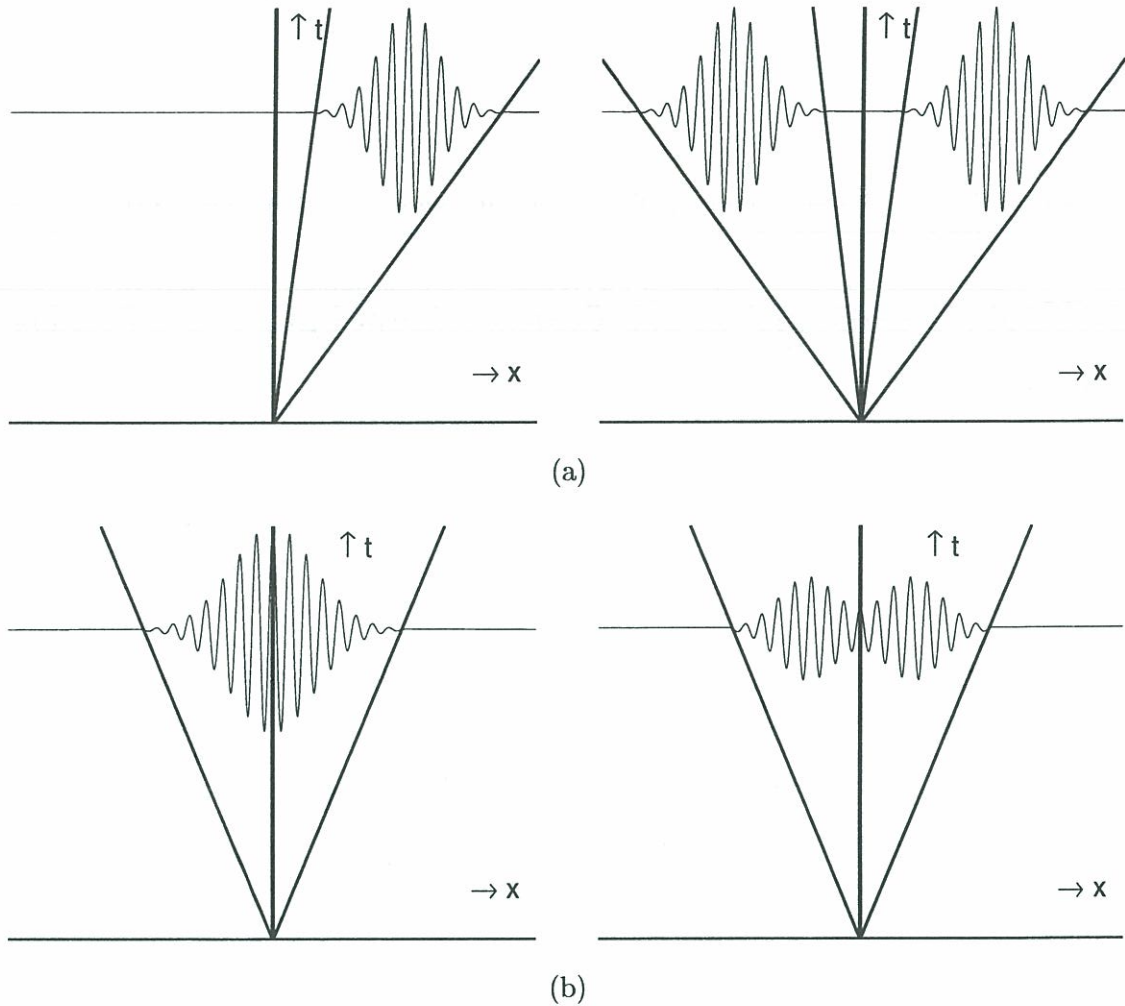
**Figure 3.14:** Amplification rate ( $\omega_i$ ) of sinuous instabilities as a function of wavenumber  $k$ . Conditions correspond to a liquid rocket injector. Wavelengths from 6mm ( $k = 10^3$ ) to 0.6mm ( $k = 10^4$ ) are shown since this is approximately the range in which the model is valid.

For wavelengths much smaller than both  $h_3$  and  $h_1$ ,  $kh_3 \rightarrow \infty$  and  $kh_1 \rightarrow \infty$ . Consequently,  $\Sigma_{sin}$  and  $\Sigma_{var}$  both tend to the density ratio  $\rho_1/\rho_2$  (which is typically  $\mathcal{O}(100)$  in a rocket engine). As the annular width  $h_3$  decreases below  $\mathcal{O}(\lambda)$ ,  $\coth(kh_3)$  increases. The effect is equivalent to increasing the density of the annular fluid, making  $\Sigma$  closer to 1. This makes the instability more unstable. The effect of decreasing the wake thickness  $h_1$  is equivalent to decreasing (increasing) the wake density for sinuous (varicose) instabilities. Thus, for  $\Sigma > 1$ , the sinuous instability is always more unstable than the varicose and decreasing the annular thickness makes them both more unstable.

The physical explanation for this is straightforward. The aerodynamic instability arises because the annular flow is faster over wake crests and slower over troughs. This effect extends either side of the wake to within a distance of  $\mathcal{O}(\lambda)$ . This causes a lower pressure over the crests and higher pressure in troughs, which therefore tends to augment the instability. This effect is enhanced when the annulus is bounded to within  $\mathcal{O}(\lambda)$ , since the flow is more accelerated over crests than in the unbounded case. This happens on both sides of the dense fluid but in the sinuous case both sides work together, whereas in the varicose case they tend to cancel out.

This tendency is shown in figure 3.14 for typical conditions of a rocket injector. Taking the typical recessed length to be 6 mm and the mixing layer width to be 0.6 mm, the model will be valid in the range  $10^4 > k > 10^3$ . It is encouraging to note that  $\omega_i$  does increase in the longer wavelengths of this band, when  $h_3/h_1$  decreases below 1. The ratio  $h_3/h_1$  is typically 0.25 in the recessed injector of a rocket motor. However, the temporal analysis alone is not sufficient to explain the effect of recess at  $h_3/h_1 > 1$ , which is observed experimentally in section 3.8.6.





**Figure 3.15:** Possible responses of a flow to an impulse at  $(x, t) = (0, 0)$ . Disturbances grow exponentially along all rays contained within the indicated wedges. (a) Convective instability, where the instabilities move away from the source and ultimately leave it undisturbed. (b) Absolute instability, where the instabilities affect the entire flow after sufficient time.

### 3.8.5 Space-time Instability analysis

#### 3.8.5.1 Introduction

This introduction contains a brief overview of absolute and convective instabilities. Complete reviews can be found in Huerre and Monkewitz (1990) and Huerre (2000).

The instability characteristics of a flow are most easily demonstrated by considering its response to an impulse. If the resulting perturbation dies away everywhere, the flow is stable. On the other hand if it is amplified a further distinction is necessary. Convectively stable flows (figure 3.15a) give rise to wave packets which move away from the source and ultimately leave the medium in its undisturbed state. Absolutely unstable flows by contrast (figure 3.15b) are gradually contaminated everywhere by a point-source impulse. This distinction is determined by the contribution of the absolute wavenumber,  $k_0$ , defined as the wavenumber with zero group velocity:  $\partial\omega/\partial k = 0$ . The associated absolute frequency  $\omega_0 = \omega(k_0)$  has an absolute growth rate  $\omega_{0i}$ . If this is negative, the instability is convective. If it is positive, the instability is absolute, subject to fulfilment of the ‘‘pinch’’ criterion which is defined below.

There is a convenient geometrical approach to this problem. Let  $D(\omega, k; P) = 0$  represent the dispersion relation, where  $P$  denotes all control parameters. The partial derivatives  $\partial\omega/\partial k$  and  $\partial D/\partial k$  are related via:

$$\left. \frac{\partial\omega}{\partial k} \right|_P \left. \frac{\partial D}{\partial\omega} \right|_{P,k} + \left. \frac{\partial D}{\partial k} \right|_{P,\omega} = 0 \quad (3.32)$$

Thus  $\partial\omega/\partial k = 0$  when  $\partial D/\partial k = 0$ , subject to  $\partial D/\partial\omega \neq 0$ . The surface  $D = 0$  can be traced in the complex  $k$ -plane. This is demonstrated in figure 3.16b, where contours of  $\omega_i = \text{constant}$  (figure 3.16a) are shown. Saddle points of  $D = 0$  in the complex  $k$ -plane satisfy  $\partial D/\partial k = 0$ . Consequently, by equation (3.32), they are points of zero group velocity:  $(\omega_0, k_0)$ . The paths of these saddle points can be followed in  $(\omega, k)$  space as the control parameters  $P$  are varied. By this method, regions of convective instability ( $\omega_{0i} < 0$ ) and absolute instability ( $\omega_{0i} > 0$ ) are determined in parameter space.

There is a further criterion for absolute instability: the regions of unstable flow in figure 3.15b must propagate into both the  $x > 0$  and the  $x < 0$  half planes. This condition can be visualized as the pinching of a  $k^+$  and a  $k^-$  branch at a saddle point. The  $k^+$  branch is defined as that which moves into the  $k_i > 0$  half-plane as  $\omega_i$  is increased. The  $k^-$  branch always remains in the  $k_i < 0$  half-plane as  $\omega_i$  is increased. This is the previously mentioned ‘‘pinch’’ criterion.

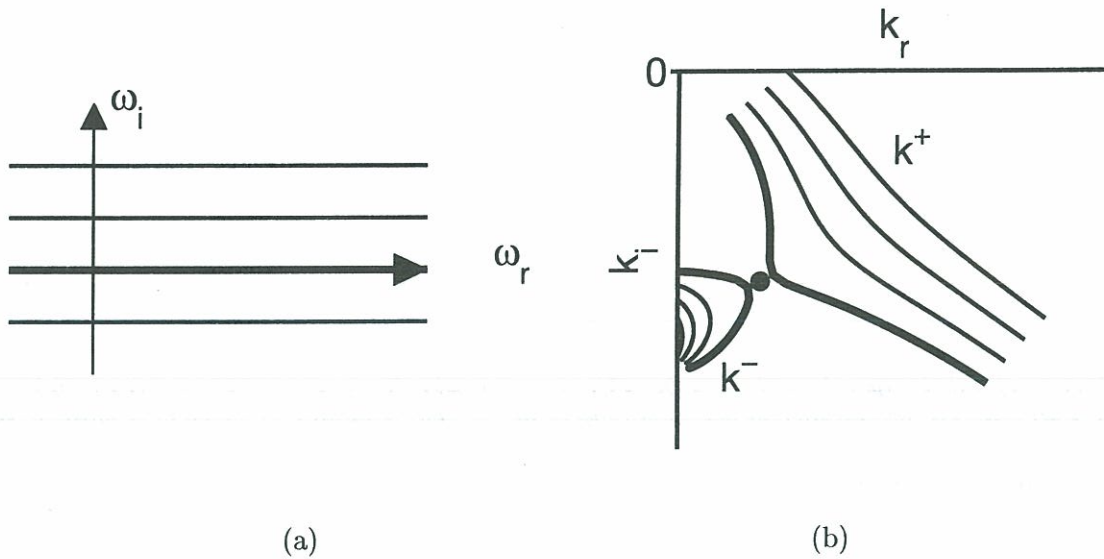
There is one final point to make in this brief overview: a flow that is convectively unstable in one reference plane becomes absolutely unstable in another. Consequently, these concepts become relevant only when a reference frame is chosen. For a coaxial injector, this frame is obviously centered on the exit plane of the injector.

### 3.8.5.2 Convective/absolute transition in the unbounded wake

The geometrical approach outlined in section 3.8.5.1 is used in order to evaluate points of zero group velocity  $(\omega_0, k_0)$  as the control parameters are varied. Points of zero group velocity are saddle points of  $D = 0$ . This is demonstrated in this section for sinuous disturbances of the unbounded wake, equation (3.33). From this point, the superscript \* is dropped from dimensionless variables.

$$D \equiv S \frac{(1 + \Lambda - c)^2}{(1 - \Lambda - c)^2} + \coth(k) = 0 \quad (3.33)$$



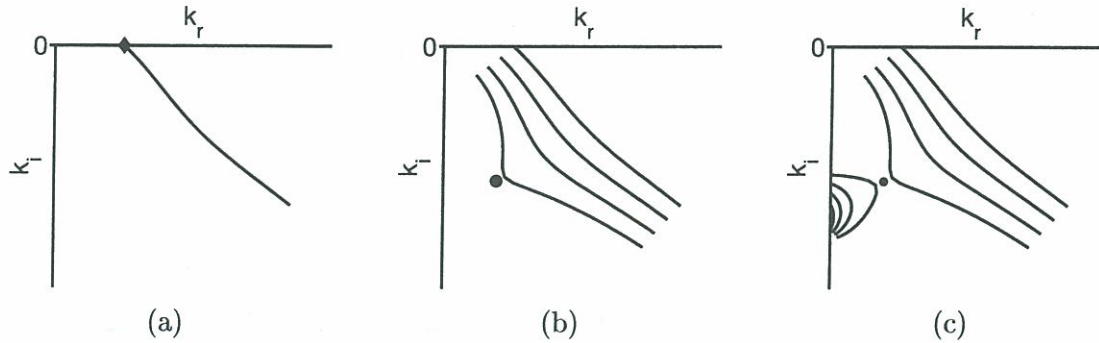


**Figure 3.16:** Contours of  $\omega_i = \text{constant}$  traced in (a) the complex  $\omega$ -plane and (b) the complex  $k$ -plane. • denotes a saddle point of the dispersion relation  $D = 0$  in the complex  $k$ -plane (where  $D = 0$  and  $\partial D/\partial k = 0$ ). The saddle point is formed by the pinching of a  $k^+(\omega)$  branch and a  $k^-(\omega)$  branch. By definition, the hill related to the  $k^-$  branch is confined to the  $k_i < 0$  half plane. Similarly, the hill related to the  $k^+$  branch extends into the  $k_i > 0$  half plane.

The procedure is similar to that used by Loiseleux et al. (1998) where, starting from an approximate solution, saddle points of  $D = 0$  are found numerically by solving the non-linear simultaneous equations  $D = 0$  and  $\partial D/\partial k = 0$ . A standard Matlab routine `fsolve.m` is used, which with today's computers is easier and faster than implementing the more elegant procedure presented by Monkewitz and Sohn (1988).

To locate the  $k^+$  branch at given parameter values we make use of the fact that it crosses the line  $k_i = 0$  and is therefore a solution to the temporal instability analysis. The procedure is as follows:

1. For sufficiently large  $k \in \mathbb{R}$ , the complex function  $D(\omega, k; S, \Lambda)$  is evaluated in the complex  $\omega$ -plane. The solutions of  $D = 0$  are estimated from the intersections of the isolines  $\Re\{D\} = 0$  and  $\Im\{D\} = 0$ . They are then evaluated exactly with the Matlab routine, searching for solutions of  $\Re\{D\} = 0$  and  $\Im\{D\} = 0$ . Thus the conjugate pair  $\omega_r \pm i\omega_i$  of the unstable temporal mode is found.
2. The path of the unstable solution ( $\omega_r + i\omega_i$ ) is then followed in the complex  $k$ -plane as  $\omega_r$  is increased at constant  $\omega_i$  (Figure 3.17a). This is the  $k^+$  branch. It starts on the  $k_r$  axis and moves into the  $k_i < 0$  half plane. The initial value of  $k_r$  in step (1) was chosen so that all saddle points in the  $k_i < 0$  half plane lie to the left of this line.



**Figure 3.17:** (a) Path of the  $k^+$  branch in the complex  $k$ -plane, starting from an unstable solution of the temporal mode (diamond).  $\omega_i = \text{constant}$ ,  $\omega_r$  varies as in figure 3.16a. (b) Paths of the  $k^+$  branch at various values of  $\omega_i$ . On reducing  $\omega_i$  a saddle point  $\bullet$  is reached at  $(\omega_0, k_0)$ . (c) At the same values of  $\omega_i$  there are contours on the other side of the saddle point. This must be confirmed as a  $k^-$  branch by increasing  $\omega_i$  and ensuring that all contours remain in the  $k_i < 0$  half plane.

3. The value of  $\omega_i$  is reduced and the new locus of the  $k^+$  branch evaluated as illustrated in figure 3.17b. This process continues until a saddle point is encountered.
4. The saddle point is then traversed and  $\omega_i$  increased in order to check that the other branch is a  $k^-$  branch, as shown in figure 3.17c.
5. The first saddle point which is encountered as  $\omega_i$  is reduced must be the most unstable.
6. Now that the saddle point has been located, two more simultaneous equations are added to the Matlab routine:  $\Re\{\partial D/\partial k\} = 0$  and  $\Im\{\partial D/\partial k\} = 0$ . The saddle point is followed as the parameters of the dispersion relation are varied incrementally. The convective/absolute instability transition line is found by following the path  $\omega_{0i} = 0$  in parameter space.

In this case, it is useful to study an overall map of the dispersion relation (3.33) in the complex  $k$ -plane. The function  $\coth(k)$  is periodic, repeating in strips of width  $\pi i$  in the  $k_i$  direction. It has essential singularities at  $k = n\pi i$  and zeros at  $k = (n + 1/2)\pi i$ ;  $n \in \mathbb{Z}$ . These poles and zeros determine the positions of saddle points. Contours of  $\omega_i$  in the complex  $k$ -plane are shown in figure 3.18a for a density ratio of 1 and in figure 3.18b for a density ratio of 830, which corresponds to water/air at atmospheric pressure. The contours at higher  $\omega_{0i}$  than the saddle points are  $k^+$  or  $k^-$  branches. There is a  $k^-$  branch associated with the pole/zero pair in each strip. Since there is a single  $k^+$  branch, one expects an infinite number of  $k^+/k^-$  saddle points, one in each strip  $n\pi i > k_i > (n - 1)\pi i$ . These saddle points, which scale with  $h_1$ , are labelled  $R, 2R, 3R \dots$ . When  $S$  is large, a large value of  $\coth(k)$  is required for  $D = 0$  to be satisfied, which tends to bunch contours around poles. At large  $S$ , saddles are closer to poles than they are at small  $S$ .

At given parameter values  $(S, \Lambda)$ , each saddle point has position  $(\omega_0, k_0)$ . The saddle with the highest value of  $\omega_{0i}$  causes a local absolute instability if that  $\omega_{0i} > 0$ . In this



study, saddle points were followed over a wide range of parameter space and the results presented here apply to almost any wake encountered in nature. The convective/absolute (CI/AI) transition line can be calculated for each saddle point. Saddle  $R$  is always the first to become absolutely unstable so only its contribution is shown in figure 3.19a. This fits exactly the results of Yu and Monkewitz (1990) but is extended here to a higher density ratio. For comparison, the transition line for the varicose instability is shown in figure 3.19b. Operating conditions of the experiments presented in section 3.8.6 are shown as a circle symbol for the cryogenic injector and a square symbol for the laboratory injector.

Operating conditions of the cryogenic injector lie just inside the absolutely unstable region. As a reminder, this analysis was performed in the limit of infinitely thin shear layers. When these shear layers have finite size they tend to reduce the flow's absolutely unstable nature. Consequently only a very small region of the flow is absolutely unstable, just at the base of the wake. This suggests that the flow will be marginally globally stable. Huerre and Monkewitz (1990) demonstrate that marginally globally stable flows behave like slightly damped linear oscillators. An impulse can set off an instability very similar to the global mode but it dies away after sufficient time. This behaviour is seen very clearly on high frame rate images by (Gicquel 2001) of the cryogenic test facility.

### 3.8.5.3 Convective/absolute transition in the bounded wake

For sinuous disturbances in the bounded wake, the  $\coth(k)$  term is replaced with a  $\coth(k)\coth(kh_3)$  term. Before tackling this case, it is useful to consider the shape of the dispersion relation with  $\coth(k)$  replaced with  $\coth(kh_3)$ . This is shown in figure 3.20a for  $h_3 = 7$ . As before, there is a saddle associated with each  $k^-$  branch and there is a  $k^-$  branch associated with each pole/zero pair. The poles and zeros are at  $n\pi i/h_3$  and  $(n + 1/2)\pi i/h_3$ . As expected, the map is qualitatively identical to that for  $\coth(k)$  but with the saddles closer together. The saddle points, which scale with  $h_3$ , are labelled  $1L$ ,  $2L$ ,  $3L$ . The CI/AI transition line in  $(S, \Lambda)$  space is identical to that for  $\coth(k)$ .

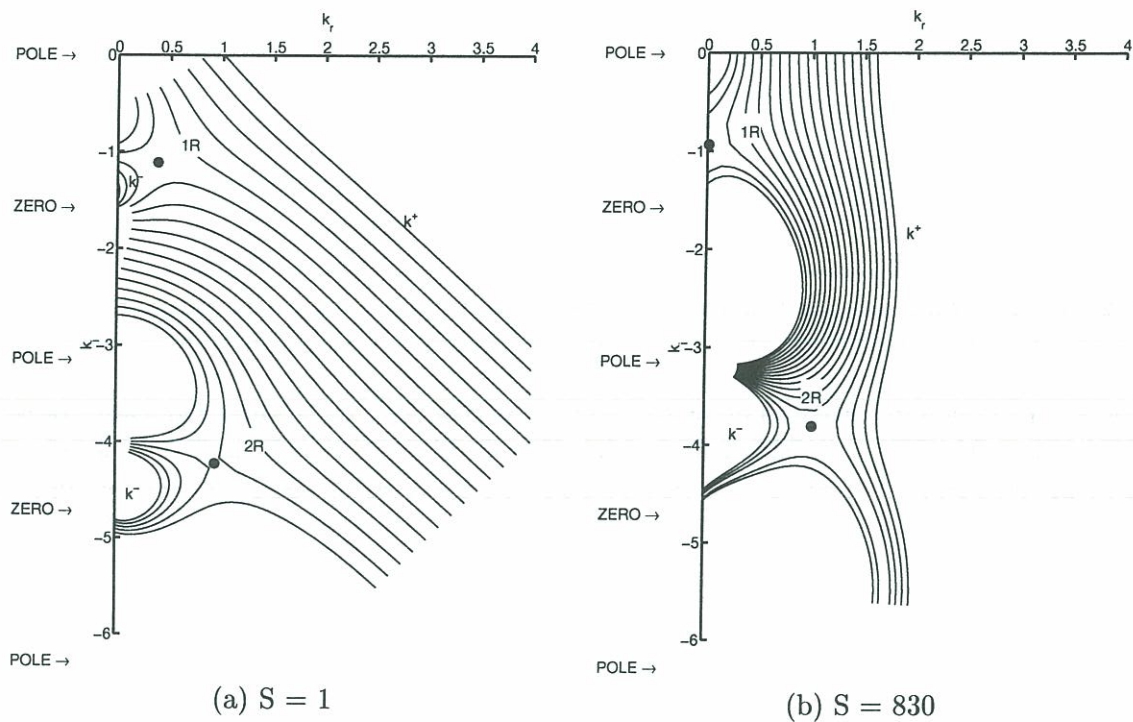
When the dispersion relation contains the term  $\coth(k)\coth(kh_3)$ , there are crucial interactions where poles or zeros associated with  $\coth(k)$  are close to those associated with  $\coth(kh_3)$ . This happens, for example, around the first zero of  $\coth(k)$  at  $k = -\pi i/2$  and where the two poles coincide at  $k = 0$ . This is shown in figure 3.20b.

Let us examine the effect around  $k = -\pi i/2$  first. This concerns the interaction between saddle  $3L$  and saddle  $R$ . Saddle  $3L$  has become more unstable and has a higher wavenumber. In addition, saddle  $R$  has become a  $k^-/k^-$  pinch point.

The effect around the pole at  $k = 0$  is more significant, although it is less evident at the density ratio of unity shown in figure 3.20b. The associated saddle point is denoted  $C$ , in order to distinguish it from the  $L$  and  $R$  family of saddles. Its position changes considerably, particularly at high  $S$ , when saddle points approach poles. This effect is most pronounced when  $h_3 = 1$  as can be seen from the CI/AI line in  $(S, \Lambda)$  space, figure 3.21a. The bounded wake is absolutely unstable over a much wider range of parameter space. This is the key result of this analysis.

Similar effects can be seen for  $h_3 = 2.1$  and  $h_3 = 7$  in figures 3.21b and 3.21c. There is one CI/AI line per saddle point. As  $h_3$  increases, saddle  $C$  is unstable over a wide range of velocity ratio but only at high density ratio. The absolutely unstable wavelength that it predicts becomes very large. At lower density ratios, saddle  $R$  and the nearby  $L$ -saddles





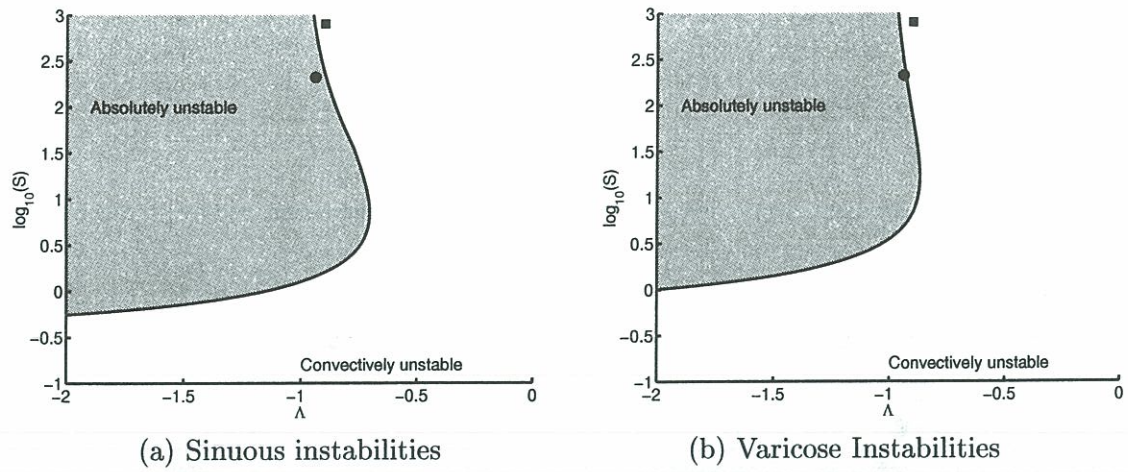
**Figure 3.18:** Contours of  $\omega_i = \text{constant}$  in the complex  $k$ -plane. In both diagrams, the  $k^+$  branch pinches with two  $k^-$  branches in this range, forming two saddle points, which are marked  $\bullet$ . The dispersion relation is that of the unbounded wake. The velocity parameter,  $\Lambda$  is equal to  $-1$ , corresponding to a static central fluid. On the left, the density ratio  $S$  is equal to 1. On the right,  $S = 830$ .

are more unstable. As  $h_3 \rightarrow \infty$ , saddle  $C$  affects only infinitely high density ratios and all  $L$ -saddles collapse to the  $k_i$  axis, where they have zero wavenumber. The family of  $R$ -saddles becomes the most unstable as  $h_3 \rightarrow \infty$  and the behaviour of the unbounded wake is retrieved. As explained in section 3.8.3 the behaviour at  $h'_3 < 1$  is identical to the behaviour at  $h_3 > 1$ , where  $h'_3 \equiv 1/h_3$ . It is also worth mentioning that the varicose instability becomes entirely convective as  $h_3 \rightarrow 1$ .

To summarize, sinuous instabilities in the bounded wake flow are absolutely unstable over a much larger region of parameter space when  $h_3 \sim 1$ . As pointed out already, this model assumes infinitely thin shear layers. As the shear layers grow, they inhibit the absolutely unstable nature of the flow. However, the operating conditions of both injectors lie well within the absolutely unstable region of parameter space. This suggests that the region of local absolute instability in physical space extends much further into the wake when it is bounded. This encourages transition to a global mode, causing self-sustained oscillations.

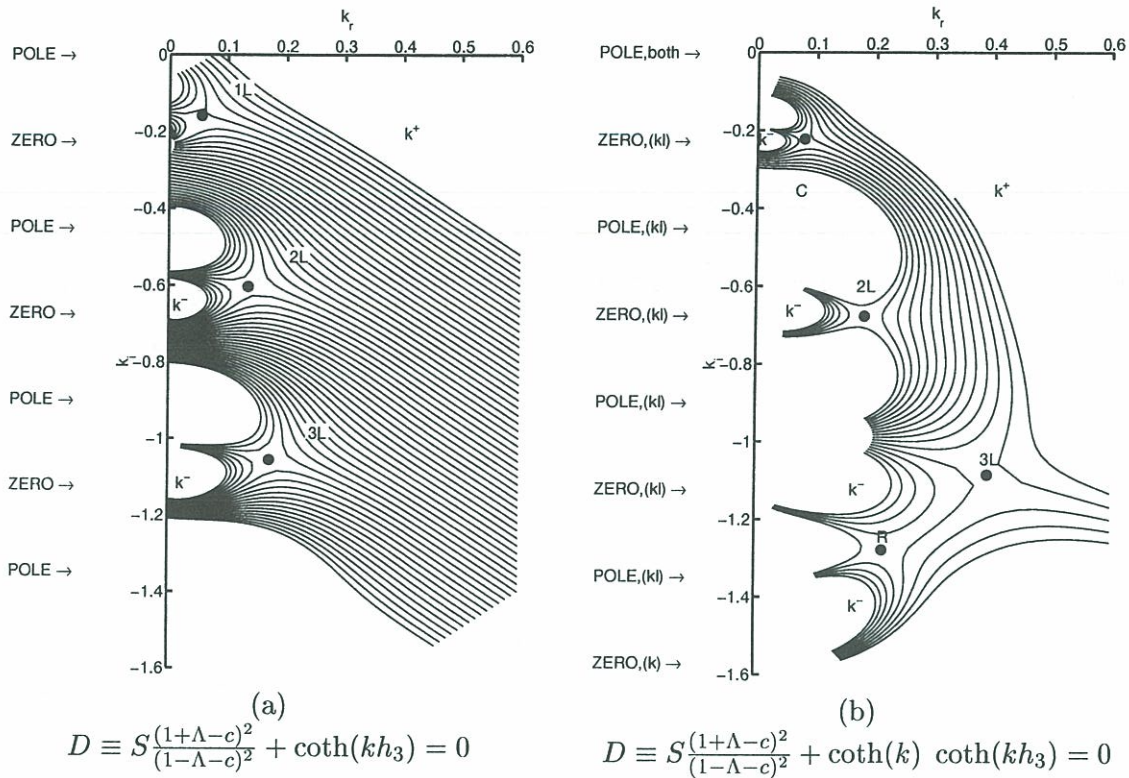
It is likely that the same effect occurs in the axisymmetric case. The region at the base of the wake is most influential in promoting a global instability. Recessing a coaxial





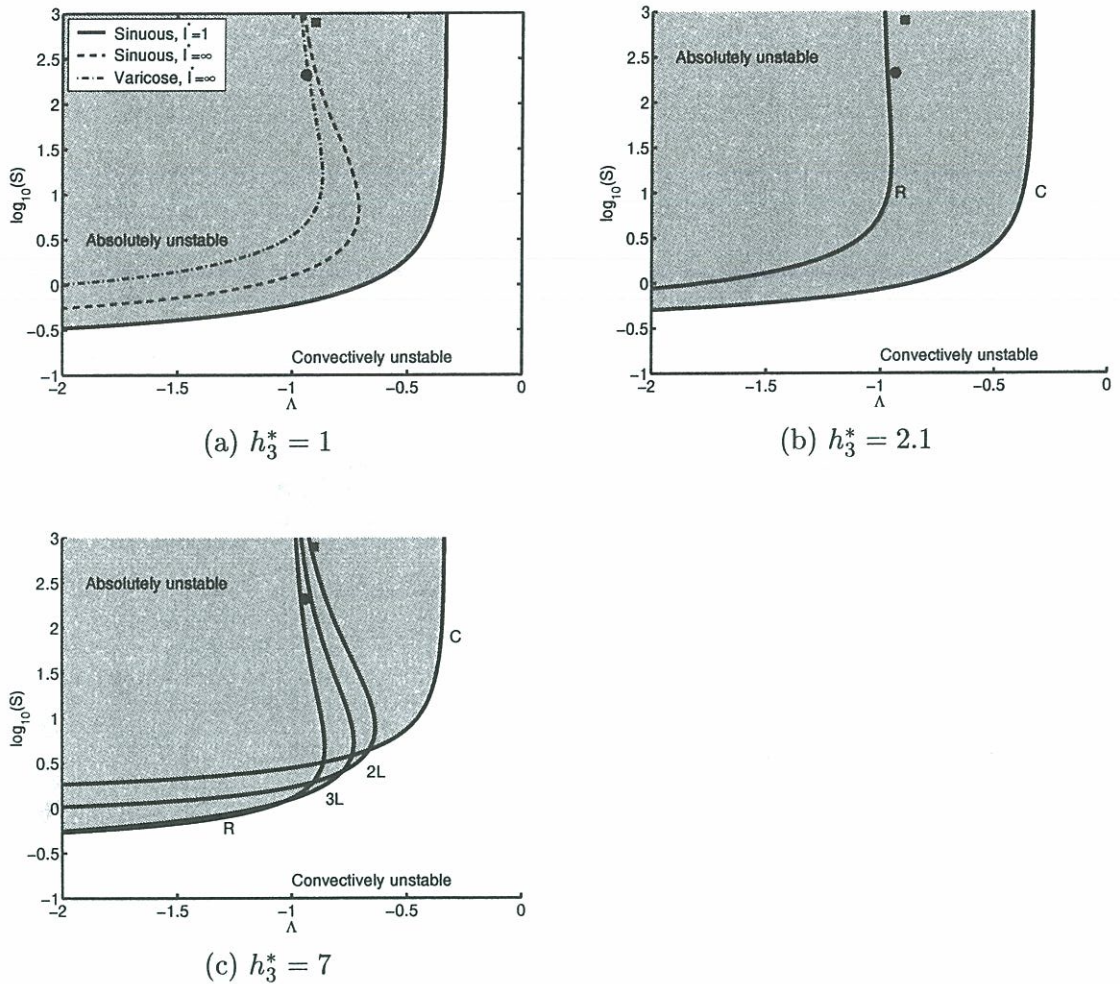
**Figure 3.19:** Convective/Absolute instability transition line for instabilities of an unbounded wake. Vertical axis:  $\log$  of the density ratio  $S$ . Horizontal axis: non-dimensional velocity ratio,  $\Lambda$ . For  $-1 < \Lambda < 0$ , the wake is co-flow. For  $\Lambda < -1$  it is counter-flow. The circular symbol marks the operating conditions in a cryogenic injector. The square symbol marks conditions in the laboratory injector presented in section 3.8.6. The absolutely unstable domain of sinuous instabilities extends further than that of varicose instabilities.

injector is equivalent to bounding this particular region and in practical situations,  $h_3 \sim 1$ . This suggests that recess lengthens the absolutely unstable region of the flow and therefore encourages transition to a global mode (figure 3.22)

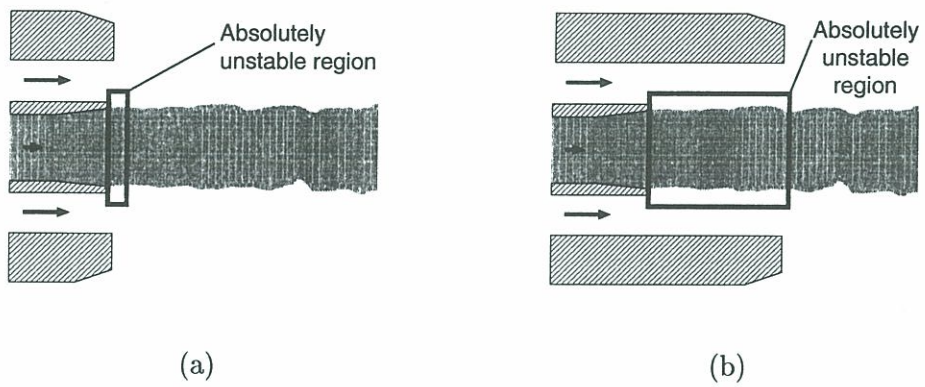


**Figure 3.20:** Contours of  $\omega_i = \text{constant}$  in the complex  $k$ -plane when  $S = 1$ ,  $\Lambda = -1$ ,  $h_3 = 7$ . In figure (a), the second term in the dispersion relation is  $\coth(kh_3)$ . The  $k^+$  branch pinches with three  $k^-$  branches in this range, forming saddle points 1L, 2L and 3L, which are marked with a bullet ( $\bullet$ ). In figure (b), the second term in the dispersion relation is  $\coth(k) \coth(kh_3)$ , which corresponds to the bounded wake flow. The 1R pole of figure 3.18a is now “superimposed” onto the landscape of figure 3.20a. The zero of  $\coth(k)$  lies close to the 3<sup>rd</sup> pole of  $\coth(kh_3)$ , having a strong effect on the contours. With this interaction, saddle 3L is more unstable and has a higher wavenumber. It should also be noted that saddle R has become a  $k^-/k^-$  pinch point. The saddle point close to the central poles at  $k = 0$  is the most affected. This is less visible at  $S = 1$  than at  $S \gg 1$ .





**Figure 3.21:** Convective / Absolute instability transition lines for sinuous instabilities of a bounded wake at different values of  $h_3^*$ , the ratio of the annular width to the wake's half-width. For comparison, the sinuous and varicose transition lines of the un-ducted wake are shown in the first diagram. The letter next to each line in the second and third diagrams denotes the saddle point associated with the line. The square symbol denotes the operating point of the laboratory injector. The circular symbol denotes the point of the cryogenic combustion facility. Ducting the wake causes both operating points to become absolutely unstable to sinuous perturbations.



**Figure 3.22:** *Regions of absolute instability in a coaxial injector at typical cryogenic flame injection conditions. (a) Without recess. (b) With recess. When the injector is recessed, the larger region of absolute instability is likely to trigger a global mode. This is characterized by self-sustained sinuous or helicoidal oscillations and will cause better mixing of the central jet.*



### 3.8.6 Experiments

The theory in this section suggests that recessing a coaxial injector could promote the development of a global helicoidal instability. This mechanism has been examined experimentally on two facilities at high density ratio. The first is a laboratory scale coaxial water/air injector created by Leroux (2001). The second is the cryogenic injector. Operating conditions are shown in table 3.2. The only diagnostic presented here is shadowgraphy. An attempt was made on the laboratory injector to measure the frequency of passage of wave crests with a laser and a photodiode. However, this technique was too sensitive to the optical alignment and the results were not repeatable. At low gas velocities it is possible to estimate the wavelength of perturbations by measuring the distance between peaks and troughs. This process was automated and applied to 1000 images at two operating points. The resulting distribution shows a peak, which is taken to be the predominant wavelength. Spread arises because the jet is not perfectly sinuous and consequently the positions of crests and troughs, as measured by the computer, vary randomly about the predominant value. These experiments are not intended as rigorous confirmation of the theory. They can however indicate whether recess enhances instability and, if so, give an indication of its behaviour.

As explained in section 3.8.1, the model considers only wake-like behaviour, ignoring instabilities in the individual shear layers. This justifies an inviscid analysis. Fortunately, this separation can be achieved experimentally on the laboratory injector by exploiting the stabilizing effect of surface tension. In a certain velocity range, surface tension will stabilize potential small wavelength instabilities in the individual shear layers while not stabilizing the potential long wavelength instabilities associated with wake-like behaviour. The optimum point is found by choosing air and water velocities at which the water jet is just unperturbed at zero recess.

Results are shown in figures 3.23 to 3.30. In the laboratory injector, the exit of the liquid jet remains in the same position on the image. The initial part of the liquid jet is obscured when there is recess and only the latter part of the jet can be compared.

Figures 3.23 and 3.24 show the jet when it is still in the lightly-perturbed regime. In both cases there is clearly an enhancement of the helicoidal instability mode when the injector is recessed. Figures 3.25 and 3.26 show the jet at a slightly higher gas velocity. Again, there is clearly an enhancement of the helicoidal instability mode when recessed. A single operating point is available for the cryogenic injector in figure 3.30 and the same phenomenon can be observed.

It is possible that the observed instability is due to acoustic feedback between the gas exit plane and the liquid exit plane, as described in section 3.7. This form of long-range feedback is not dealt with by the model. If this were the active mechanism, the instability wavelength would be expected to scale with the recessed length, in accordance with equation (3.25). In figure 3.27, images of the laboratory injector are shown for various recessed lengths. At zero recess, wavelengths are typically 5 mm. At a recessed length of 4 mm, a wavelength of approximately 8 mm appears intermittently. At recess of 8 mm to 10 mm the wavelength at 8 mm appears permanently. Automated measurements of the instability's wavelength in figure 3.28 show the same effect. The wavelength does not scale with recessed length, which implies that the mechanism does not involve long-range pressure feedback. This also explains the observation that, in rocket motors, the length



	Fig.	$U_l$ m/s	$U_g$ m/s	$h_1$ mm	$h_3$ mm	recess mm	$S$	$\Lambda$	$h_3^*$
LABORATORY INJECTOR	3.23	0.83	15	1.3	1.7	0 & 8	830	-0.90	1.3
	3.24	0.86	15	1.3	2.7	0 & 8	830	-0.89	2.1
	3.25	0.83	20	1.3	1.7	0 & 8	830	-0.92	1.3
	3.26	0.86	20	1.3	2.7	0 & 8	830	-0.92	2.1
	3.27	0.86	20	1.3	2.7	0 to 10.3	830	-0.92	2.1
	3.29	4	100	1.3	1.7	0 to 3.0	830	-0.92	1.3
ROCKET INJECTOR	3.30	4.2	140	2.5	2.5	0 & 5	210	-0.94	1.0

**Table 3.2 :** Experimental operating conditions

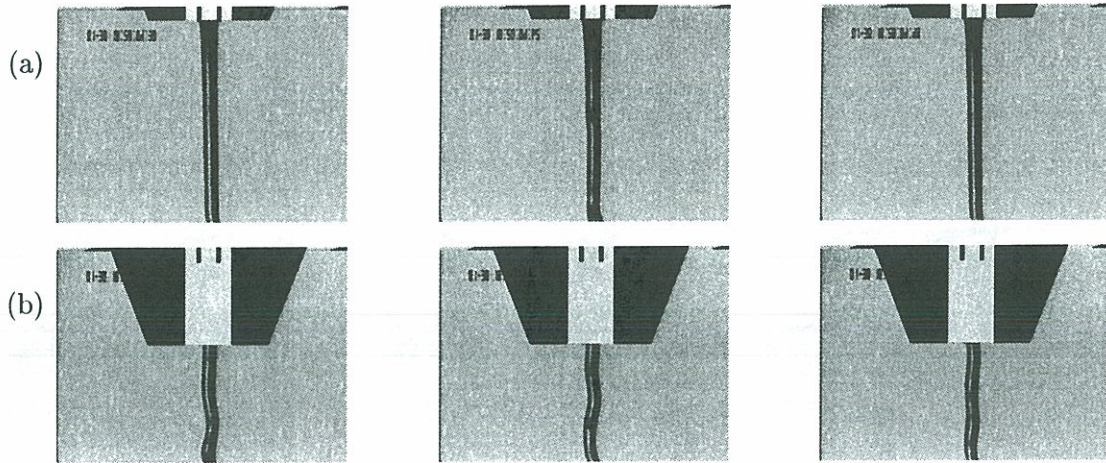
of recess has no further effect beyond a certain point. This is because once the global instability has been triggered, further recess will not affect it.

These results can be compared with those of Rehab et al. (1997) on water/water coaxial injectors without recess. At high velocity ratios, they find that a recirculation zone forms at the end of the central fluid's core. This is described in section 3.3.2.4. At slightly higher velocity ratios, the combined jets develop a low frequency helicoidal mode, corresponding to an azimuthal wavenumber of unity. This is exactly the mode one would expect from the theory in this chapter. It can be seen in figure 3.19a that the 2-D equivalent of this mode, even without recess, becomes absolutely unstable as the velocity ratio increases (or  $\Lambda$  decreases). Rehab et al. note that this is similar to the mode observed by Berger and Schumm (1990) in the wake behind a sphere. This observation can be explained convincingly by a convective/absolute instability transition.

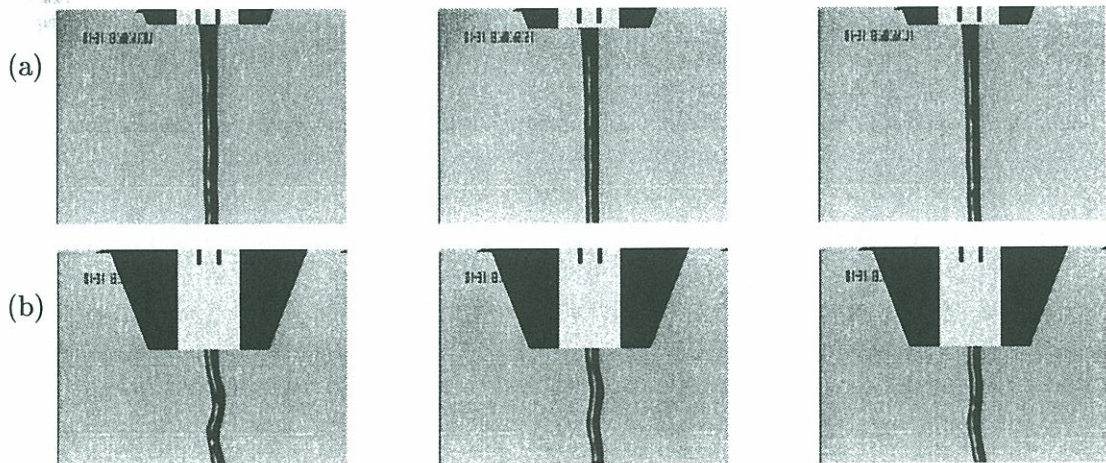
Visualizations of the LOx jet in the model cryogenic injector clearly show that there is no recirculating zone. The rupture mode is fibrous, with or without recess. However, there does seem to be transition to a helicoidal instability. This could be interpreted as a transition to a superpulsating mode, given the similarity to the original visualizations of Farago and Chigier (1991).

It must be emphasized once again that rigorous experimental confirmation would require more sophisticated measurements. Nevertheless, these findings do suggest that recess enhances a helicoidal instability inherent to the wake-like nature of the flow.

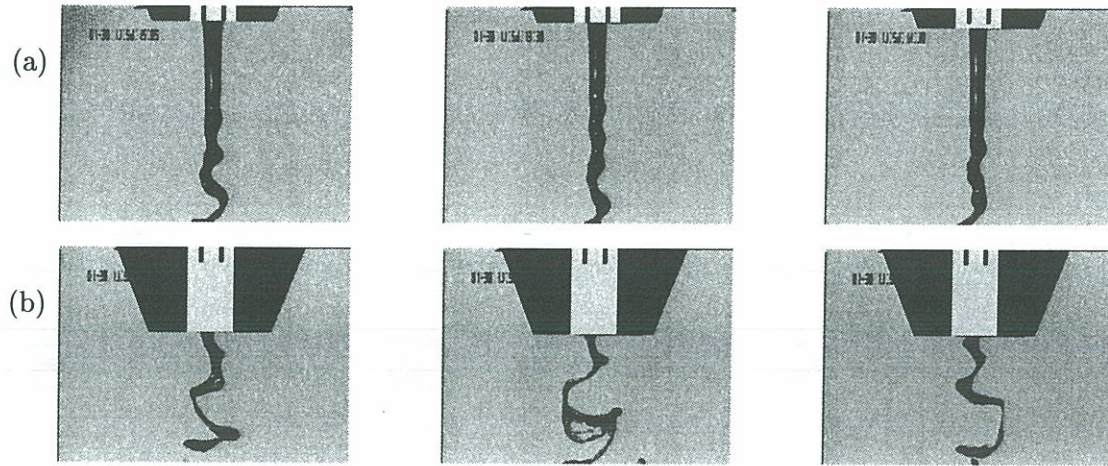




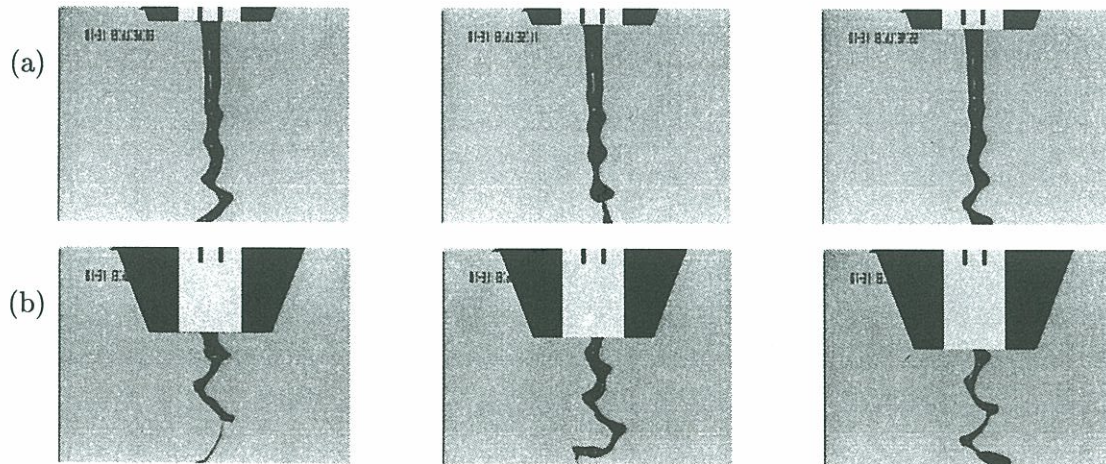
**Figure 3.23:** Visualisation of the water jet in a laboratory-scale coaxial injector.  $U_l = 0.83 \text{ ms}^{-1}$ ,  $U_g = 15 \text{ ms}^{-1}$ ,  $h_1 = 1.3 \text{ mm}$ ,  $h_3 = 1.7 \text{ mm}$ , (a) zero recess. (b) recess 810.3mm.



**Figure 3.24:** Visualisation of the water jet in a laboratory-scale coaxial injector.  $U_l = 0.86 \text{ ms}^{-1}$ ,  $U_g = 15 \text{ ms}^{-1}$ ,  $h_1 = 1.3 \text{ mm}$ ,  $h_3 = 2.7 \text{ mm}$ , (a) zero recess. (b) recess 10.3 mm.

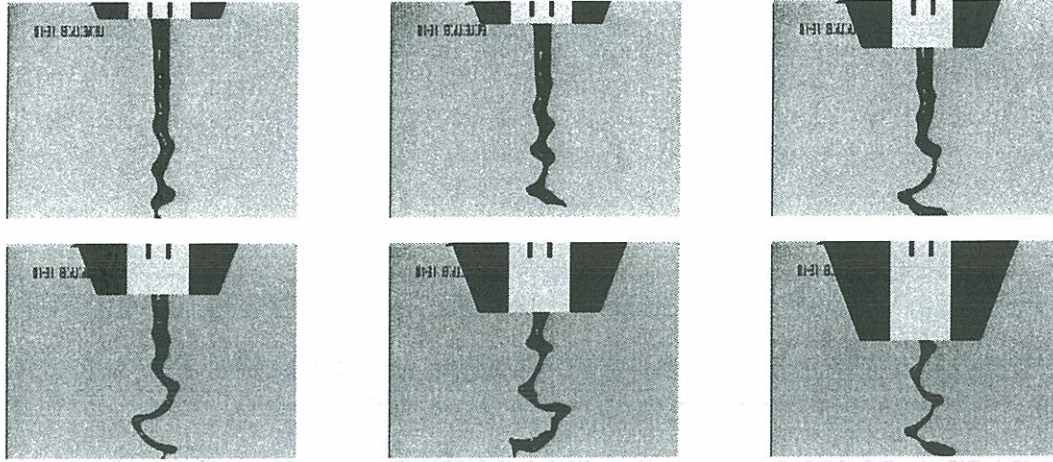


**Figure 3.25:** Visualisation of the water jet in a laboratory-scale coaxial injector.  $U_l = 0.83 \text{ ms}^{-1}$ ,  $U_g = 20 \text{ ms}^{-1}$ ,  $h_1 = 1.3 \text{ mm}$ ,  $h_3 = 1.7 \text{ mm}$ , (a) zero recess. (b) recess 8 mm.

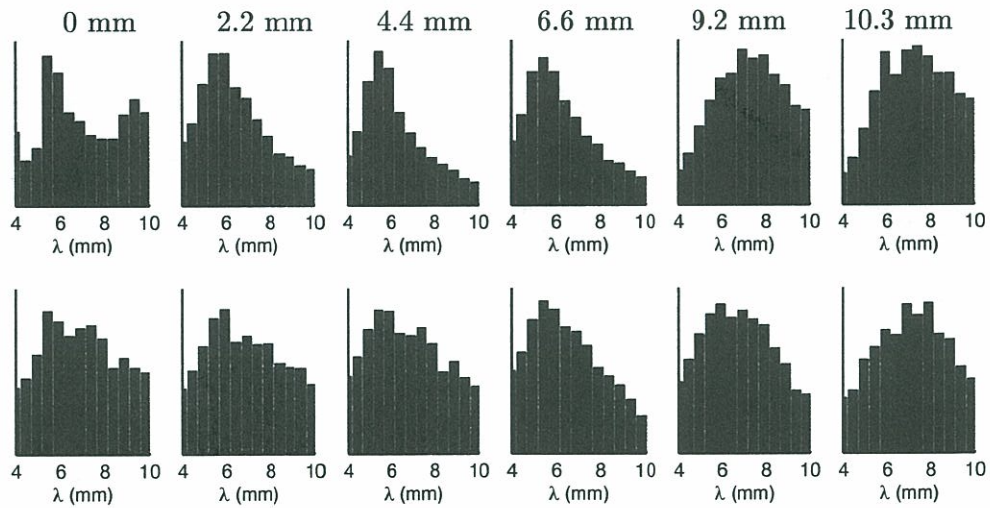


**Figure 3.26:** Visualisation of the water jet in a laboratory-scale coaxial injector.  $U_l = 0.86 \text{ ms}^{-1}$ ,  $U_g = 20 \text{ ms}^{-1}$ ,  $h_1 = 1.3 \text{ mm}$ ,  $h_3 = 2.7 \text{ mm}$ , (a) zero recess. (b) recess 8 mm.

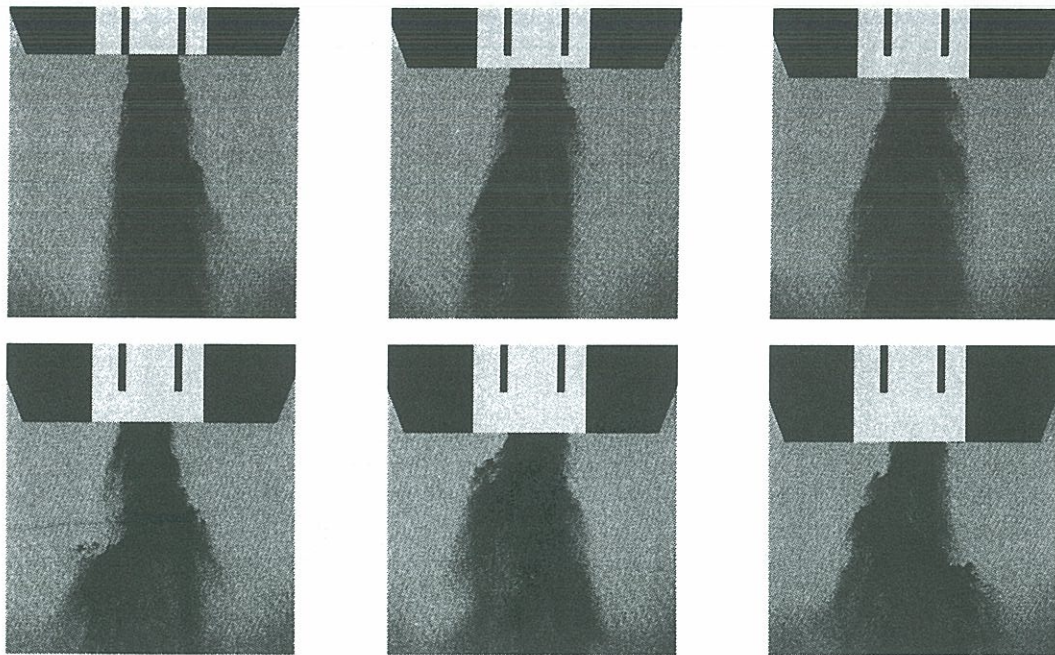




**Figure 3.27:** Visualisation of the water jet in a laboratory-scale coaxial injector.  $U_l = 0.86 \text{ ms}^{-1}$ ,  $U_g = 20 \text{ ms}^{-1}$ ,  $h_1 = 1.3 \text{ mm}$ ,  $h_3 = 2.7 \text{ mm}$ , Recess values: 0 mm, 1 mm, 4 mm, 5 mm, 8 mm, 10 mm.

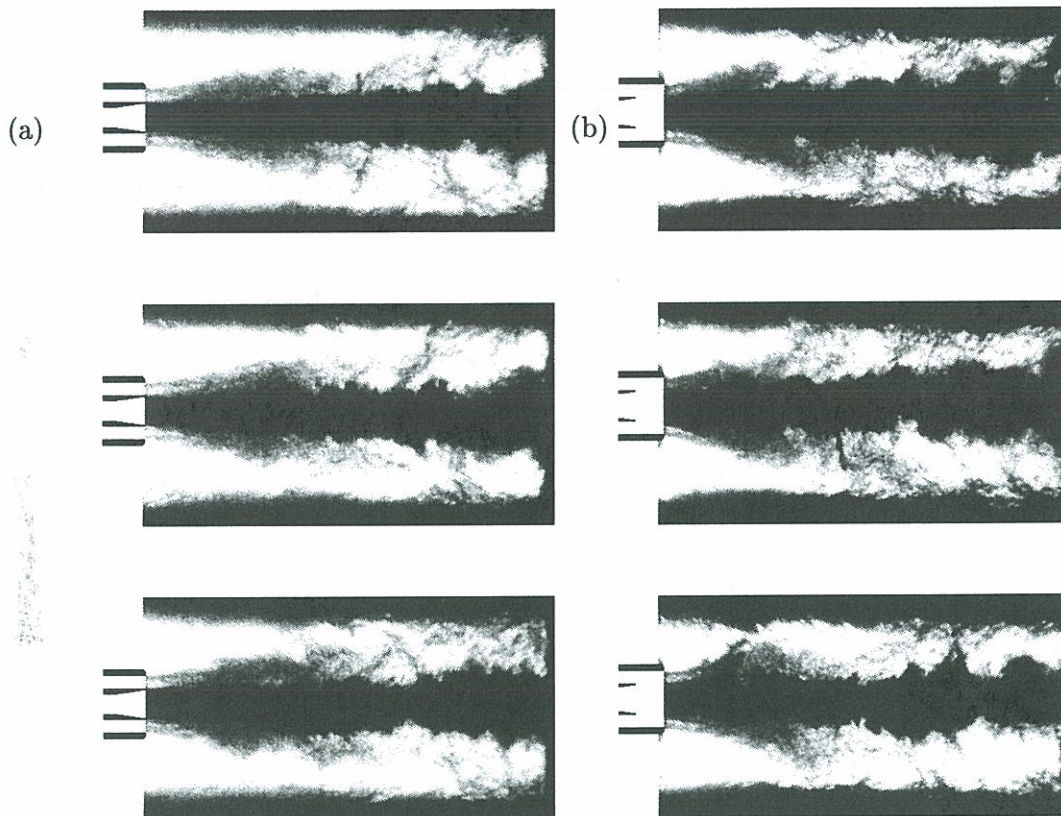


**Figure 3.28:** Wavelength distributions on the surface of the central stream. The recessed length  $l_r$  is shown above the histograms. The fluid velocities are:  $u_1 = 0.83 \text{ ms}^{-1}$  and  $u_2 = 15 \text{ ms}^{-1}$ . In the top row, the central stream radius,  $h_1$ , is 1.3 mm and the outer stream's thickness,  $h_3$ , is 1.7 mm. In the bottom row, the central stream radius,  $h_1$ , is 1.3 mm and the outer stream's thickness,  $h_3$ , is 2.7 mm.



**Figure 3.29:** Visualization of the water jet in the laboratory injector.  $u_1 = 4 \text{ ms}^{-1}$ ,  $u_2 = 100 \text{ ms}^{-1}$ ,  $h_1 = 1.3 \text{ mm}$ ,  $h_3 = 1.7 \text{ mm}$ ,  $J = 0.8$ . Recessed length,  $l_r$  is 0 mm, 1.5 mm, 1 mm, 1.5 mm, 2 mm, 2.5 mm.





**Figure 3.30:** Visualisation of the liquid oxygen jet in the cryogenic test facility.  $U_L = 4.2 \text{ ms}^{-1}$ ,  $U_g = 140 \text{ ms}^{-1}$ ,  $h_1 = 2.5 \text{ mm}$ ,  $h_3 = 2.5 \text{ mm}$ , (a) zero recess. (b) recess 5 mm.

### 3.8.7 Development of an improved model

The model presented in section 3.8.3 produces a simple dispersion relation providing useful qualitative information. To produce quantitative results, the model must be axisymmetric and take into account shear layers of finite width. This situation has been considered by Monkewitz (1988a) for an unbounded axisymmetric wake with uniform density. A useful start would be to take the inviscid wake in this reference and simulate a boundary by altering equation (A3). This reference also deals with a viscous wake and, combined with the procedure in Yu and Monkewitz (1990) could perhaps include a density profile. The dispersion relations which are created are significantly more complicated and must be solved numerically.

### 3.8.8 Conclusions - stability of a bounded wake flow

The effect of recess on the behaviour of coaxial injectors is studied here from a new angle. The central flow behaves as a wake within the outer flow, which can be bounded in order to model recess. A two-dimensional inviscid model, which allows a qualitative understanding of the axisymmetric case, demonstrates that bounding the flow extends the conditions under which sinuous disturbances are absolutely unstable. Previous studies have shown that a global instability is triggered when a sufficiently large portion of a wake is locally absolutely unstable. This occurs at the base of a wake where the shear layers are thin. This is precisely the region which is bounded when a coaxial injector is recessed, implying that recess could encourage a global instability.

Experiments on a laboratory injector and the cryogenic injector show that recess does enhance a helicoidal instability. Together, these results give a strong indication that recess improves mixing in coaxial injectors by triggering a global wake-like helicoidal instability.

Once this mechanism is triggered, further recess has no effect but to channel the flow. This accounts for the optimum recessed length which is observed experimentally. The global instability, in itself, may not affect the rupture length. However, when coupled with non-linear effects such as pinching against the side of the injector, droplet break-up may be improved.

To explain how a helicoidal instability would affect mixing, let us consider a more conventional application of this phenomenon. The aerodynamic drag on an artillery shell can be reduced by injecting gas into its wake. This is called "base bleed". Without this feature the shell's wake is absolutely unstable: ( $S = 1$ ,  $\Lambda = 0.98$ ) in figure 3.19a. This leads to helicoidal instabilities which drain much of the shell's momentum due to the creation of energetic structures behind it. The injection of gas behind the shell moves the wake out of the absolutely unstable region, which greatly reduces drag. The reverse effect occurs in coaxial injectors. When the cryogenic injector is recessed, the resulting global instability transforms a large amount of the free streams' energy into helicoidal motion and large scale turbulence. This leads to better jet break-up and increased mixing.



### 3.9 Conclusion - effect of recess

Experimental results show that recessing the LOx tube inside the hydrogen tube increases the flame expansion angle at subcritical pressures and at low  $J$ . This is consistent with cold-flow experiments which show that recess improves break-up of the central stream. Some of these studies also indicate that there is a recessed length at which droplet distribution in the spray is optimized.

Two mechanisms are responsible for this effect. When there is a flame in the recessed portion of the injector, blockage by combustion products forces the velocity of the hydrogen flow to increase, which aids jet break-up. There is some experimental evidence from the cryogenic combustion facility to support this, although the experimental error is large. In the second mechanism, recess triggers a global instability in the oxygen stream, which behaves as a wake within the hydrogen flow. A theoretical development presented here demonstrates that the 2-D analog of the coaxial injector behaves in this way. Furthermore, this behaviour is seen in the cryogenic facility, a laboratory-scale coaxial injector and other results already presented in the literature.





## Part II

# Stabilization of a cryogenic spray flame

Cette seconde partie est consacrée à l'analyse de la stabilisation de la flamme. L'étude comprend:

- Une analyse de l'extinction d'une flamme de diffusion stable au voisinage d'un combustible ou comburant condensé (chapitres 4 et 5).
- Une étude des mécanismes d'accrochage d'une tête de flamme dans plusieurs configurations. On envisage successivement la stabilisation d'une flamme:
  - dans un coin (chapitre 6),
  - au-dessus d'une plaque poreuse avec injection d'un des réactifs au travers de la plaque (chapitre 7),
  - au-dessus d'une nappe liquide (chapitre 7),
  - au-dessus d'une nappe liquide derrière une marche, qui représente ici la lèvre de l'injecteur d'oxygène (chapitre 8).

Ces analyses successives permettent d'identifier les configurations et de dégager les paramètres de contrôle.

The successful launch of a high performance rocket requires steady thrust from the motor with a well controlled ignition transient and a minimum level of vibration. Stabilization of the flames at the fuel injectors inside the motor is essential. In the present context, "stabilization" refers to attachment of the flame to the lip of the oxygen injector. As well as leading to extinction, lack of stabilization could be a factor in the emergence of combustion instabilities. Given the power generated by the motor, these vibrations can lead to payload damage or even catastrophic failure of the rocket.

In a high performance rocket engine gaseous hydrogen and liquid oxygen are injected coaxially. The flame stabilizes in the wake of the oxygen injector lip and develops in the near vicinity of the oxygen stream. This is illustrated in the numerical studies of Oefelein and Yang (1998), in the experimental studies of Mayer and Tamura (1996), in the experimental studies of Herding et al. (1996) and in chapter 1 of this thesis. A diagram of this process is shown in figure 3.31. Under normal operating conditions the flame is stable

and it spreads as a highly turbulent brush. Below a critical hydrogen feed temperature, Preclik and Spagna (1988) have observed oscillations at frequencies corresponding to the chamber's acoustic modes. Temperature seems to control the onset of these oscillations, which suggests that the flame could lift off the oxygen injector making it more sensitive to acoustic coupling. With appropriate feedback this would lead to the observed oscillations. There was no optical access in the experimental investigation so the exact mechanism could not be observed visually.

It is clear that the flame base plays a central role, which is not yet fully documented. This can be considered in two parts:

- A hot slow-moving zone just behind the oxygen injector lip in which the flow is laminar.
- A thin spreading diffusion flame which becomes turbulent within a few millimetres.

Three mechanisms of flame blow-out are possible.

1. A pilot flame remains shielded in the recirculation zone but the turbulent flame is extinguished just downstream in regions of excessive strain rate.
2. The flame can no longer support itself in the recirculation zone.
3. Insufficient oxygen evaporates to feed the flame and it is quenched on the cold liquid surface.

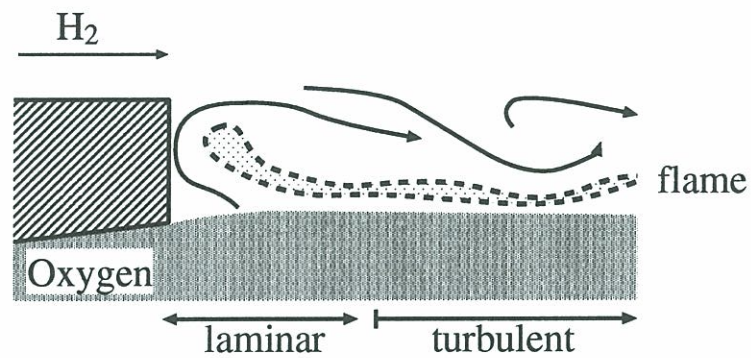
The first blow-out mechanism is explored in chapter 4 by considering a counterflow hydrogen flame above condensed oxygen. It is shown that, at pressures of 1 bar and above, extinction by strain is impossible, even if the flame is pinched against the liquid oxygen surface. This reduces the study to the region just behind the lip of the oxygen injector.

In chapter 5, the counterflow diffusion flame is used to evaluate a reduced reaction scheme for hydrogen/oxygen. While not essential to this thesis, it does ensure that the numerical simulations of chapter 8 resemble conditions in the cryogenic spray flame.

The second and third extinction mechanisms are explored in chapter 8 with particular reference to three non-dimensional parameters, which are introduced in carefully planned stages. The first parameter is examined in chapter 6. It is a Damköhler number affecting flame stand-off distance in a corner flame. This configuration is simple enough to permit theoretical analysis, although this is not performed in the current study. Chapter 7 concerns a flame above a liquid fuel. This introduces a new physical feature, vaporization, which requires another non-dimensional parameter: the ratio of heat release on reaction to the liquid's latent heat of vaporization. The final parameter, the ratio of the LOx tube thickness to the flame thickness is introduced in chapter 8. This is found to be the most influential parameter.

The conclusions presented here are for a  $\text{H}_2/\text{O}_2$  flame at 1 bar. For reasons explained in chapter 8 this approach is valid at all pressures. It is also valid for all reactant combinations and will provide a useful tool for evaluating these.





**Figure 3.31:** *Diagram of a possible stabilization mechanism in the wake of the lip of the oxygen injector. The flow is laminar in the hot zone just behind the lip. Conditions become turbulent within a short distance. The flame is pinched between the cold hydrogen flow and the liquid oxygen surface, which must evaporate in order to supply the flame. These harsh conditions could lead to local extinction and blow-off.*





## Chapter 4

# Extinction limits of a counterflow flame fed by a condensed reactant

On souhaite ici envisager les conditions qui pourraient mener à une extinction de la flamme dans la zone proche de l'injecteur. Cette extinction semble possible si un tourbillon d'hydrogène gazeux et de grande intensité vient pincer la flamme en la poussant vers l'oxygène liquide condensé. Cette situation ressemble à une flamme à contre courant entre un liquide et un gaz. On étudie dans ce chapitre cette situation en utilisant une cinétique chimique détaillée et une représentation du transport multiespèces. Les conditions aux limites sont d'abord envisagées par des conditions de pression subcritiques et supercritiques. La situation subcritique est seule considérée dans la suite. A une pression de 1 bar, on trouve que le taux d'étirement d'extinction est d'un ordre de grandeur plus élevé que l'étirement maximum dans la chambre de combustion d'un moteur fusée typique. De plus, aux pressions plus élevées, le taux d'étirement d'extinction augmente. Les calculs montrent que l'extinction par étirement ne semble pas être possible dans le cas du couple d'ergols  $H_2/O_2$ . Cette conclusion pourrait cependant être à revoir dans d'autres cas, comme par exemple le  $CH_4/O_2$ .

## Nomenclature

$B$	Pre-exponential factor
$c_{pk}$	Specific heat of species $k$
$D$	Mass diffusivity
$h_k$	Enthalpy of species $k$
$\Delta h_v$	Latent heat of vaporization
$J$	Transverse pressure gradient
$\dot{m}$	Mass flux at liquid/vapour interface
$p$	Pressure
$p_s$	Saturation pressure (Appendix C)
$p_0$	A saturation pressure on the equilibrium line (Appendix C)
$R$	Gas constant
$T$	Temperature
$u$ or $U$	Axial / horizontal velocity
$v$ or $V$	Radial / vertical velocity
$V_k$	Diffusion velocity of species $k$
$Y_k$	Mass fraction of species $k$
$W_k$	Molar mass of species $k$
$X_k$	Mole fraction
$\epsilon_s$	Strain rate
$\epsilon_{sc}$	Extinction strain rate
$\lambda_l$	Thermal conductivity in liquid
$\lambda_v$	Thermal conductivity in vapour



## 4.1 Introduction

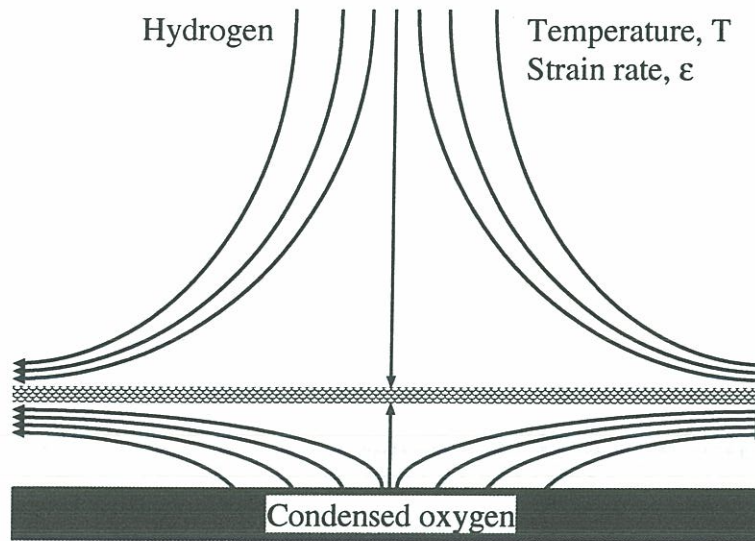
This chapter examines extinction of a cryogenic spray flame by excessive strain, taking the liquid phase into account. A one-dimensional test case is introduced in section 4.2, which resembles the most severe situation possible in a cryogenic spray flame. In section 4.3 the governing equations and boundary conditions of a detailed numerical simulation are introduced and the results are presented in section 4.4. These demonstrate that extinction by strain is impossible under normal operating conditions. In addition, these calculations provide some insight into the flame structure and reaction rate when the flame is close to a liquid reactant.

## 4.2 One-dimensional test case

Once it is established, the flame runs approximately parallel to the hydrogen flow in the near-injector region. Although strain parallel to the flame will not affect it, a turbulent eddy could impinge directly onto the surface, pinching the flame between the cold condensed oxygen and a fast perpendicular flow of cold hydrogen. It is known that diffusion flames formed between two low temperature reactant streams extinguish relatively easily, since heat loss takes place on both sides of the flame. This is unlike premixed flames which are backed by hot gases. The proximity of the condensed oxygen might significantly lower the strain rate at which this occurs. Once a hole has been punched in the diffusion flame an edge flame forms. The consequences of this have been studied in a different context by Lee et al. (2000). This edge flame does not then close up, even if the strain rate is immediately reduced. This has two consequences for the case under consideration here. Firstly, holes will tend to grow if the extinction strain rate is exceeded for even a short time, and the flame will blow off. Secondly, this analysis cannot be extended to ignition of the flame. It can only indicate the conditions under which a pre-existing flame will be stable.

This scenario can be modelled as a counterflow flame above a condensed fuel, as shown in figure 4.1. The flat flame formed in this configuration is submitted to an external strain rate. Extinction conditions may be studied by progressively increasing the strain rate until the temperature and reaction rate suddenly drop to vanishingly small values. Under a standard transformation (see section 4.3.2) this configuration can be reduced to a one-dimensional problem. While gaseous strained flames have been studied extensively, the case of a gaseous stream on a liquid surface is less well documented. It is first considered by Fendell (1965) in an asymptotic analysis with finite rate chemistry in the thermodiffusive limit. Fendell demonstrates that extinction occurs when a Damköhler number based on the flow time divided by the chemical time is reduced. This Damköhler number is proportional to  $B/\epsilon_s$ , where  $B$  is the pre-exponential factor and  $\epsilon_s$  the strain rate. Vaporization processes seem not to be influential, a fact which is confirmed later in this chapter. The asymptotic analysis of Hamins and Seshadri (1984) provides a way of calculating the extinction Damköhler number but their experimental results show that this method does not always lead to accurate results. Burluka and Borghi (2000) repeat the analysis in the infinitely fast chemistry limit in order to evaluate the vaporization rate and the flame position. This study also shows that when  $Le = 1$  the counterflow flame is stable with respect to small fluctuations in strain rate and thermodynamic parameters at the liquid surface.





**Figure 4.1:** Configuration of the model problem. A counterflow hydrogen diffusion flame is situated above a pool of condensed oxygen. This can be reduced to a one-dimensional problem from which the extinction strain rate can be calculated as a function of the operating condition.

It is assumed here that this remains true in the general case. With this assumption it is sufficient to calculate the extinction strain rate in steady flow. This assumption is backed up, for example, by the work of Katta and Roquemore (2000), who find that the flame can survive even higher strain rates when it is unsteady, but not pierced. The situation is also considered in experiments by Niioka et al. (1991) and Kent and Williams (1975), although neither tests the influence of the liquid properties.

The extinction strain rate in gas/gas counterflow flames can be estimated via the asymptotic analysis of Liñán (1974). For pure hydrogen and oxygen this gives an extinction strain rate of  $\epsilon_{sc} = 2.8 \times 10^6 \text{ s}^{-1}$ , which is extremely large. This is because a single step chemical reaction must be assumed, which precludes equilibrium chemistry effects. This leads to a high adiabatic flame temperature of 5700 K. Reducing the maximum temperature to 3000 K gives a strain rate of  $\epsilon_{sc} = 1.7 \times 10^4 \text{ s}^{-1}$ , which is probably too small. The calculated extinction strain rate is highly dependent on the choice of adiabatic flame temperature, as well as on other thermochemical parameters such as the pre-exponential factor and the activation energy.

In summary, there is no reliable analytical method for evaluating the extinction strain rate of a counterflow diffusion flame above a condensed reactant. This leads us to perform a detailed numerical simulation using complex chemistry and multi-species transport. The effects of three parameters are examined: (1) the strain rate, (2) the hydrogen stream temperature and (3) the heat conduction into the condensed oxygen core. As well as being useful for this research project, the results provide confirmation of some previously cited analyses and highlight some discrepancies which could be examined further in future work.



### 4.3 Boundary conditions and governing equations

The formulation of the governing equations including complex chemistry and detailed transport is straightforward. The boundary conditions at the condensed phase require some care and this is discussed first.

#### 4.3.1 Formulation of subcritical vs. supercritical problems

To one side of the flame is pure hydrogen at constant temperature. This is an easy boundary condition to model. The operating pressure of rocket engines is around 100 bar, above the critical pressure of both fluids. However, during the ignition process when oscillations have been observed, the pressure is below oxygen's critical pressure. The flame lies close to this condensed oxygen so particular attention must be paid to the boundary condition on this side. This is examined in appendix C for both subcritical and supercritical oxygen.

Below the critical pressure of pure oxygen, a liquid/vapour interface will always exist. Conditions at this interface are well known: the Clausius-Clapeyron equation (4.1) relates the saturation pressure to the surface temperature. The definition of symbols is given in appendix C. From this relation, the composition at the surface can be evaluated.

$$p_s(T_s) = p_0 \exp \left( \frac{\Delta h_v}{r_g} \left[ \frac{1}{T_0} - \frac{1}{T_s} \right] \right) \quad (4.1)$$

The heat flux is also related to the mass flux at the interface by equation (4.2).

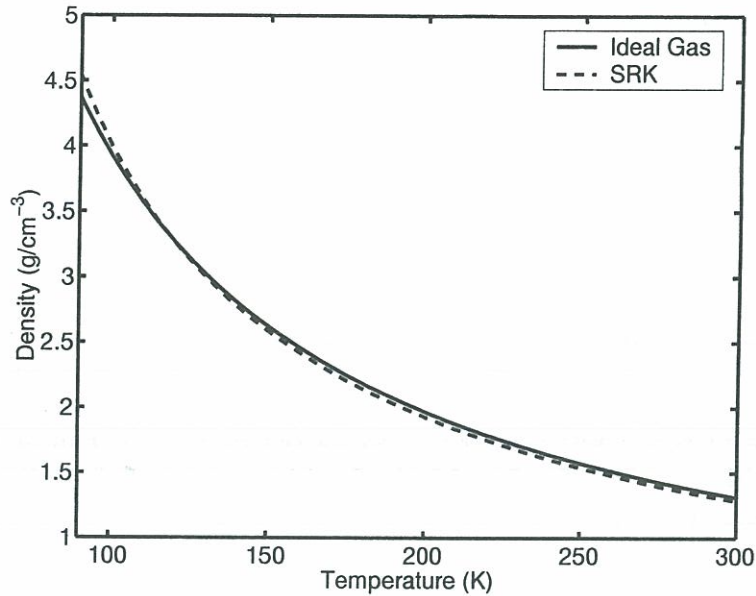
$$\lambda_v \frac{dT}{dx} \Big|_v = \dot{m} \Delta h_v + \lambda_l \frac{dT}{dx} \Big|_l \quad (4.2)$$

The liquid and vapour phases can be simulated separately, with jump conditions at the interface linking the two simulations. This permits the use of an optimized equation of state and transport quantity correlations in each phase. At the expense of some accuracy, simulation of the liquid phase can be replaced by the assumption that it is pure oxygen. Thus only the gaseous phase needs to be simulated. It can be checked *a posteriori* that the concentrations of other species gathering at the interface are very small. If they are not, the assumption is not acceptable.

Above the critical pressure of pure oxygen, it cannot be assumed *a priori* that an interface will exist. Consequently it is not possible to split the simulation up into liquid and vapour phases. The entire domain must be simulated, allowing an interface to form if this is dictated by the equation of state. This approach requires much care in the choice of equation of state, which has to be valid over a wide range of temperatures and compositions. The same is true of transport properties, particularly around the critical pressure. The steep gradients and discontinuities which occur could cause numerical problems and would necessitate the use of an adaptative grid.

#### 4.3.2 Governing equations

Given the difficulty of modelling the supercritical case, only the subcritical case will be examined in this study. This is acceptable if the extinction conditions determined at low



**Figure 4.2:** Comparison of the ideal gas equation of state with the Soave-Redlich-Kwong (SRK) equation of state for gaseous oxygen at 1 bar.

pressure are a lower bound for the values at high pressures. This property is found in the experimental results of Niioka et al. (1991) and is also confirmed in section 4.4.5 for hydrogen/liquid oxygen flames. Only the gaseous phase is simulated, assuming that the liquid phase is pure oxygen. It is convenient to choose a pressure of 1 atmosphere, since reaction schemes and transport data are well validated. The process is then repeated at 2 atmospheres in order to confirm the trend with increasing pressure.

The numerical technique is similar to that employed by Aguerre (1994). Transport properties are obtained from the Transport package described by Kee et al. (1986). Complex chemistry and thermodynamic properties are handled with the Chemkin software described by Kee et al. (1989). These have been verified between 80K and 3000K. The reaction mechanism is that described in Lindstedt (1998) with 9 species and 14 reactions. For convenience the ideal gas equation of state is used, since it is very close to the Soave-Redlich-Kwong (SRK) equation of state in the gaseous phase at 1 bar. This is shown in figure 4.2 to a temperature of 90 K.

The planar counterflow flame is reduced to a one-dimensional problem in the  $(x,z)$  plane by assuming that the flow-field is of the form:

$$u = U(z)x \quad (4.3)$$

$$\rho v = V(z) \quad (4.4)$$

where  $u$  is the velocity in the  $x$ -direction, parallel to the surface and  $v$  is the velocity in the  $z$ -direction, perpendicular to the surface. The transverse pressure gradient,  $J$ , is unknown but is assumed to be constant in the  $z$ -direction. In the stationary case the



balance equations for mass, momentum, species and energy take the following form:

$$\rho U + \frac{\partial(\rho v)}{\partial z} = 0 \quad (4.5)$$

$$\rho U^2 + \rho v \frac{\partial U}{\partial z} - J - \frac{\partial}{\partial z} \left( \mu \frac{\partial U}{\partial z} \right) = 0 \quad (4.6)$$

$$\rho v \frac{\partial Y_k}{\partial z} + \frac{\partial}{\partial z} (\rho Y_k V_k) - \omega_k W_k = 0 \quad , k = 1, \dots, N \quad (4.7)$$

$$\rho v c_p \frac{\partial T}{\partial z} - \frac{\partial}{\partial z} \left( \lambda \frac{\partial T}{\partial z} \right) + \left( \sum_{k=1}^N \rho Y_k V_k c_{p_k} \right) \frac{\partial T}{\partial z} + \sum_{k=1}^N (h_k W_k \omega_k) = 0 \quad (4.8)$$

In addition, the transverse pressure gradient is taken to be a constant:

$$\frac{\partial J}{\partial z} = 0 \quad (4.9)$$

and the equation of state for a mixture of perfect gases can be written:

$$\rho = \frac{pW}{RT} \quad (4.10)$$

where  $W$  is the molar mass such that :

$$\frac{1}{W} = \sum_{k=1}^N \frac{Y_k}{W_k}$$

For species  $k$ ,  $Y_k$  is the mass fraction,  $V_k$  is the diffusion velocity in the  $z$ -direction,  $W_k$  is the molar mass,  $\omega_k$  is the rate of reaction,  $c_{p_k}$  is the heat capacity and  $h_k$  is the enthalpy. Variables without subscripts refer to the mixture properties.

### 4.3.3 Boundary conditions

A strain rate  $\epsilon_s$  is imposed on the hydrogen side, leading to the following boundary conditions at  $z = +\infty$ :

$$U = \epsilon_s \quad (4.11)$$

$$T = T_{H2} \quad (4.12)$$

$$Y_k = \begin{cases} 1 & \text{for hydrogen} \\ 0 & \text{otherwise} \end{cases} \quad (4.13)$$

$$\frac{\partial v}{\partial z} = -\epsilon_s \quad (4.14)$$

The boundary conditions at the oxygen surface are quite different. These are derived in appendix C. Assuming that the liquid oxygen is at rest, the no-slip condition is expressed as:

$$U = 0 \quad (4.15)$$

If  $k = 1$  defines the oxygen species, the Clausius-Clapeyron equation defines the state at the liquid/gas interface:

$$Y_1 \frac{W_1}{W} = X_1 = \frac{p_0}{p} \exp \left( \frac{\Delta h_v W_1}{R} \left[ \frac{1}{T_0} - \frac{1}{T} \right] \right) \quad (4.16)$$

The heat and mass balance at the surface gives:

$$\lambda_v \frac{dT}{dz} \Big|_v = \rho v \Delta h_v + \lambda_l \frac{dT}{dz} \Big|_l \quad (4.17)$$

The remaining constraints are expressed in terms of the diffusion velocities  $V_k$ . Oxygen, which is the only species which can cross the interface, is labelled species 1. The mass flux of oxygen across the surface must equal the bulk mass flux away from the surface:

$$(\rho Y_{1s}) v_{net1} = \rho v \quad (4.18)$$

where  $v_{net1} \equiv (v - V_1)$  is the net velocity of species 1. This leads to

$$V_1 = v \frac{(1 - Y_{1s})}{Y_{1s}} \quad (4.19)$$

As would be expected,  $V_1$  tends to zero as  $Y_{1s}$  tends to 1. The net velocities of the remaining species must be zero. Hence:

$$V_k = -v \quad \text{for } k = 2, N \quad (4.20)$$

The previous equations are discretized using a centered finite difference scheme. Integration is achieved by combining a time-stepping scheme with Newton iterations on an adaptive mesh, as described in Darabiha (1992).

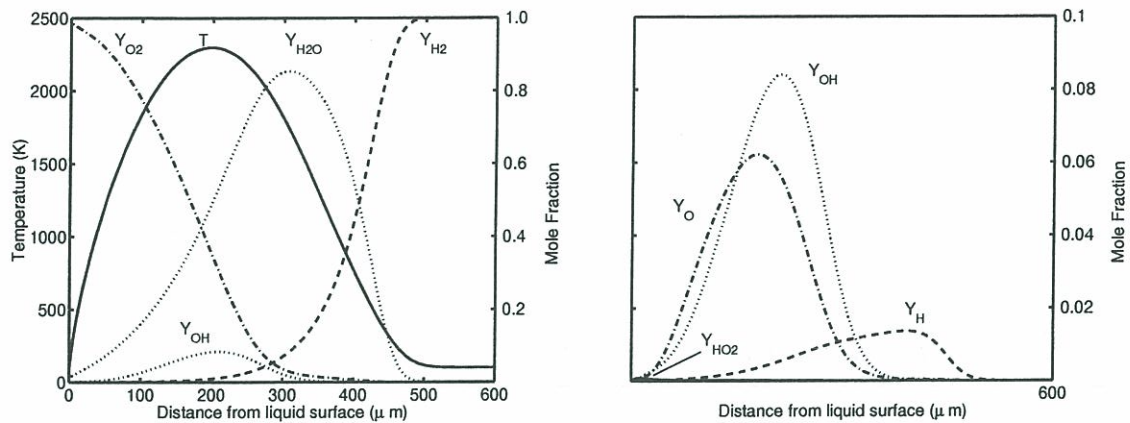
## 4.4 Results

In rocket engines, oxygen is injected at around 80 K. The surface temperature is around 90 K. The first set of simulations assumes that the amount of energy used to heat up the liquid oxygen is negligible compared with the amount required to transform it from liquid to gas. Consequently the second term on the right hand side of equation (4.17) is set to zero. This assumption is shown to be acceptable in section 4.4.4.

### 4.4.1 Species profiles in the flame

Profiles of temperature and mole fractions of species are shown in figure 4.3. For comparison the same profiles are shown in figure 4.4 for a gaseous  $H_2$  / gaseous  $O_2$  flame calculated by Schreiber (1991). In both cases the hydrogen temperature is 100K and the strain rate on the hydrogen side is  $\epsilon_s = 6.0 \times 10^4 \text{ s}^{-1}$ . The major species profiles are similar and the flames are about the same width. The temperature profile differs on the oxygen side in order to ensure that a temperature gradient exists at the liquid surface. The temperature is also consistently higher, which probably reflects improved correlations for the heat capacities used in this more recent analysis. It is interesting to note that,





**Figure 4.3:** Temperature and mole fraction profiles for a counterflow hydrogen flame above a condensed oxygen surface. Major species are on the left, minor species on the right. The inlet hydrogen temperature is 100K and the strain rate is  $6 \times 10^4 \text{ s}^{-1}$  on the hydrogen side.

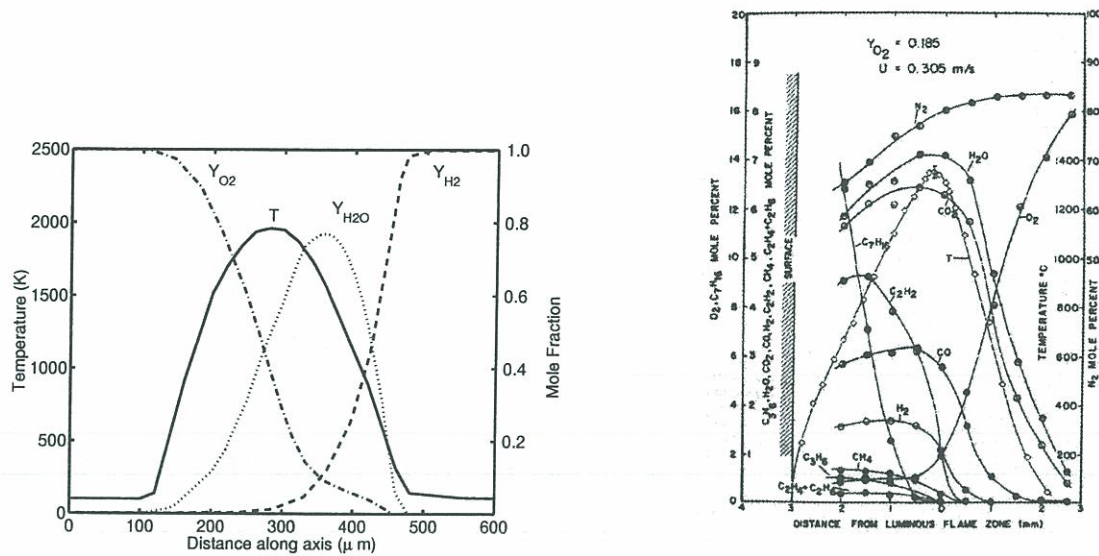
in both cases, the temperature profile does not coincide with the  $\text{H}_2\text{O}$  profile, an effect which is probably associated with the very different diffusivities of hydrogen and oxygen. This can be compared with the experimental results of Kent and Williams (1975) for a heptane/air flame. All major features are qualitatively identical but the  $\text{H}_2\text{O}$  profile is coincident with the temperature profile.

The flame is around  $400 \mu\text{m}$  thick and its location, defined here by the position of the maximum flame temperature is situated  $200 \mu\text{m}$  from the liquid surface. This latter value is an order of magnitude larger than that found by Burluka and Borghi (2000) and this does not change when a faster chemistry is employed, leading to a thinner flame. The flame position, it seems, is determined by the transport properties of the fluids and this may explain the difference between results obtained with a detailed model and estimates from a simplified analysis relying on a constant Lewis number approximation.

The oxygen mass fraction at the surface is 0.986. This reinforces the assumption that the amount of gas dissolved in the oxygen is negligible. The remaining fraction of 0.014 is almost entirely comprised of  $\text{H}_2\text{O}$  and a more rigorous analysis could consider this binary mixture at the interface.

#### 4.4.2 Effect of strain rate

The maximum flame temperature is plotted as a function of strain rate,  $\epsilon_s$ , in figure 4.5. It is shown for five values of the inlet hydrogen temperature between 10K and 80K. The maximum flame temperature decreases as strain increases since the increased gradients in the flame lead to a higher heat flux. Around 1600K, chain-breaking reactions overtake



**Figure 4.4:** *Left: Temperature and mole fraction profiles for a counterflow gaseous hydrogen / gaseous oxygen flame calculated by Schreiber (1991). Both gases are injected at 100K. The strain rate is  $6 \times 10^4 \text{ s}^{-1}$  on both sides. The axis position is arbitrarily defined. Right: Temperature and concentration profiles above a heptane fuel burning in an  $\text{O}_2/\text{N}_2$  mixture, from Kent and Williams (1975).*

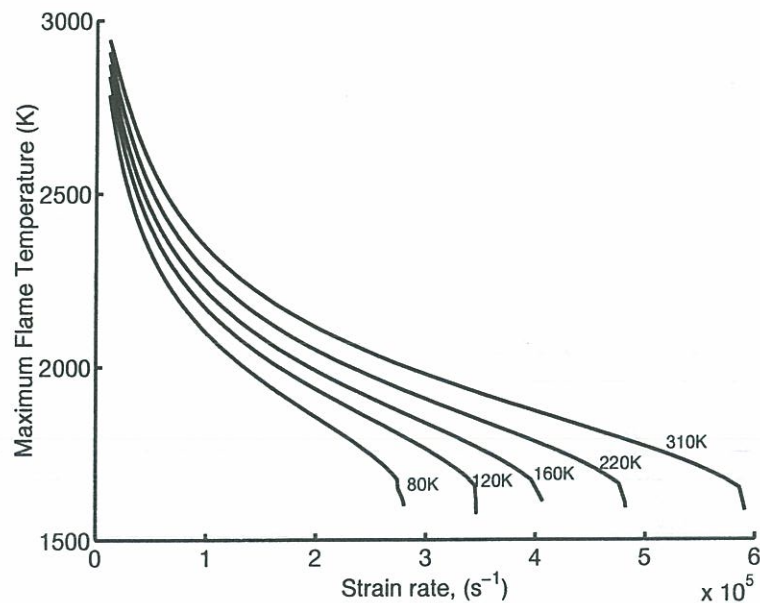
chain-branching steps and the flame is extinguished.

The heat release rate per unit area is shown in figure 4.6 as a function of strain rate. In steady state, the heat release rate is equivalent to the oxygen evaporation rate. These quantities are proportional to  $\epsilon_s^{1/2}$  in the gas/gas counterflow situation according to the infinitely fast chemistry theory. The same dependence is obtained by Burluka and Borghi (2000) for the flame above a liquid fuel in the infinitely fast chemistry limit. The results from the simulations presented here are interesting, since they show that the heat release rate is approximately proportional to  $\epsilon_s^{1/2}$  at low strain rates, where the flame is far from the surface but that the tendency is towards  $\epsilon_s^{1/3}$  at high strain rates, where the flame is close to the surface. When the reaction expression is altered to make the flame thinner, as in figure 4.7, the dependence on  $\epsilon_s^{1/2}$  is retained over a wider range of strain rates. Thus it seems that, when the ratio of flame stand-off distance ( $L_c$ ) to flame thickness is small, the classical relationship between reaction rate and strain rate is altered.

The numerical values of the heat release rate found here are very similar to those obtained by Schreiber (1991), although his study did not extend to extinction. The heat release increases with strain rate up to the point of extinction because the species and temperature gradients become steeper, leading to faster mass diffusion to the flame. As the inlet hydrogen temperature decreases, the heat release per unit area increases. This is due to the higher density, which is a consequence of the lower flame temperature at a given strain rate.

The flame stand-off distance is defined here as the distance from the oxygen surface to the point of maximum temperature. It is shown as a function of strain rate in figure





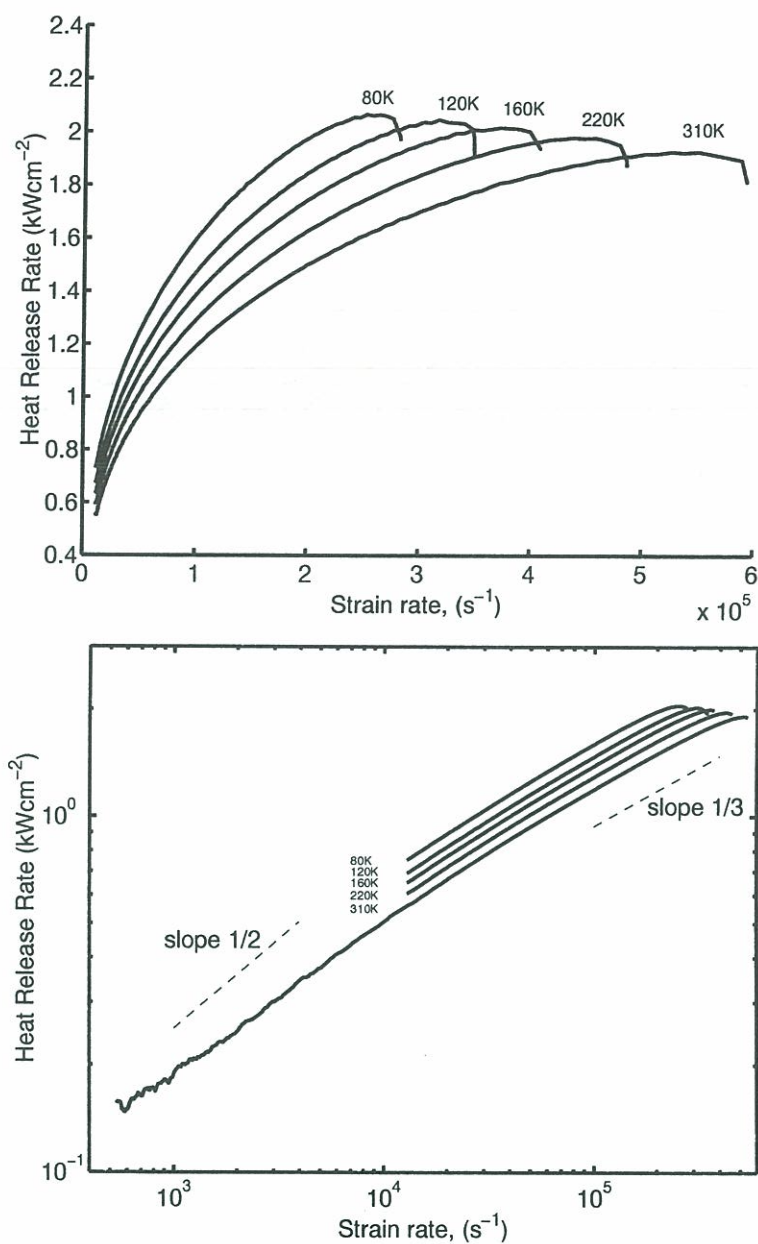
**Figure 4.5:** *Maximum flame temperature as a function of strain rate for a counterflow hydrogen flame above a condensed oxygen surface. The inlet hydrogen temperatures are shown next to each curve.*

4.8. This distance is proportional to  $\epsilon_s^{-1/2}$ , which agrees with the results of Burluka and Borghi (2000).

#### 4.4.3 Effect of inlet hydrogen temperature on extinction strain rate

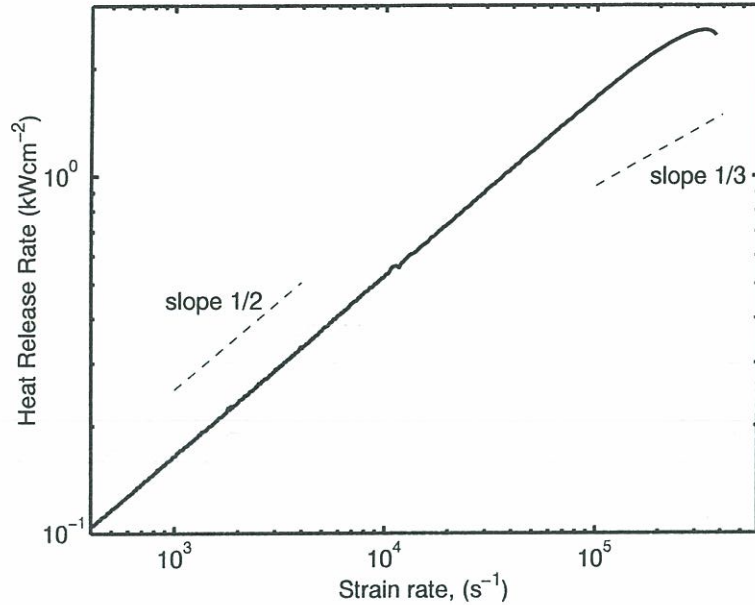
Having verified the results of the numerical code, the extinction strain rate can be plotted as a function of inlet hydrogen temperature. The solid line in figure 4.9 represents conditions under which the thermodynamic and transport data have been verified for all species. The dotted line represents the results at lower inlet hydrogen temperatures. The correlations for the thermodynamic and transport data have been checked in this temperature range only for pure hydrogen. At the outer edge of the convection/diffusion zone other species are present below 80 K in very small concentrations. The transport correlations for these species are reasonable in this range and, although they are not strictly valid, the error is likely to be minimal.

In any case, it is apparent that the extinction strain rates are far in excess of those expected in the turbulent jet flames formed by a coaxial injector in a typical rocket motor. For instance, if a hydrogen jet at  $100 \text{ ms}^{-1}$  impinged perpendicularly onto the oxygen surface and came to a stagnation point within 1 mm, the strain rate, at  $\epsilon_s = 10^5 \text{ s}^{-1}$ , would still not be sufficient to extinguish the flame. Real conditions are less severe than this.



**Figure 4.6:** Heat release rate as a function of strain rate for a counterflow hydrogen flame above a condensed oxygen surface. The inlet hydrogen temperatures are shown next to each curve. At low strain rates, the heat release rate increases as  $\epsilon_s^{1/2}$  in line with calculations in the infinitely-fast chemistry limit. When the flame thickness is of the same order as the flame stand-off distance, the slope becomes nearer to  $\epsilon_s^{1/3}$ .





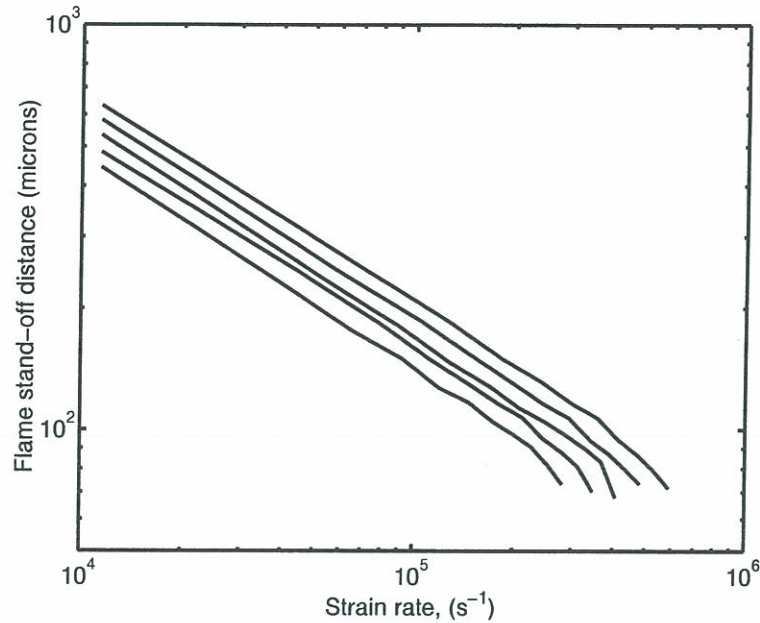
**Figure 4.7:** Heat release rate as a function of strain rate for a flame above a liquid surface. Complex chemistry is replaced with a single step reaction and the parameters are chosen to give a thin flame with a similar value of heat release. The heat release rate increases as  $\epsilon_s^{1/2}$  in line with calculations in the infinitely-fast chemistry limit.

#### 4.4.4 Effect of a temperature gradient in the liquid oxygen

Heat conduction into the liquid oxygen core only affects the flame when it is of the same order of magnitude or greater than the vaporization heat flux. The simulations show that the latter is greater than  $10^5 \text{ Wm}^{-2}$  for strain rates above  $10^4 \text{ s}^{-1}$ . Given that the thermal conductivity of liquid oxygen is  $\lambda = 0.16 \text{ Wm}^{-1}\text{K}^{-1}$ , a temperature gradient of at least  $10^6 \text{ Km}^{-1}$  is required for the flame to be affected. The oxygen's surface temperature is around 10 K higher than its core temperature. If a linear temperature profile is assumed in the thermal boundary layer at the surface, this layer must be less than  $10 \mu\text{m}$  thick to affect the flame. This is confirmed in figure 4.10, where the maximum flame temperature is shown as a function of thermal boundary layer thickness at a strain rate of  $1.4 \times 10^4 \text{ s}^{-1}$ . The flame is only affected when the layer is less than  $10 \mu\text{m}$  thick and extinguishes when it is  $0.5 \mu\text{m}$  thick. A layer this thin will not last for any appreciable distance beyond the injection plane. Therefore it is valid to neglect heat conduction into the liquid oxygen.

#### 4.4.5 Effect of pressure

The effect of pressure on strained laminar diffusion flames is studied via an asymptotic analysis in appendix D, assuming infinitely fast chemistry, equal diffusivities,  $\rho^2 \mathcal{D}$  independent of temperature and  $\mathcal{D} \propto p^{-1}$ . The analysis indicates that the heat release is proportional to  $(\epsilon_s p)^{1/2}$ . The fact that the heat release rate increases with pressure while the thermal conductivity remains approximately constant suggests that the extinction



**Figure 4.8:** *Flame stand-off distance as a function of strain rate for a hydrogen flame above a condensed oxygen surface. It is proportional to  $\epsilon_s^{-1/2}$ , in line with predictions in the infinitely fast chemistry limit. The inlet hydrogen temperature is shown next to each curve.*

strain rate will also increase with pressure. This is consistent with the experimental results of Niioka et al. (1991) who found that it increased to a maximum between 3 and 10 bar for a heptane/air flame.

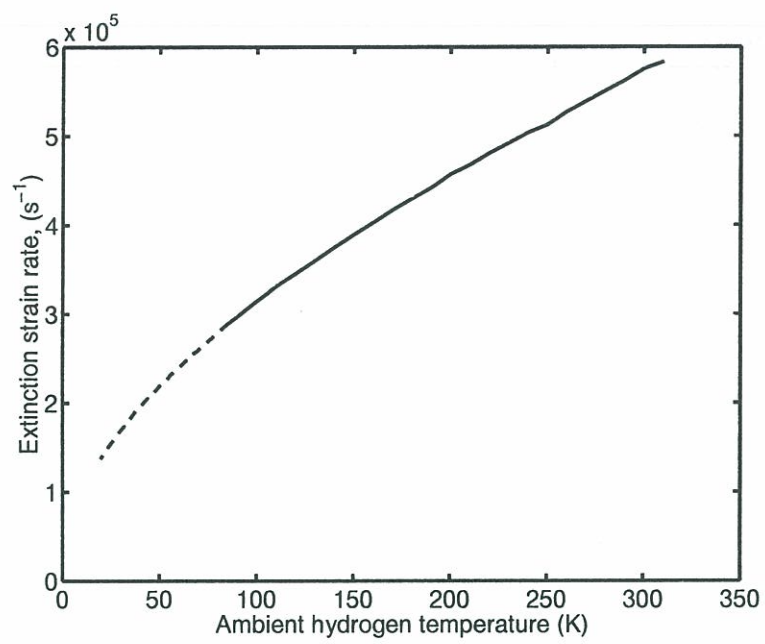
The 1-D simulations were repeated at 2 bar to check this effect. The flame is thinner and is slightly closer to the condensed surface at a given strain rate. Figure 4.11 shows the heat release rate as a function of strain rate. In accordance with the asymptotic analysis, the heat release increases (although in proportion to  $\epsilon_s^{1/2} p^{4/5}$ ) and can withstand higher strain rates before extinction.

## 4.5 Conclusions

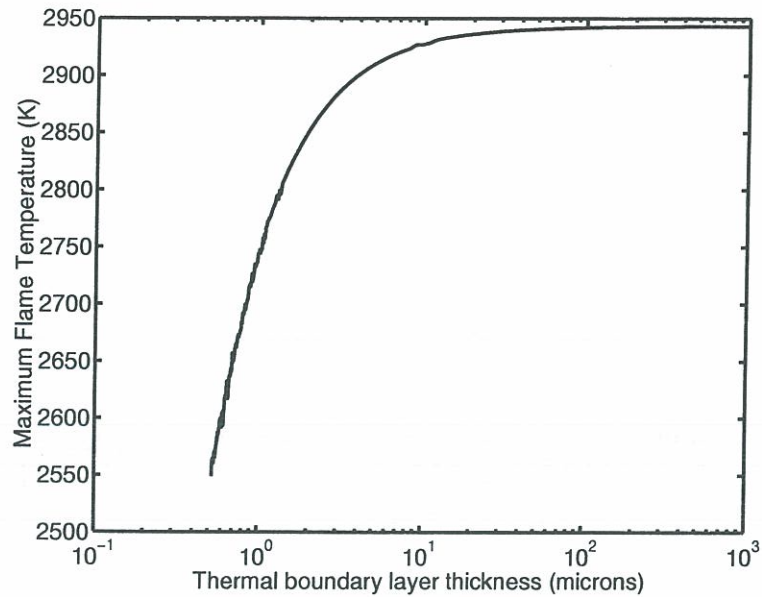
A counterflow diffusion flame between a hydrogen stream and a surface of condensed oxygen has been studied at 1 and 2 bar pressure using a one-dimensional numerical code. Temperature and composition profiles are similar to those found in gaseous diffusion flames with the exception of the temperature profile at the surface, where a gradient is required to evaporate the oxygen. The flame structures are also in qualitative agreement with those of Burluka and Borghi (2000) who studied this configuration with infinitely-fast chemistry and did not determine the extinction strain rate. The present calculations provide numerical values for the rate of heat release per unit flame surface, the flame stand-off distance, the extinction strain rates and extinction temperatures.

The extinction strain rate decreases as the ambient hydrogen temperature decreases

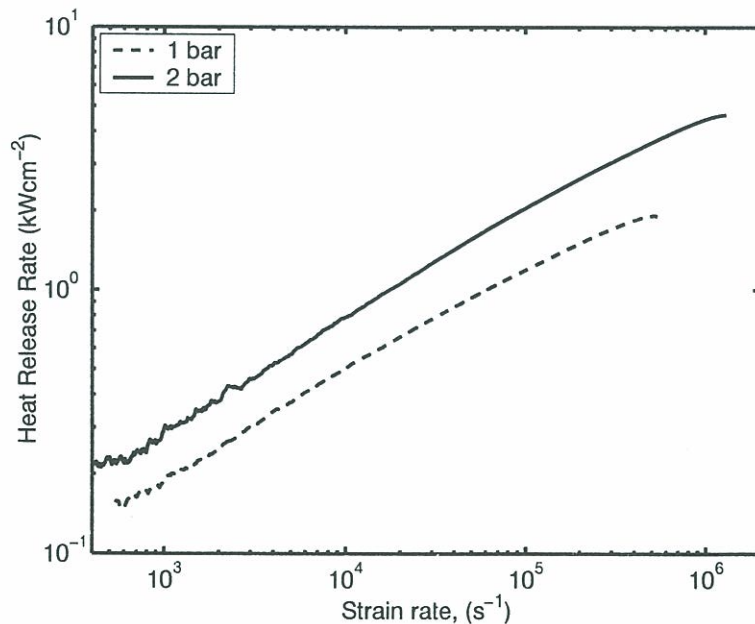




**Figure 4.9:** *Extinction strain rate plotted as a function of inlet hydrogen temperature. The solid line represents the region in which thermodynamic and transport properties have been verified. The dotted line represents the region in which only hydrogen properties have been verified.*



**Figure 4.10:** Maximum flame temperature as a function of thermal boundary layer thickness at the condensed oxygen surface. The temperature drop across the layer is 10 K and the profile is assumed to be linear. The strain rate is  $1.4 \times 10^4 \text{ s}^{-1}$ . It can be seen that the thermal layer needs to be unrealistically thin before it can have an effect on the flame.



**Figure 4.11:** Heat release rate per unit area as a function of strain rate for a hydrogen flame above a condensed oxygen surface at 1 bar and 2 bar pressure. The extinction strain rate increases by a factor of 2. The inlet hydrogen temperature is 310 K.



but it remains extremely high. It is an order of magnitude greater than the highest strain rates found in jet flames formed by typical rocket motor injectors. In addition, the extinction strain rate increases with pressure. This means that if a flame edge exists in the wake of the oxygen injector lip, the subsequent diffusion flame cannot be extinguished downstream. This reduces the question of flame stabilization to a study of the zone behind the lip, which is approached via a 2-D numerical calculation in chapter 8.

Heat conduction into the liquid oxygen is negligible compared with the heat flux required to vaporize it. This suggests that the temperature of the oxygen jet is not a critical factor and is confirmed in chapter 7 when a similar problem in two dimensions is considered.

Around and above the critical pressure of oxygen, the oxygen surface boundary condition of this one-dimensional model is no longer valid. In this case a light gas/dense gas situation must be modelled and the existence of a liquid surface resolved by a well-chosen equation of state.

With confirmation that extinction by strain is not possible, infinitely fast chemistry can be used reliably in analytical calculations. For example, Emmons (1956) makes this assumption in order to model the flame in a boundary layer above a liquid fuel. The basic steps of his classical article are summarized in chapter 7. The result of Emmons is also used in chapter 3 to estimate the rate of oxygen evaporation within the recessed injector. Emmons assumes laminar flow. The turbulent case is considered by Jones et al. (1971). These references would be a useful starting point for an analysis of the flame just downstream of the LOx post wake.





## Chapter 5

# Selection of a suitable $\text{H}_2/\text{O}_2$ reaction mechanism

Les simulations numériques multidimensionnelles qui sont envisagées dans le cadre de ce projet de recherche nécessitent l'utilisation d'un schéma réactionnel réduit. Les coefficients de transport doivent aussi être modélisés d'une façon simple. Cette réduction est réalisée dans ce chapitre. L'analyse effectuée ici n'est pas strictement nécessaire et on aurait pu prendre une représentation arbitraire de la cinétique. Cependant, il est intéressant de choisir d'une façon logique les coefficients du schéma réduit pour que les simulations du chapitre 8 puissent conduire à une structure de flamme proche de celle formée par le couple d'ergols hydrogène et oxygène.

## Nomenclature

$B$	Pre-exponential factor
$c_p$	Specific heat capacity
$D$	Mass diffusivity
$k$	Reaction rate
$Pr$	Prandlt number
$q$	Heat release per mass of fuel burnt
$\dot{q}_s$	Heat release per unit flame surface
$s_e$	Edge flame velocity
$s_L$	Premixed laminar flame velocity
$Sc$	Schmidt number
$T_a$	Activation temperature
$T_b$	Burnt gas temperature
$T_u$	Unburnt gas temperature
$T_{in}$	Inlet gas temperature
$Y$	Mass fraction
$\dot{W}$	Molar rate of reaction
$[\cdot]$	Concentration in moles per m <sup>3</sup>
$\delta_g$	Gradient flame thickness (equation 5.6)
$\delta_r$	Reaction flame thickness (equation 5.7)
$\epsilon_s$	Strain rate
$\lambda$	Thermal conductivity
$\mu$	viscosity
$\rho_b$	Burnt gas density
$\rho_u$	Unburnt gas density
$\tau_c$	Chemical time
$\tau_i$	Ignition time



## 5.1 Introduction

In stable operation of a liquid oxygen/gaseous hydrogen coaxial injector, the base of the flame is situated just behind the lip of the oxygen injector. In chapter 8 this zone is examined in detail via a 2-D numerical simulation. A complete numerical study with complex chemistry under supercritical conditions has already been performed by Oefelein (1997). This demonstrates the structure of the flame in this region but only six operating conditions could be studied since each took several weeks on a supercomputer. In the study presented here, several hundred simulations are performed and the entry conditions are changed incrementally. This is intended to outline the parameters most affecting flame stabilization. For this to be practical, the calculation time must be a matter of hours. A numerical holding effect has been observed by Deshpande et al. (1997) on coarse grids demonstrating that the grid size must be small in order to ensure that the attachment mechanism is physical. This leads to the decision to use simplified reaction kinetics, thermodynamics and transport models.

The numerical platform chosen for the 2D calculations is Fluent 5.1. The standard reaction and transport models are replaced with those developed in this chapter. In addition, specific boundary conditions have been derived in order to represent the condensed phase surface. This combined software package will be designated FSP<sub>n</sub> (Fluent Stabilization Package, version n). Modelling requirements are specified in section 5.2. Methods for fulfilling those requirements are discussed in section 5.3. The development of a simplified model is pursued in sections 5.4 and 5.5.

## 5.2 Modelling Requirements

A perfect match cannot be obtained between simple and complex reaction/transport models. It is necessary to match certain factors by assuming a flame holding mechanism *a priori*. Two mechanisms seem likely:

- A balance between a flow velocity and the flame edge velocity,  $s_e$ , which is generally proportional to the premixed laminar flame speed:  $s_e = s_l \sqrt{(\rho_u/\rho_b)}$
- A balance between a residence time and the ignition time. Ignition can be dominated by either thermal runaway or free radical runaway.

Since the flame is stabilized in a slow-moving zone behind the lip of the oxygen injector, a balance between a residence time and an ignition time would seem to be most pertinent. The important factors to match are the ignition time, the heat release, and - perhaps less so - the maximum temperature of the flame. However, it is important to check that the premixed laminar flame speed is not considerably different from the true value. Another factor which will be found to be of great importance is the thickness of the flame relative to the width of the wake in which it is stabilized.



## 5.3 Approaches to simple reaction and transport models

### 5.3.1 Flame prolongation of ILDM

The Intrinsic Low Dimensional Manifold (ILDM) relies on a clever analysis of the characteristic time scales of the chemical system. Multi-species chemistry may be described by evaluating the chemical composition as a function of a few tracer species. One species,  $\text{H}_2\text{O}$  for example, indicates the extent of reaction. Another, an inert tracer for example, indicates the extent of diffusion. This method loses information about non-equilibrium effects and must be complemented to account for the low temperature regions.

It is possible to take into account low temperature regions in stable flames with the flame prolongation method described by Gicquel (1999). This has been implemented in the numerical platform chosen for the 2D calculations. This combination might seem to be perfectly adapted to the stabilization problem, enabling complex chemistry to be taken into account at low computational cost. However, the current version can only be applied to flows with constant enthalpy. This is because there is no transport equation for the temperature field, which is calculated from the species fields. Heat loss is fundamental to the situation we wish to simulate and could play an important role in destabilizing the flame. Indeed, the condition at the surface of the condensed oxygen cannot be taken to be adiabatic since a temperature gradient next to it is required to supply the energy for vaporization. The ILDM method, which cannot yet cope with a heat loss, is inappropriate to this situation.

### 5.3.2 The global reaction concept

The classical method of modelling chemical reactions is via a global one step reaction between the major species. In pre-mixed flames, the pre-exponential factor and activation energy can be evaluated by examining the heat release through the flame, using temperature as the abscissa. The parameters are chosen such that the difference between the simple reaction profile and the complex chemistry profile is minimized, a method well exemplified by Coffee et al. (1983). This exact procedure does not work for non-premixed flames because the temperature profile is not monotonic, although a different abscissa could probably be found. The approach taken here is similar. The parameters of the simple chemistry are evaluated by comparing the result with the flame above a liquid reactant in chapter 4, which was calculated using complex chemistry.

The reduction to simple chemistry and transport is presented here in two stages. In section 5.4, the chemistry is reduced, retaining complex transport. The calculation time may be reduced by this method, while retaining the particularly high diffusivity of molecular hydrogen. This may be a convenient approximation for future calculations, but is not taken further in this research project. In section 5.5, the transport correlations are simplified. The Lewis and Prandtl numbers are taken to be unity, which removes the peculiarity of hydrogen. The results can only be qualitative but it is hoped that they will provide insight into the flame holding mechanisms.

The reduction of chemistry to a single step reaction is in the present context a gross simplification. It is known that radicals play a central role in the ignition processes. All chemical reactions that consume molecular hydrogen in the  $\text{H}_2/\text{O}_2$  system produce atomic hydrogen which is an extremely reactive and diffusive species. This is the most impor-



tant radical for flame propagation and ignition in virtually all combustion systems. In numerical studies, Deshpande et al. (1997) found that adding small amounts of elemental hydrogen to a  $H_2/O_2$  mixture dramatically reduced its ignition time. This suggests that radical runaway, rather than thermal runaway, could be responsible. Unfortunately, it is impossible to model the hydrogen atom with a global reaction mechanism and simple transport. Consequently, one of two assumptions must be made: (1) The flame holding mechanism is mainly thermal or (2) Some or all of the factors affecting a thermal mechanism will also affect the radical mechanism.

## 5.4 Reduction to a global reaction model with complex thermodynamics and transport

### 5.4.1 Analytical correlations for flame properties

The computational time may be reduced by simplifying the reaction models while retaining complex thermodynamic and transport models. Differential diffusion effects are retained in this framework. Two numerical tools are available to help determine the simple chemistry. With the first, one can calculate ignition delay times in a constant pressure well-stirred reactor model. The other is the 1-D strained flame model introduced in chapter 4. Analytically-derived expressions can be used as a guide. For premixed ignition at constant pressure and premixed flame propagation:

$$\tau_i \propto \frac{c_p}{qB} f(T_a, T_b, T_u) \quad (5.1)$$

$$s_l \propto \sqrt{BD} f(T_a, T_b, T_u) \quad (5.2)$$

$$T_b - T_u = (Y_{Fu} - Y_{Fb}) q / c_p \quad (5.3)$$

$$T_{fl} \propto q / c_p \quad (5.4)$$

and for non-premixed flame strained flames:

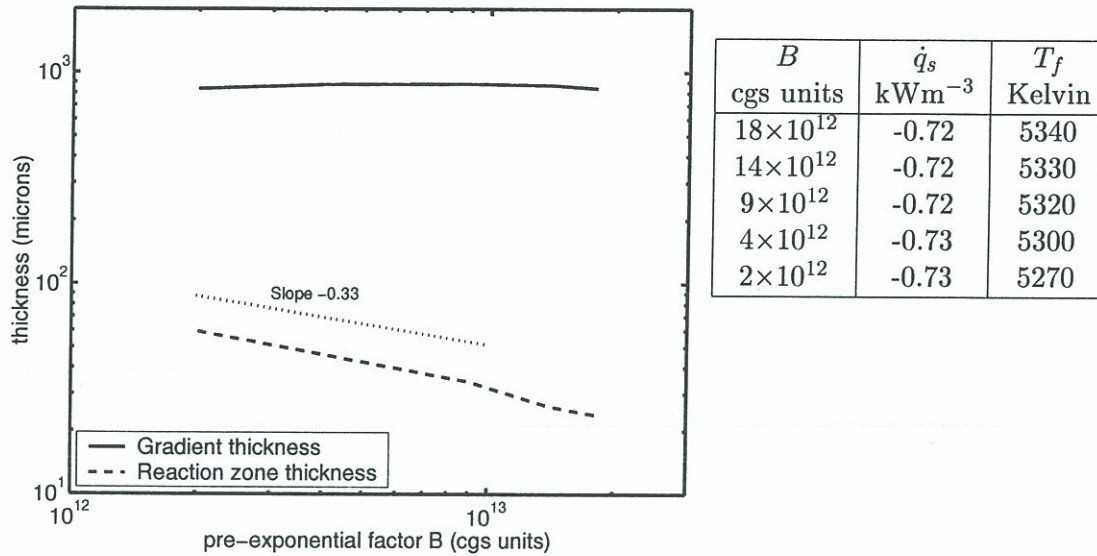
$$\dot{q}_s \propto \sqrt{\mathcal{D}\epsilon_s} q \quad (5.5)$$

where  $\tau_i$  is the ignition time,  $s_l$  is the laminar flame speed,  $\dot{q}_s$  is the heat release rate per unit flame surface ( $J s^{-1} m^{-2}$ ),  $q$  is the heat release per unit mass of fuel ( $J kg^{-1}$ ),  $T_a$  is the activation energy,  $B$  is the pre-exponential factor and  $\mathcal{D}$  is the diffusivity. Given that the diffusivity shall not be changed, this leaves four factors to match by altering four parameters:  $T_a$ ,  $B$ ,  $q$ ,  $c_p$ .

The effect of these parameters on the flame thickness can also be estimated analytically. There are two lengthscales associated with the diffusion flame.

- $\delta_g$ , the “gradient thickness”, which is dominated by a convection/diffusion balance. Here, this is measured as the width at half maximum height of the temperature profile.

$$\delta_g \sim (\mathcal{D}/\epsilon_s)^{1/2} \quad (5.6)$$



**Figure 5.1:** The effect of changing the pre-exponential factor  $B$  in a counter-flow diffusion flame above a condensed fuel. Single step chemistry is assumed:  $k = B[H_2][O_2]^{1/2} \exp(-17614/T)$ . The strain rate is  $\epsilon_s = 11400\text{s}^{-1}$ . The heat release per unit surface  $\dot{q}_s$ , maximum temperature  $T_f$  and gradient thickness  $\delta_g$  are unchanged. The reaction thickness  $\delta_r$  changes in proportional to  $B^{-1/3}$ .

- $\delta_r$ , the “reaction zone thickness”, which is dominated by a reaction/diffusion balance. This is measured as the width at half maximum height of the heat release profile. The reaction zone thickness is a function of both the strain rate and the characteristic chemical time:

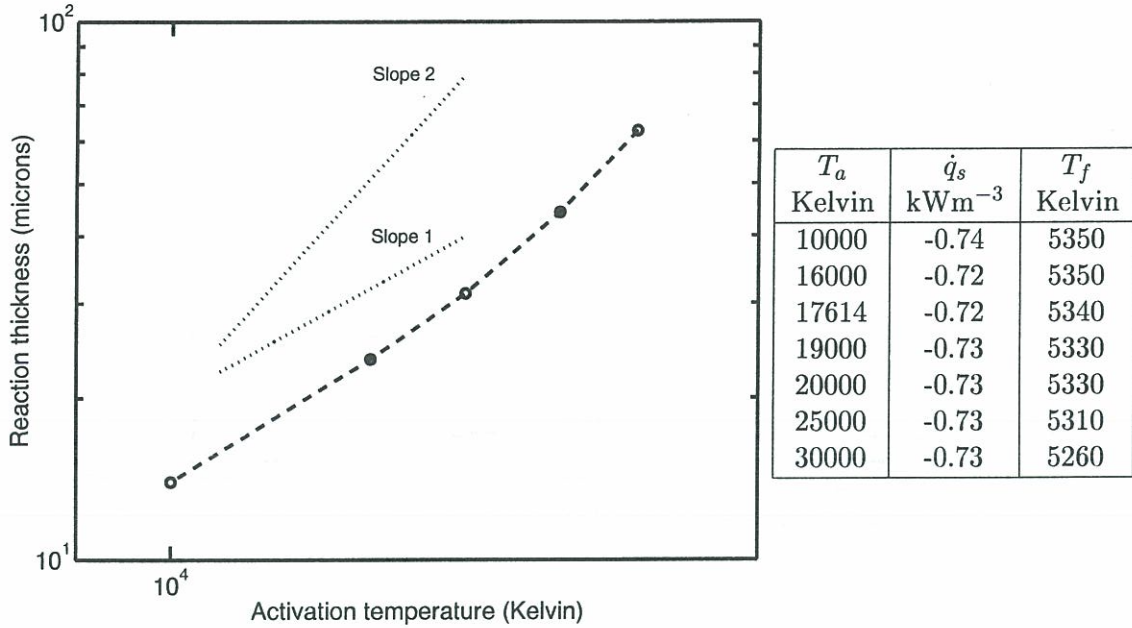
$$\delta_r \sim \delta_g (\tau_c \epsilon_s)^{1/3} \quad (5.7)$$

As a check, the 1D code is used to show that  $B$  and  $T_a$  do not have a significant effect on  $\dot{q}_s$ ,  $T_f$  or  $\delta_g$ . They do, however, affect the reaction zone thickness  $\delta_r$  by changing the chemical time  $\tau_c$ . In figure 5.1 it can be seen that  $\delta_r$  is proportional to  $B^{-1/3}$ , as would be expected from equations (5.1) and (5.7), if one assumes that the characteristic time  $\tau_c \sim \tau_i$ . In figure 5.2 it can be seen that  $\delta_r$  increases with  $T_a$ . This is expected since the chemical time  $\tau_i$  increases as the activation temperature increases ( $\tau_i \sim \exp\{T_a/T_u\}$ ). Finally, the effect of the strain rate on the flame thicknesses is presented in figure 5.3. The gradient thickness is proportional to  $\epsilon_s^{-1/2}$ , as expected from equation (5.6). The reaction zone thickness is proportional to  $\epsilon_s^{-1/10}$ , which is similar to the dependence predicted by equations (5.6) and (5.7), which predict  $\delta_r \propto \epsilon_s^{-1/6}$ .

#### 5.4.2 Procedure for reduction to a global reaction model

The objective of the following analysis is to develop a global reaction model which will preserve the main features of strained diffusion flames. It is interesting to examine first the global model defined by Zitoun and Deshaies (1997) from experimental measurements





**Figure 5.2:** The effect of changing the activation temperature  $T_a$  in a counter-flow diffusion flame above a condensed fuel. Single step chemistry is assumed:  $k = 18 \times 10^{12} [H_2][O_2]^{1/2} \exp(-T_a/T)$ . The strain rate is  $\epsilon_s = 11400 \text{s}^{-1}$ . The heat release per unit surface  $\dot{q}_s$ , maximum temperature  $T_f$  and gradient thickness  $\delta_g$  are unchanged. The reaction thickness  $\delta_r$  increases with  $T_a$ .

of the burning velocities of rich  $H_2/O_2$  flames under cryogenic conditions. These authors conclude that an activation temperature of 11560 K is consistent with the experimental results if the flame is represented by a global single step reaction:



The reaction rate may be cast in the form:

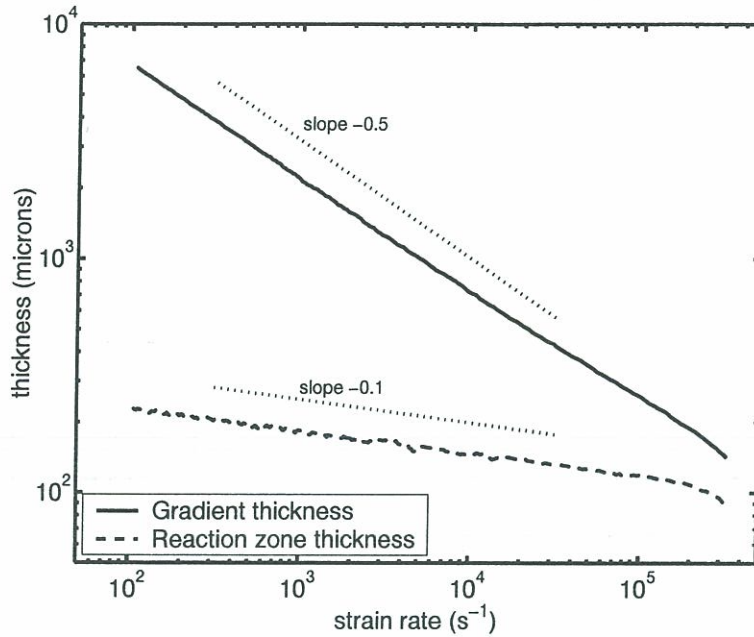
$$k = B[H_2][O_2]^{1/2} \exp(-T_a/T)$$

and the molar rates of reaction are given by:

$$\dot{W}_{H_2} = -k; \quad \dot{W}_{O_2} = -k/2; \quad \dot{W}_{H_2O} = k$$

This expression was derived by varying the equivalence ratio at fixed initial temperature and then by varying the initial temperature at fixed equivalence ratio. The laminar flame speed varies from  $1 \text{ms}^{-1}$  (at equivalence ratio of 5 and initial temperature 120K) to  $12 \text{ms}^{-1}$  (at equivalence ratio of 1 and initial temperature 300K).

This activation energy is introduced into the 1-D code with accurate transport and thermodynamic properties. Initially,  $B$  is arbitrarily chosen at  $3.5 \times 10^{10}$  (in cgs units). A strain rate of  $11400 \text{s}^{-1}$  is chosen since it is typical of strain rates found near the base of the injector. The heat release  $q$  has to be adjusted so that the heat release per unit



**Figure 5.3:** *The effect of strain rate on the gradient thickness  $\delta_g$  and the reaction zone thickness  $\delta_r$  in a counterflow diffusion flame above a condensed fuel. Single step chemistry is assumed:  $k = 7 \times 10^{12}[H_2][O_2]^{1/2} \exp(-11560/T)$ . These tendencies follow the analytical predictions reasonably well.*

flame area matches the value obtained for the complex chemistry flame at this strain rate:  $\dot{q}_s = -0.53 \text{ kWm}^{-3}$ . It is known that  $\dot{q}_s$  is a function of  $q$  only. The results obtained with the single step reaction are shown in figure 5.4.

With  $q$  at 50% of its actual value,  $\dot{q}_s$  is reasonable but  $T_f$  is too high. The difference is reduced by multiplying  $c_p$  of each species by 2.25. The last remaining factor to match is the ignition time, which is evaluated with the 0-D code as the pre-exponential factor is changed. The final result, which gives correct  $T_f$ ,  $\dot{q}_s$  and  $\tau_i$  is:

$$k = 12 \times 10^{10}[H_2][O_2]^{1/2} \exp(-11560/T)$$

$q$  at 0.50 times the values in the CHEMKIN database

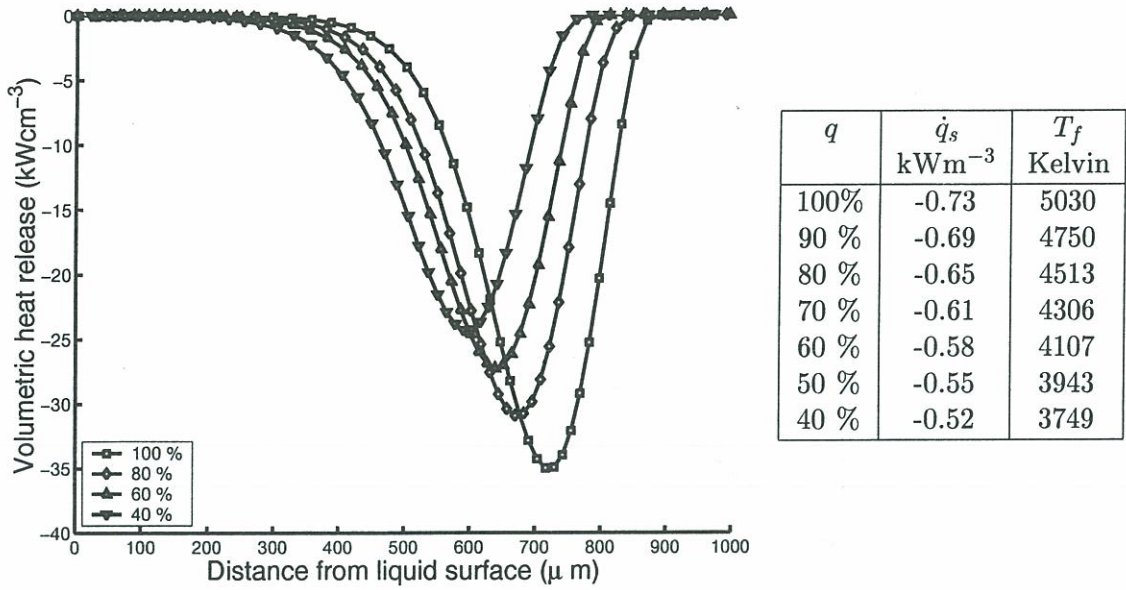
$c_p$  at 2.25 times the values in the CHEMKIN database

This scheme is compared, in figure 5.5, with the results using complex chemistry. The heat release shows good agreement over a wide range of strain rates.

## 5.5 Reduction to simple transport and thermodynamic properties

The objective now is to derive a simple model for kinetics, thermodynamics and transport. The simplest transport expressions have constant  $c_p$ ,  $\lambda$ ,  $\mu$  and  $\mathcal{D}$ . A conventional choice





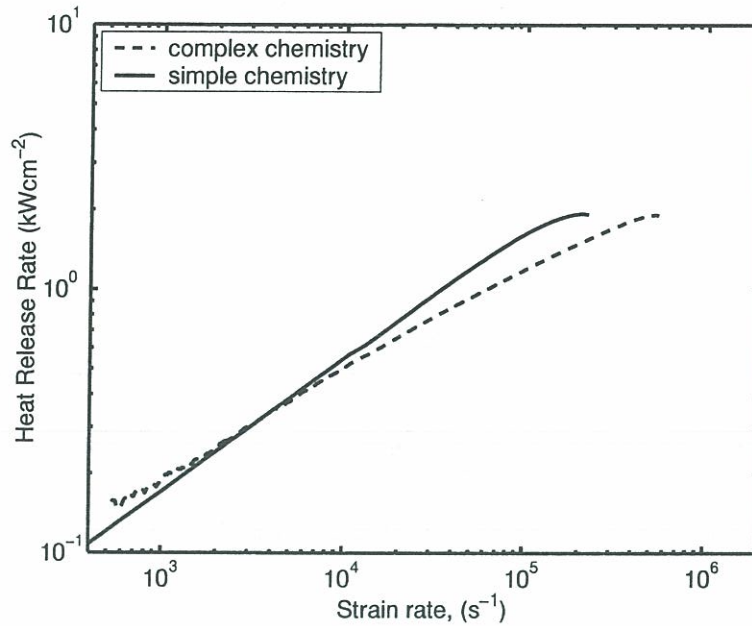
**Figure 5.4:** Volumetric heat release profile for a counterflow diffusion flame above a condensed fuel at strain rate  $\epsilon_s = 11400\text{s}^{-1}$ . Single step chemistry is assumed:  $k = 3.5 \times 10^{10}[\text{H}_2][\text{O}_2]^{1/2} \exp(-11560/T)$ . The heat release per kg,  $q$ , is expressed as a percentage of the actual value for hydrogen/oxygen combustion. This has only a very small effect on the reaction thickness  $\delta_r$ , and no effect on the gradient thickness.

for these values is to add 2/3 of the value at the liquid surface to 1/3 of the value in the ambient gas. This, however, leads to an unrealistically large value of  $\lambda$  at the oxygen surface. This is influential since it determines the vaporization rate of oxygen and therefore the entry velocity of this species to the domain. A simple alternative is to use power law expressions for  $\lambda$ ,  $\mu$  and  $\mathcal{D}$ . If  $c_p$  is constant, these can be chosen to give constant Lewis, Schmidt and Prandtl numbers. If  $c_p$  is not constant then no simple alternative exists and the full complex transport polynomials must be used.

The specific heat capacity is chosen to be 2/3 of the heat capacity of oxygen at 90K plus 1/3 of the heat capacity of hydrogen at 300K. This gives  $c_p = 5348 \text{ Jkg}^{-1}\text{K}^{-1}$ . Following Mahalingam et al. (1999), the viscosity is taken to be  $\mu = 1.5449 \times 10^{-7} \times T^{0.76} \text{ Nsm}^{-2}$ . Assuming that  $\text{Pr} = 1$ , this gives  $\lambda = 8.2621 \times 10^{-4} \times T^{0.76} \text{ Wm}^{-1}\text{K}^{-1}$ . Assuming that  $\text{Sc} = 1$ , this gives  $\mathcal{D} = 2.409 \times 10^{-9} \times T^{1.76} \text{ m}^2\text{s}^{-1}$ . These values are shown between 0 and 3000K in figure 5.6, next to the actual values for pure  $\text{H}_2$  and  $\text{O}_2$ . The trends with temperature are modelled reasonably well.

Ideally, these values of  $c_p$ ,  $\lambda$ ,  $\mu$  and  $\mathcal{D}$  would be tested in the 1-D code to examine the differences in flame structure. However, because time was too short, this approach was abandoned in favour of examining these quantities with the 2-D code. The 0-D well stirred reactor model was used to obtain  $q$  and  $B$  which give the correct ignition time and adiabatic flame temperature for the value assigned to  $c_p$ . The end result in cgs units is :

$$k = 8.0 \times 10^{10}[\text{H}_2][\text{O}_2]^{1/2} \exp(-11560/T)$$



**Figure 5.5:** Heat release rate as a function of strain rate for a hydrogen flame above condensed oxygen. The dotted line corresponds to a complex reaction mechanism and the solid line corresponds to the simplified reaction mechanism introduced in this chapter. The surface heat release rate shows good agreement over a wide range of strain rates.

$$q \text{ at } 0.75 \text{ times the actual value for pure H}_2 \text{ and O}_2$$

$$c_p = 5.348 \text{ Jkg}^{-1}\text{K}^{-1}$$

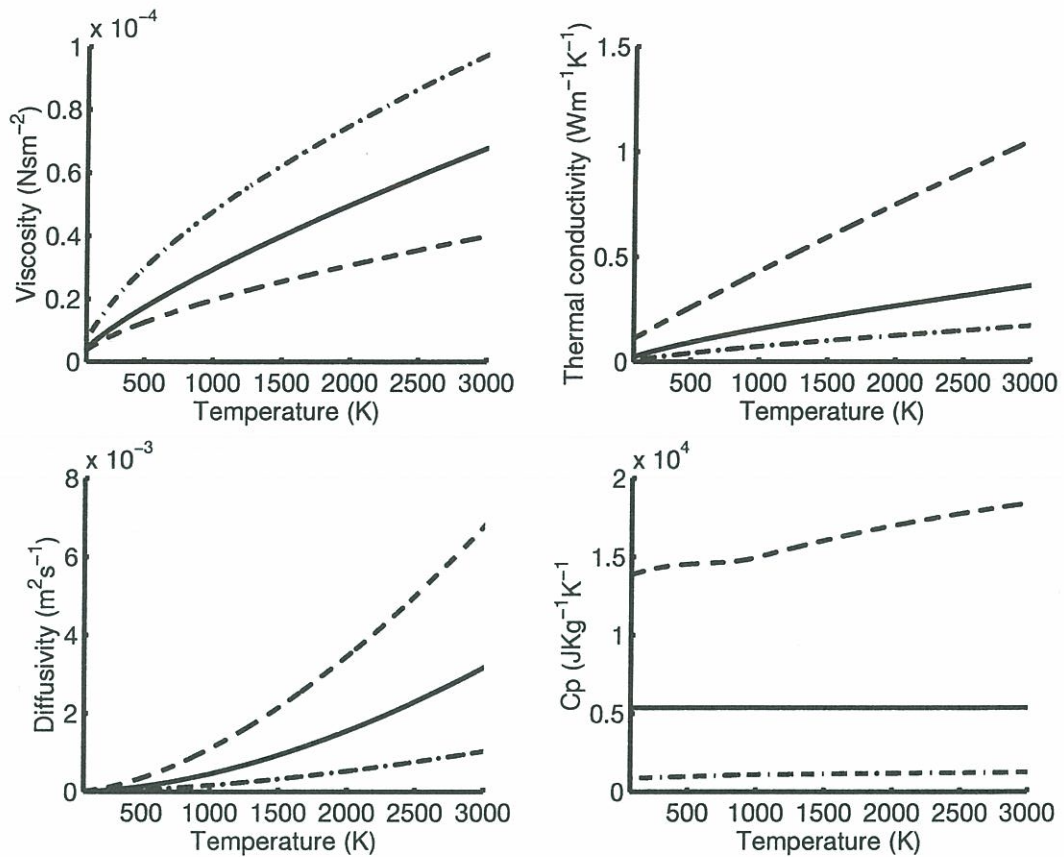
This must be converted to  $\text{kmol/m}^3$  for inclusion in the 2D code. This gives:

$$k = 2.53 \times 10^9 [\text{H}_2][\text{O}_2]^{1/2} \exp(-9.61 \times 10^7 / RT)$$

$$q = 0.75 \times (-241.8) \text{ kJ/mol} = -1.8135 \times 10^8 \text{ J/kmol}$$

A counterflow  $\text{H}_2/\text{O}_2$  flame was simulated with the 2-D code FSP<sub>1</sub> and the results compared with those obtained from complex chemistry. This is shown in table 5.1. The results show good agreement for the value  $T_f - T_{in}$  and agree to within 40% for the heat release per unit surface. A higher value of  $c_p$  and a higher value of  $q$  could rectify this. However, this was considered sufficiently accurate for the 2-D calculations, which are in any case intended only to provide qualitative information. The gradient thickness, measured as the half width of the temperature profile, shows reasonable agreement. The reaction thickness does not, but this is to be expected since FSP<sub>1</sub> uses a single step reaction whereas the 1-D code has multiple reactions.





**Figure 5.6:** Simplified expressions for transport properties of the mixture (solid lines) compared with transport properties for pure hydrogen (dashed lines) and pure oxygen (dot-dashed lines). These properties are chosen in accordance with two criteria: (1)  $Le = Pr = Sc = 1$ . (2) coefficient  $\approx 2/3$  ( $\text{O}_2$ ) +  $1/3$  ( $\text{H}_2$ ).

## 5.6 Conclusions

In this chapter a simple reaction and transport scheme has been developed in order to resemble a hydrogen/oxygen diffusion flame. This has been tested on the 2-D numerical platform used in chapter 8 and is found to be in reasonable agreement with the complex chemistry simulations performed in chapter 4. While this link is not essential to the conclusions of this research project, it does ensure that the results of chapter 8 resemble results which would be expected from hydrogen/oxygen flames.

$\epsilon_s$ ( $s^{-1}$ )	2-D code						1-D code					
	$T_{H_2}$	$T_{O_2}$	$T_f$	$\dot{q}_s$	$\delta_r$	$\delta_g$	$T_{H_2}$	$T_{O_2}$	$T_f$	$\dot{q}_s$	$\delta_r$	$\delta_g$
	Kelvin			$kWcm^{-2}$	$\mu m$	$\mu m$	Kelvin			$kWcm^{-2}$	$\mu m$	$\mu m$
356	700	700	3370	-0.094	266	4200	310	90	3042	-0.150	1390	6490
580	700	700	3580	-0.105	267	3530	310	90	3042	-0.155	1300	5120
721	700	700	3491	-0.118	258	3521	310	90	3041	-0.166	1250	4560
1137	700	700	3483	-0.129	251	3502	310	90	3041	-0.200	1130	3610
1269	700	700	3514	-0.139	256	3360	310	90	3040	-0.208	1060	3410
1380	700	700	3539	-0.148	255	3210	310	90	3040	-0.214	1010	3280

**Table 5.1:** Comparison of maximum temperature and heat release per unit surface for a counterflow hydrogen/oxygen flame. Left: the 2-D code with a global reaction model and simple thermodynamic and transport correlations. Right: the 1-D code with complex chemistry.



## Chapter 6

# Corner flames

L'écoulement correspondant à l'accrochage d'une flamme derrière une marche au dessus d'un combustible condensé est difficile à aborder sur un plan théorique. Le problème peut être traité numériquement, comme on va le voir (chapitre 8). Il est utile au préalable d'aborder des problèmes géométriquement plus simples et de dégager les nombres sans dimensions qui contrôlent la stabilisation de la flamme. Les résultats obtenus pourront ensuite être appliqués sur un plan plus général et ils faciliteront l'interprétation des calculs. Trois nombres importants sans dimensions seront introduits successivement.

Dans ce chapitre, la marche et la surface de réactif condensé sont remplacées par des conditions plus simples pour que l'on puisse considérer le premier nombre sans dimension: un nombre de Damköhler. La configuration est celle d'une flamme dans un coin, alimentée par des réactifs qui confluent à  $90^\circ$  l'un de l'autre. Une expression pour la position d'accrochage de la flamme, aussi adimensionnée, est trouvée en fonction du nombre de Damköhler. Une méthode numérique est utilisée car c'est l'approche choisie pour les chapitres suivants. L'approche théorique du problème est apparue récemment, au cours de la rédaction de ce mémoire.

## Nomenclature

$A$	Velocity gradient
$B$	Pre-exponential factor in Arrhenius reaction expression
$c_p$	Constant pressure heat capacity
$c_v$	Constant volume heat capacity
$Da$	Damköhler number
$Da_1$	Damköhler number based on strain rate
$Da_2$	Damköhler number based on convection
$k$	Reaction rate
$l_N$	Characteristic shear length scale
$L_c$	Flame stand-off distance
$L_{ref}$	Reference length based on flame thickness, $\delta_f$
$q$	Heat release per mass of fuel burnt
$s_L$	Premixed laminar flame speed
$T_a$	Activation temperature
$T_f$	Adiabatic flame temperature
$T_{in}$	Inlet temperature
$T_2$	Inlet temperature of hot stream
$U$	Velocity
$U_N$	Characteristic velocity scale
$U_2$	Velocity of hot stream
$Y$	Mass fraction
$\dot{w}_F$	Molar reaction rate (Fuel)
$\dot{w}_T$	Thermal reaction rate
$W$	Molar mass
$\alpha$	Heat release parameter $\equiv (T_f - T_{in})/T_f$
$\beta$	Zeldovich number $\equiv T_a(T_f - T_{in})/T_f^2$
$\delta_f$	Flame thickness
$\eta_i$	Non-dimensional axis variable used in Blasius decomposition
$\nu$	Kinematic viscosity
$\lambda$	Thermal conductivity
$\mathcal{D}$	Mass diffusivity
$\rho$	Density
$\Pi$	Ratio of flame stand-off distance to flame thickness
$\tau_c$	Chemical time
$\tau_i$	Ignition time



## 6.1 Introduction

This chapter contains a first step towards resolving the problem of extinction in the zone behind the oxygen injector lip. Two features of the full configuration are removed: the oxygen injector lip and the liquid reactant. This reduces the configuration to a corner flame, which is a model problem recently introduced to the field of combustion.

Corner flames are formed when the edge of a diffusion flame propagates into a localized pre-mixed region between two reactants which approach at  $90^\circ$ . This is similar to an edge flame, although here the reactant streams are initially parallel. Edge flames have been studied in some detail and a brief review is presented in section 6.2. This analysis is extended to corner flames in sections 6.3 to 6.6. A numerical approach is used to determine the parameters affecting the flame stand-off distance of a corner flame in two situations: (1) When the strain rate dominates. (2) When convection processes dominate.

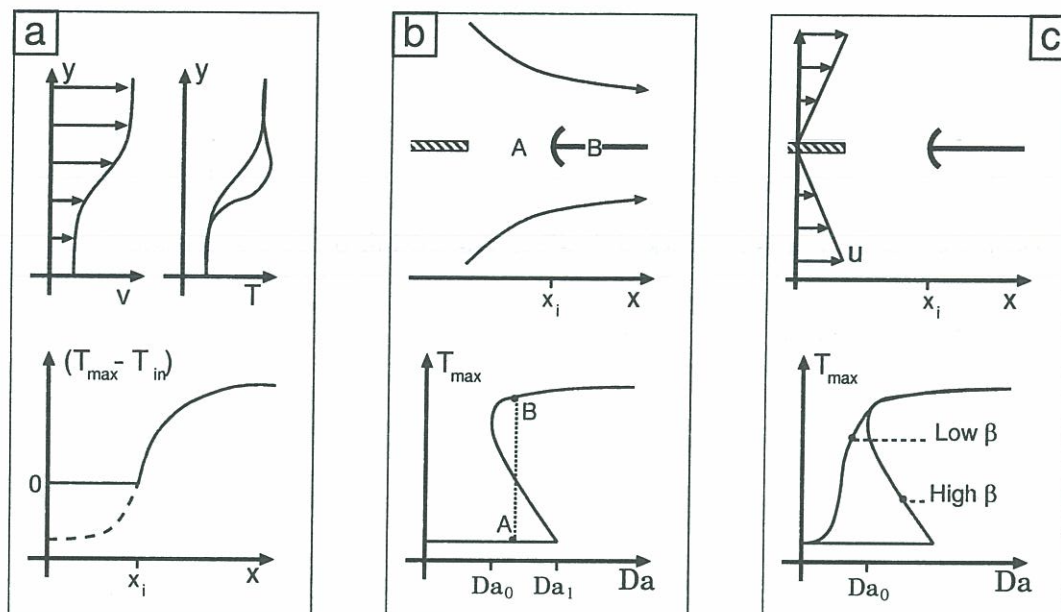
## 6.2 Edge flames

An extensive review of edge flames, comprising experimental, analytical and numerical approaches, can be found in Takahashi et al. (1998). Analytical models require great simplification because the flow is complicated. Examples of such an approach can be found in the early analysis of Marble and Adamson (1954) and in more recent studies such as those of Buckmaster and Weber (1996), Buckmaster (1997) and Buckmaster and Jackson (2000). The presence of a splitter plate leads to even greater complexity and has been tackled by Higuera and Liñán (1996). A useful numerical approach is given in Fernández et al. (2000). Experimental results by Takahashi et al. (1998) indicate that the flame stand-off distance,  $L_c$ , is a strong function of the velocities of the two reactant streams. If there is a reasonably high degree of pre-mixing, a triple flame forms. When there is less pre-mixing in front of the flame, the triple flame loses its lean and rich arms to become a reaction kernel. In the kernel, the reaction rate is significantly greater than that characterizing the diffusion flame which trails behind it. When there is very little pre-mixing, for example where preheated reactants meet behind a heated splitter plate, a diffusion flame forms instantly and there is no discernable edge. In this section we shall review this work on edge flames, particularly with regard to the stand-off distance and non-dimensional parameters.

In a classical article, Marble and Adamson (1954) study ignition in a laminar mixing zone between premixed reactants and a stream of hot gases at different temperatures, using analytical methods derived for the study of boundary layers. They pose two questions which remain central to future work:

1. Do the reactants ignite?
2. How far downstream of the splitter plate does ignition occur?

These authors calculate the development of the temperature profile across the mixing layer. They judge ignition to have occurred when the maximum temperature has exceeded the inlet temperature of the hotter stream. This is shown in figure 6.1a. Their analysis gives a self-similar result - i.e. there is a single solution which is valid over all length scales. This means that, in their model, the reactants always ignite, although the distance over



- (a) Marble and Adamson (1954) study a laminar mixing layer between two reactants. They consider that ignition occurs when the temperature in the mixing layer first exceeds the inlet temperature of the hotter reactant. This model predicts a smooth transition from cold flow to flame in all situations.
- (b) Buckmaster (1996) studies the flow behind a splitter plate in uniformly accelerating flow. Ignition is regarded as corresponding to a sudden jump from state A to state B on the S-shaped diagram.
- (c) Fernández and Liñan (2000) study the third configuration, which is found to exhibit either smooth transition or a sudden jump to combusting flow depending on a Zeldovich number:  $\beta = T_a/T_f$ . Smooth transition corresponds to the S-shaped curve which does not double back on itself.

**Figure 6.1 :** Three approaches to the modelling of ignition in edge flames:



which this occurs can be extremely large. The analytical expression which they derive for the flame stand-off distance is complicated. It can be re-arranged in the following form:

$$L_c = \eta_i^2 U_2 \tau_c \exp \left\{ \frac{T_a}{T_2} \right\} \{ \mathcal{O}(1) \} \quad (6.1)$$

In their notation,  $\eta$  is a non-dimensional axis variable used in the Blasius-like decomposition and its value at ignition,  $\eta_i$ , is approximately constant.  $T_a$  is an activation temperature, the subscript '2' refers to the hot stream and  $\tau_c$  is a chemical time, equivalent to the inverse of the pre-exponential factor. This leads to an approximate expression, which we shall return to later :

$$\frac{L_c}{U_2 \tau_c} \propto \exp \left\{ \frac{T_a}{T_2} \right\} \quad (6.2)$$

The non-dimensional parameter governing  $L_c$  is a strong function of the temperature of the hotter reactant. This feature is also found for ignition times in counterflow diffusion flames formed between hot and cold reactant streams, Thévenin and Candel (1994).

Buckmaster and Weber (1996) examine a similar problem somewhat differently. Conditions prevailing in steady diffusion flames can be characterized by a Damköhler number, as shown in the S-shaped curve in figure 6.1b. This behaviour is seen very clearly in one-dimensional counterflow diffusion flames, as shown in (Darabiha 1992). Solutions along the bottom branch correspond to premixing with negligible reaction. Solutions along the top branch correspond to a thin and highly exothermic flame. The central part corresponds to unstable solutions which are never seen in practice. These authors envisage an edge flame as the transition of a flow from a solution at point A on the bottom branch to a solution at point B on the top branch. This transition occurs at a point in space which can move upstream or downstream, depending on inlet conditions.

Note that this approach is physically distinct from that of Marble and Adamson (1954). In their model there is a continuously increasing reaction rate along the interface between the two reactants. A single solution is obtained, which means that if the results are presented in terms of a Damköhler number, the response will not take the form of an S-shaped curve.

The model presented by Buckmaster and Weber (1996) contains 2-D features, as shown in figure 6.1b. The edge flame is situated in an accelerating flow ( $u = Ax$ ) and loses heat by diffusion on both sides. By crudely modelling this latter feature the flow is reduced to 1-D form. There are no solutions for  $Da < Da_0$ , two solutions for  $Da_0 < Da < Da_1$  and one solution for  $Da > Da_1$ . Thus this model accounts for the top and middle branches of the S-shaped curve. Only the extinct solution can exist below  $Da_0$ , so the reactants cannot ignite under these conditions.

The edge flame directly behind an infinitely thin splitter plate is considered by Fernández et al. (2000), figure 6.1c. Boundary layers are modelled by imposing the velocity profile  $u = A|y|$ , where  $y$  is the vertical distance from the plate. Molecular mixing in this thin region creates a small volume of combustible mixture which sustains a pre-mixed flame propagating against the flow. Characteristic dimensions are chosen to reflect the role played by molecular transport. The velocity gradient  $A$ , where  $u = Ay$  gives the characteristic time scale  $1/A$ . The shear length scale is given by  $l_N = (D/A)^{1/2}$  and the velocity scale by  $u_N = (DA)^{1/2}$ . It is found that the Damköhler number  $Da = s_L/u_N$  is influential



in determining the structure of the flow. Here,  $s_L$  is the laminar burning velocity. It is also suggested that the wall thickness relative to  $l_N$  will be influential but this aspect is not pursued.

These authors also define a Zeldovich number:  $\beta \equiv T_a(T_f - T_{in})/T_f^2$ . This approximates to  $\beta = T_a/T_f$  which is a measure of the activation energy relative to the adiabatic flame temperature. Very often the Zeldovich number is defined as  $Ze = T_a(T_f - T_{in})/T_{in}^2$ , taking values much larger than  $\beta$ . At  $\beta > 10$  they discover that three solutions exist above a critical value of  $Da$ :

- The frozen solution
- The unstable solution
- The strong flame solution.

This is exactly the development described by Buckmaster and Weber (1996) relating to the S-shaped curve in figure 6.1b. The flame edge is close to the splitter plate for high values of  $Da$  but blows off suddenly below  $Da_0$ . On the other hand, at  $\beta < 10$ , a single solution exists. In other words the S-shaped curve no longer doubles back on itself and the behaviour described by the model of Marble and Adamson (1954) is recovered. In this case, a flame kernel forms which moves smoothly away from the splitter plate as the Damköhler number decreases. It eventually becomes a triple flame because the premixed region forming in front of the flame becomes large compared with the diffusion flame thickness.

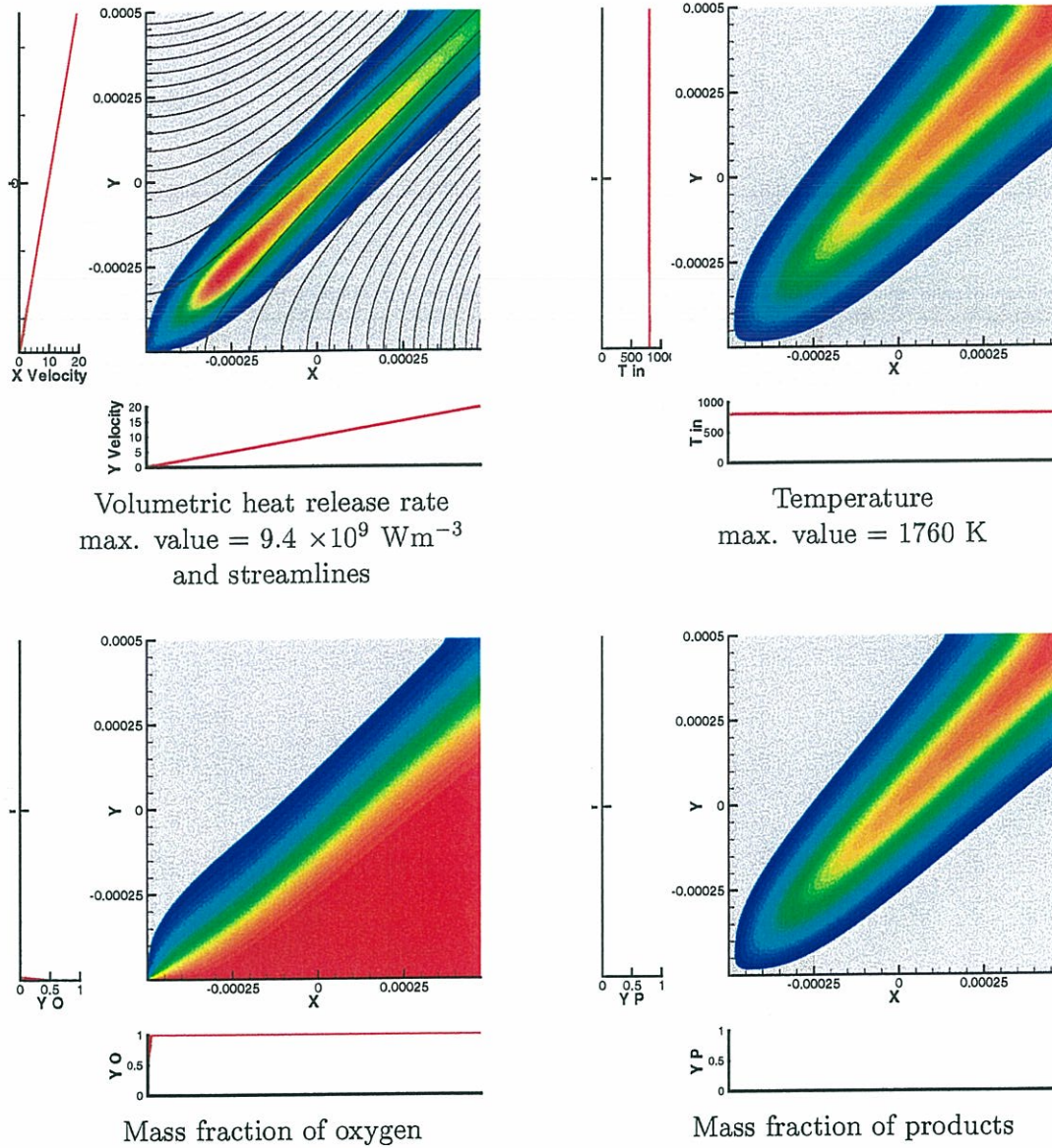
In multi-species reaction mechanisms a single activation energy is not suitable. Nevertheless, in the single step reaction mechanism for  $H_2/O_2$  developed in chapter 5 the value of  $\beta$  is 3.9. Consequently in the rest of this research project we shall restrict the study uniquely to the low Zeldovich number range, where flame stand-off distance increases smoothly as the Damköhler number decreases.

It must be added that the results of Fernández et al. (2000) were obtained mainly in the thermodiffusive limit, where modification of the flow field by heat release is ignored. Mahalingam et al. (1999) and Hirano and Kinoshita (1975) maintain that this modification must be taken into account in order to determine the flame holding mechanism. In simulations outside the thermodiffusive limit, Fernández et al. (2000) found that  $Da_0$  decreases as the heat release parameter is increased. This parameter is given by  $\alpha = (T_f - T_{in})/T_f$ . This demonstrates the destabilizing nature of thermal expansion within the reaction kernel and concurs with the findings of Mahalingam et al. (1999). Unfortunately, it seems that the numerical simulations were performed at a single value of  $u_N$  or  $s_L$ , meaning that  $Da$  defined as the ratio of these two quantities is not necessarily the only parameter controlling the flame position.

### 6.3 Corner flames - Introduction

Corner flames can be formed when one reactant is blown through a porous plate into a cross-flowing stream of another reactant. This situation is similar to the flame stationed in a convecting stream above a vaporizing fuel, a classical problem in combustion theory - see Williams (1985). Conventional approaches to this problem, such as that developed by





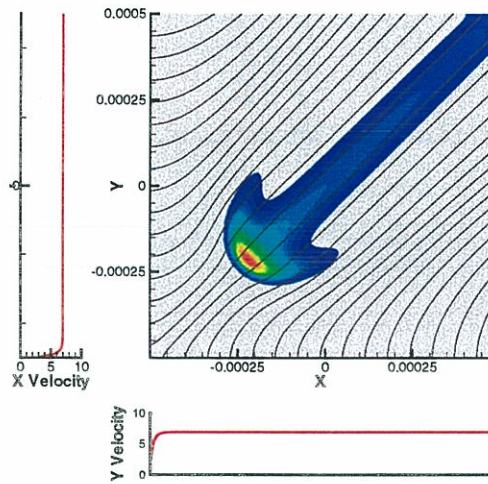
Volumetric heat release rate  
max. value =  $9.4 \times 10^9 \text{ Wm}^{-3}$   
and streamlines

Temperature  
max. value = 1760 K

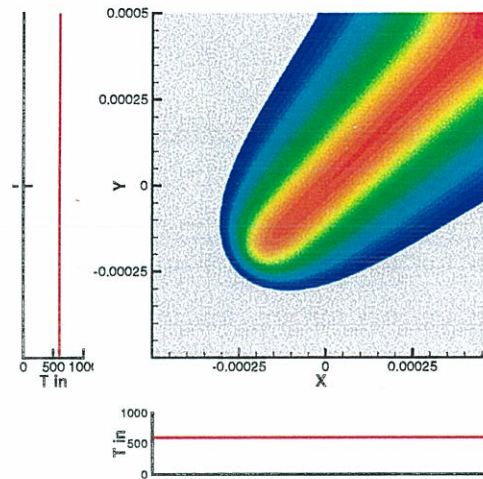
Mass fraction of oxygen

Mass fraction of products

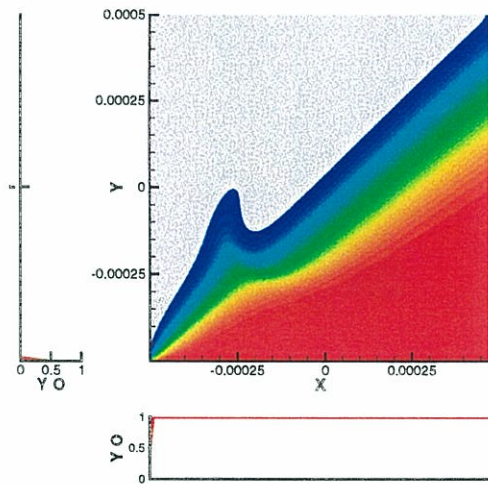
**Figure 6.2:** Strain rate-controlled diffusion flame in a corner. Oxidiser enters from the bottom, fuel from the left. Inlet profiles are shown next to the main field. The inlet velocity profiles follow  $u = Ay$  and  $v = Ax$ . The inlet temperature (900 K) is high enough for the reactants to react on contact. The grid was refined in the corner to check that flame-holding was not numerical.



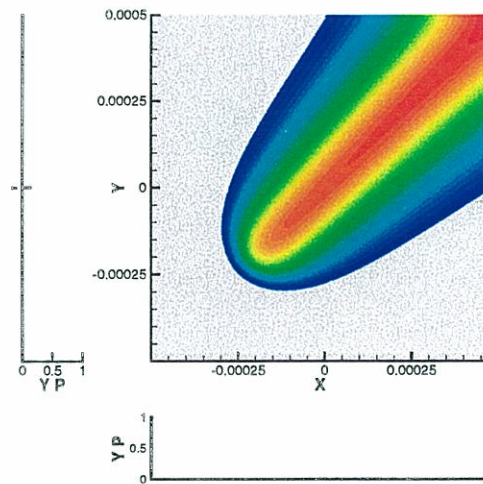
Volumetric heat release rate  
max. value =  $1.4 \times 10^{11} \text{ Wm}^{-3}$   
and streamlines



Temperature  
max. value = 3022 K



Mass fraction of oxygen



Mass fraction of products

**Figure 6.3:** Convection-controlled diffusion flame in a corner. Oxidiser enters from the bottom, fuel from the left. Inlet profiles are shown next to the main field. The inlet temperature is 600 K.



Emmons (1956), cannot model the flame tip. Interest in this small region led Mahalingam et al. (1999) to study the situation where two reactants approach each other at  $90^\circ$ . The resulting flame is similar in many respects to the edge flame formed between two initially parallel flows.

In this chapter we examine two types of corner flames: strain rate-controlled and convection-controlled. The aim is to determine expressions for the flame stand-off distances  $L_c$  in the low activation energy range where the flame does not lift off suddenly.

- In the strain rate-controlled situation, velocity profiles at entry to the domain are of the form  $u = Ay$ ;  $v = Ax$ , where  $A$  is the strain rate. Inlet temperatures are chosen such that the flame is stabilized in the corner. This situation might be encountered when the boundary layer thickness at entry is large compared with the flame thickness and stand-off distance. This configuration is shown in figure 6.2 and the corresponding results are deduced from the numerical platform explained in section 6.5.
- In the convection-controlled situation, velocity profiles at entry are flat (with the exception of a small region at the corner where hyperbolic tangent profiles ensure smooth convergence of the two flows). The entry speed is designated as  $U$ . This situation might be encountered when the boundary layer is thin compared with the flame thickness and stand-off distance. This configuration is shown in figure 6.3 and the results are taken from the numerical platform explained in section 6.5.

The studies of Buckmaster and Weber (1996) and Fernández et al. (2000) suggest that the flow can be described by a single Damköhler number.

## 6.4 Corner flames - Dimensional analysis

It is useful at this point to use dimensional arguments and derive Damköhler numbers which could be used to characterize the flame anchoring process. Two approaches can be taken to determine Damköhler numbers: One based on characteristic times, the other based on characteristic velocities. We show here that these techniques are equivalent. In this analysis, the Lewis and Prandtl numbers are assumed to be constant, which means that the mass diffusivity  $\mathcal{D}$  also describes thermal transfer ( $\alpha = \lambda/\rho c_p$ ) and kinematic viscosity ( $\nu = \mu/\rho$ ).

### 6.4.1 Damköhler number based on characteristic times

There are several ways to define a characteristic chemical time:  $\tau_c$ . The processes which we wish to investigate in this chapter concern a balance between flow processes and ignition. This leads us to choose the ignition time of a well stirred mixture:

$$\tau_i = \frac{T_{in}}{T_a} \frac{c_v T_{in}}{q B \rho} \left( \frac{W_F W_O}{Y_F Y_O} \right) \exp \left\{ \frac{T_a}{T_{in}} \right\} \quad (6.3)$$

Given the complexity of this expression, we leave it as  $\tau_c$  and note that it is both proportional to the inverse pre-exponential factor  $B^{-1}$  and is a complicated function of  $T_a/T_{in}$ , which is dominated by the exponential term. A characteristic chemical time

pertaining to for instance, the width of a steady flame, would have a similar dependence on  $B$  but would not have this dependence on  $T_{in}$ . A characteristic time of the strain rate is simply  $A^{-1}$ . This leads to a strain rate Damköhler number:

$$\text{Da}_1 = A^{-1/2} \tau_c^{-1/2} \quad (6.4)$$

where exponents of  $1/2$  are used in order to aid comparison with future results.

A characteristic convection time is given by  $L_{ref} U^{-1}$ . The only characteristic length which is independent of the velocity field is given by the flame itself, which has thickness  $\delta_f \sim \tau_c^{1/2} \mathcal{D}^{1/2}$ . This leads to a convection Damköhler number:

$$\text{Da}_2 = L_{ref} U^{-1} \tau_c^{-1} = \mathcal{D}^{1/2} U^{-1} \tau_c^{-1/2}. \quad (6.5)$$

### 6.4.2 Damköhler number based on characteristic velocities

The characteristic velocity of the flame can be given by the laminar flame speed  $s_L$ . A velocity characteristic of molecular diffusion processes dependent on the strain rate is given by  $\mathcal{D}^{1/2} A^{1/2}$ . This leads to a strain rate Damköhler number identical to that used by Fernández et al. (2000).

$$\text{Da}_3 = s_L \mathcal{D}^{-1/2} A^{-1/2} \quad (6.6)$$

The convection Damköhler number is given simply by:

$$\text{Da}_4 = s_L U^{-1} \quad (6.7)$$

The laminar flame speed is related to the diffusivity and the chemical time by:  $s_L \sim \mathcal{D}^{1/2} \tau_c^{-1/2}$ . On substitution into expressions (6.6) and (6.7),  $\text{Da}_3$  and  $\text{Da}_4$  reduce to  $\text{Da}_1$  and  $\text{Da}_2$ .

### 6.4.3 Other dimensionless parameters

If the physical behaviour of a system is independent of scale then the number of independent controlling parameters is somewhat less than the number of dimensional variables used to describe the situation. Evidently, these controlling parameters must also be independent of scale.

A strain rate-controlled flame can be described by four dimensional variables:  $L_c$ ,  $\mathcal{D}$ ,  $\tau_c$  and  $A$ . As shown in equation (6.3), several further variables are encapsulated within the chemical time. These variables are constructed from two dimensions (length and time), which means that  $4 - 2 = 2$  dimensionless parameters are required to describe the situation. One of these is the Damköhler number. The other can be taken to be  $\Pi$ , the ratio of the flame stand-off distance to the flame thickness. This parameter has the advantage that it can be used for both the strain rate-controlled flame and the convection-controlled flame:

$$\text{Da}_1 \equiv A^{-1/2} \tau_c^{-1/2} = f_s(\Pi)$$

which may also be written as:

$$\Pi \equiv L_c \tau_c^{-1/2} \mathcal{D}^{-1/2} = g_s(\text{Da}_1) \quad (6.8)$$



A convection-controlled flame can also be described by four dimensional variables:  $L_c$ ,  $\mathcal{D}$ ,  $\tau_c$  and  $U$ . This leads to two similar dimensionless parameters:

$$\text{Da}_2 \equiv \mathcal{D}^{1/2} U^{-1} \tau_c^{-1/2} = f_c(\Pi)$$

which is equivalent to the relation:

$$\Pi \equiv L_c \tau_c^{-1/2} \mathcal{D}^{-1/2} = g_c(\text{Da}_2) \quad (6.9)$$

The relationships  $g_s$  and  $g_c$  between the non-dimensional parameters have yet to be determined. This can be achieved experimentally, numerically or by theoretical arguments.

Systematic numerical simulations are carried out in this chapter on corner flame configurations over a wide range of  $\mathcal{D}$ ,  $\tau_c$  and  $A$  or  $U$ . By determining the scale-invariant relationship between  $\Pi$  and  $\text{Da}_1$  or  $\text{Da}_2$  we can obtain an expression for the stand-off distance. In a further step, which is not included in this research project, a physical justification for this relationship could be proposed.

## 6.5 Numerical study of a corner flame

### 6.5.1 Introduction

In this section, a numerical platform is developed to study corner flames. Any form of entry velocity profile can be used. In chapters 7 and 8 this feature will be employed to model evaporation from a condensed surface. In section 6.5.2 the new platform is validated against results existing in the literature. Then two types of corner flames are explored: (1) the strain rate-controlled flame and (2) the convection controlled flame introduced in figures 6.2 and 6.3. The relationship between the previously introduced dimensionless parameters is investigated by performing several hundred simulations. One end result is a numerically-validated expression for the stand-off distance for both types of flames.

### 6.5.2 Validation of the numerical model

The model problem of a flame in a corner already studied by Mahalingam et al. (1999) is taken as a reference case. Two codes were used by these authors, both with single step chemistry:

- The DNS code NTMIX described in Baum et al. (1994). This code is 6<sup>th</sup> order in space and 3<sup>rd</sup> order in time.
- The TDF code, which is formulated in the thermodiffusive limit, originally developed by Thévenin and Candel (1994).

The TDF code requires considerably less CPU time than the DNS code. However, it cannot simulate modification of the flow by heat release. Comparison with the DNS code, as well as the results of Hirano and Kinoshita (1975) and those of Fernández et al. (2000) suggest that the expansion process is influential in determining flame stabilization. The DNS code can only deal with simple rectangular geometries, uses a uniform mesh and requires a large amount of CPU time to converge to a steady solution because it uses an

NTMIX		
Reaction	$F + sO \rightarrow (1+s)P$	$s = 1$
Reaction rate	$\dot{w}_T$	$B(\rho Y_F)(\rho Y_O) \exp\left(-\frac{T_a}{T}\right)$
Pre-exponential factor	$B$	$1 \times 10^{15} \text{ m}^5 \text{ kg}^{-1} \text{ s}^{-3}$
Activation temperature	$T_a$	8000 K
Heat release (/kg fuel)	$q$	$2.26 \times 10^6 \text{ J kg}^{-1}$
Inlet temperature	$T_{in}$	1200 K
Molar masses	$W_O, W_F, W_P$	not required
Heat capacity	$c_p$	$965.8 \text{ J kg}^{-1} \text{ K}^{-1}$

FSP <sub>2</sub>		
Reaction	$F + sO \rightarrow (1+s)P$	$s = 1$
Molar reaction rate	$-\dot{w}_F = k$	$B[F][O] \exp\left(-\frac{T_a}{T}\right)$
Pre-exponential factor	$B$	$8.85 \times 10^9 \text{ m}^3 \text{ kmol}^{-1} \text{ s}^{-1}$
Activation temperature	$T_a$	8000 K
Heat release (/kmol fuel)	$q$	$q = 4.52 \times 10^7 \text{ J kmol}^{-1}$
Inlet temperature	$T_{in}$	1200 K
Molar masses	$W_O, W_F, W_P$	20 kg kmol <sup>-1</sup>
Heat capacity	$c_p$	$965.8 \text{ J kg}^{-1} \text{ K}^{-1}$

**Table 6.1:** Thermochemical constants and rate expressions for the numerical test case, which is performed on two numerical platforms: NTMIX and FSP<sub>2</sub>

explicit time integration scheme. Because the interest is in steady-state solutions one may use an alternative scheme which is less time consuming. The Navier-Stokes equations are solved with first and second order schemes included in the Fluent package. This solution is developed on an un-structured mesh which can be changed during convergence. This allows finer resolution of steep gradients, a feature which is used in later chapters. The flow solver is optimized for workstations and requires less CPU time to achieve convergence than the thermodiffusive code. The solver in the corner flame configuration, with the flame model defined below is designated FSP<sub>2</sub> (Fluent Solver Package, version 2). FSP<sub>1</sub> was used in chapter 5 to simulate a counterflow diffusion flame.

In order to validate FSP<sub>2</sub> against the DNS results, the test case of Mahalingam et al. (1999) is repeated. NTMIX is a dimensionless code, while FSP<sub>2</sub> is dimensional, so care is required when comparing the two. Thermochemical constants and rate expressions are gathered in table 6.1 for both codes. Oxidizer enters from the bottom boundary and fuel from the left. The flow exits through the top and right boundaries, where a linear term  $\sigma(p - p_a)$  is included in the characteristic condition to force the pressure towards the ambient value ( $\sigma$  is a small parameter). The inlet profiles are given in table 6.2. The domain is square with sides of  $L_{ref} = 0.72 \text{ mm}$  in NTMIX and  $1.0 \text{ mm}$  in FSP<sub>2</sub>. In the test case,  $U = V = 6.94 \text{ ms}^{-1}$  and  $a = 2.78 \times 10^3 \text{ m}^{-1}$ , where  $a$  characterizes the steepness of the hyperbolic tangent velocity profile.

The volumetric heat release rate and temperature fields obtained from both codes are shown in figure 6.4. The contours nearly coincide, although FSP<sub>2</sub> gives a lower volumetric



Bottom boundary			Left boundary		
General expression	$\lim_{ax \rightarrow 0}$	$\lim_{ax \rightarrow \infty}$	General expression	$\lim_{ax \rightarrow 0}$	$\lim_{ax \rightarrow \infty}$
$v = V \tanh(ax)$	$v = (aV)x$	$v = V$	$v = 0$	$v = 0$	$v = 0$
$u = 0$	$u = 0$	$u = 0$	$u = U \tanh(ax)$	$u = (aU)x$	$u = U$
$Y_O = \tanh(ax)$	$Y_O = ax$	$Y_O = 1$	$Y_O = 0$	$Y_O = 0$	$Y_O = 0$
$Y_P = 1 - \tanh(ax)$	$Y_P = 1 - ax$	$Y_P = 0$	$Y_P = 1 - \tanh(ax)$	$Y_P = 1 - ax$	$Y_P = 0$
$Y_F = 0$	$Y_F = 0$	$Y_F = 0$	$Y_F = \tanh(ax)$	$Y_F = ax$	$Y_F = 1$

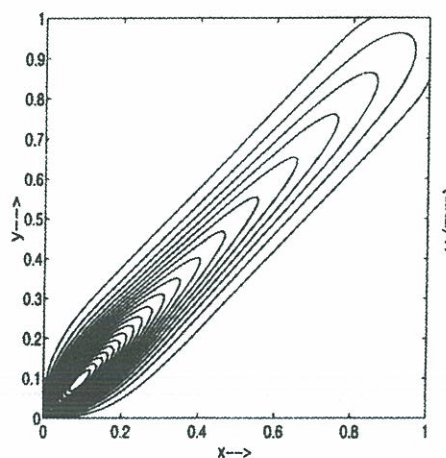
**Table 6.2:** Boundary conditions for the test case of a diffusion flame in a corner. In the limit  $ax \rightarrow 0$  the flame is strain-rate controlled. In the limit  $ax \rightarrow \infty$  the flame is convection-controlled.

heat release rate and lower temperature than NTMIX. There are various possible reasons for the difference:

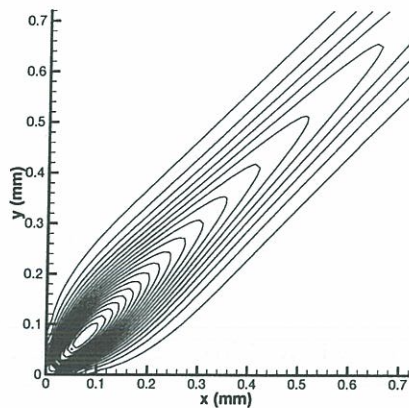
- Numerical diffusion is greater for FSP<sub>2</sub> (1<sup>st</sup> order in space) than for NTMIX (6<sup>th</sup> order in space).
- The thermochemical models do not match exactly.

In addition, both codes force the contour lines to tend towards being normal to the exit boundaries. In figure 6.4 this effect can only be seen in the NTMIX results because only part of the computational domain of the FSP<sub>2</sub> code is shown.

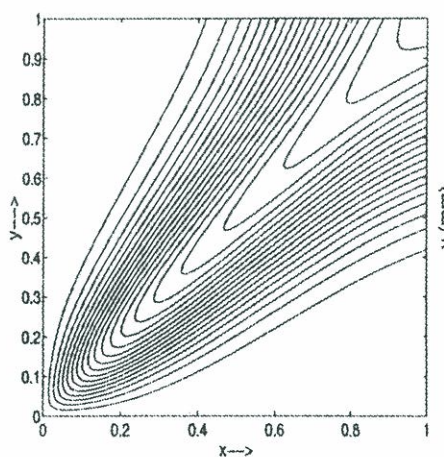
In conclusion, results of FSP<sub>2</sub> are sufficiently close to the results of NTMIX that we can use it with confidence. It solves the full Navier-Stokes equations and can therefore take into account the effect of heat release on the velocity field. The CPU time required is at least an order of magnitude smaller than NTMIX, which makes it well suited for a parametric study.



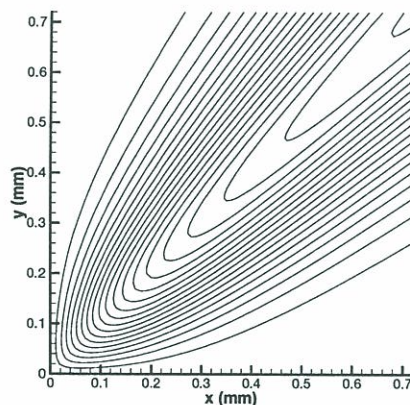
(a) Contours of heat release rate.  
Maximum value  $3.0 \times 10^{10} \text{ J m}^{-3} \text{ s}^{-1}$   
NTMIX,  $L_{ref} = 0.72 \text{ mm}$



(b) Contours of heat release rate.  
Maximum value  $1.5 \times 10^{10} \text{ J m}^{-3} \text{ s}^{-1}$   
calculated with  $\text{FSP}_2$



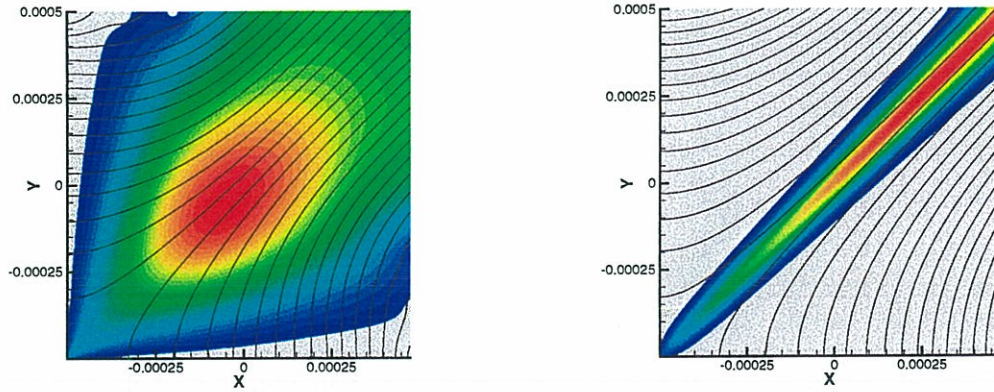
(c) Contours of Temperature. Maximum  
value 2244K  
NTMIX,  $L_{ref} = 0.72 \text{ mm}$



(d) Contours of Temperature. Maximum  
value 2080K  
calculated with  $\text{FSP}_2$

**Figure 6.4:** Contours of volumetric heat release rate,  $\dot{q}_v$ , and temperature,  $T$  for the test case in section 6.5.2. Results of NTMIX, from Mahalingam et al (1999), are given on the left. Results of  $\text{FSP}_2$  are shown on the right.



(a)  $L_c/\delta_f$  limited by size of domain(b)  $L_c/\delta_f$  limited by size of grid

**Figure 6.5:** *The numerical simulations are only valid within a certain range of  $L_c/\delta_f$  due to the size of the grid relative to the domain. This valid range is estimated to correspond to  $100 < \Pi < 10$ . However, the results suggest that the true valid range is closer to  $30 < \Pi < 10$ , probably due to artificially high numerical diffusivity inherent in the numerical platform when the flame spans only a few grid points.*

### 6.5.3 Results - strain rate-controlled corner flame

Entry velocity profiles for the strain rate-controlled flame are shown in figure 6.2 with a typical solution. Species inlet profiles are flat. The domain is otherwise the same as the test case in section 6.5.2. If this flame is scale-invariant, the non-dimensional parameters controlling its shape are (section 6.4):

$$\Pi \equiv L_c \tau_c^{-1/2} \mathcal{D}^{-1/2} = g_s(\text{Da}_1)$$

where

$$\text{Da}_1 \equiv A^{-1/2} \tau_c^{-1/2}$$

The chemical time  $\tau_c$  is proportional to the inverse pre-exponential factor  $1/B$ , which is varied by a factor of 64.  $A$  and  $\mathcal{D}$  are both varied by a factor of 256 in various combinations with  $B$ . The molecular diffusivities  $\lambda$  and  $\nu$  are altered such that  $\text{Le} = \text{Pr} = 1$ . Each of the 130 different simulations provides the flame stand-off distance  $L_c$ , defined as the distance from the corner to the position of highest reaction rate. This is expressed as a multiple of the flame thickness. The relatively coarse grid size ( $100 \times 100$  cells) means that these simulations are only valid over a narrow range of  $L_c/\delta_f$ , which can be estimated as follows: A fat flame close to the corner, such as that in figure 6.5a, is limited by the bottom and left boundaries such that  $L_c/\delta_f(\text{min}) \approx 1$ . On the other hand a thin flame far from the corner, such as that in figure 6.5b, is limited by the grid size:  $L_c/\delta_f(\text{max}) \approx 100/10 = 10$ . This valid range corresponds to  $100 < \Pi < 10$  because for the material properties in use here,  $\tau_c^{1/2} \mathcal{D}^{1/2} \approx 10\delta_f$ .

The results are plotted in figure 6.6 with  $\Pi$  as a function of  $\text{Da}_1$ . There are two distinct regions in the figure, both denoting power laws. Below  $\Pi = 30$ ,  $\Pi \propto \text{Da}_1^{-2}$ .

However above  $\Pi = 30$ ,  $\Pi \propto \text{Da}_1^{-8}$ , which is an unrealistically strong dependence. It is probable that the latter range is caused by the artificially high numerical diffusivity which is inherent in the numerical platform when the flame spans only a few grid points. This can account for the artificially high values of  $\Pi$  which were observed. The results in this region may not be correct.

Taking the relation to be  $\Pi \propto \text{Da}_1^{-2}$  leads to:

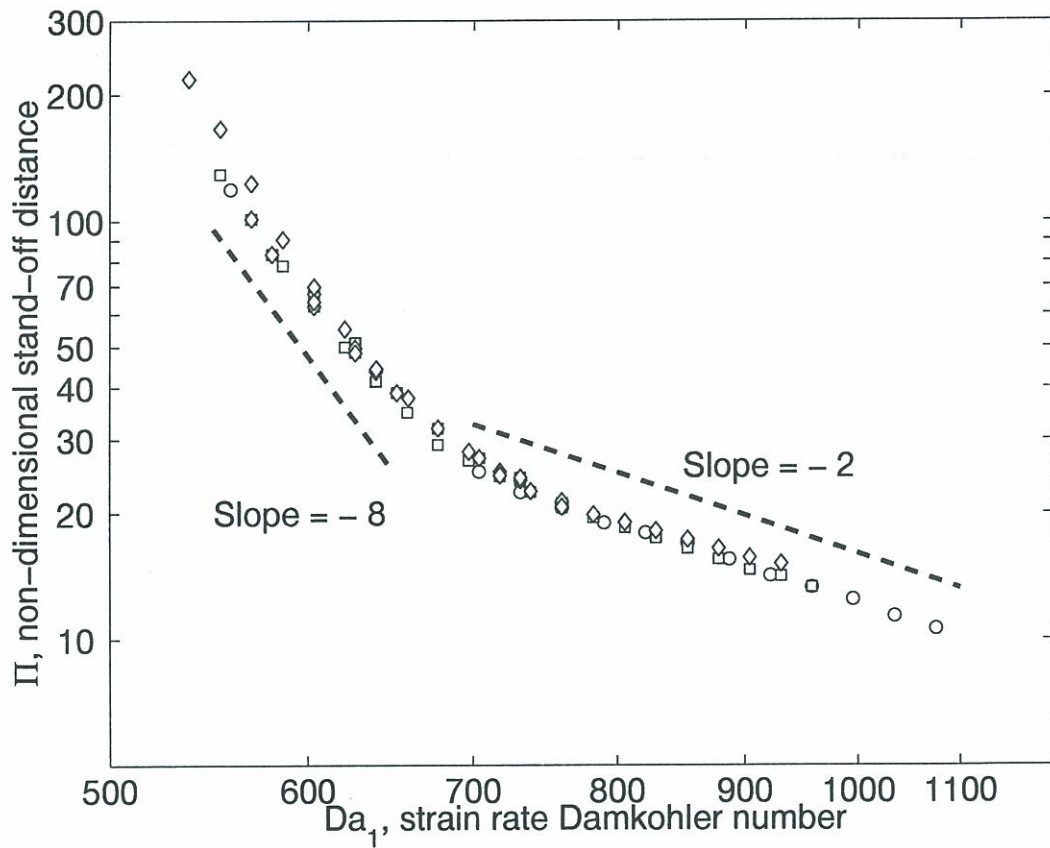
$$L_c \propto A \mathcal{D}^{1/2} \tau_c^{3/2} \quad (6.10)$$

The stand-off length increases as the strain rate,  $A$ , increases. It decreases rapidly as the chemical time decreases. These features are to be expected. It is slightly curious that  $L_c$  increases when the diffusivity increases because this would usually increase the flame speed. However, in this case increasing  $\mathcal{D}$  also increases the rate at which heat drains to the incoming flow. Since the incoming streams are held at a fixed temperature in this model, this energy is lost. This feature is similar to the temperature boundary condition of a condensed fuel. Finally, equation 6.3 for the chemical time can be substituted into equation 6.10 to give:

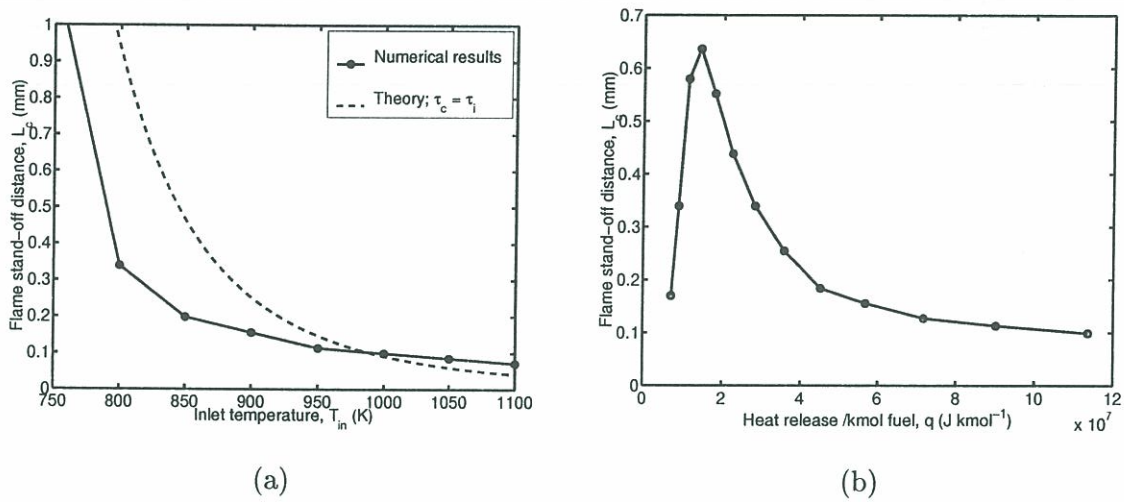
$$L_c \propto A \mathcal{D}^{1/2} \left[ \frac{T_{in}}{T_a} \frac{c_v T_{in}}{qB\rho} \exp \left\{ \frac{T_a}{T_{in}} \right\} \right]^{3/2} \quad (6.11)$$

This expression indicates that  $L_c$  is proportional to  $A\mathcal{D}^{1/2}B^{-3/2}$ , a result which is well supported by the calculations. Further simulations are performed in which the inlet temperature is changed. It is assumed that this has no effect on the flame thickness. These results are reported in figure 6.7, showing that the relation predicted by equation (6.11), while reasonable, is only approximate. A final set of simulations is performed with  $q$  and  $B$  altered such that the factor  $qB$  is constant. Here,  $q$  is the molar heat release of the chemical reaction and the factor  $qB$  appears in the chemical time (6.11). If  $q$  intervenes only by changing the chemical time, the non-dimensional stand off distance will be constant. (In this case, the flame thickness is measured from the numerical results since it is not known what effect  $q$  will have on it). These results show that  $q$  can have a stabilizing or destabilizing effect. It would be interesting to continue this study but this is not pursued here because  $q$  is fixed for a given fuel and will not be varied in the industrial application which motivates this study.



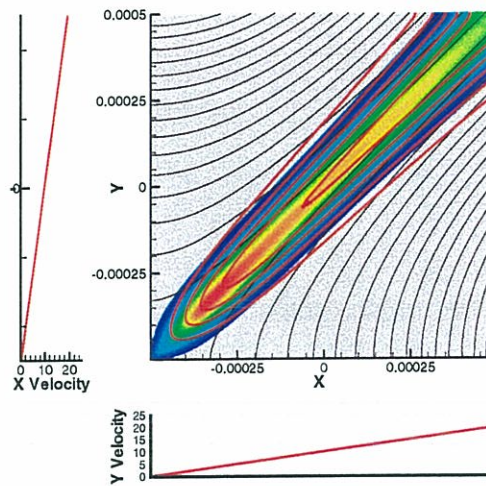


**Figure 6.6:** Non-dimensional stand-off distance,  $\Pi = L_c \tau_c^{-1/2} \mathcal{D}^{-1/2}$  as a function of the strain rate Damköhler number,  $Da_1 = A^{-1/2} \tau_c^{-1/2}$ , for a flame in a corner. Above  $Da_1 = 700$  these follow the relation:  $\Pi \propto Da_1^{-2}$ . Circles denote simulations where  $\tau_c$  was held constant. For squares,  $A$  was held constant and for diamonds  $\mathcal{D}$  was held constant.



**Figure 6.7:** Further sets of simulations performed on the strain rate-controlled corner flame to test dependence on  $T_{in}$  and  $q$ . (a) Flame stand-off distance as a function of inlet temperature. The dotted line is that predicted from equation (6.11). (b) Flame stand-off distance as a function of  $q$ , the heat released per kmol of fuel. In these simulations the factor  $qB$  is kept constant.

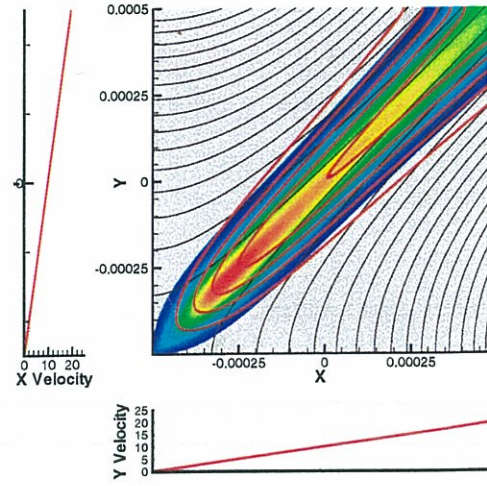




$$D = 0.50 \times D_0.$$

$$T_{max} = 1762 \text{ K};$$

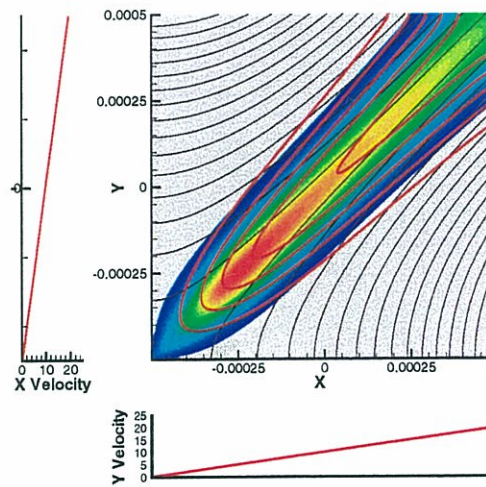
$$\dot{\omega}_{max} = 9.37 \times 10^9 \text{ Jm}^{-3}\text{s}^{-1}.$$



$$D = 0.79 \times D_0.$$

$$T_{max} = 1761 \text{ K};$$

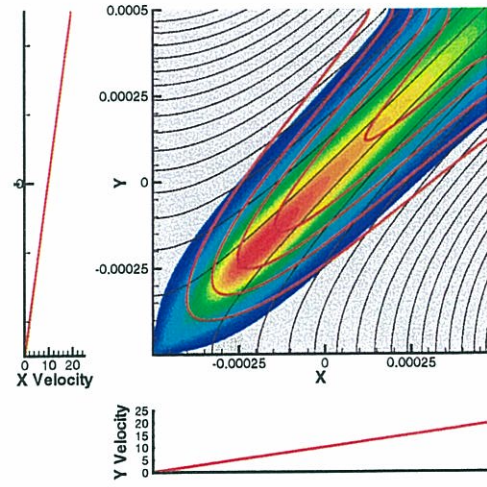
$$\dot{\omega}_{max} = 9.37 \times 10^9 \text{ Jm}^{-3}\text{s}^{-1}.$$



$$D = 1.26 \times D_0.$$

$$T_{max} = 1755 \text{ K};$$

$$\dot{\omega}_{max} = 9.37 \times 10^9 \text{ Jm}^{-3}\text{s}^{-1}.$$



$$D = 2.00 \times D_0.$$

$$T_{max} = 1760 \text{ K};$$

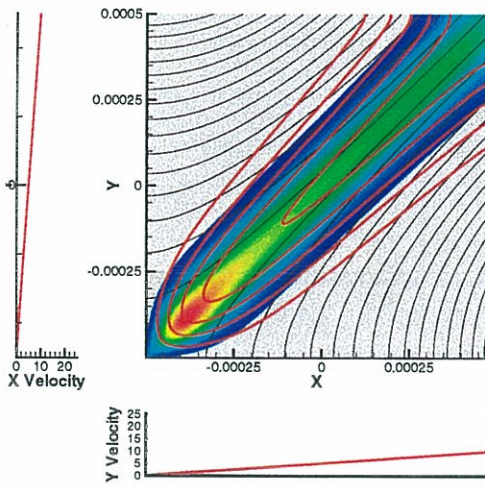
$$\dot{\omega}_{max} = 9.42 \times 10^9 \text{ Jm}^{-3}\text{s}^{-1}.$$

Strain rate-controlled flame. Colourmap: contours of heat release rate,  $\dot{\omega}$ .

Red lines: contours of temperature,  $T$ . Black lines: streamlines.

$$A = 19280 \text{ s}^{-1}; \quad T_{in} = 800\text{K}; \quad q = 2.84 \times 10^6 \text{ JKg}^{-1};$$

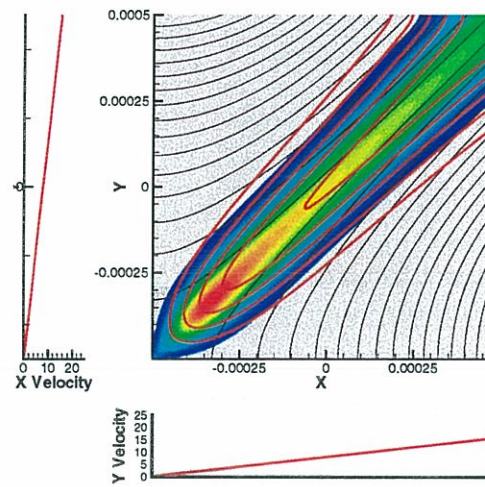
$$k = 8.85 \times 10^9 \exp(-8000\text{K}/T).$$



$$A = 9640 \text{ s}^{-1}$$

$$T_{max} = 1894 \text{ K};$$

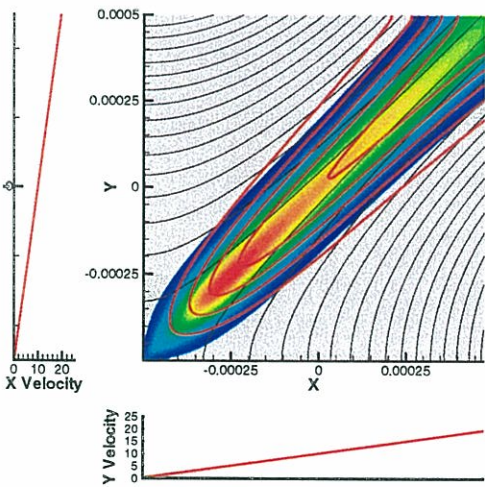
$$\dot{w}_{max} = 8.29 \times 10^9 \text{ Jm}^{-3}\text{s}^{-1}.$$



$$A = 15300 \text{ s}^{-1}$$

$$T_{max} = 1793 \text{ K};$$

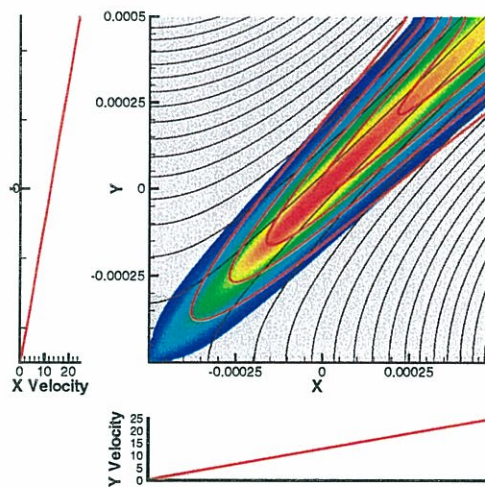
$$\dot{w}_{max} = 8.97 \times 10^9 \text{ Jm}^{-3}\text{s}^{-1}.$$



$$A = 19280 \text{ s}^{-1}$$

$$T_{max} = 1763 \text{ K};$$

$$\dot{w}_{max} = 9.37 \times 10^9 \text{ Jm}^{-3}\text{s}^{-1}.$$



$$A = 24290 \text{ s}^{-1}$$

$$T_{max} = 1702 \text{ K};$$

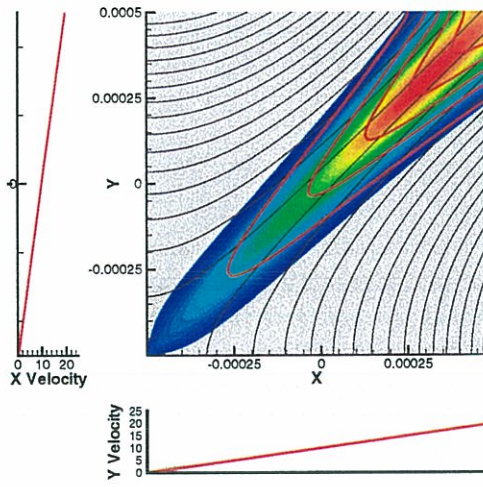
$$\dot{w}_{max} = 9.60 \times 10^9 \text{ Jm}^{-3}\text{s}^{-1}.$$

Strain rate-controlled flame. Colourmap: contours of heat release rate,  $\dot{w}$ .

Red lines: contours of temperature,  $T$ . Black lines: streamlines.

$$D = D_0; \quad T_{in} = 800\text{K}; \quad q = 2.84 \times 10^6 \text{ JKg}^{-1}; \quad k = 8.85 \times 10^9 \exp(-8000\text{K}/T).$$

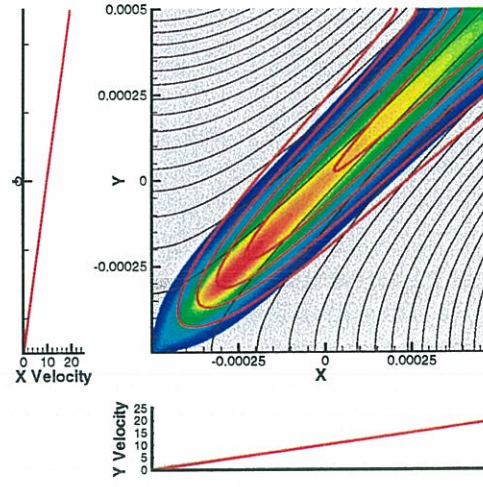




$$T_{in} = 750 \text{ K}$$

$$T_{max} = 1614 \text{ K};$$

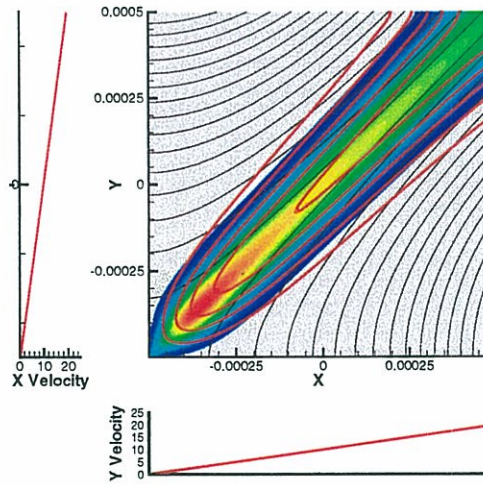
$$\dot{\omega}_{max} = 8.63 \times 10^9 \text{ Jm}^{-3}\text{s}^{-1}.$$



$$T_{in} = 800 \text{ K}$$

$$T_{max} = 1763 \text{ K};$$

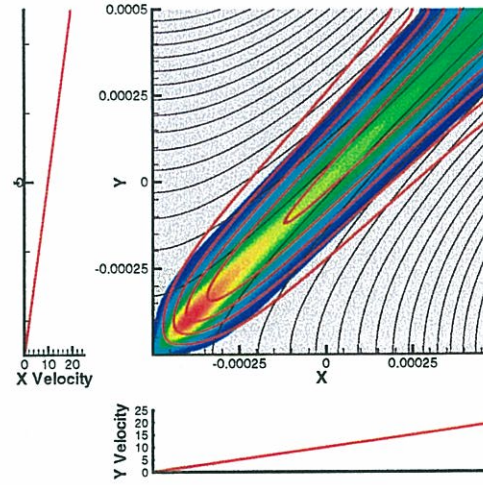
$$\dot{\omega}_{max} = 9.37 \times 10^9 \text{ Jm}^{-3}\text{s}^{-1}.$$



$$T_{in} = 850 \text{ K}$$

$$T_{max} = 1822 \text{ K};$$

$$\dot{\omega}_{max} = 10.16 \times 10^9 \text{ Jm}^{-3}\text{s}^{-1}.$$



$$T_{in} = 900 \text{ K}$$

$$T_{max} = 1888 \text{ K};$$

$$\dot{\omega}_{max} = 11.19 \times 10^9 \text{ Jm}^{-3}\text{s}^{-1}.$$

Strain rate-controlled flame. Colourmap: contours of heat release rate,  $\dot{\omega}$ .

Red lines: contours of temperature,  $T$ . Black lines: streamlines.

$$D = D_0; \quad A = 19280 \text{ s}^{-1}; \quad q = 2.84 \times 10^6 \text{ JKg}^{-1}; \quad k = 8.85 \times 10^9 \exp(-8000\text{K}/T).$$

### 6.5.4 Results - convection-controlled corner flame

The test case in section 6.5.2 is adapted to create a convection-controlled environment and the species inlet profiles are made flat. The domain and velocity inlet profiles are shown in figure 6.3.

The chemical time  $\tau_c$  is proportional to the inverse pre-exponential factor  $1/B$ , which is varied by four orders of magnitude.  $U$  and  $\mathcal{D}$  are both varied by three orders of magnitude in various combinations with  $B$ . The coefficients  $\lambda$  and  $\nu$  are altered such that  $Le = Pr = 1$ . In each of the 100 simulations the flame stand-off distance  $L_c$  is measured. This quantity is defined as the distance from the corner to the position of highest reaction rate. The simulations only give reasonable solutions over the range of  $\Pi = L_c/\delta_f$  to which the computational domain is well adapted. At high  $\Pi$  the flame becomes too thin to be resolved by the mesh. At low  $\Pi$  the flame is very thick and is strongly affected by the boundary conditions, which are somewhat artificial. The results are plotted in figure 6.8 with  $\Pi$  as a function of  $Da_2$ . In the valid range, which corresponds here to  $100 > \Pi > 10$ , the points collapse to the same line, which obeys the relation:  $\Pi \propto Da_2^{-3}$ . This leads to:

$$L_c \propto U^3 \tau_c^2 \mathcal{D}^{-1} \quad (6.12)$$

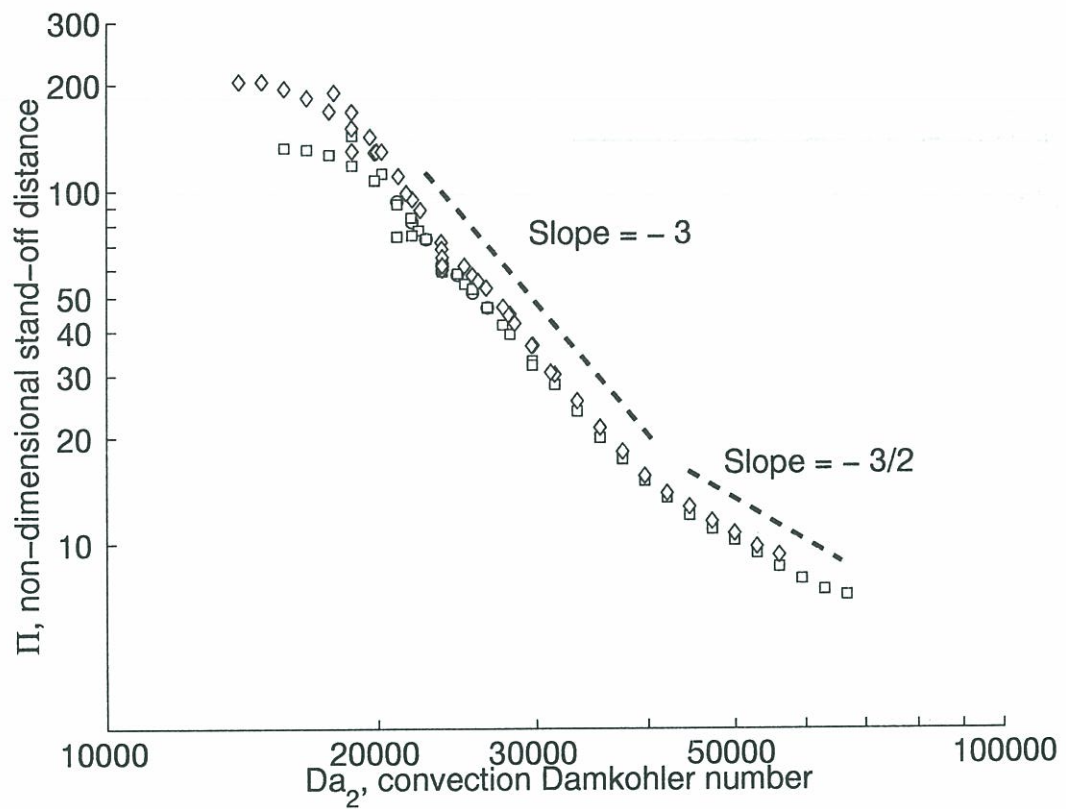
This can also be written as  $L_c \propto (U/s_L)^2 U \tau_c$ . The stand-off length is a strong function of the flow velocity, as would be expected for a convection-controlled flame. The stand-off distance reduces when  $\mathcal{D}$  increases because the triple flame speed increases. This can be compared with the results of (Marble and Adamson 1954) for an edge flame which gives:  $\Pi \propto Da_2^{-1}$ .

In terms of the ignition time in equation (6.3), equation (6.12) can be written as:

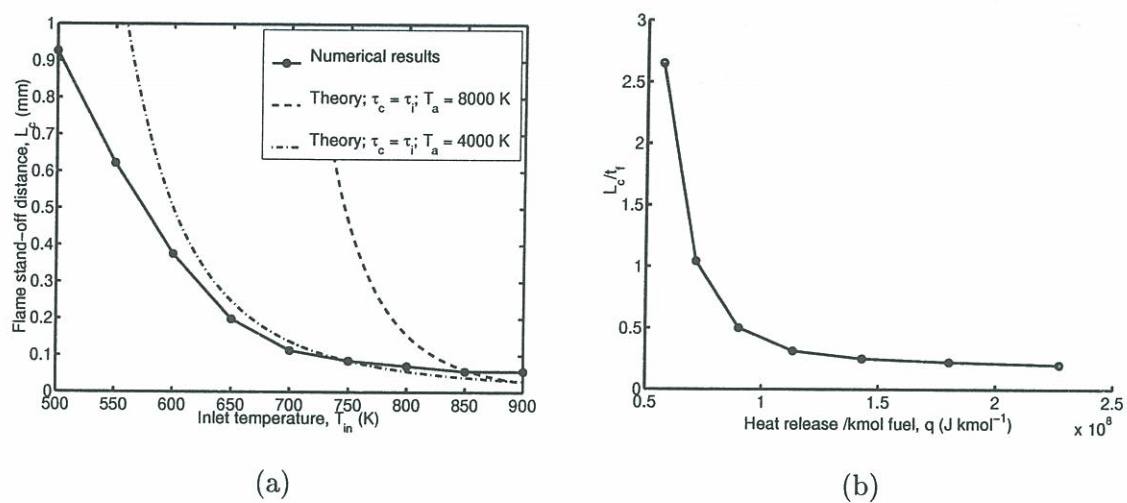
$$L_c \propto \frac{U^3}{\mathcal{D}} \left[ \frac{T_{in}}{T_a} \frac{c_v T_{in}}{qB\rho} \exp \left\{ \frac{T_a}{T_{in}} \right\} \right]^2 \quad (6.13)$$

Further simulations are performed in which the inlet temperature is changed. These are reported in figure 6.7. The relation given by equation (6.11) predicts a sharper change in the stand-off distance than is actually observed. A final set of simulations are performed with  $q$  and  $B$  altered such that the factor  $qB$  is constant. Here again,  $q$  is the molar heat release of chemical reaction. If  $q$  intervened only by changing the chemical time, the  $L_c$  would be constant. Interestingly, in the range studied, increasing  $q$  has a stabilizing effect.



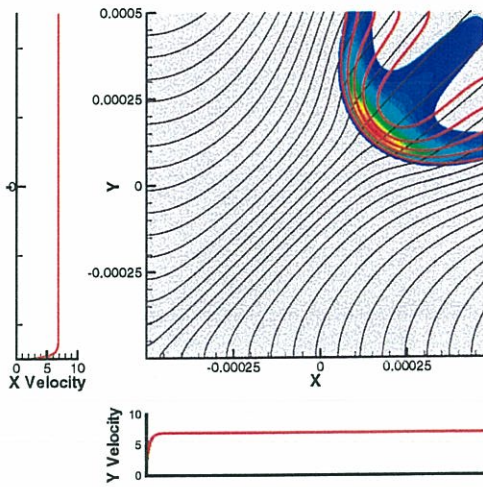


**Figure 6.8:** Non-dimensional stand-off distance,  $L_c \tau_c^{-1/2} \mathcal{D}^{-1/2}$  as a function of the convection Damköhler number,  $\mathcal{D}^{1/2} U^{-1} \tau_c^{-1/2}$ , for a flame in a corner. Circles denote simulations where  $\tau_c$  was held constant. For squares,  $U$  was held constant and for diamonds  $\mathcal{D}$  was held constant.



**Figure 6.9:** Further sets of simulations performed on the convection-controlled corner flame to test dependence on  $T_{in}$  and  $q$ . (a) Flame stand-off distance as a function of inlet temperature. The dotted line is that predicted from equation 6.13 (b) Flame stand-off distance as a function of  $q$ , the heat released per kmol of fuel. In these simulations the factor  $qB$  is kept constant.

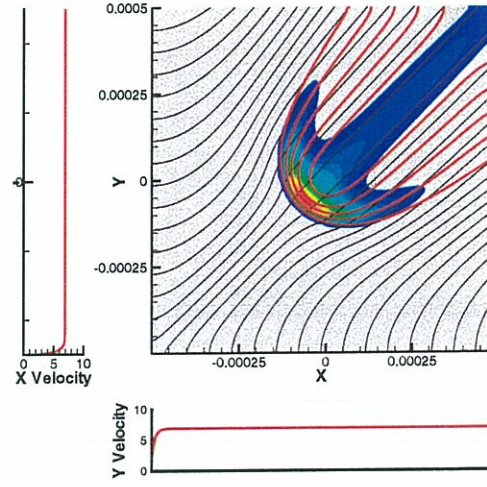




$$T_{in} = 500 \text{ K}$$

$$T_{max} = 3077 \text{ K};$$

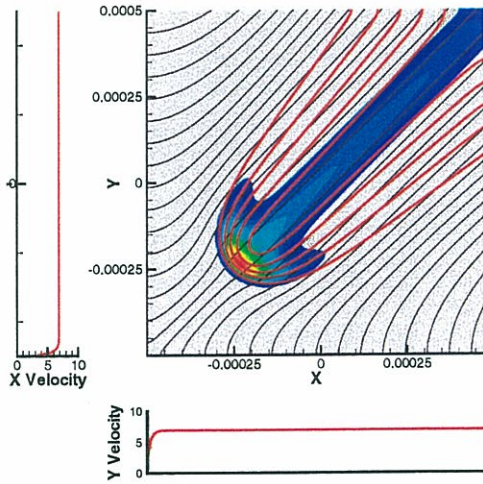
$$\dot{w}_{max} = 1.45 \times 10^{11} \text{ Jm}^{-3}\text{s}^{-1}.$$



$$T_{in} = 550 \text{ K}$$

$$T_{max} = 3061 \text{ K};$$

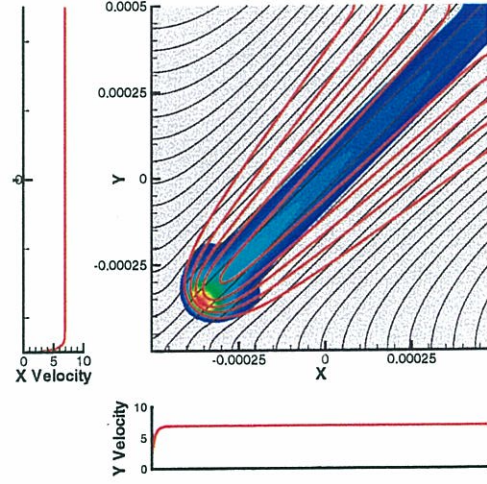
$$\dot{w}_{max} = 1.48 \times 10^{11} \text{ Jm}^{-3}\text{s}^{-1}.$$



$$T_{in} = 600 \text{ K}$$

$$T_{max} = 3022 \text{ K};$$

$$\dot{w}_{max} = 1.42 \times 10^{11} \text{ Jm}^{-3}\text{s}^{-1}.$$



$$T_{in} = 650 \text{ K}$$

$$T_{max} = 3053 \text{ K};$$

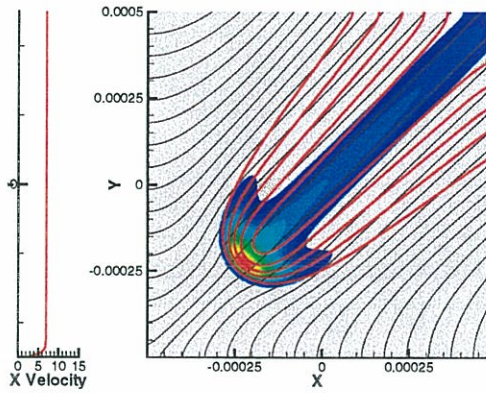
$$\dot{w}_{max} = 1.46 \times 10^{11} \text{ Jm}^{-3}\text{s}^{-1}.$$

Convection-controlled flame. Colourmap: contours of heat release rate,  $\dot{w}$ .

Red lines: contours of temperature,  $T$ . Black lines: streamlines.

$$D = D_0; \quad U_{max} = 6.94 \text{ ms}^{-1}; \quad q = 5.68 \times 10^6 \text{ JKg}^{-1};$$

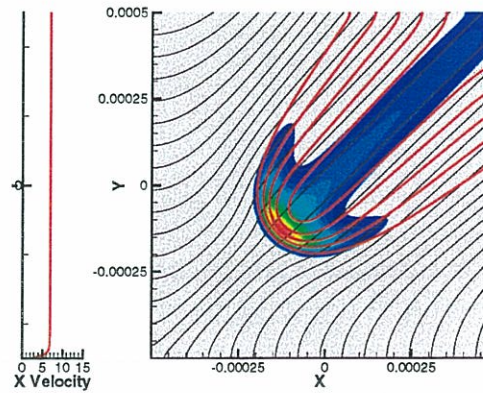
$$k = 2.68 \times 10^{10} \exp(-8000\text{K}/T).$$



$$k = 2.68 \times 10^{10} \exp(-8000\text{K}/T)$$

$$T_{max} = 3029\text{K};$$

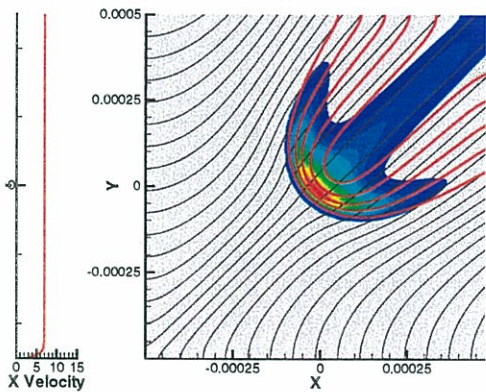
$$\dot{w}_{max} = 1.44 \times 10^{11} \text{Jm}^{-3}\text{s}^{-1}.$$



$$k = 2.41 \times 10^{10} \exp(-8000\text{K}/T)$$

$$T_{max} = 3049\text{K};$$

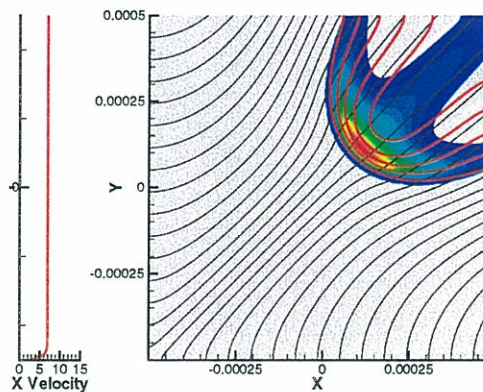
$$\dot{w}_{max} = 1.34 \times 10^{11} \text{Jm}^{-3}\text{s}^{-1}.$$



$$k = 2.14 \times 10^{10} \exp(-8000\text{K}/T)$$

$$T_{max} = 3098\text{K};$$

$$\dot{w}_{max} = 1.21 \times 10^{11} \text{Jm}^{-3}\text{s}^{-1}.$$



$$k = 1.88 \times 10^{10} \exp(-8000\text{K}/T)$$

$$T_{max} = 3159\text{K};$$

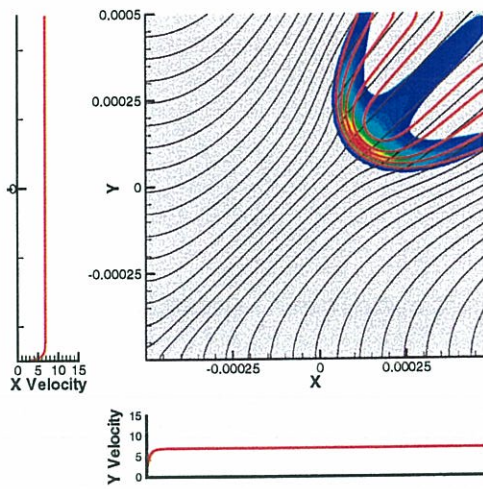
$$\dot{w}_{max} = 1.08 \times 10^{11} \text{Jm}^{-3}\text{s}^{-1}.$$

Convection-controlled flame. Colourmap: contours of heat release rate,  $\dot{w}$ .

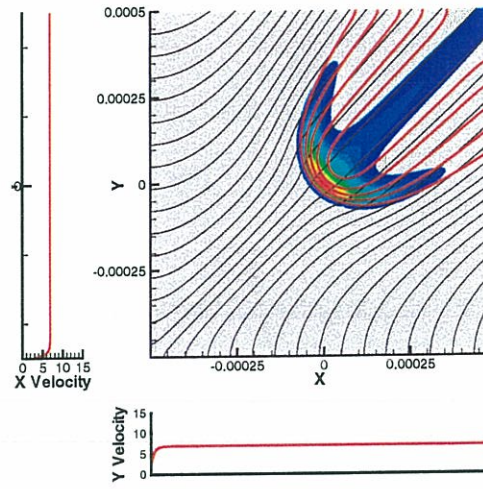
Red lines: contours of temperature,  $T$ . Black lines: streamlines.

$$D = D_0; \quad U_{max} = 6.94 \text{ ms}^{-1}; \quad q = 5.68 \times 10^6 \text{ JKg}^{-1}; \quad T_{in} = 600 \text{ K}.$$

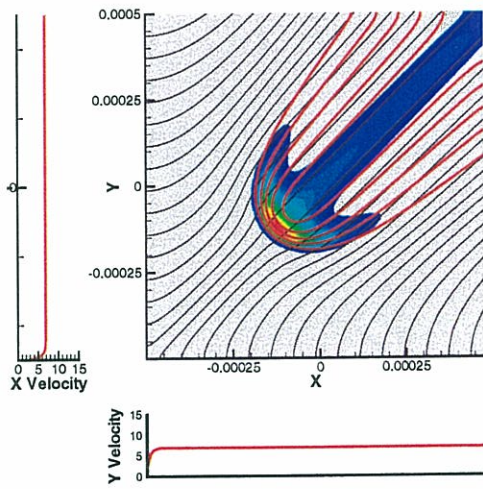




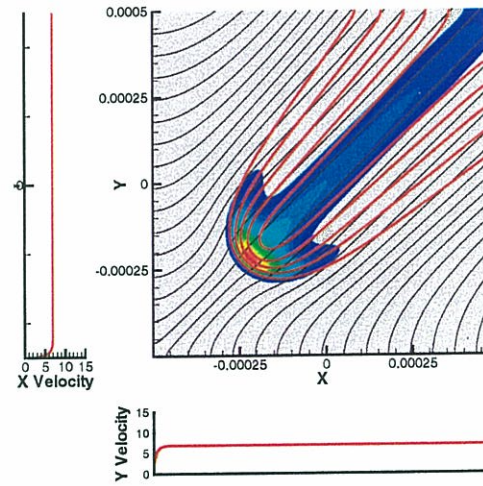
$$\begin{aligned}
 \mathcal{D} &= 0.5 \times \mathcal{D}_0. \\
 T_{max} &= 3201\text{K}; \\
 \dot{\omega}_{max} &= 1.45 \times 10^{11} \text{Jm}^{-3}\text{s}^{-1}.
 \end{aligned}$$



$$\begin{aligned}
 \mathcal{D} &= 0.63 \times \mathcal{D}_0. \\
 T_{max} &= 3139\text{K}; \\
 \dot{\omega}_{max} &= 1.50 \times 10^{11} \text{Jm}^{-3}\text{s}^{-1}.
 \end{aligned}$$



$$\begin{aligned}
 \mathcal{D} &= 0.79 \times \mathcal{D}_0. \\
 T_{max} &= 3068\text{K}; \\
 \dot{\omega}_{max} &= 1.47 \times 10^{11} \text{Jm}^{-3}\text{s}^{-1}.
 \end{aligned}$$

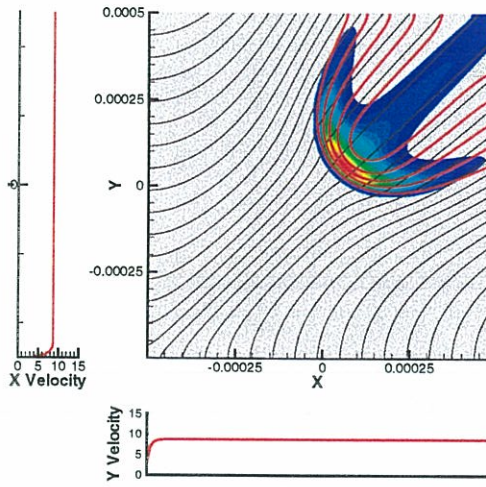


$$\begin{aligned}
 \mathcal{D} &= \mathcal{D}_0. \\
 T_{max} &= 2992\text{K}; \\
 \dot{\omega}_{max} &= 1.37 \times 10^{11} \text{Jm}^{-3}\text{s}^{-1}.
 \end{aligned}$$

Convection-controlled flame. Colourmap: contours of heat release rate,  $\dot{\omega}$ .

Red lines: contours of temperature,  $T$ . Black lines: streamlines.

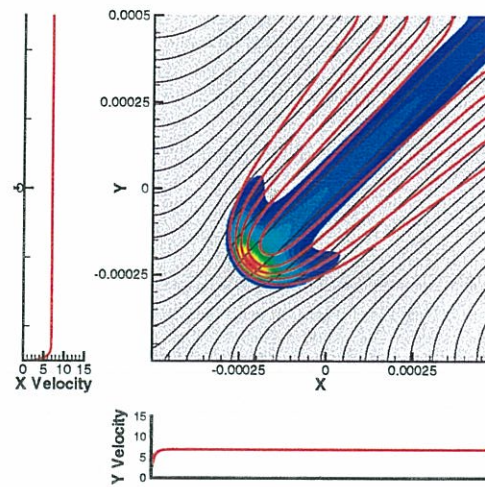
$$k = 2.68 \times 10^{10} \exp(-8000\text{K}/T); \quad U_{max} = 6.94 \text{ ms}^{-1}; \quad q = 5.68 \times 10^6 \text{JKg}^{-1}; \quad T_{in} = 600 \text{ K}.$$



$$U_{max} = 8.74 \text{ ms}^{-1}$$

$$T_{max} = 3182\text{K};$$

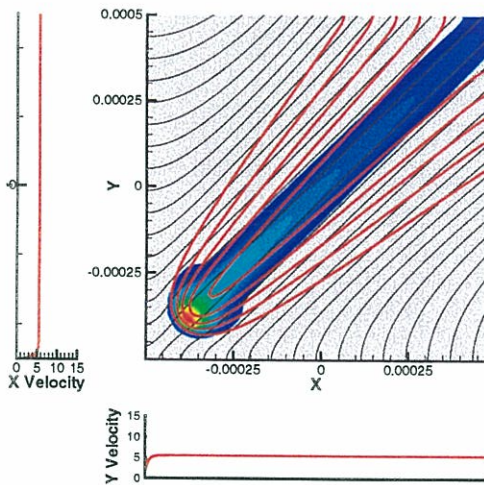
$$\dot{\omega}_{max} = 1.58 \times 10^{11} \text{ Jm}^{-3}\text{s}^{-1}.$$



$$U_{max} = 6.94 \text{ ms}^{-1}$$

$$T_{max} = 3029\text{K};$$

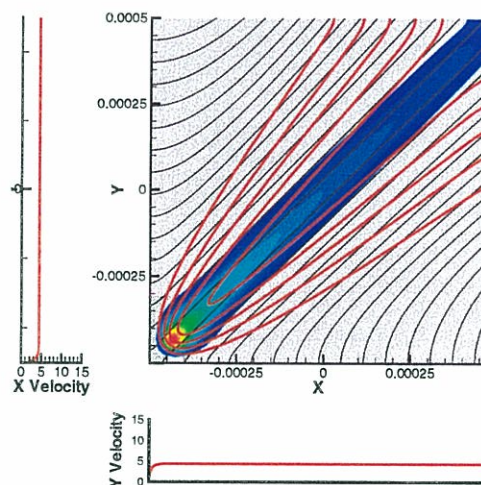
$$\dot{\omega}_{max} = 1.44 \times 10^{11} \text{ Jm}^{-3}\text{s}^{-1}.$$



$$U_{max} = 5.51 \text{ ms}^{-1}$$

$$T_{max} = 3018\text{K};$$

$$\dot{\omega}_{max} = 1.36 \times 10^{11} \text{ Jm}^{-3}\text{s}^{-1}.$$



$$U_{max} = 4.37 \text{ ms}^{-1}$$

$$T_{max} = 3019\text{K};$$

$$\dot{\omega}_{max} = 1.26 \times 10^{11} \text{ Jm}^{-3}\text{s}^{-1}.$$

Convection-controlled flame. Colourmap: contours of heat release rate,  $\dot{\omega}$ .

Red lines: contours of temperature,  $T$ . Black lines: streamlines.

$$k = 2.68 \times 10^{10} \exp(-8000\text{K}/T); \quad D = D_0; \quad q = 5.68 \times 10^6 \text{ JKg}^{-1}; \quad T_{in} = 600 \text{ K}.$$



## 6.6 Corner flames - conclusion

The aim of this chapter is to determine an expression for the flame stand-off distance in a corner flame for a given chemical heat release and a given activation temperature. A dimensional analysis shows that when this distance is expressed in terms of the flame thickness, it is a function only of the Damköhler number,  $Da$ . The form of this Damköhler number depends on whether strain or convection is the dominant flow process. A numerical approach is employed to evaluate the relation between the non-dimensional flame stand-off distance,  $\Pi$  and  $Da$ . This enables an expression for  $L_c$  to be developed, from which it can be seen that the inlet temperature and, in the case of a convection-controlled situation, the inlet velocity are particularly influential parameters. The advantage of using a numerical approach is that it can readily be extended to complex geometries, unlike a theoretical approach.

Corner flames are still a new problem in combustion science. As this research project was being completed a new study involving activation energy asymptotics was presented by (Mahalingam and Weidman 2002). This is included as a reference for future work. The results presented here need to be confirmed over a wider range of  $\Pi$  by employing a finer grid. It would also be interesting, and relatively easy, to explore the effects of a heat release parameter and a Zeldovich parameter. However, these studies are not relevant to the industrial situation which motivates this research project.





## Chapter 7

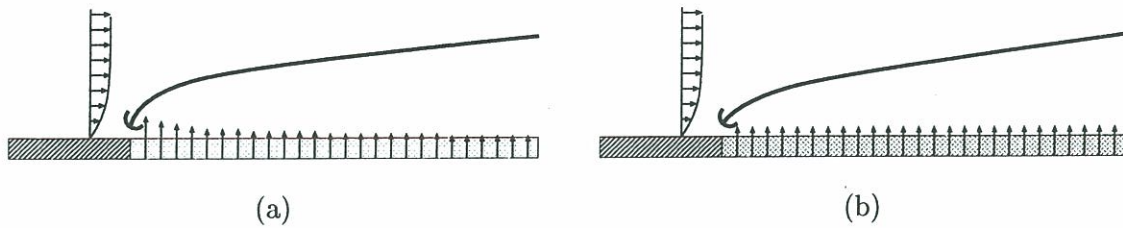
# Flame over a condensed reactant

On introduit dans ce chapitre que l'un des réactifs se trouve sous forme d'une phase condensée. La vaporisation devient alors un phénomène qui risque d'avoir de l'influence sur la stabilisation de la flamme et il faut introduire un deuxième nombre sans dimension. On va montrer au moyen d'analyses théoriques et numériques, que la vaporisation n'a que peu d'influence sur la stabilisation de la flamme lorsque le dégagement de chaleur correspondant à la réaction est très supérieur à la chaleur latente de vaporisation.

## Nomenclature

$A$	Strain rate
$b$	coupling variable: $b \equiv h^* + q_{O_2}^* Y_{O_2}$
$B_{sp}$	Spalding transfer coefficient
$c_p$	Heat capacity at constant pressure
$Da$	Damköhler number
$\mathcal{D}$	Mass diffusivity
$h$	Enthalpy
$L$	Distance from leading edge of boundary layer
$L_c$	Flame stand off distance
$L_{ref}$	Reference length, based on flame thickness
$Le$	Lewis number
$\Delta h_v$	Latent heat of vaporization
$q_{O_2}$	Heat released per mass of $O_2$ burnt
$Re$	Reynolds number
$Sc$	Schmidt number
$T$	Temperature
$T_f$	Flame temperature
$T_{in}$	Inlet temperature
$U$	Free stream axial / horizontal velocity
$V_w$	Wall inlet velocity
$\dot{w}_T$	Thermal reaction rate
$\dot{w}_{O_2}$	Oxygen consumption/production reaction rate
$Y$	Mass fraction
$\dot{m}_v$	vaporization rate
$\cdot^*$	Non-dimensional number
$\cdot_\infty$	Free stream variable
$\delta_f$	Flame thickness
$\lambda$	Thermal conductivity
$\nu$	Kinematic viscosity
$\Pi$	Ratio of flame stand-off distance to flame thickness
$\tau_c$	Characteristic chemical time





**Figure 7.1:** (a) Flame formed in a convecting stream above a condensed fuel. (b) Flame formed in a convecting stream above a porous plate with fuel injection. The two situations are similar.

## 7.1 Introduction

The presence of a condensed reactant is one of the features of a cryogenic spray flame which could change its stability characteristics. Vaporization of this reactant couples heat loss from the flame to the inlet velocity of one reactant. As shown in this chapter, it is necessary to introduce a further dimensionless parameter. This is explored using the classic problem of the flame in a convecting stream above a condensed fuel (figure 7.1a). This situation resembles the base of a cryogenic spray flame when the thickness of the oxygen injector lip tends to zero. There are also many similarities with the corner flame studied in the previous chapter. In section 7.2 we start by examining the flame formed in a convecting stream above a porous plate through which fuel is injected (figure 7.1b). Dimensional analysis is used in section 7.3 to derive the main characteristic parameters controlling the flame spread. However, as demonstrated in section 7.4, the new parameter has little effect. A numerical simulation is performed in section 7.4.2 confirms this and demonstrates the flow structure at the flame tip. This leads to the numerical studies in chapter 8.

## 7.2 Flame over a porous plate

The development of a diffusion flame in a laminar boundary layer over a porous plate is a standard problem in combustion theory. This problem is investigated in the context of fire research because it has some of the features found in situations involving flame spread over a condensed fuel. The studies of Hirano and Kanno (1973) and Rohmat et al. (1998) provide basic experimental data. The flame is stabilized at the upstream edge of the plate. There is a velocity gradient in the cross-flow boundary layer but the velocity profile of the fuel injected through the porous plate is generally flat. The situation therefore has characteristics of both the strain rate-controlled and the convection-controlled corner flame in chapter 6.

The experimental study of Hirano and Kanno (1973) presents the velocity and temperature profiles in the boundary layer and a discussion of the flame position and extinction mechanisms. Flame-holding is studied in further depth by Rohmat et al. (1998). Two extinction mechanisms, summarized in figure 7.2, are observed in these experiments:

- If the injection velocity through the porous plate is high, the flame tip is situated

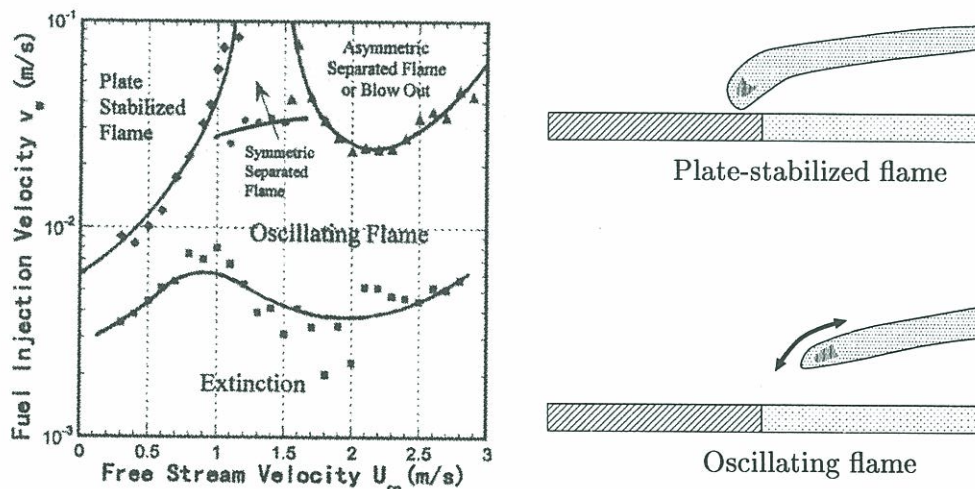
upstream of the plate. As  $U$  increases, the flame edge moves downstream, in a similar manner to the convection-controlled corner flame. When it retreats behind the leading edge of the plate the flame tip oscillates. This is because the flame propagates into the pre-mixed region formed upstream and is then blown back. At higher  $U$  the flame blows off entirely.

- As the injection velocity through the porous plate  $V_w$  decreases, the flame approaches the plate until it extinguishes through quenching.

The first of these mechanisms will be the same for porous plates and condensed fuel layers. However, the second of these mechanisms will be different because, in the case of a condensed fuel, the injection velocity,  $V_w$  is a function of the flame position. This is analyzed in the next section.

### 7.3 Dimensional analysis

It is worth considering this problem in terms of dimensional analysis. This provides the main characteristic numbers and serves as a guide in the numerical calculations. In the study of a corner flame there are four dimensional variables: the flame stand-off distance,  $L_c$ , the chemical time,  $\tau_c$ , the molecular diffusivities,  $\mathcal{D}$  and either the free stream velocity,  $U$ , or the strain rate,  $A$ . There are two dimensions, so two dimensionless parameters are required: The non-dimensional flame stand-off distance  $\Pi = L_c \tau_c^{-1/2} \mathcal{D}^{-1/2}$  and a



**Figure 7.2:** On the left: A stability diagram for a flame above a porous plate, from Rohmat et al. (1998). The “plate-stabilized” flame has a flame edge upstream of the porous plate and is stable. To the right of this region, when  $U$  is increased, the flame edge retreats downstream of the edge of the porous plate and becomes unstable. It separates, oscillates or blows off entirely. At the bottom, when the fuel injection velocity,  $V_w$ , decreases, the flame quenches on the porous surface.



Damköhler number  $Da = \tau_c^{-1/2} A^{-1/2}$  or  $Da = \mathcal{D}^{1/2} U^{-1} \tau_c^{-1/2}$ . In the situations studied in this chapter, a further dimensional variable  $V_w$  is introduced. The number of dimensions has not increased, so a third dimensionless parameter is required.

The convection-controlled situation is used to demonstrate this, but the procedure is identical for the strain rate-controlled situation. The new parameter could be taken to be  $V_w/U$  for both the porous plate and the condensed fuel situations. In the following development we show that this is equivalent to using the parameter  $q/\Delta h_v$  in the condensed fuel situation, where  $\Delta h_v$  is the latent heat of the fuel per unit mass and  $q$  is the heat release per unit mass of fuel burned.

The Stephan flow velocity due to evaporation from a condensed layer is given (Appendix C) by:

$$V_w = \frac{\lambda}{\rho \Delta h_v} \frac{\partial T}{\partial x} \sim \frac{\lambda}{\rho \Delta h_v} \frac{(T_f - T_{in})}{L_{ref}} \quad (7.1)$$

The increase in temperature between the surface and the flame ( $T_f - T_{in}$ ) is given by  $q/c_p$ . In order for the approximate expression to be realistic,  $L_{ref}$  must scale with the distance from the surface to the flame. A convenient length scale here is the flame's thickness, given by  $L_{ref} \sim \tau_c^{1/2} \mathcal{D}^{1/2}$ . This leads to:

$$\frac{V_w}{U} = \frac{\lambda}{\rho c_p \mathcal{D}} \frac{\mathcal{D}^{1/2}}{U \tau_c^{1/2}} \frac{q}{\Delta h_v} \equiv Le Da \frac{q}{\Delta h_v} \quad (7.2)$$

The first term on the right hand side is the Lewis number, the second is the Damköhler number and the third is a non-dimensional parameter which can be used in place of  $V_w/U$ . This parameter is proportional to the Spalding transfer coefficient  $B_{sp}$ , the effect of which is examined analytically in the next section.

## 7.4 Analysis of a flame above a condensed fuel

The following analysis is adapted from Emmons (1956) and the important points are explained in detail here. It is based on simplifying assumptions, some of which are not valid for a hydrogen flame over liquid oxygen. However it is useful as a tool for understanding the influence of certain parameters on a flame over a liquid fuel. Specifically, we will develop an expression for the vaporization rate. The notation is for a condensed fuel in a stream containing oxidizer.

The Navier-Stokes equations of motion are reduced using standard arguments relating to the flow in a boundary layer:  $\partial p/\partial y \sim 0$ ;  $\partial u/\partial y \gg \partial u/\partial x$ ,  $u \gg v$  and  $\partial T/\partial y \gg \partial T/\partial x$ . The following dimensionless variables are employed, where  $L$  is the length of combustion surface and the subscript  $\infty$  refers to the free stream:

$$\begin{aligned} x^* &= \frac{x}{L}; & u^* &= \frac{u}{U_\infty}; & \rho^* &= \frac{\rho}{\rho_\infty}; & h^* &= \frac{h}{c_{p\infty} T_\infty}; & \dot{w}_T^* &= \frac{\dot{w}_T L}{\rho_\infty U_\infty c_{p\infty} T_\infty}; \\ y^* &= \frac{y}{L}; & v^* &= \frac{v}{U_\infty}; & \mu^* &= \frac{\mu}{\mu_\infty}; & Re &= \frac{\rho_\infty U_\infty L}{\mu_\infty}; & \dot{w}_{O_2}^* &= \frac{\dot{w}_{O_2} L}{\rho_\infty U_\infty}; \end{aligned}$$

The equations of motion, below, are expressed in dimensional form on the left and dimensionless form on the right:

The continuity equation:

$$\frac{\partial \rho u}{\partial x} + \frac{\partial \rho v}{\partial y} = 0$$

The  $x$ -momentum equation:

$$\rho \left\{ u \frac{\partial u}{\partial x} + v \frac{\partial u}{\partial y} \right\} = \frac{\partial}{\partial y} \mu \frac{\partial u}{\partial y}$$

Energy equation (in terms of enthalpy):

$$\rho \left\{ u \frac{\partial h}{\partial x} + v \frac{\partial h}{\partial y} \right\} = \frac{\partial}{\partial y} \lambda \frac{\partial T}{\partial y} + \dot{w}_T$$

Conservation of oxygen:

$$\rho \left\{ u \frac{\partial Y_{O_2}}{\partial x} + v \frac{\partial Y_{O_2}}{\partial y} \right\} = \frac{\partial}{\partial y} \mathcal{D}_{O_2} \rho \frac{\partial Y_{O_2}}{\partial y} + \dot{w}_{O_2}$$

$$\frac{\partial \rho^* u^*}{\partial x^*} + \frac{\partial \rho^* v^*}{\partial y^*} = 0$$

$$\rho^* \left\{ u^* \frac{\partial u^*}{\partial x^*} + v^* \frac{\partial u^*}{\partial y^*} \right\} = \frac{1}{\text{Re}} \frac{\partial}{\partial y^*} \mu^* \frac{\partial u^*}{\partial y^*}$$

$$\rho^* \left\{ u^* \frac{\partial h^*}{\partial x^*} + v^* \frac{\partial h^*}{\partial y^*} \right\} = \frac{1}{\text{Re}} \frac{\partial}{\partial y^*} \frac{\mu^*}{\text{Pr}} \frac{\partial h^*}{\partial y^*} + \dot{w}_T^*$$

$$\rho^* \left\{ u^* \frac{\partial Y_{O_2}}{\partial x^*} + v^* \frac{\partial Y_{O_2}}{\partial y^*} \right\} = \frac{1}{\text{Re}} \frac{\partial}{\partial y^*} \frac{\mu^*}{\text{Sc}} \frac{\partial Y_{O_2}}{\partial y^*} + \dot{w}_{O_2}^*$$

A crucial point here is that all the gaseous species have the same specific heats so that the enthalpy may be expressed as  $dh = c_p dT$ . This enthalpy does not contain any information about the potential energy release due to chemical reaction. This is contained in a variable  $b$ , which is defined as:

$$b = h^* + q_{O_2}^* Y_{O_2} \quad (7.3)$$

where  $q_{O_2}^*$  is the non-dimensional heat release per unit mass of combusting oxygen. Considering a single step reaction between oxidizer and fuel one may write  $\dot{w}_T = q_{O_2} \dot{w}_{O_2}$ . Furthermore, if  $\text{Pr} = \text{Sc} = \text{Le} = 1$  then the energy and species equations can be combined to give:

$$\rho^* \left\{ u^* \frac{\partial b}{\partial x^*} + v^* \frac{\partial b}{\partial y^*} \right\} = \frac{1}{\text{Re}} \frac{\partial}{\partial y^*} \mu^* \frac{\partial b}{\partial y^*} \quad (7.4)$$

which is, on inspection, equivalent to the momentum equation, with  $u^*$  replaced with  $b$  in every differential. The variable  $b$  is therefore moved around in the boundary layer in the same manner as the  $x$ -momentum per unit mass:  $u$ . If a field  $u^*(x^*, y^*)$  has been found which satisfies the equation of motion for  $u^*$  then it is true that the field:

$$b(x^*, y^*) = \alpha u^* + \beta \quad (7.5)$$

satisfies the equation of motion for  $b$ , where  $\alpha$  and  $\beta$  are constants. However, it will only be a physical solution if the boundary conditions for  $b$  are the same as the boundary conditions for  $u^*$ .

Conveniently, this turns out to be the case. In the free stream, where  $y \rightarrow \infty$ ,  $u^*$ ,  $h^*$  and  $Y_{O_2}$  are constant, so  $b$  is also constant. Similarly, at the surface,  $h^*$  and  $Y_{O_2}$  can be assumed to be constant since it is an evaporating liquid. At this position,  $u^* = 0$ . The constants in equation (7.5) are  $\alpha = (b_\infty - b_s)$  and  $\beta = b_s$ .



The shear stress at the liquid surface is:

$$\tau_s = \mu \left. \frac{\partial u}{\partial y} \right|_{y=0} \quad (7.6)$$

The heat conduction into the liquid surface is given by:

$$q_s = -\lambda \left. \frac{\partial T}{\partial y} \right|_{y=0} \equiv -c_{p\infty} T_\infty \frac{\lambda}{c_p} \left. \frac{\partial h^*}{\partial y} \right|_{y=0} \quad (7.7)$$

When equation (7.3) is differentiated,  $\partial Y_{O_2}/\partial y$  can be taken to be zero at the surface because there is no diffusion of oxygen into the liquid. Noting that  $Pr = 1$ , one obtains:

$$q_s = -c_{p\infty} T_\infty \mu \left. \frac{\partial b}{\partial y} \right|_{y=0} \quad (7.8)$$

However, we know from (7.5) with its boundary conditions that  $\partial b/\partial y = (b_\infty - b_s) \partial u^*/\partial y$ , which leads to:

$$q_s = -c_{p\infty} T_\infty \frac{(b_\infty - b_s)}{U_\infty} \mu \left. \frac{\partial u}{\partial y} \right|_{y=0} \quad (7.9)$$

The vaporization rate  $\dot{m}_v$ , in  $\text{kgs}^{-1}\text{m}^{-2}$ , is given by  $\dot{m}_v = q_s/(-\Delta h_v)$ . From equations (7.9) and (7.6), this can be expressed in terms of the shear stress at the surface,  $\tau_s$ :

$$\dot{m}_v = B_{sp} \frac{\tau_s}{u_\infty} \quad (7.10)$$

where

$$B_{sp} = \frac{c_{p\infty} T_\infty (b_\infty - b_s)}{\Delta h_v} \equiv \frac{c_p (T_\infty - T_s) + q_{O_2} Y_{O_2\infty}}{\Delta h_v} \quad (7.11)$$

where  $c_p$  is taken to be constant and  $Y_{O_2s}$  is zero. The parameter  $B_{sp}$  is the ratio of the thermal energy per unit mass of the main stream to the thermal energy required to put a unit mass of fuel into the boundary layer. This is identical to the dimensionless function introduced by de Ris (1969) to study the propagation velocity of a flame over a thick fuel bed. Emmons (1956) assumes that  $\rho\mu$  is constant and performs a Blasius-like exercise to reduce the situation to an incompressible boundary layer problem. The novelty here is that the boundary condition for  $v$ -velocity at the liquid surface is a fraction  $B_{sp}$  of the shear stress at the wall. This is why  $B_{sp}$  is such a useful parameter governing the shape of the boundary layer flow. From this analysis the vaporization rate is:

$$\dot{m}_v = \frac{1}{2} \frac{\mu_\infty}{x} \sqrt{\text{Re}_x} f(B_{sp}) \quad (7.12)$$

Numerical calculations for  $f(B_{sp})$  presented by Emmons show that the results are well correlated to the function:

$$f(B_{sp}) = \frac{\ln(1 + B_{sp})}{1.7 B_{sp}^{0.18}} \quad (7.13)$$

A very important and not intuitively obvious point is that  $B_{sp}$  only has a significant effect on the vaporization rate when  $B_{sp} < 10$  (figure 7.6). Note also the relatively large dependence on  $\mu_\infty$  and, by extension, the other molecular transport coefficients. We shall test this inference numerically in section 7.4.2. This analysis fits very well the results of Hirano and Kinoshita (1975) on pools of liquid hydrocarbons in an air stream. These authors find that the fuel consumption rate increases monotonically with  $U_\infty$ . Furthermore, the consumption rate of ethanol is very close to that of methanol, despite the different latent heats and heat release of these two fuels. The distance between the flame and the plate increases approximately in proportion to  $x^{1/2}$  and the flame's intensity decreases with  $x$ .

In all but the most dilute situations, the heat release term exceeds the enthalpy difference between the free stream and the surface:  $q_{O_2}Y_{O_2\infty} \gg c_p(T_\infty - T_s)$ . Therefore, with combustion,  $B_{sp}$  is approximately equal to  $q_{O_2}Y_{O_2\infty}/\Delta h_v$ , which is of order 10 to 100. In this range,  $B_{sp}$  has little influence on the vaporization rate. Consequently  $q_{O_2}$  and  $\Delta h_v$  have little influence. Without combustion,  $B_{sp} = c_p(T_\infty - T_s)/\Delta h_v$ , which depends greatly on the relative temperatures but which might typically be of order 0.1 to 1. The ratio of the values of  $f(B_{sp})$  calculated at these two values of  $B_{sp}$  is around 50. This correlates well with the observation of Hirano and Kinoshita (1975) that the fuel evaporation rate increases by a factor of 10 to 100 when there is a flame over the condensed fuel.

#### 7.4.1 Stability of a flame over condensed fuel

The main conclusion of the previous section is that, when there is a flame above a condensed surface, the parameter  $B_{sp}$  has little influence on flame stability. Unlike the situation with a porous plate, the flame cannot quench on the surface because the vaporization rate increases as it approaches the surface. This reduces the stability question to an analysis of the tip of the flame, which has many characteristics similar to the corner flame studied in chapter 6. The non-dimensional stand-off distance is affected by only one non-dimensional parameter: the Damköhler number. Whether this is based on strain rate or convection is determined by the flame stand-off distance relative to the boundary layer thickness.

When the free stream velocity is increased, Hirano and Kinoshita (1975) observe that the flame retreats over the upstream edge of the fuel. Its position then oscillates, as for the flame over a porous plate. It is not intuitively obvious that these oscillations will occur since, unlike for the porous plate, the injection velocity of the fuel decreases when the flame retreats. The flame must, therefore, be able to propagate upstream above the liquid fuel surface. This phenomenon has been studied by de Ris (1969), Frey and T'ien (1979) and Kuwana et al. (1999). Heat transfer to the fuel in front of the flame is fundamental to the models proposed in these studies. Consequently, they are not relevant to situations where the flame is stabilized upstream of the condensed reactant - such as in a stable flame over a condensed phase - or in situations where the fuel is shielded from the flame by the fact that it flows out of a pipe - as in the cryogenic injector. They are however relevant to ignition studies if the cryogenic flame reaches the LOx injector by propagating along the LOx jet. This is probable, although we have not yet seen evidence to support this mechanism.

As a final point, the models proposed by de Ris (1969), Frey and T'ien (1979) and



Kuwana et al. (1999) depend strongly on pre-heating of the condensed phase. Pre-heating is less influential in the cryogenic flame because the condensed phase is nearly at its boiling temperature. In this case the latent heat of oxygen, at  $\Delta h_v = 216 \text{ kJ kg}^{-1}$ , is an order of magnitude greater than the energy required to raise its temperature from its injection temperature: 80 K to boiling point: 90 K, which is  $c_{p_{LO_2}}(T_v - T_{in}) = 17 \text{ kJ kg}^{-1}$ .

#### 7.4.2 Numerical study of a flame over a condensed surface

The formulation of the corner flame in chapter 6 is adapted to study the flame over a condensed surface. The combination of the numerical solver and boundary conditions is denoted FSP<sub>3</sub>. As well as providing a useful step towards chapter 8, it reveals more clearly the flow structure near the flame tip and can be used to verify that  $B_{sp}$  has little effect except where  $B_{sp} < 10$ . The domain is lengthened, in order to provide room for the flame upstream of the condensed surface. The velocity profile at the bottom boundary depends on the temperature gradient:

$$V_w = \frac{\lambda_s}{\rho_s \Delta h_v} \left. \frac{\partial T}{\partial x} \right|_{y=0} \quad (7.14)$$

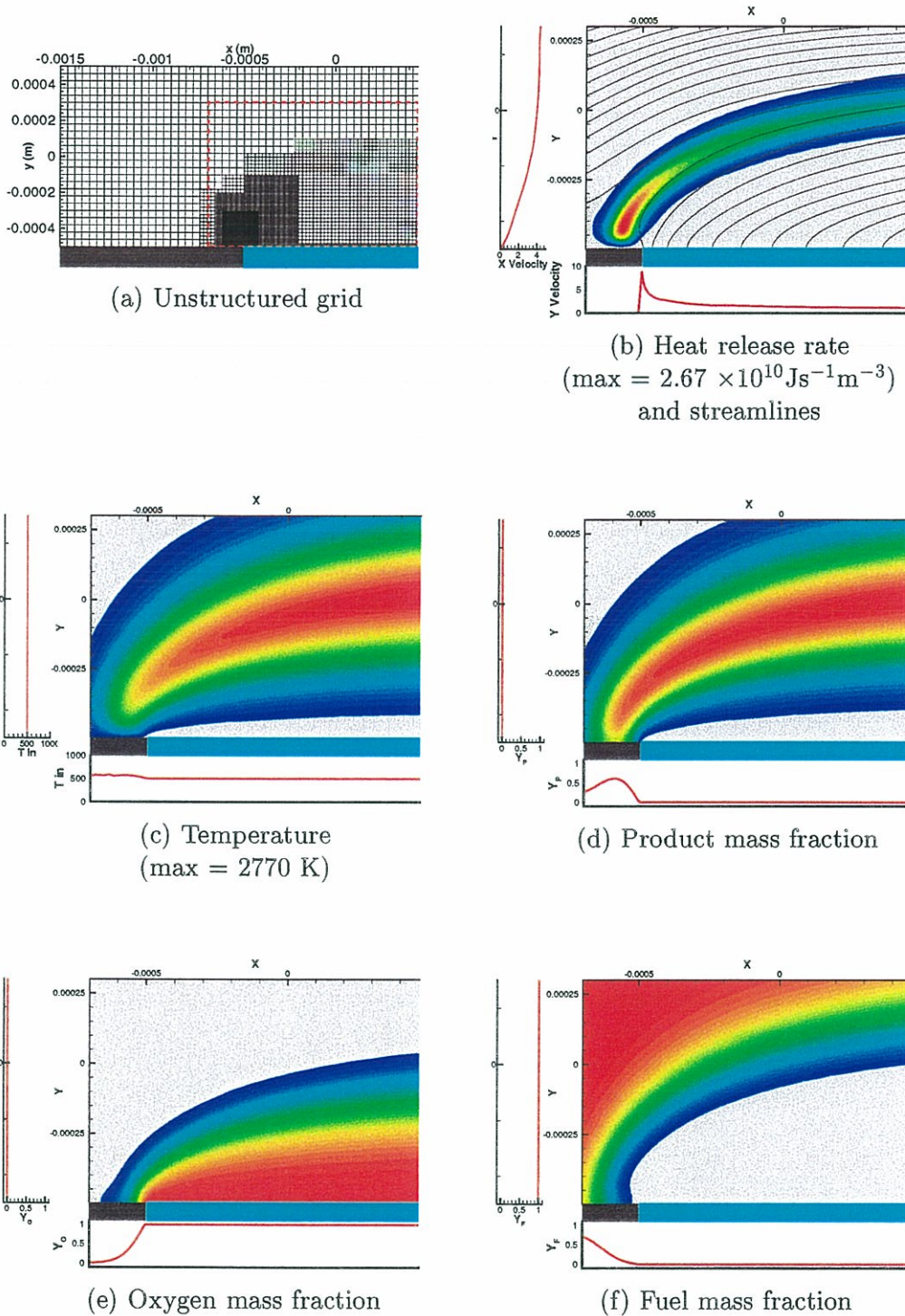
The un-structured grid used for this problem is shown in figure 7.3 along with a sample solution. The latent heat of vaporization,  $\Delta h_v$ , is initially chosen such that the injection velocity is of the same order of magnitude as the corner flame.

The velocity and temperature profiles above a condensed hydrocarbon have been measured by Hirano and Kinoshita (1975). These results are compared with the simulation's results in figures 7.4 and 7.5. They are qualitatively similar. It is difficult to define reference lengths for the two situations so they are left in dimensional terms. The vaporization profile of the simulations is compared in figure 7.6a with that predicted in section 7.4, which is proportional to  $x^{-1/2}$ . They agree remarkably well. In figure 7.6b,  $V_w/U$  at a point 0.5 mm downstream from the flame tip is plotted as a function of  $B_{sp}$ . This shows that, as predicted by the analysis in section 7.4,  $V_w$  does not vary greatly when  $B_{sp}$  is above approximately 10, which is the case in any situation involving combustion. Further tests show that the vaporization rate increases in proportion to  $\mathcal{D}^{1/2}$  and  $U^{1/2}$ . This also serves as confirmation of the FSP<sub>3</sub> package.

In the case of the corner flame, it was easy to define and measure the flame stand-off distance from the numerical simulations. For the flame above a condensed phase this is less easy because both the  $x$ -position and the  $y$ -position of the flame kernel change. One possibility is to measure the distance along the line of stoichiometric mixture fraction. This path was not pursued in this research project because it is not relevant to the problem of flame stabilization behind a lip. In any case, the parameters affecting flame position are likely to be similar to those defined for the corner flame. A selection of flow fields near the flame tip is presented in figure 7.7 for various flow conditions. These demonstrate that the situation is similar to the corner flame or a counterflow flame with a quenched centre.

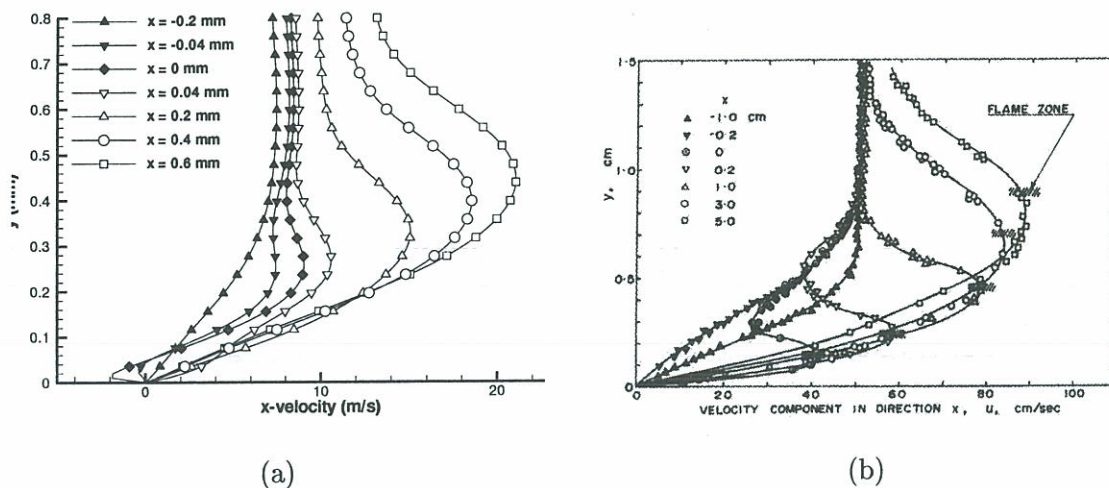
## 7.5 Conclusions

In this chapter a condensed reactant is introduced into the corner flame configuration of chapter 6. A further dimensionless parameter is required to describe the problem: the

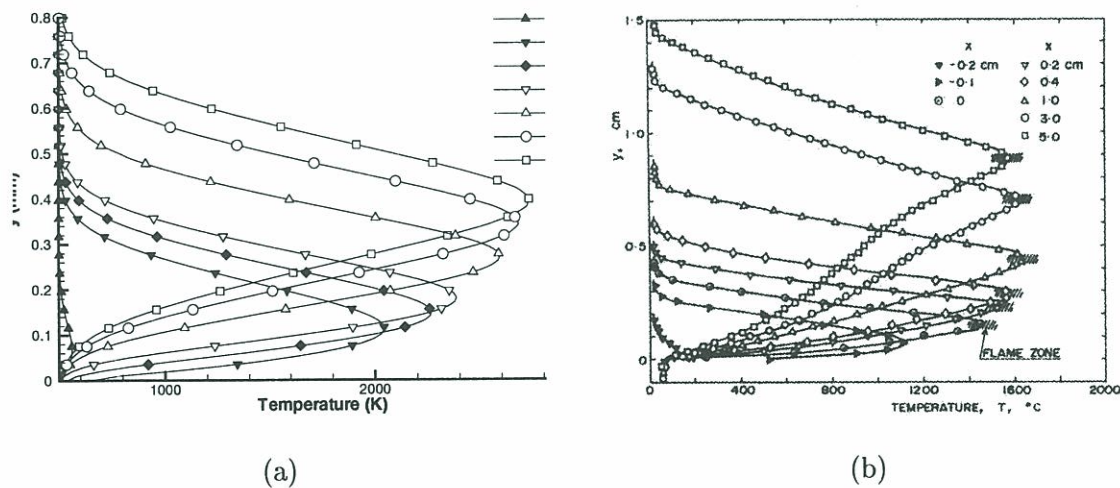


**Figure 7.3:** Unstructured grid and numerical results for the simulation of a flame over a liquid fuel. Results are shown from the domain outlined in red on the grid in figure (a). The profiles shown below and to the left of each figure are taken, respectively, from the bottom and the left boundaries of the entire domain.

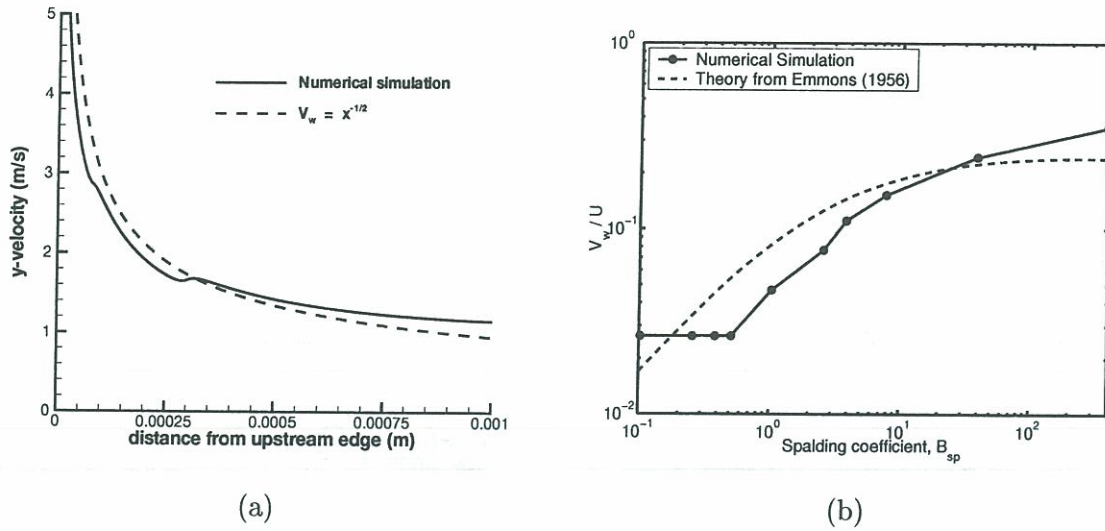




**Figure 7.4:** Velocity profiles for a flame above a liquid fuel. (a) from a simulation similar to that shown in figure 7.3. (b) from experimental measurements by Hirano and Kinoshita (1975). The results are qualitatively similar.



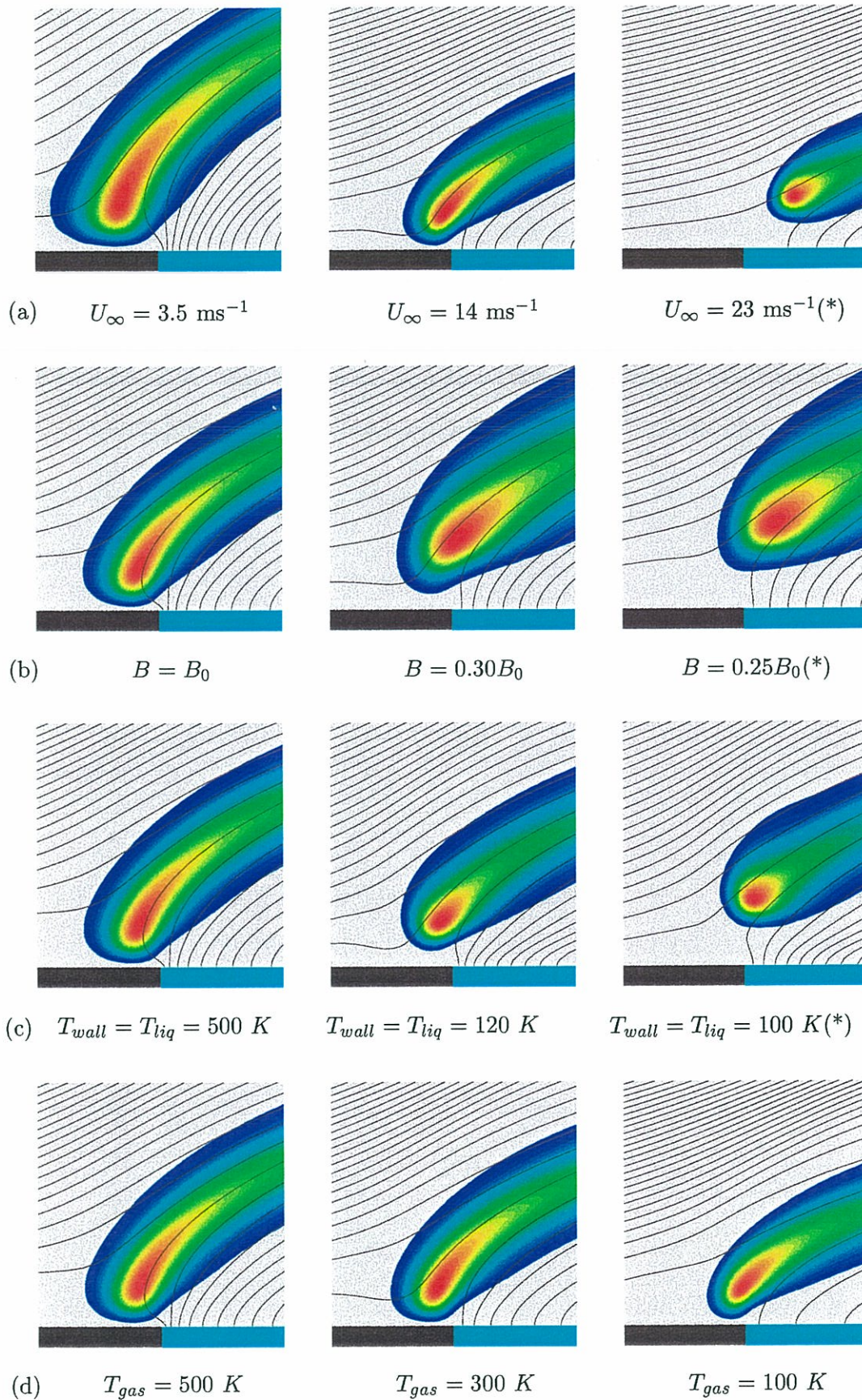
**Figure 7.5:** Temperature profiles for a flame above a liquid fuel. (a) from a simulation similar to that shown in figure 7.3. (b) from experimental measurements by Hirano and Kinoshita (1975). The results are qualitatively similar.



**Figure 7.6:** (a) Liquid vaporization profile. The results of the simulation are compared with results expected from equation 7.12. The small jumps in the simulation's profile arise from changes in the grid size around these points, which alters the apparent thermal diffusivity and hence the vaporization rate. (b) The vaporization rate as a function of  $B_{sp}$  is evaluated from numerical simulations and compared with that predicted by Emmons (1956).

Spalding transfer coefficient:  $B_{sp}$ . In combusting situations,  $B_{sp} \approx q/\Delta h_v$ , where  $q$  is the heat release on chemical reaction and  $\Delta h_v$  is the latent heat of vaporization. It is shown both analytically and numerically that  $B_{sp}$  has no effect on the stability of a flame in a boundary layer above a liquid reactant. Consequently, the only parameter affecting stability is the Damköhler number introduced in chapter 6.





**Figure 7.7:** Numerical simulations of a flame above a liquid fuel. Colour: heat release rate. Black lines: streamlines. (\*) denotes unstable solutions.





## Chapter 8

# Flame stabilization behind a step over a liquid fuel

On a vu au chapitre 4 qu'il est possible de réduire l'étude de la stabilisation de la flamme cryotechnique à l'analyse de la région derrière la lèvre du conduit d'oxygène. L'introduction d'une marche, équivalente à la lèvre, introduit une nouvelle échelle de longueur au problème envisagé au chapitre 7. On doit aussi introduire un nouveau nombre sans dimension.

Il est démontré d'une façon numérique que ce paramètre, qui est le rapport de la hauteur de la marche à l'épaisseur de la flamme, est le paramètre ayant le plus d'influence sur la stabilisation de la flamme. Quand ce paramètre est plus grand que 1, la flamme peut s'installer dans la région d'écoulement lent derrière la marche, et elle est peu affectée par l'écoulement d'hydrogène et le nombre de Damköhler. De plus, si ce rapport n'est pas proche de 1, les tourbillons détachés de la marche passent au dessus de la tête de la flamme. Par contre, si ce rapport est plus grand que 1, la flamme est exposée à l'écoulement libre et elle est très influencée par le nombre de Damköhler. En gros, lorsque la flamme est placée dans cette configuration, tout se passe comme dans la situation d'une flamme au dessus d'une nappe liquide sans marche. Pour les vitesses typiques des moteurs cryotechniques, la stabilisation n'est pas possible dans cette situation.

## Nomenclature

$B_{sp}$	Spalding transfer coefficient
$B$	Pre-exponential factor in Arrhenius reaction rate expression
Da	Damköhler number
$D$	Mass diffusivity
$d_l$	Diameter of liquid stream
$h$	Surface heat transfer coefficient
$h_s$	Step height
$\Delta h_v$	Latent heat of vaporization
$J$	Momentum flux ratio
Nu	Nusselt number
$q$	Heat release per unit mass of fuel burnt
$q_s$	Heat transfer from flame to step
$T$	Temperature
$T_{in}$	Inlet temperature
$U$	Axial / Horizontal velocity
$V_w$	Stephan flow velocity
$Y$	Mass fraction
$\beta$	Zeldovich number $\equiv T_a(T_f - T_{in})/T_f^2$
$\delta_f$	Flame thickness
$\lambda$	Thermal conductivity
$\lambda_m$	Thermal conductivity in step
$\mu$	Viscosity
$\nu$	Kinematic viscosity
$\rho$	Density
$\Pi$	Ratio of flame stand-off distance to flame thickness
$\Psi$	Ratio of step height to flame thickness
$\tau_c$	Characteristic chemical time



## 8.1 Introduction

The previous chapter considers the flame in a boundary layer over a porous plate or a condensed fuel. This chapter concerns the flow when a backwards-facing step is placed upstream of the condensed phase. This acts in the same way as the lip of the oxygen injector in the cryogenic flame. We know from chapter 4 that if the flame tip is stabilized just behind the step, the subsequent flame sheet cannot be extinguished downstream. The question of stabilization has thus been reduced to a study of the small zone behind the LOx tube lip.

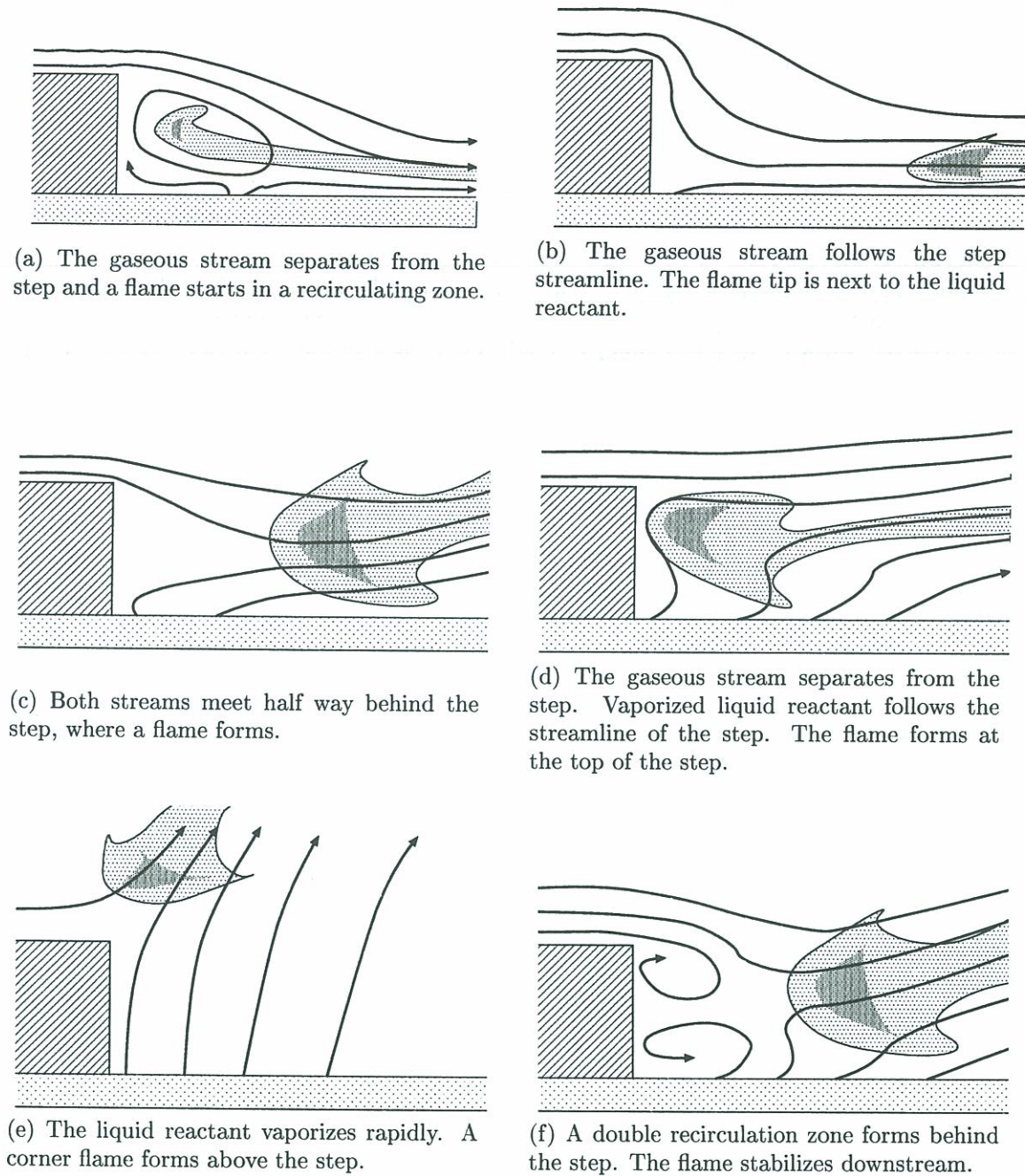
The aim therefore is to study the extinction of a flame in this zone. Six possible stabilization mechanisms are shown in figure 8.1. Flame stabilization behind a bluff body and a splitter plate is reviewed briefly in the first two sections. A porous plate is introduced in section 8.4 and a numerical platform for simulating a liquid fuel is described in section 8.6. Numerical results are presented in section 8.7. Two particular extinction mechanisms are observed, both of which depend strongly on a new non-dimensional parameter  $\Psi$ , which is the step height divided by the flame thickness. The heat transfer to the step is also calculated at the end of this section.

## 8.2 Premixed flame stabilization behind a bluff body

It is worth, at this point, reviewing the experimental and theoretical results of Zukoski and Marble (1955) and Zukoski (1985) for a premixed flame stabilized in the wake of a bluff body. In the recirculating zone behind the body there is a mixture of hot combustion products and residual quantities of one reactant. The incoming flow of fresh gas separates at the edge of the bluff body and diffuses into the hot mixture. Ignition occurs where the local mixture ratio is nearly stoichiometric. Stabilization is enhanced when the stoichiometric contour is further towards the hot products because the ignition time is strongly dependent on the initial temperature. This mechanism determines the flame stand-off distance. On the other hand, if the residence time of the flow along this contour is not sufficient for ignition to occur, the flame blows off. The crucial point in this premixed study is that molecular diffusion of the incoming fluid into the fluid behind the obstacle is the dominant process. This occurs in a thin layer between the main flow and the slower flow behind the obstacle. A similar mechanism will exist in diffusion flames behind a bluff body. In addition, Zukoski's work suggests that it is instructive to follow the velocity and temperature along the mixture fraction contour at which ignition will occur.

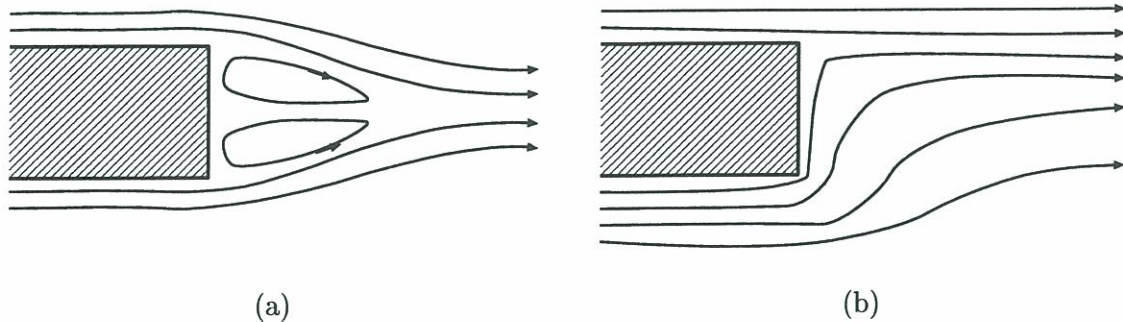
## 8.3 Non-premixed flame stabilization behind a splitter plate

Deshpande et al. (1997) have performed numerical simulations and experiments on the flame formed behind a splitter plate between non-premixed gaseous hydrogen and gaseous oxygen flows. When the momentum flux ratio ( $J = (\rho_{H_2} U_{H_2}^2 / \rho_{O_2} U_{O_2}^2)$ ) of the two flows is unity, the double recirculation zone is found which is characteristic of the wake behind a bluff body in section 8.2. However, this is the exception rather than the rule. There is usually no recirculation zone behind the splitter plate. Even a small departure of  $J$  from unity leads to a situation where the flow with high momentum flux separates at the corner



**Figure 8.1:** Various possible flow configurations of a flame behind a step over a liquid fuel.





**Figure 8.2:** *The flow behind a splitter plate (a) when the momentum flux ratios of the two flows are identical and (b) when the top flow has a higher momentum flux than the bottom flow.*

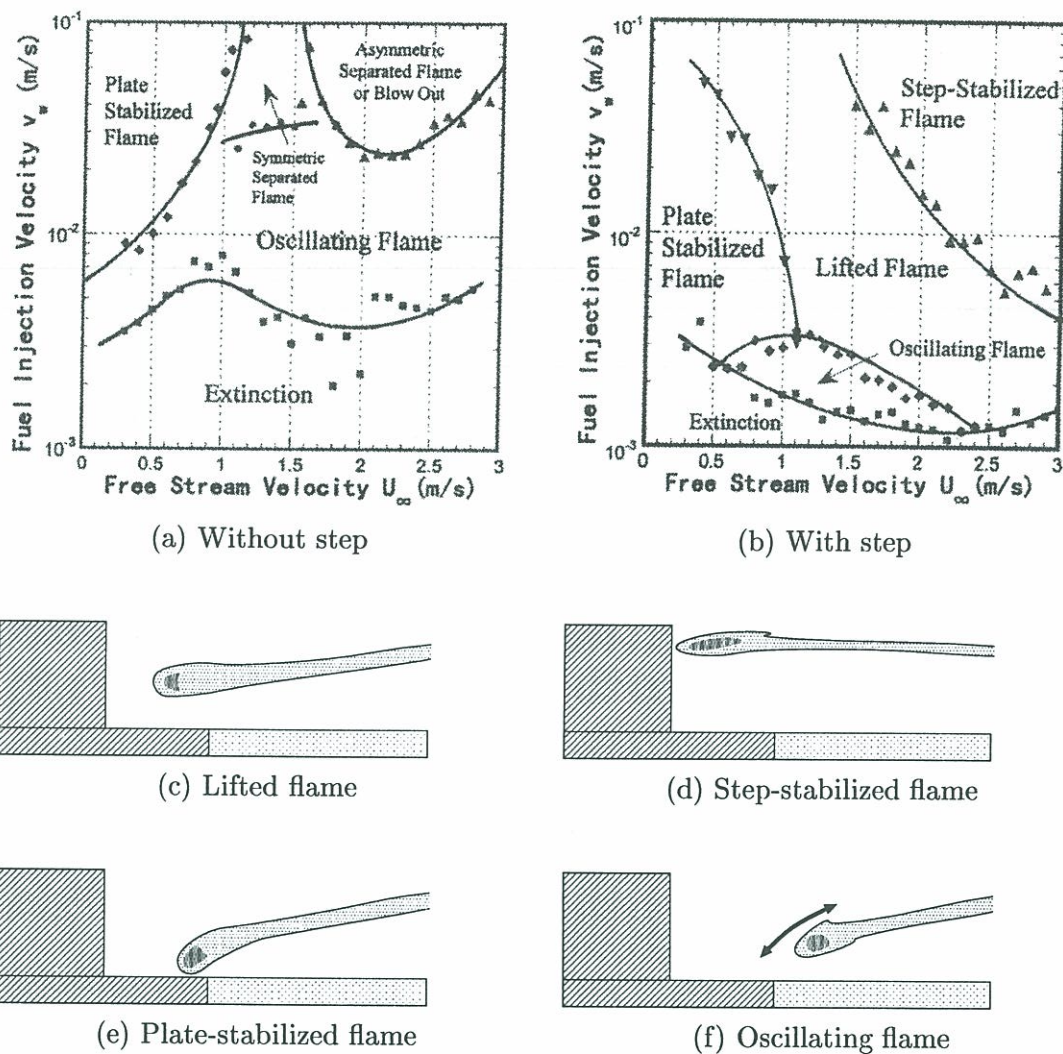
of the splitter plate and the flow with low momentum flux follows the curvature of the plate. This is shown in figure 8.2. Consequently, the diffusion flame tends to place itself towards the flow with high momentum flux. Despite the fact that there is no recirculation zone, the plate thickness is crucial. It gives the fluid with low momentum flux some time to heat up and it ensures that the flame edge remains in a region of relatively low velocity, which aids stabilization. On the other hand, Deshpande et al. find that the flame requires a great deal of pre-heating in order to remain attached when the thickness of the plate tends to zero.

#### 8.4 Flame stabilization behind a step over a porous plate

The flow over a porous plate behind a backwards facing step has been studied by Rohmat et al. (1998), following on from their studies without a step introduced in chapter 7. It is worth recalling that with no step the flame edge is situated just upstream of the edge of the porous plate or oscillates just downstream of this edge or is blown out completely. With the backwards-facing step, two new modes of stabilisation appear. These limit the occurrence of oscillations and, in the range of parameters studied, replace blow-out. The flow configurations are shown in figure 8.3. In the “lifted flame” mode, the flame is positioned half way between the plate and the top of the step. In the “step-stabilized” mode, which occurs at higher gas velocities, the flame is stabilized on the lip of the step. As the step increases in size, these modes of stabilization are obtained more readily.

Rohmat et al. interpret these modes of stabilization in terms of a recirculating vortex behind the step, although there is no direct experimental evidence for this. A more likely explanation is that the flows have similar features to the numerical simulations of Deshpande et al. in figure 8.2. At low free stream velocities, the upper flow follows the curvature of the step, leading to a plate-stabilized flame. At high free-stream velocities, the upper flow separates instantly from the top of the step, leading to a step-stabilized flame. The lifted flame corresponds to a flow somewhat between the two.

In conclusion, numerical results, which are consistent with experimental observations, indicate that there is rarely a recirculation zone behind the step. The flow-field here is



**Figure 8.3:** Diagrams which describe the type of flame holding over a porous plate (a) without a step (as in chapter 7) (b) with a step just upstream of the plate, from Rohmat et al. (1998). The domain of the oscillating flame is greatly reduced in the presence of a step. Also, two new modes replace blow-off. These are the lifted flame (c), the tip of which is positioned half way between the top of the step and the porous plate and (d) the step-stabilized flame, the tip of which is aligned with the top of the step.



nonetheless crucial, since it provides a region of slow velocity for the edge of the flame and allows time for at least one of the reactants to heat up. It will be instructive to follow the position of the contour of mixture fraction at which ignition occurs, which is approximately the stoichiometric contour. Stability will be enhanced when this lies in a hot and slow region.

## 8.5 Dimensional analysis

For the flame in a corner, in chapter 6, the non-dimensional flame stand-off distance was a function of one parameter: the Damköhler number. For the flame above a condensed phase, in chapter 7, it was necessary to introduce a new parameter: the Spalding transfer coefficient  $B_{sp}$ . When there is a step of height  $h_s$  behind the condensed fuel we introduce a further lengthscale into the problem without increasing the number of dimensions. This suggests that another non-dimensional parameter is required.

The reference length in this situation is the flame thickness  $\delta_f \sim \tau_c^{1/2} \mathcal{D}^{1/2}$ . The new parameter is therefore  $\Psi = h_s \tau_c^{-1/2} \mathcal{D}^{-1/2}$ . The analysis of Emmons (1956) demonstrated that, without a step ( $\Psi = 0$ ),  $B_{sp}$  has very little influence on a flame above a liquid fuel. However this no longer applies when there is a step because the boundary layer approximation is no longer valid. Consequently, unlike the situations in chapters 6 and 7, all three parameters:  $Da$ ,  $B_{sp}$  and  $\Psi$  could be influential.

This situation is quite possibly beyond the scope of theoretical analysis. Consequently the numerical formulation developed during the previous chapters, FSP, is used. It demonstrates qualitative aspects of the flow and, since it is relatively fast, permits a parametric study of the most critical variables. Intuitively, one would expect  $\Psi$  to be the most influential parameter. In the limit  $\Psi \rightarrow 0$ , the situation without a step is recovered. The other limit,  $\Psi \rightarrow \infty$ , corresponds to an infinitely-thin flame sheet which can readily tuck behind the step. In the following numerical simulations,  $\Psi$  is varied first.

## 8.6 Numerical platform

The numerical platform developed in chapters 6 and 7 is combined with the chemical model evaluated in chapter 5. The code is two-dimensional, which is acceptable in this situation because the radius of curvature of the oxygen injector is considerably larger than typical length scales in the problem. This numerical platform, called FSP<sub>4</sub>, requires relatively little CPU time, which means that several parameters can be varied. The Reynolds number (based on the free stream hydrogen velocity, the lip height and gas properties in the hot region behind the lip) is around  $10^3$ . This means that laminar transport can be assumed without the introduction of turbulence models. Evaporation from the liquid is modelled but the surface itself is assumed to be aerodynamically undisturbed by the gaseous stream in this region. According to the results of (Oefelein 1997) this is a valid approximation.

Four values of lip thickness are studied numerically, from 0.2 mm to 0.4 mm. Each requires a different grid and these are shown in figure 8.4. The meshes are un-structured in order to permit a high resolution in the influential region just behind the lip. Injection conditions of the base cases are summarized in table 8.1. All numerical experiments were performed at 1 bar. At higher pressures, the flame is thinner and more intense,

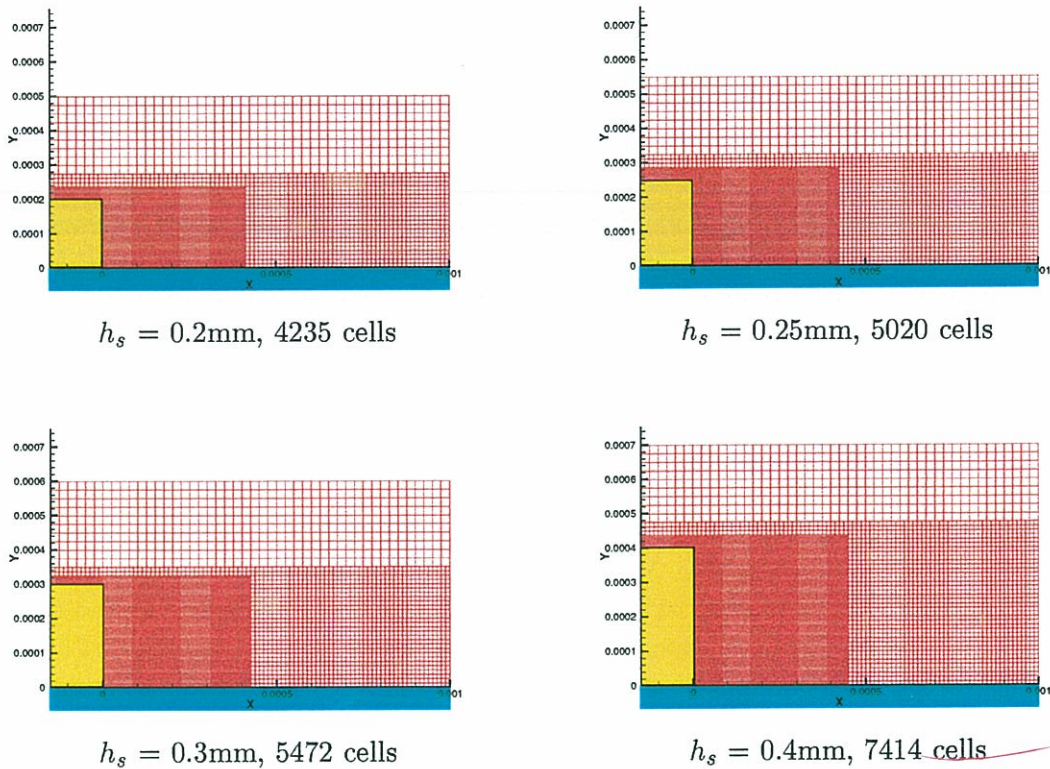
	$h_s \leq 0.2mm$
$T_{H_2}, T_{lip}$	350 K
$U_{H_2}$	$150 \text{ ms}^{-1}$
$T_{LOx}$	90 K
$U_{LOx}$	$2 \text{ ms}^{-1}$
$B$	$2.53 \times 10^9$
$E_a$	$9.61 \times 10^7 \text{ Jkmol}^{-1}$
$\mathcal{D}$	$2.41 \times 10^{-9} T^{1.76} \text{ m}^2\text{s}^{-1}$
$\lambda$	$8.26 \times 10^{-4} T^{0.76} \text{ Wm}^{-1}\text{K}^{-1}$
$\mu$	$1.55 \times 10^7 T^{0.76} \text{ Nsm}^{-2}$

**Table 8.1** : Operating conditions for the base cases.

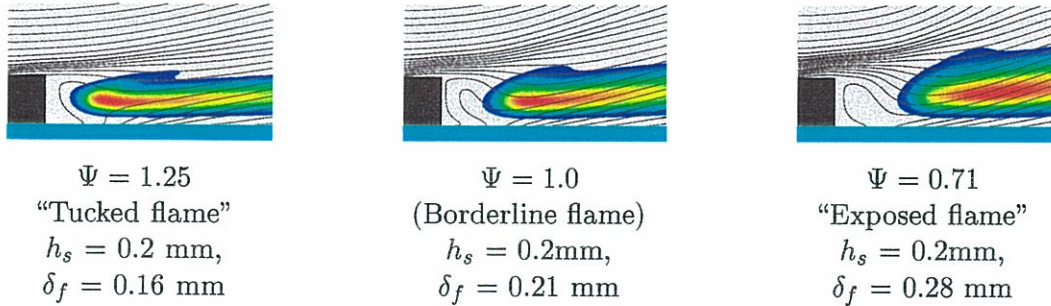
as demonstrated clearly in Oefelein (1997) and Oefelein and Yang (1998). The effect of pressure can be encapsulated within the chemical time, which affects both  $\Psi$  and the Damköhler number. The results here will be applicable to all situations which are scale-invariant with respect to these simulations. We anticipate that this will be the case up to the critical pressure of pure oxygen. Above this pressure the physics pertaining to vaporization changes, increasing the factor  $B_{sp}$ . This has no effect on the flame's stability and is unlikely to affect the pertinence of  $\Psi$ , which is the ratio of the lip thickness to the flame thickness.

In an edge flame behind a splitter plate, Fernández et al. (2000) finds that blow-out occurs gradually when  $\beta < 10$  and suddenly when  $\beta > 10$ . The parameter  $\beta$  is the Zeldovich number and is approximately equal to  $T_a/T_f$ . The corner flame in chapter 6 was studied at  $\beta = 3.5$  and blow-out was found to be gradual. The reaction scheme developed in chapter 5, which is used in this chapter, is characterized by  $\beta = 3.8$  and would also result in a gradual blow-out in the corner flame configuration. However, in this chapter the flame is sometimes tucked behind the step and sudden blow-out is possible. FSP<sub>4</sub> attempts to converge to a stationary solution. If a stationary solution cannot be found, sudden blow-out could have taken place. Another possibility is that the stationary solution is aerodynamically unstable.





**Figure 8.4:** *Grids used for numerical calculations of the flame behind a step over a liquid reactant, which corresponds to the case of a cryogenic injector. At the bottom boundary, gaseous oxygen enters at a speed dictated by the temperature gradient (Appendix C). At the left boundary, hydrogen enters at a uniform velocity. The lip is maintained at the temperature of the incoming hydrogen flow. (The temperature of the lip has little influence when it is between the temperature of the hydrogen and oxygen streams). Pressure feedback is prescribed at the top and the right boundary.*



**Figure 8.5:** Flow configurations at different values of  $\Psi$ , which is the ratio of the step height,  $h_s$ , to the flame thickness,  $\delta_f$ . For  $\Psi > 1$  the flame tip is tucked into a slow-moving region behind the step. For  $\Psi < 1$  the flame cannot support itself in this region. It becomes exposed to the free stream and blows off.  $U_{H_2} = 150 \text{ ms}^{-1}$ ,  $T_{H_2} = 350 \text{ K}$ .

## 8.7 Tests and results

### 8.7.1 Non-dimensional step height, $\Psi$

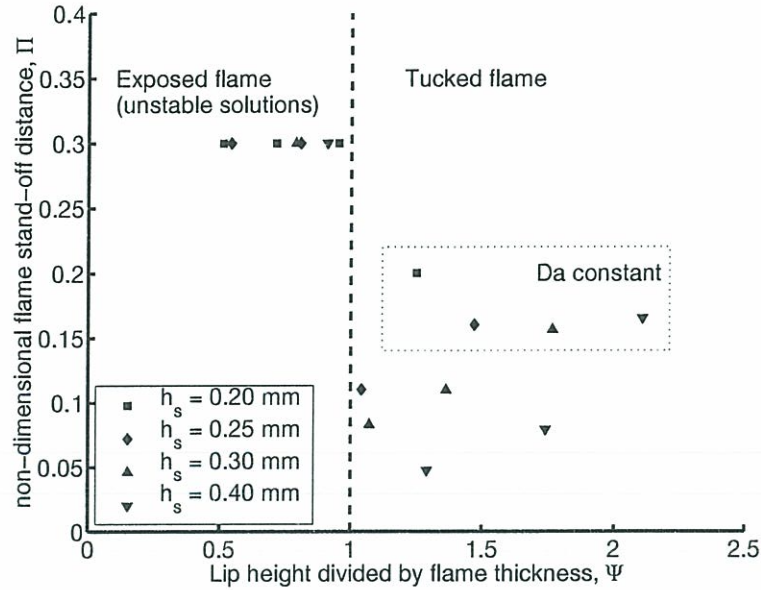
The first set of simulations concern the parameter  $\Psi$ , which denotes the ratio of the step height,  $h_s$ , to the flame thickness,  $\delta_f$ . Both the flame thickness and the step height are varied in order to check scale-invariance with respect to  $\Psi$ . The flame thickness scales with  $\tau_c^{1/2} \mathcal{D}^{1/2}$ , so either the chemical time or the diffusivity can be changed. This risks changing the Damköhler number since in these simulations,  $U$  is held constant. ( $Da = \mathcal{D}^{1/2} U^{-1} \tau_c^{-1/2}$  if convection-controlled and  $Da = A^{-1/2} \tau_c^{-1/2}$  if strain rate-controlled). We choose to increase  $\mathcal{D}$  since increasing  $\tau_c$  risks causing extinction via a mechanism involving the Damköhler number.

For each value of  $h_s$ , simulations are performed at four values of  $\mathcal{D}$ . The other molecular transport coefficients,  $\nu$  and  $\lambda$  are changed so that the Lewis and Prandtl numbers  $Le = Pr = 1$ . Rather than rely on the relation  $\delta_f \sim \tau_c^{1/2} \mathcal{D}^{1/2}$ , which is only approximate, the flame’s thickness across the trailing diffusion flame is measured from the results. It is defined as the distance between the points where the heat release rate is 5% of the maximum.

A sample of the results with  $h_s = 0.20 \text{ mm}$  is shown in figure 8.5. In all cases at this high value of  $U_{H_2}$ , the hydrogen stream separates from the edge of the step. There are two types of result, depending on  $\Psi$ . When the step is thick, figure 8.5a, the flame can tuck into the slow-moving region behind the step. All the fields corresponding to this situation are shown in figure 8.7. This is similar to the results of Oefelein (1997) and Deshpande et al. (1997). However, when the step is small, figure 8.5c, the flame is forced out of this zone. It then finds itself exposed to the main stream and is swept away. In the stationary numerical platform FSP<sub>4</sub>, the latter type of solution is stable only for low hydrogen velocity.

Results from all simulations at all step heights are summarized in figure 8.6. The transition from a “tucked” flame to an unstable “exposed” flame is seen very clearly at





**Figure 8.6:** Flame stand-off distance as a function of  $\Psi$  for four values of the step height,  $h_s$ . For  $\Psi > 1$  the flame stabilizes just behind the step and  $L_c$  is measured along the stoichiometric contour. For  $\Psi < 1$  the flame is exposed to the main stream. These solutions are unstable and eventually exit the domain.  $U_{H_2} = 150 \text{ ms}^{-1}$ ,  $T_{H_2} = 350 \text{ K}$ .

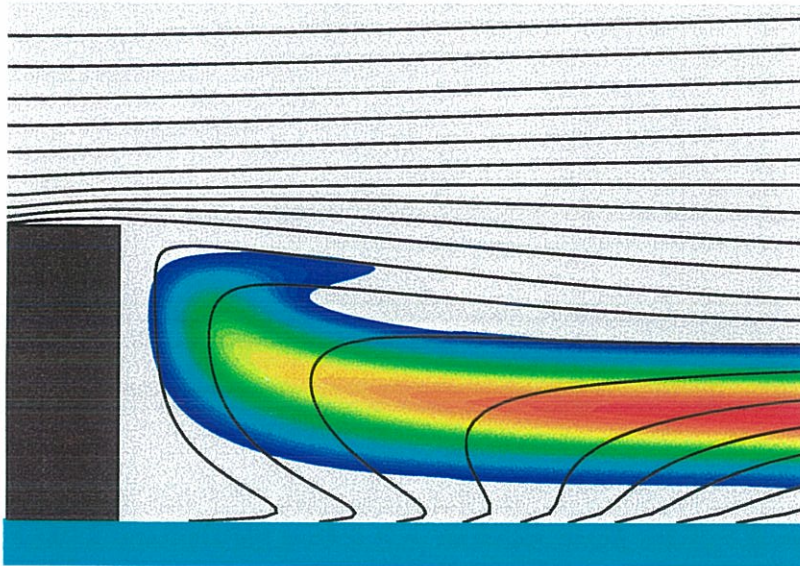
$\Psi = 1$ . The four simulations in the box in figure 8.6 are at the same Damköhler number but have different values of  $h_s$ . The flame stand-off distance is approximately constant, which demonstrates that  $\Psi$  has a relatively small effect except around  $\Psi = 1$ . One can see that at a given value of  $h_s$ ,  $\Pi$  diminishes as  $\Psi$  reduces but this is only because, in these simulations, the Damköhler number increases simultaneously.

### 8.7.2 Exposed flame

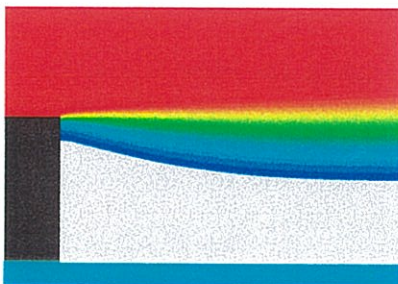
Two sets of simulations are carried out on the exposed flame:

- The hydrogen temperature is reduced from 350K to 30K in steps of 40K
- The velocity is swept from 10 to 290  $\text{ms}^{-1}$  in steps of 20  $\text{ms}^{-1}$ .

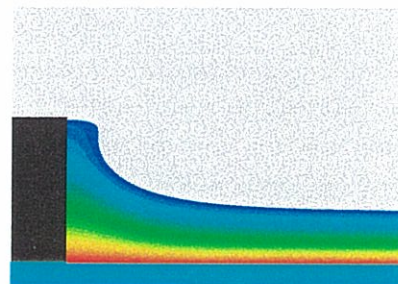
When the flame is exposed to the hydrogen stream it is very sensitive to this stream's velocity and temperature. The flame is only stable at low hydrogen velocities (below 30  $\text{ms}^{-1}$ ). At higher velocities, the simulations show a flame kernel which is convected downstream, exiting the domain after sufficient time. This non-steady feature should be interpreted with caution, since the numerical platform can only resolve stationary solutions. By comparing the numerical studies of a flame over a liquid fuel in chapter 7 with the experimental results of Rohmat et al. (1998), we can conclude that the early part of this regime probably corresponds to an oscillation of the flame kernel which our simulations cannot capture. The later part certainly corresponds to flame blow-off.



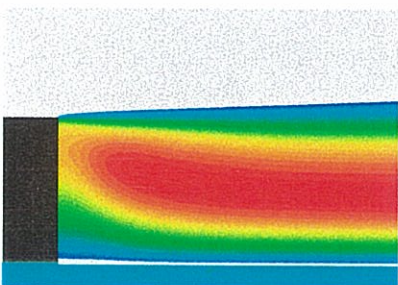
(a) Streamlines and volumetric heat release ( $\text{max} = 1.2 \times 10^{11} \text{ Jm}^{-3}\text{s}^{-1}$ )



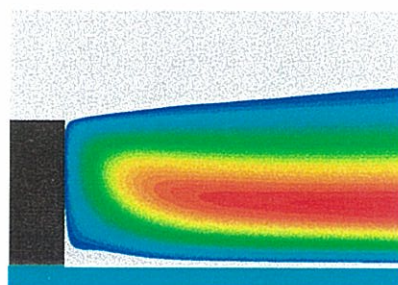
(b) Mass fraction of  $\text{H}_2$



(c) Mass fraction of  $\text{O}_2$



(d) Mass fraction of  $\text{H}_2\text{O}$



(e) Temperature ( $\text{max} = 3200 \text{ K}$ )

**Figure 8.7:** *Hydrogen flame above condensed oxygen tucked behind a step of height 0.4 mm.  $U_{\text{H}_2} = 190 \text{ ms}^{-1}$ ,  $T_{\text{H}_2} = 350 \text{ K}$ ,  $T_{\text{LO}_2} = 90 \text{ K}$ ,  $p = 1 \text{ bar}$ .*



This leads to the conclusion that at realistic operating points ( $U_{H_2} > 30\text{ms}^{-1}$ )  $\Psi$  must be greater than unity for a stable flame to exist. i.e. the lip of the oxygen tube must be thicker than the flame.

### 8.7.3 Tucked flame - effect of Spalding transfer coefficient

In chapter 7 it was shown that  $B_{sp}$  has little influence on a flame in a boundary layer flow above a liquid fuel. However, when the flame tip is tucked behind the step, the flow is not at all like a boundary layer. Consequently the effect of  $B_{sp}$  needs to be re-examined. Since  $B_{sp} \approx Y_{O_2\infty}q/\Delta h_v$  either the latent heat of vaporization,  $\Delta h_v$ , or the heat release on reaction,  $q$ , can be altered. ( $Y_{O_2\infty}$  is the mass fraction of oxygen in the free stream. For the cryogenic situation this should be replaced with  $Y_{H_2\infty}$  and is, in any case, equal to 1). In these simulations,  $\Delta h_v$  is changed because altering  $q$  would affect the chemical time.

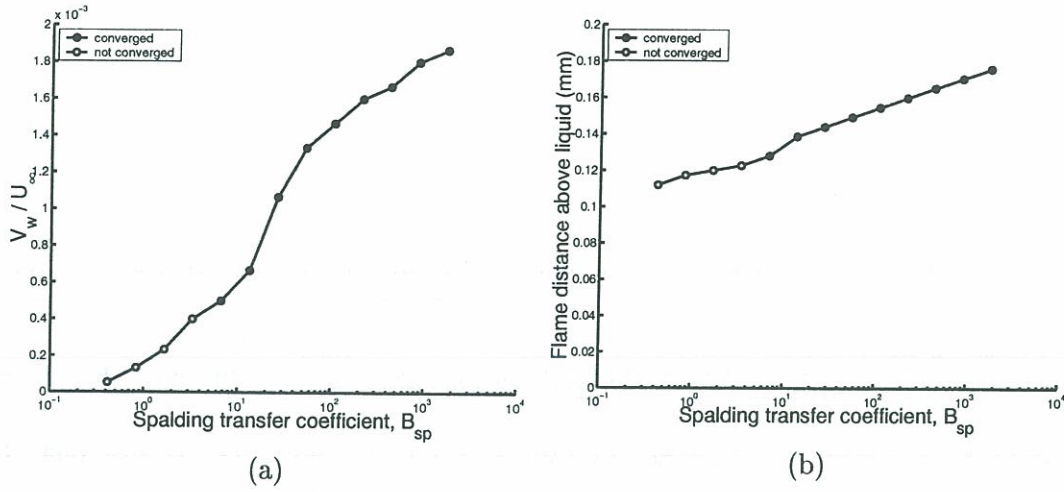
With  $h_s = 0.4\text{mm}$ ,  $B_{sp}$  is varied by over 3 orders of magnitude. The Stephan flow velocity,  $V_w$ , is measured at a distance of 0.6 mm from the lip, where the profile has become flat. This is plotted as a function of  $B_{sp}$  in figure 8.8.  $B_{sp}$  is approximately 60 in a cryogenic injector. It can be seen from the graph that, at this point,  $B_{sp}$  has some effect on  $V_w/U$ . However, increasing  $V_w$  has little effect on the flame position and no effect on the flame thickness. Consequently in the range found in cryogenic injectors,  $B_{sp}$  does not affect flame stabilization.

At  $B_{sp} < 3$ , corresponding to a value of  $\Delta h_v$  which is twenty times higher than the actual value for oxygen, the solution which the numerical platform finds is not stable. This could correspond to quenching on the liquid surface or could simply be a numerical problem. Refining the grid does not lead to a stable solution and neither is the instability due to vortex shedding from the lip. This point is not explored further because it is beyond a physically realistic range of  $B_{sp}$ .

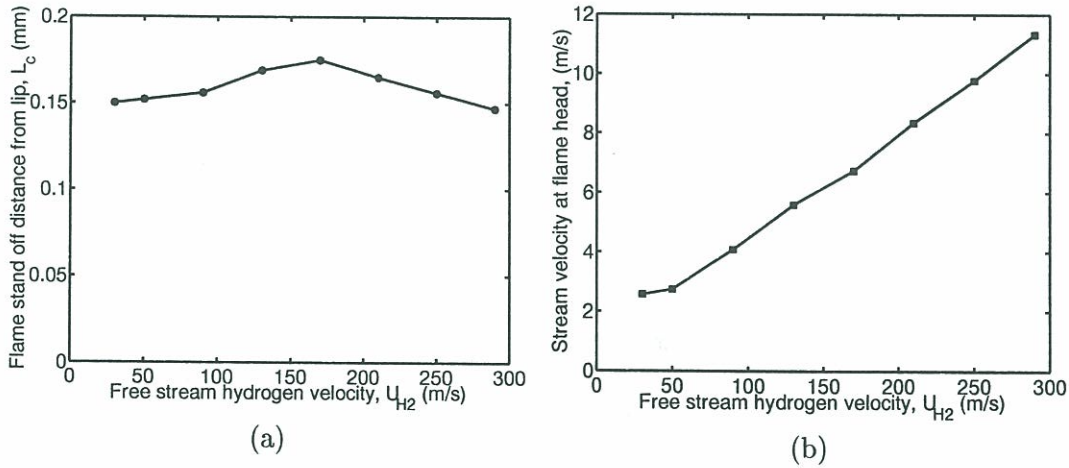
### 8.7.4 Tucked flame - effect of Damköhler number via changing hydrogen velocity

A flame in a corner can be described by a convection Damköhler number or a strain-rate Damköhler number. When the flame is tucked behind a step it is not clear which Damköhler should be used or on which velocity it should be based. In this section the effect of the free stream velocity is examined at four step thicknesses: 0.2 mm, 0.25 mm, 0.3 mm and 0.4 mm. The results are presented in figures 8.11 to 8.14 over a velocity range from  $2\text{ms}^{-1}$  to  $270\text{ms}^{-1}$ . One notes that at high  $U_{H_2}$ , the tip of the flame remains tucked in a region of slow flow behind the lip, relatively unaffected by the free stream velocity.

This effect is quantified for the case where the step height is 0.4 mm. Variables are extracted along the contour of mixture fraction which passes through the centre of the flame. (When the flame is close to the liquid core, this is slightly different from the stoichiometric mixture fraction contour). The flame stand-off distance is defined as the position along this contour where the reaction rate passes a certain threshold. This is plotted in figure 8.9a and the velocity magnitude at this point is plotted in figure 8.9b. While the velocity at the flame edge is proportional to  $U_{H_2}$ , the flame stand-off distance is affected very little by  $U_{H_2}$ .



**Figure 8.8:** (a) Stephan flow velocity and (b) distance between the liquid and the center of the trailing diffusion flame as a function of  $B_{sp}$  for a hydrogen flame above condensed oxygen behind a step. Step height = 0.4 mm,  $U_{H_2} = 150 \text{ ms}^{-1}$ ,  $T_{H_2} = 350 \text{ K}$ ,  $T_{LOx} = 90 \text{ K}$ ,  $p = 1 \text{ bar}$ .



**Figure 8.9:** (a) Flame stand-off distance and (b) velocity at the flame tip as a function of free stream hydrogen velocity. Step height = 0.4 mm,  $B_{sp} = 60 \text{ ms}^{-1}$ ,  $T_{H_2} = 350 \text{ K}$ ,  $T_{LOx} = 90 \text{ K}$ ,  $p = 1 \text{ bar}$ .



When the velocity is increased further the numerical platform fails to converge. This is due to aerodynamic instabilities which would lead to vortex shedding off the step in an unsteady simulation. This feature is studied in section 8.7.5. This does not affect the main point of this section which is that flame stability is relatively unaffected by the hydrogen velocity.

### 8.7.5 Tucked flame - effect of Damköhler number - varying hydrogen temperature

In chapters 6 and 7 the chemical time was approximated by the ignition time of a homogenous mixture in order to model the effect of  $T_{in}$ . This was successful because the stand-off distance of the corner flame is determined by a balance between convection and ignition and the flame thickness is not crucial. However, in the situation behind a step, the flame's thickness,  $\delta_f$ , relative to the step size becomes a crucial parameter. One must ensure that, when one alters the Damköhler number, one does not cause the parameter  $\Psi \equiv h_s/\delta_f$  to increase above unity, since this causes a qualitative change in the flow. The flame thickness scales with  $\tau_c^{1/2} \mathcal{D}^{1/2}$  but it is important to note that this particular chemical time has little dependence on  $T_{in}$  and should not therefore be equated to the ignition time. Consequently, altering the pre-exponential factor  $B$  changes the flame thickness while altering  $T_{in}$  does not. For this reason  $T_{in}$  was altered and  $B$  was held constant in the following simulations on step sizes of 0.4 mm and 0.2 mm. The temperature of the step is held at the free stream temperature.

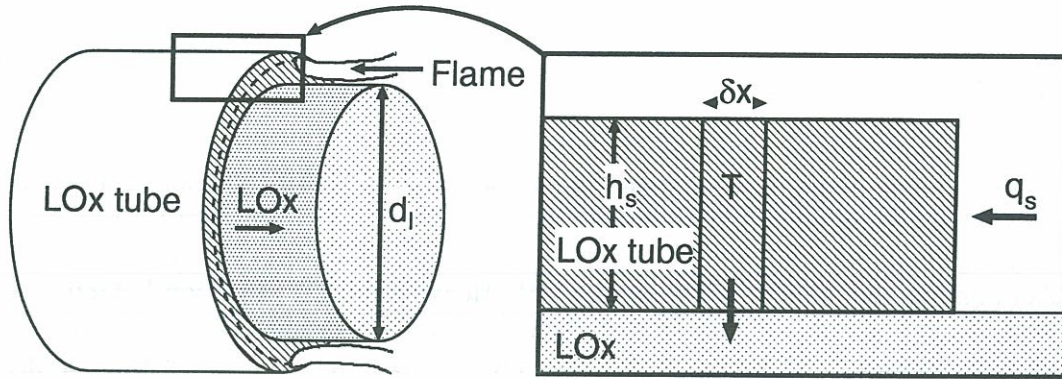
Results are shown in figures 8.15 and 8.16 for hydrogen temperatures between 150 K and 310 K. When the step is large, the flame position changes very little and the flame remains tucked within a region of slow flow. With a smaller step, the stand-off distance increases slightly as the inlet temperature reduces. In both cases, reducing  $T_{in}$  reduces the viscosity, which increases the Reynolds number. Below 150 K there is no stationary solution, due to aerodynamic instabilities, so the numerical platform cannot converge. By artificially increasing the viscosity one can achieve a stable flame once more, even at low inlet temperatures, which suggests that the flame can remain stabilized below 150 K. However, this cannot be taken to be a rigorous demonstration of this proposal.

To study this feature further, two unsteady numerical simulations were performed, one with a step of 0.20 mm, the other with a step of 0.40 mm. The hydrogen inlet temperature was reduced to 130 K for  $h_s = 0.20$  mm and to 100K for  $h_s = 0.40$  mm. Frames from these unsteady simulations are shown in figures 8.17 and 8.18. In the first situation, the flame is almost as thick as the step and, at this low temperature, starts at the downstream end of the slow-moving zone behind the step. Vortices released from the back of the step interact strongly with the flame head and this eventually leads to extinction. In the second situation, the flame is much thinner than the step and the tip remains well inside the region of slowly rotating flow despite the fact that the step is at a low temperature. The flame is some distance from the vortices shed from the step and is unaffected by them. This behaviour is seen by Delhay et al. (1994) for a flame to one side of a mixing layer. Vortex shedding is also seen by Oefelein (1997) in his numerical study of the stabilization zone of a cryogenic flame and, similarly, the flame is situated far from this region.

The crucial point here is that if the step is large with respect to the flame thickness, the flame can remain in the region just behind the step, unaffected by vortex shedding,



even at low Damköhler numbers. On the other hand if the step is small, the vortices which are shed react strongly with the flame tip and can lead to extinction. Consequently, this study of the effect of the Damköhler number highlights the importance of the parameter  $\Psi$ .



**Figure 8.10:** The temperature at the tip of the LOx tube can be estimated by balancing the heat conduction from the flame with heat conduction to the LOx stream. This development is in section 8.7.6.

### 8.7.6 Heat transfer to the step

A flame which is stabilized close to the step could cause damage due to excessive heat transfer. The heat transfer can be estimated from the adiabatic flame temperature (3200 K in these simulations), the stand-off distance  $L_c$  (figure 8.9a) and the thermal conductivity, calculated from table 8.1. By this method, however, it would be necessary to assume a linear temperature profile which would not take into account the possibility of cold fluid coming between the step and the flame. Alternatively, one can simply extract this information from the numerical simulations.

The numerical simulations were performed assuming that the step is at a constant predetermined temperature. This is a gross simplification, so these results should be treated with caution. In figure 8.19a the heat transfer profile is shown for three step heights. The maximum value of  $q_s = 3 \times 10^6 \text{ Wm}^{-2}$  seems high but is reasonable when one compares it with the heat transfer to a sparking electrode, which is around  $150 \times 10^6 \text{ Wm}^{-2}$  for a plasma at 12000 K. Generally speaking, the larger the step is the closer the flame approaches, leading to increased heat transfer. In this set of simulations, the step had a constant temperature of 330 K. In figures 8.19b and 8.19c the heat transfer profile is shown for the 0.4 mm and 0.25 mm steps at different values of step temperature. One might expect the flame to approach the step when it is at higher temperature, an effect which is observed when one assumes that the step is adiabatic. However, the constant temperature step also transfers heat to the flow, particularly close to the liquid, increasing the vaporization rate of the oxygen. This pushes the flame tip away from the step.

Heat conduction within the step and transfer to the incoming oxygen and hydrogen streams must be taken into account. The model demonstrated in figure 8.10 can be used.



Across a section of the LOx tube of width  $\delta x$ , the difference in heat flow within the metal equals the heat flow out to the oxygen stream. (The heat flow to the hydrogen stream is neglected since it will be considerably lower). This can be expressed as:

$$(\pi d_l h_s) \left[ \left( -\lambda_m \frac{dT}{dx} \right)_x - \left( -\lambda_m \frac{dT}{dx} \right)_{x+\delta x} \right] = h(T - T_{LOx})(\pi d_l \delta x) \quad (8.1)$$

where  $h_s$  is the thickness and  $d_l$  is the diameter of the LOx tube. The coefficient  $h$  is the surface heat transfer coefficient to the liquid and  $\lambda_m$  is the thermal transfer coefficient of the metal which constitutes the LOx tube. In the limit  $\delta x \rightarrow 0$ , equation (8.1) becomes:

$$\frac{d^2 T}{dx^2} - \frac{h}{\lambda_m h_s} (T - T_{LOx}) = 0 \quad (8.2)$$

which has general solution:

$$T = T_{LOx} + A \cosh(mx) + B \sinh(mx) \quad (8.3)$$

where

$$m = \left( \frac{h}{\lambda_m h_s} \right)^{1/2}$$

With the boundary condition that  $T = T_{LOx}$  at  $x = 0$  and that  $q_s$  is the heat flux (in  $\text{Wm}^{-2}$ ) at  $x = L$ , one obtains:

$$T = T_{LOx} + q_s \left( \frac{h_s}{h \lambda_m} \right)^{1/2} \frac{\sinh(mx)}{\cosh(mL)} \quad (8.4)$$

If  $mL$  is large then:

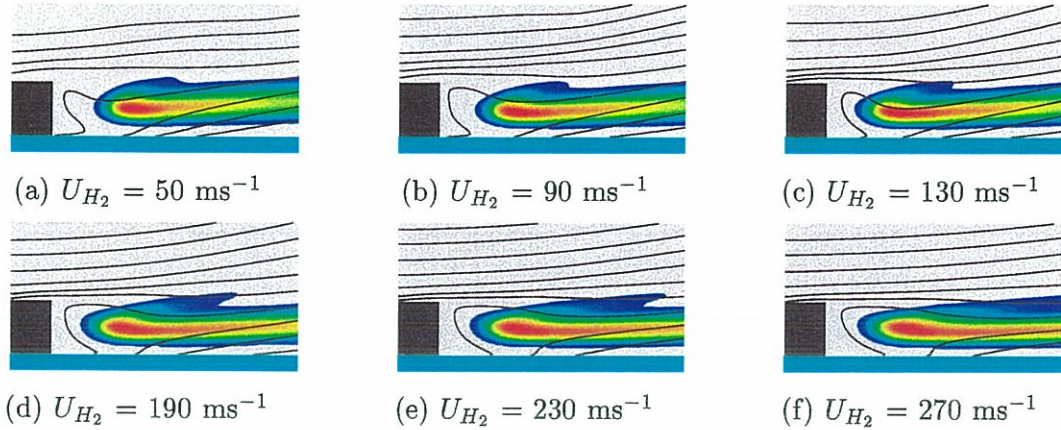
$$T(x = L) \approx T_{LOx} + q_s \left( \frac{h_s}{h \lambda_m} \right)^{1/2} \quad (8.5)$$

The temperature at the tip of the oxygen tube can now be estimated. One can use the following properties for liquid oxygen:  $\mu = 2.5 \times 10^{-4} \text{ Pa s}$ ,  $\rho = 1180 \text{ kgm}^{-3}$ ,  $\lambda = 0.166 \text{ Wm}^{-1}\text{K}^{-1}$ ,  $c_p = 1656 \text{ Jkg}^{-1}\text{K}^{-1}$ . With these properties, the Prandtl number is  $\text{Pr} = 2.49$ . The Reynolds number based on the tube diameter and a typical velocity is 52000. The Nusselt number can be estimated from  $\text{Nu} = 150 \text{ Pr}^{0.4} = 216$ . Since  $\text{Nu} \equiv h d_l / \lambda$  one can estimate  $h$  as  $7200 \text{ WK}^{-1}$ . If the metal is steel,  $\lambda_m = 50 \text{ Wm}^{-1}\text{K}^{-1}$  and the average thickness can be taken to be 1 mm. Assuming that the heat flux to the tip is  $q_s = 4 \times 10^6 \text{ Wm}^{-2}$ , equation (8.5) gives the temperature as:

$$T(x = L) = T_{LOx} + 210 \approx 300 \text{ K}$$

This is consistent with a heat transfer of around  $q_s = 4 \times 10^6 \text{ Wm}^{-2}$  from figure 8.19b. Note that if the oxygen becomes gaseous, the surface transfer coefficient,  $h$ , decreases by at least an order of magnitude. This leads to a much higher value for the temperature of the tip of the tube.

In conclusion, heat conduction within the step must be taken into account in order to calculate the step temperature and, consequently, the heat transfer to the step from the flame. Even when the heat transfer to the step is large, the cooling effect of the liquid oxygen stream ensures that its temperature is not excessive. This will not be the case if the oxygen stream separates from the tube.



**Figure 8.11:** Heat release rate (colour) and streamlines for a hydrogen flame above condensed oxygen behind a step. Step height = 0.20 mm,  $T_{H_2} = 350 \text{ K}$ ,  $T_{LOx} = 90 \text{ K}$ ,  $p = 1 \text{ bar}$ .

## 8.8 Conclusion

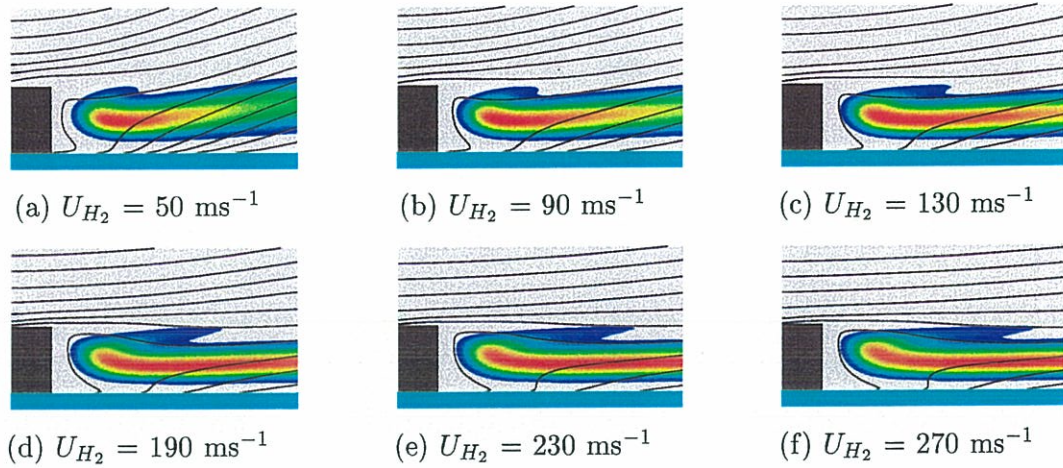
In this chapter it is shown that stabilization of a flame behind a step over a liquid fuel is dominated by the height of the step relative to the flame thickness. When this factor,  $\Psi$ , is small, one approaches the situation with no step in chapter 7. Under these conditions the flame is very sensitive to the free stream velocity and temperature. At conditions found in a typical cryogenic rocket motor the flame will not be stabilized.

On the other hand, when the step is thick relative to the flame thickness, the flame can tuck into the slow-moving region behind the step. In this position it is insensitive to the free stream velocity and is only slightly sensitive to the free stream and step temperature.

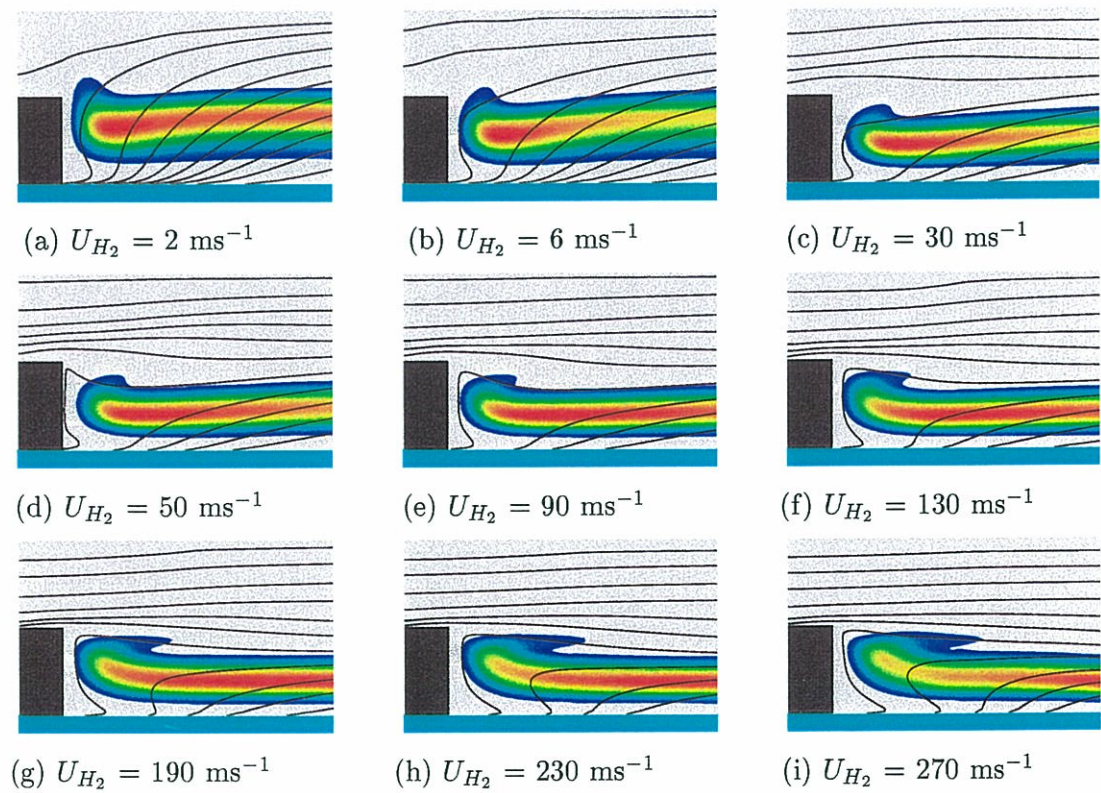
There is a further feature of flow behind a step which confirms the influence of  $\Psi$ . If  $\Psi$  is around unity, vortices shed off the back of the step interact with the flame tip, which can also lead to extinction. If, however,  $\Psi$  is sufficiently greater than 1 (above around 1.5), the vortices form above the flame tip and do not affect it.

Some of these results can be extrapolated to analyse ignition of the cryogenic flame. This is dealt with in chapter 9.

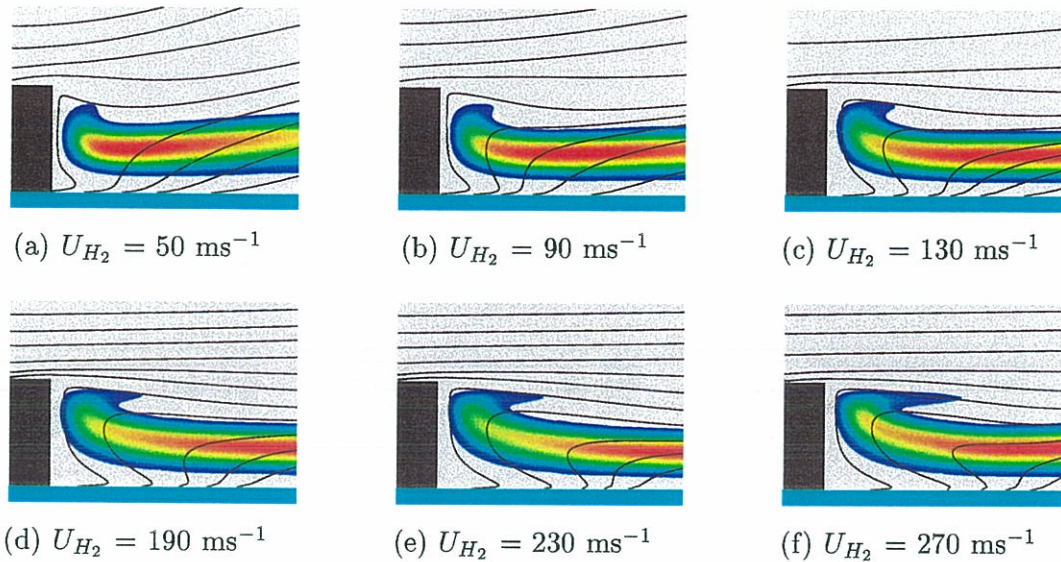




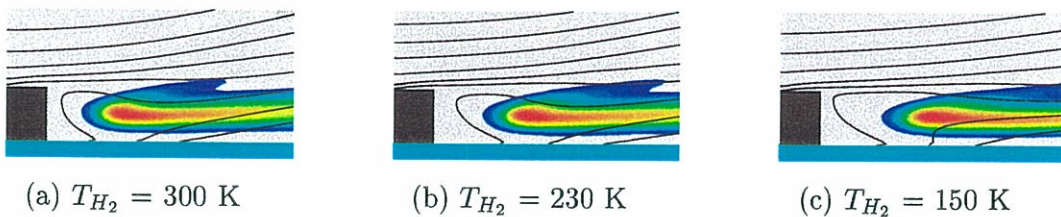
**Figure 8.12:** Heat release rate (colour) and streamlines for a hydrogen flame above condensed oxygen behind a step. Step height = 0.25 mm,  $T_{H_2} = 350 \text{ K}$ ,  $T_{LOx} = 90 \text{ K}$ ,  $p = 1 \text{ bar}$ .



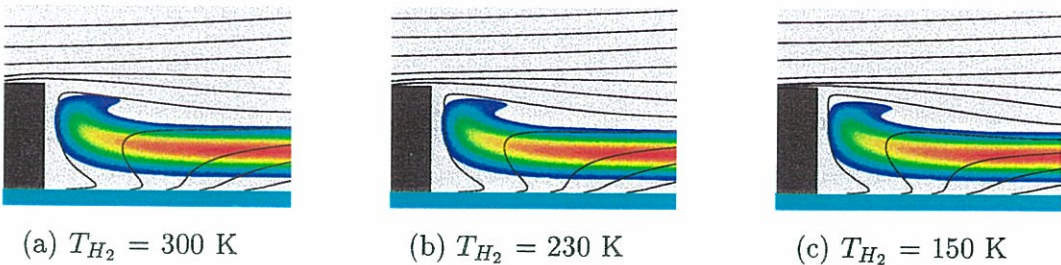
**Figure 8.13:** Heat release rate (colour) and streamlines for a hydrogen flame above condensed oxygen behind a step. Step height = 0.30 mm,  $T_{H_2} = 350 \text{ K}$ ,  $T_{LOx} = 90 \text{ K}$ ,  $p = 1 \text{ bar}$ .



**Figure 8.14:** Heat release rate (colour) and streamlines for a hydrogen flame above condensed oxygen behind a step. Step height = 0.40 mm,  $T_{H_2} = 350 \text{ K}$ ,  $T_{LOx} = 90 \text{ K}$ ,  $p = 1 \text{ bar}$ .

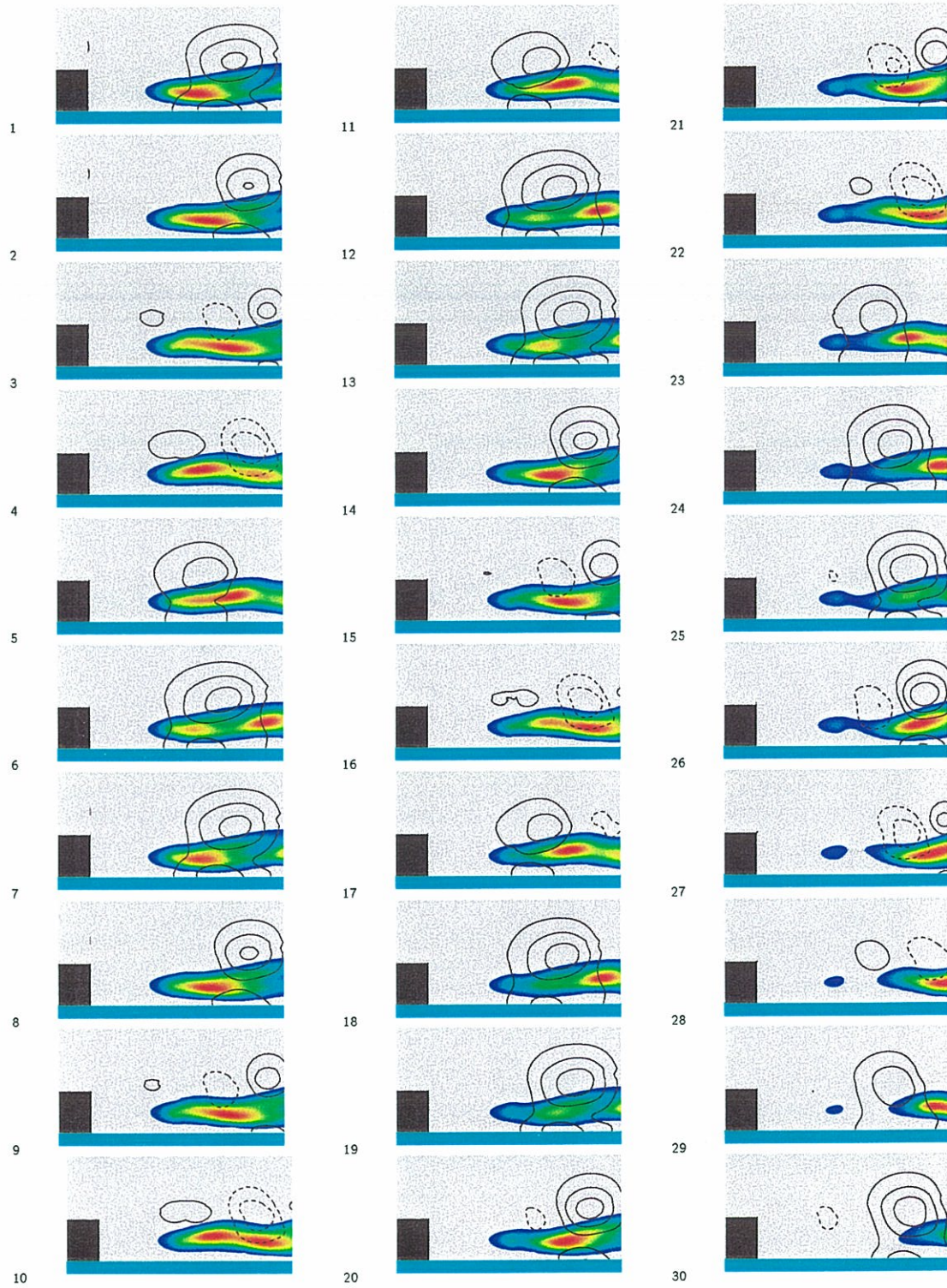


**Figure 8.15:** Heat release rate (colour) and streamlines for a hydrogen flame above condensed oxygen behind a step. Step height = 0.20 mm,  $U_{H_2} = 150 \text{ ms}^{-1}$ ,  $T_{LOx} = 90 \text{ K}$ ,  $p = 1 \text{ bar}$ .



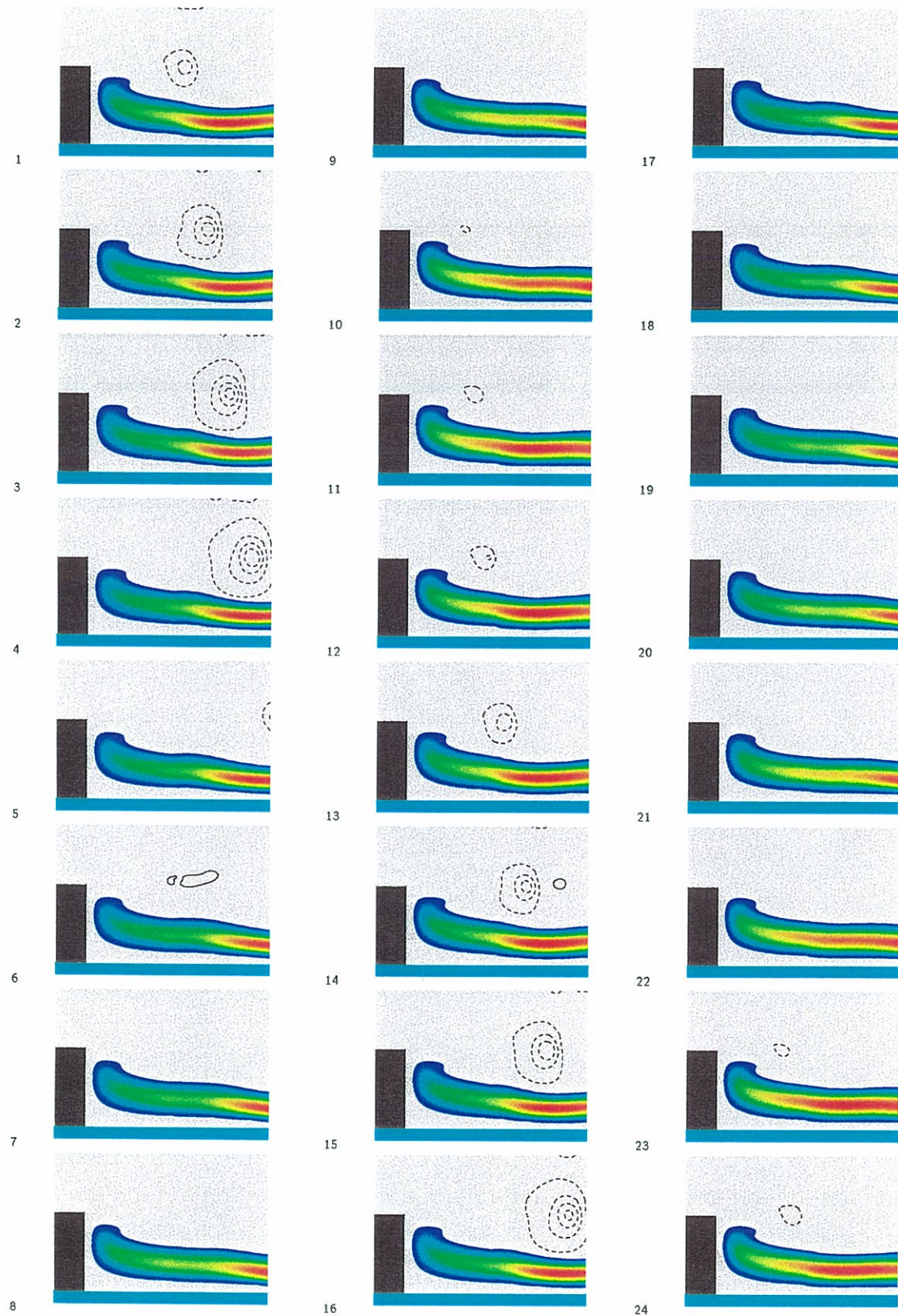
**Figure 8.16:** Heat release rate (colour) and streamlines for a hydrogen flame above condensed oxygen behind a step. Step height = 0.40 mm,  $U_{H_2} = 150 \text{ ms}^{-1}$ ,  $T_{LOx} = 90 \text{ K}$ ,  $p = 1 \text{ bar}$ .





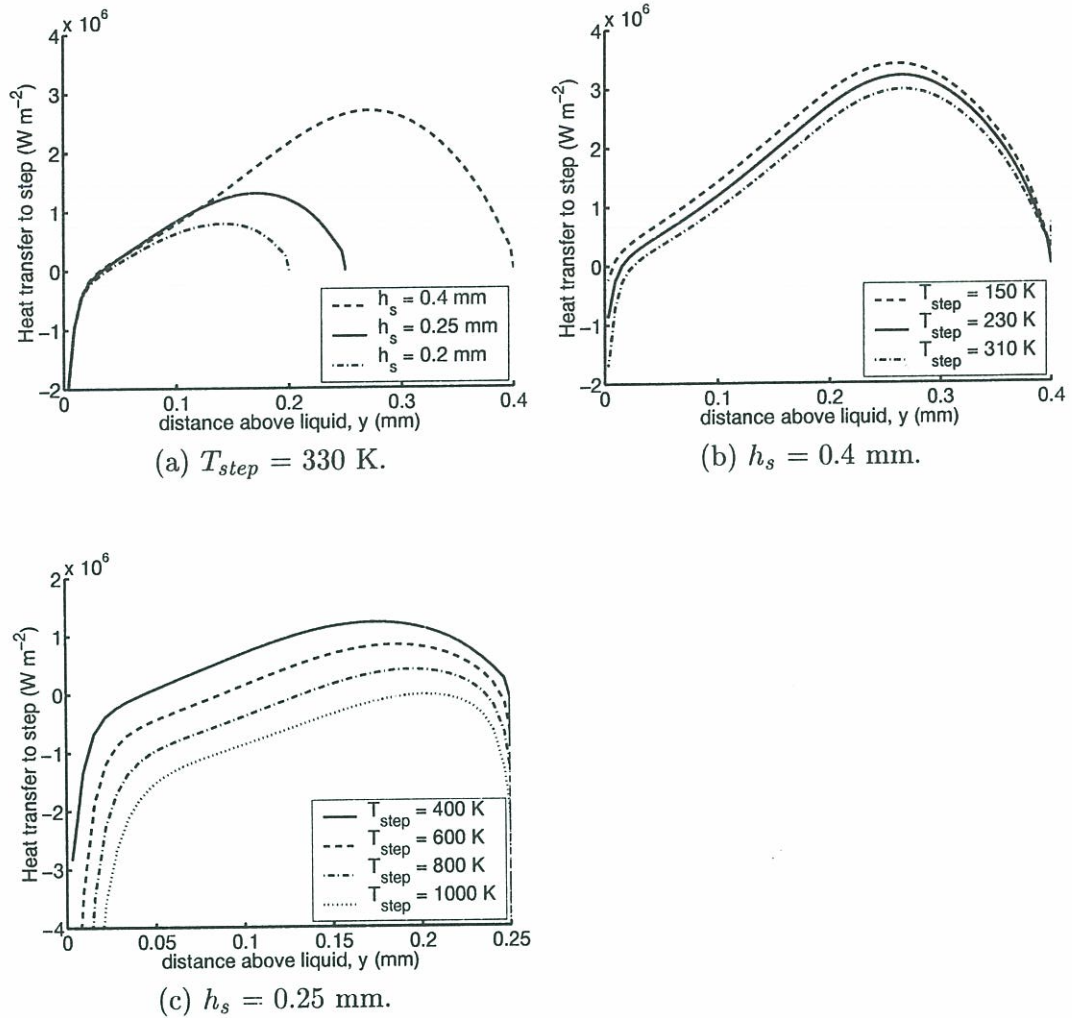
**Figure 8.17:** Heat release rate (colour) and pressure contours in an unstationary simulation of a hydrogen flame above a condensed oxygen surface behind a step. Dotted contours, of negative gauge pressure, correspond to vortex cores. Step height = 0.20 mm,  $U_{H_2} = 150 \text{ ms}^{-1}$ ,  $T_{H_2} = 130 \text{ K}$ ,  $T_{LOx} = 90 \text{ K}$ ,  $p = 1 \text{ bar}$ ,  $\Delta t = 0.25 \text{ ms}$ .





**Figure 8.18:** Heat release rate (colour) and pressure contours in an unstationary simulation of a hydrogen flame above a condensed oxygen surface behind a step. Dotted contours, of negative gauge pressure, correspond to vortex cores. Step height = 0.40 mm,  $U_{H_2} = 150 \text{ ms}^{-1}$ ,  $T_{H_2} = 100 \text{ K}$ ,  $T_{LOx} = 90 \text{ K}$ ,  $p = 1 \text{ bar}$ ,  $\Delta t = 0.05 \text{ ms}$ .





**Figure 8.19:** Heat transfer to the step as a function of step height and step temperature.  $U_{H_2} = 150 \text{ ms}^{-1}$ ,  $T_{H_2} = 350 \text{ K}$ ,  $T_{LOx} = 90 \text{ K}$ ,  $p = 1 \text{ bar}$ . (a) Step temperature is constant, step height is changed. (b) and (c) Step height is constant, step temperature is changed.





## Chapter 9

# Conclusions

Les conclusions de ce projet de recherche sont intéressantes sur le plan scientifique et d'un point de vue technologique. On va passer en revue les points marquants du projet en considérant successivement

- La structure de la flamme et les effets du retrait
- La stabilisation de la flamme

### Structure de flamme et effets du retrait

Des visualisations de flamme et du jet d'oxygène ont été réalisées sur le banc cryotechnique de l'ONERA. L'expérimentation a été effectuée dans une large gamme de pression avec en particulier des tirs à très haute pression (70 bar). Il a aussi été possible d'étudier l'effet de la température d'injection de l'hydrogène. Des analyses fondamentales sur les diagnostics optiques et l'utilisation simultanée de deux caméras ICCD ont permis l'acquisition d'images de bonne qualité. Les images montrent simultanément le jet d'oxygène et la flamme. La structure de cette flamme est clairement mise en évidence. De plus, la vitesse des structures dans la chambre a pu être estimée par le biais d'une technique de double imagerie dans laquelle les images de la flamme sont prises en décalant l'acquisition d'un délai très bref.

La flamme brûle dans le mode de combustion de groupe externe. Les angles d'expansion de la flamme ont été mesurés à partir des valeurs de toutes les campagnes menées sur Mascotte. La pression varie de 1 à 70 bar et le rapport des flux de quantité de mouvement de 4 à 15. En s'appuyant sur un modèle unidimensionnel simplifié pour l'expansion de la flamme, on remarque un changement de comportement entre les pressions de 10 et 70 bar. La pression exacte correspondant vraisemblablement à cette transition est la pression critique de l'oxygène à 50.5 bar. Au dessus de cette pression, le temps caractéristique de vaporisation diminue fortement. Les résultats expérimentaux et théoriques suggèrent que le taux de combustion est limité par la vaporisation en dessous de la pression critique et limité par le mélange au dessus de cette pression. On peut conclure que, dans une chambre de combustion diphasique qui fonctionne au dessus de la pression critique de l'ergol liquide, la conception devrait assurer un bon mélange plutôt qu'une bonne atomisation.

Les facteurs qui influencent la rupture dans les jets coaxiaux et les mécanismes d'instabilité primaires sont ensuite envisagés et une synthèse est proposée. Il est démontré que le mécanisme



d'instabilité de couche de cisaillement est équivalent au mécanisme de Kelvin-Helmholtz pur, sans tension superficielle, quand la longueur d'onde est grande par rapport à l'épaisseur de la couche de cisaillement. Cette équivalence justifie les simplifications dans le modèle du sillage confiné qui est utilisé pour expliquer l'effet du retrait. Par le biais de ce modèle il est démontré que le retrait provoque une instabilité absolue dans l'écoulement d'oxygène à l'origine de l'injecteur. Une instabilité globale est donc déclenchée qui augmente la rupture du jet. Cette analyse est confirmée par les observations expérimentales, à la fois sur le banc cryotechnique et sur un injecteur de laboratoire. Ce mécanisme peut aussi expliquer pourquoi il existe une valeur optimale du retrait. Le conduit d'oxygène doit être suffisamment éloigné du plan d'injection pour provoquer cette instabilité globale sans être trop en recul dans une situation où le confinement empêche l'épanouissement du brouillard. Un mécanisme indépendant de celui qui vient d'être décrit implique la combustion à l'intérieur de l'injecteur. Cette combustion entraîne une production de gaz chauds qui occupent une partie de la section de passage. La vitesse de l'hydrogène est ainsi augmentée, ce qui provoque une rupture du jet plus rapide.

Sur un plan plus général on peut observer que l'effet du confinement sur la déstabilisation du sillage ne semble pas avoir été étudié dans la littérature antérieure. La démonstration théorique de la possibilité d'une instabilité absolue est à notre connaissance originale. Ce résultat est d'un intérêt scientifique plus large avec plusieurs applications potentielles. En ce qui concerne le développement des technologies dans le domaine des moteurs fusées, la méthodologie suivie au chapitre 3 pour traiter l'effet du retrait peut être appliquée aux injecteurs tri-coaxiaux. Cependant, la relation de dispersion fournie par le modèle serait dans ce cas beaucoup plus compliquée car elle ferait intervenir cinq zones.

## Stabilisation de la flamme

Les résultats expérimentaux démontrent que la flamme est accrochée à la lèvre de l'injecteur d'oxygène sur toute la gamme de pression, vitesse d'hydrogène et température d'hydrogène. Il est démontré que l'extinction par étirement d'une flamme de diffusion entre hydrogène et oxygène n'est pas possible dans les conditions qui régissent dans les chambres de combustion typiques. Ceci est vrai même quand la flamme est pincée entre de l'hydrogène froid et de l'oxygène condensée. L'extinction par étirement pourrait se passer aux pressions bien inférieures à 1 bar, où la flamme est plus épaisse et moins intense. Cependant, la tête de flamme serait soufflée de la zone derrière la lèvre avant que ces conditions soient atteintes. Une étude de la zone située derrière la lèvre démontre que le rapport de la hauteur de la lèvre à l'épaisseur de la flamme est de loin le paramètre le plus important pour la stabilisation de la flamme. Quand ce rapport est plus grand qu'environ 1.5, la stabilisation est assurée sur une grande plage de températures et vitesses de l'hydrogène.

Des compromis doivent être nécessairement réalisés au cours de la conception d'un injecteur coaxial. La lèvre du conduit d'oxygène doit assurer la stabilisation de la flamme. Cependant, le transfert thermique de la flamme vers le conduit augmente avec l'épaisseur de cette lèvre, ce qui peut éventuellement conduire à des problèmes dans le cas où de l'oxygène gazeux est présent dans le conduit. La rupture du jet d'oxygène est aussi moins efficace lorsque cette épaisseur est plus grande. La méthodologie présentée aux chapitres 4 à 8 pour étudier la stabilisation peut être généralisée et appliquée à d'autres combinaisons d'ergols. Par exemple, une flamme de méthane/oxygène aura tendance à être plus épaisse et moins intense, ce qui devrait rendre



la stabilisation moins facile.

Du côté scientifique, l'étude numérique d'une flamme à contre courant au dessus d'une nappe liquide apporte des éléments nouveaux par rapport aux travaux théoriques antérieurs. Cette étude a notamment permis d'analyser les conditions d'extinction de ce type de flamme et d'examiner l'évolution du taux de réaction en fonction du taux d'étirement imposé à la flamme. Des études théoriques futures peuvent être évaluées à l'aide des lois d'échelle dérivées d'une façon numérique pour la position de la flamme dans un coin. Les simulations pourraient être répétées avec un maillage plus fin. Enfin l'analyse détaillée de l'écoulement qui s'établit autour d'une flamme stabilisée en amont d'un comburant liquide, avec ou sans une marche, apporte aussi des informations qui ne semblent pas actuellement disponibles dans la littérature spécialisée.

## Allumage

Bien que cette étude se limite à la stabilisation de la flamme, il est possible d'extrapoler quelques résultats pour traiter l'importante question de l'allumage. Il est probable que la tête de flamme se propage le long du jet d'oxygène afin d'atteindre la lèvre du conduit de l'oxygène. Ce jet d'oxygène est lent et déjà proche de sa température d'ébullition. Par conséquent, peu d'énergie est absorbée par la région liquide juste devant la tête de la flamme et la vitesse de l'oxygène n'aurait pas beaucoup d'influence sur la vitesse de propagation de la flamme. La vitesse de l'hydrogène et la pression par contre auront plus d'influence. Aux basses pressions qui régnent pendant la phase d'allumage, la flamme pourrait être trop épaisse pour s'établir de façon stable derrière la lèvre. La vitesse de l'hydrogène doit être réduite pendant cette phase jusqu'au point où la pression est suffisamment élevée pour que la flamme puisse s'accrocher définitivement au voisinage de l'injecteur.

The conclusions to this research project have both scientific and technological implications. The highlights of this work are reviewed by successively considering results obtained for:

- Flame structure and effect of recess
- Flame stabilization

## 9.1 Flame structure and effect of recess

Images of the flame and the oxygen jet were obtained on the cryogenic test facility at ONERA. Experiments were performed over a wide pressure range and at hydrogen temperatures between 100 K and 300 K. Fundamental analyses into the optical diagnostics and the use of two synchronized ICCD cameras has produced high quality images which show the LOx jet and the flame simultaneously. The flame structure can be seen clearly. Furthermore, by setting a short time delay between the two cameras one can estimate the convective velocities of structures in the chamber. This information is difficult to obtain from laser doppler velocimetry or particle image velocimetry, which require seeding with microscopic particles.

The flame burns in an external group combustion mode. The flame expansion angles have been compiled from all the experimental series' performed on the test facility. In these tests, the pressure ranges from 1 to 70 bar and the momentum flux ratio from 4 to 15. By comparison with a simple, but informative, one-dimensional model of flame expansion, one notices a change in behaviour at some point between 10 and 70 bar. This almost certainly corresponds to the critical pressure of oxygen at 50.5 bar, above which the characteristic vaporization time of oxygen decreases dramatically. The experimental and theoretical results indicate that the rate of combustion is vaporization-limited when below the critical pressure and is mixing-limited when above the critical pressure. This suggests that, rather than improving atomization, one should attempt to increase mixing inside two-phase combustion chambers designed to operate above the critical pressure of the liquid reactant.

A review is presented of the factors affecting rupture in coaxial jets and the mechanisms of primary instability. It is shown that the shear layer instability mechanism is equivalent to the pure Kelvin-Helmholtz mechanism, without surface tension, when the wavelength is long compared with the shear layer thickness. This equivalence is important in order to justify simplifications in the ducted wake model which is used to explain the effect of recess. With this model it is shown that recess causes an absolute instability in the oxygen stream at the base of the injector. This triggers a global instability which enhances jet break-up. There is compelling experimental evidence for this mechanism, both from the cryogenic facility and from laboratory scale tests. It can also explain why there is an optimum value of recess. This arises once the tube is recessed far enough to trigger the global instability but not so far that channelling the annular flow prohibits subsequent expansion of the spray. In a separate mechanism, the hydrogen velocity is increased due to blockage by combustion products in the recessed portion. This also enhances jet break-up.

The fact that confinement of a wake enhances its absolutely unstable nature does not appear in the literature. This is a result of scientific interest and has many potential



applications. As regards future rocket motor development, the methodology presented in chapter 3 to study the effect of recess can be applied to tricoaxial injectors, although the dispersion relation created by the model is significantly more complicated because one must consider five flow regions instead of three.

## 9.2 Flame stabilization

The experimental results show that the flame remains attached to the lip of the oxygen injector over the complete range of pressure, inlet velocity and hydrogen temperatures studied. It is shown that extinction of a hydrogen/oxygen diffusion flame by strain is impossible under typical combustion chamber conditions, even when pinched against the condensed oxygen. Extinction by strain may be possible at pressures well below 1 bar, where the flame is thicker and less intense. However, the flame tip would blow out of the zone behind the lip before such conditions could be reached. A study of the zone behind the lip reveals that the ratio of the lip height to the flame thickness is by far the most important parameter regarding stabilization. When this is greater than around 1.5, stabilization is assured over a wide range of hydrogen temperatures and velocities.

In designing an injector there will inevitably be a compromise. A thick oxygen injector lip will ensure stabilization of the flame. However, it will also lead to increased heat transfer to the tube, which may cause structural problems, and it will also have an adverse effect on rupture of the oxygen jet. The methodology presented in chapters 4 to 8 can, of course, be applied to other fuel combinations. For instance, a methane/oxygen flame will tend to be thicker and less intense, which will be detrimental to stabilization.

On the scientific side, the numerical study of a hydrogen counterflow diffusion flame above liquid oxygen produces new results regarding extinction and variation of heat release with strain rate. Future theoretical studies of a corner flame can be compared with the numerically-derived correlations for the flame stand-off distance derived here, although the simulations should be repeated with a smaller grid size. The study of the flow around a flame at the head of a liquid fuel, both with and without a step, produces results which are not currently available in the literature.

## 9.3 Ignition

Although this study is limited to flame stabilization, it is possible to extrapolate some results to ignition. It is likely that the flame edge travels up the condensed oxygen jet in order to reach the lip of the oxygen injector. The oxygen jet is slow-moving and is already near its boiling temperature. Consequently, little energy is absorbed by the region just in front of the flame edge and the LOx velocity is unlikely to have much effect on the flame head velocity. The hydrogen velocity and pressure are more significant. At the low pressures typically found during the ignition process the flame could be too thick to stabilize behind the lip. During this period, the hydrogen velocity must be kept low until a sufficiently high pressure has been obtained for the flame to be thin enough to stabilize behind the oxygen injector lip.





## Appendix A

# Shadowgraphy and Schlieren techniques

### A.1 Introduction

In shadowgraphy and schlieren techniques, an object is examined by recording the way it deflects light. Similar techniques include Moiré and laser deflectometry. Interesting references are Weinberg (1963), which is the major work in this field, Davies (1981) and Dunn-Rankin and Weinberg (1998). These well established techniques have the advantage that the apparatus can be set up and calibrated when the flame is not present, a very useful factor when the number of tests is severely limited, as is the case on the cryogenic test facility. However, the images require careful interpretation.

Confusion over the definitions of shadowgraphy and schlieren is resolved by Weinberg (p116). A shadowgraphy image is formed uniquely from the deflection of light, while a schlieren image is formed by rays being cut as a function of their deflection. However, it is often not appreciated that schlieren effects can occur in the image from a shadowgraphy set-up and vice-versa.

In this section, we shall examine the construction of shadowgraphy and schlieren images in the framework of geometric optics. Weinberg discusses the effect of the non-zero wavelength of light but concludes that geometric optics is sufficient in the overwhelming majority of cases. We shall examine only simple configurations, since they contain all the necessary physical effects. More specialized configurations are discussed in the above references. In an improvement on the current literature, we offer a mathematical description of the shadowgraphy image and show how this can be inverted to obtain the deflection profile from a shadowgraph's intensity profile. This mathematical description is used to characterize the distortion of a shadowgraphy image, a process which is useful for designing an experimental configuration. We then consider the images of three dimensional objects. Finally there is a discussion on the appropriate techniques for visualization of the cryogenic jet flame.

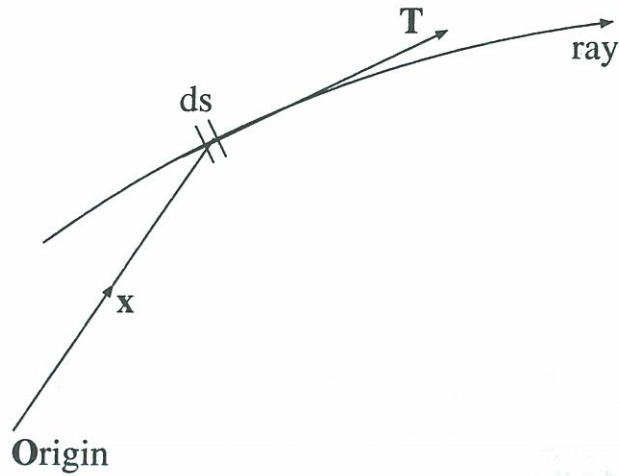


Figure A.1 : Definitions of  $\mathbf{x}$ ,  $\mathbf{T}$  and  $ds$  for a ray

## A.2 Ray deviation by a refractive index field

Light goes at different speeds through different materials. If we denote the speed of light in a vacuum as  $c$  and the speed of light in a material as  $v$ , we can define the refractive index of a material,  $n$  as the ratio of these speeds:

$$n = \frac{c}{v}$$

$n$  is always bigger than 1, being around 1.0002 for a typical gas. Different physical models have been proposed for  $n$ 's dependence on pressure and temperature. The resulting expressions, which are subtly different, diverge at larger  $n$  but are consistent for smaller  $n$ . Experimental data fail to fit any exactly, so we shall arbitrarily use the simplest: Gladstone's equation (A.1).

$$(n - 1) = k \frac{p}{T} \quad (\text{A.1})$$

The constant  $k$  depends on the chemical nature of the medium. For pure gases it increases with the molecular mass and is tabulated in, for example, Lide (1991).

### A.2.1 General Formula

Maxwell's equations in the case where the wavenumber tends to infinity reduce to give the Eikonal equation (A.2), Born and Wolf (1991).

$$(\nabla S)^2 = n^2(\mathbf{r}) \quad (\text{A.2})$$

where  $S(\mathbf{r})$  is the phase of the waves.  $S(\mathbf{r}) = \text{constant}$  defines the wavefronts.  $n(\mathbf{r})$  is the scalar refractive index field. Physically, when we assume that the wavenumber tends to infinity, we assume that the phase of the field varies much more rapidly than its



amplitude. This is not realistic near caustics, such as at the focal point of a lens or the edge of a shadow, where the amplitude variation over a small distance is appreciable.

The Poynting vector, which characterizes the energy flux of an electromagnetic field, can be derived from Maxwell's equations. It is always perpendicular to the wavefronts. We define rays of light as the field lines of the Poynting vector, thus the unit tangent to these field lines (rays) can be described by  $\mathbf{T}$  where:

$$\begin{aligned} \nabla S &= |\nabla S| \mathbf{T} \\ \text{But from equation (A.2),} \quad |\nabla S| &= n \\ \text{so that} \quad \nabla S &= n\mathbf{T} \end{aligned} \tag{A.3}$$

We shall consider one of these field lines (or rays) and define the arc length  $s$  (a scalar) as the distance along it. We now want to consider how  $\mathbf{T}$  evolves as the ray propagates through the  $n$ -field. The operator for differentiation with respect to  $s$  is :

$$\frac{d}{ds} = \mathbf{T} \cdot \nabla$$

and we apply this to both sides of equation (A.3) to find the change in the tangent for a small increment along the ray:

$$\begin{aligned} \frac{d}{ds}(n\mathbf{T}) &= \frac{d}{ds}\nabla S \\ &= (\mathbf{T} \cdot \nabla)\nabla S \\ &= \left(\frac{\nabla S}{n} \cdot \nabla\right)\nabla S \end{aligned}$$

$$\begin{aligned} \text{We now use the facts that } \nabla \mathbf{a}^2 &= 2(\mathbf{a} \cdot \nabla)\mathbf{a} + 2\mathbf{a} \times (\nabla \times \mathbf{a}) \\ \text{and } \nabla \times \nabla S &= 0 \quad \text{for any scalar function } S. \end{aligned}$$

$$\begin{aligned} \text{This yields} \quad \frac{d}{ds}(n\mathbf{T}) &= \frac{1}{2n}\nabla(\nabla S)^2 \\ &= \frac{1}{2n}\nabla n^2 \end{aligned}$$

Thus we obtain equation (A.4):

$$\frac{d}{ds}(n\mathbf{T}) = \nabla n \tag{A.4}$$

This tells us how the tangent of a ray varies along the length of a ray as it propagates through a refractive index field  $n(\mathbf{r})$ . It is independent of coordinate system. We can couple it with equation (A.5) to deduce the evolution of a given ray with position  $\mathbf{x}(s)$  and tangent  $\mathbf{T}(s)$ , through refractive index field  $n(\mathbf{r})$ .

$$\frac{d\mathbf{x}}{ds} = \mathbf{T} \tag{A.5}$$

### A.2.2 Limit for Small Deviations

For small ray deviations, we can assume that the ray deviates little from a straight line, which we can take to be the  $x$ -axis. This produces equation (A.8), which is much easier to implement than equation (A.4). The basic ray equation (A.4) is combined with the Frenet expression (A.6).

$$\frac{d\mathbf{T}}{ds} = \frac{\mathbf{N}}{\mathcal{R}} \quad (\text{A.6})$$

The ray normal,  $\mathbf{N}$ , and ray tangent,  $\mathbf{T}$ , are orthogonal, so  $\mathbf{N} \cdot \mathbf{T} = 0$ . In two dimensions, the radius of curvature is given by equation (A.7) and for small angles of deviation from the  $x$ -axis,  $\theta = \frac{dy}{dx}$ .

$$\mathcal{R} = \frac{\left(1 + \left(\frac{dy}{dx}\right)^2\right)^{\frac{3}{2}}}{\frac{d^2y}{dx^2}} \quad (\text{A.7})$$

Starting with the ray equation (A.4)  $\frac{d}{ds}(n\mathbf{T}) = \nabla n$

one obtains  $\mathbf{T} \frac{dn}{ds} + n \frac{d\mathbf{T}}{ds} = \nabla n$

Substituting the Frenet expression (A.6) yields  $\mathbf{T} \frac{dn}{ds} + n \frac{\mathbf{N}}{\mathcal{R}} = \nabla n$

This expression may be projected in the normal direction, yielding

$$\mathbf{N} \cdot \mathbf{T} \frac{dn}{ds} + \mathbf{N} \cdot \mathbf{N} \frac{n}{\mathcal{R}} = \mathbf{N} \cdot \nabla n$$

from which one deduces  $\frac{1}{\mathcal{R}} = \mathbf{N} \cdot \frac{\nabla n}{n}$

Substituting for  $\mathcal{R}$  and making the assumption that the ray deviates little from the  $x$  axis: i.e.  $\left(\frac{dy}{dx}\right)^2 \ll 1$  and  $\mathbf{N} = \mathbf{e}_y$  yields:

$$\frac{d^2y}{dx^2} = \frac{1}{n} \frac{\partial n}{\partial y}$$

which may also be written in terms of the deflection angle as:

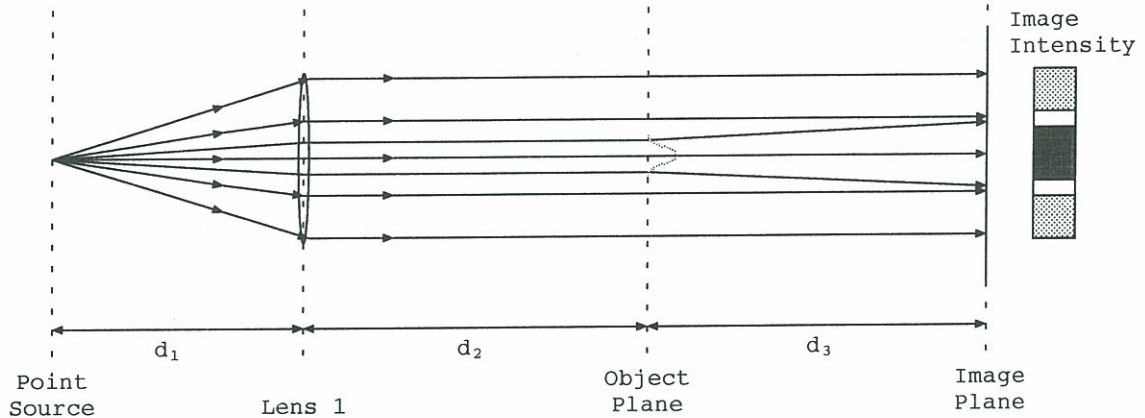
$$\frac{d\theta}{dx} = \frac{1}{n} \frac{\partial n}{\partial y} \quad (\text{A.8})$$

Equation (A.8) is integrated along the ray path from  $X_1$  to  $X_2$ . Noting that  $\frac{1}{n} \simeq 1$  for gases, we arrive at equation (A.9):

$$\theta(y) \simeq \int_{X_1}^{X_2} \frac{\partial n}{\partial y} dx \quad (\text{A.9})$$

From now on, use shall be made of the deflection profile  $\theta(y)$  of an object. Equation (A.9) shows how it is obtained from the refractive index field.





**Figure A.2:** One-lens shadowgraphy set-up with point source, lens, flame and screen. The ray paths are shown in figure (A.3) with the object at  $x = 0$ .

## A.3 Shadowgraphy

### A.3.1 Introduction

Shadowgraphy describes any set-up where the image is formed uniquely by ray deviation rather than by blocking rays according to their deviation. Two types of shadowgraphy can be distinguished. In the first, parallel rays are used. These are formed, for example, by a point source of light being placed at the focal point of a lens behind the test section. In the second, diffused light is used. This is formed by replacing the point light source with a large source, or by placing a piece of frosted glass behind the test section. The first type shall be described in detail and extension to the second is then simple.

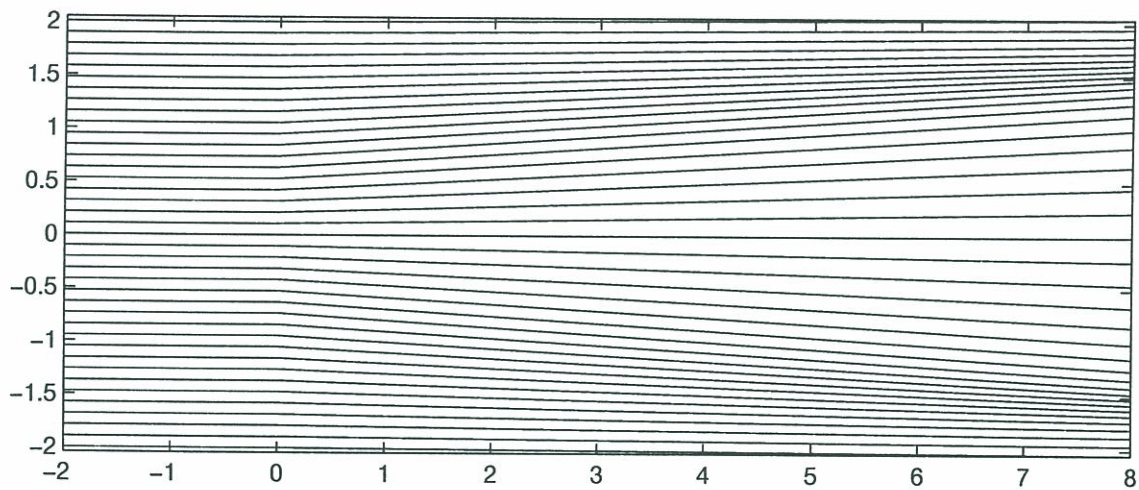
### A.3.2 Parallel ray shadowgraphy

Let us first consider figure A.2. Initially parallel rays, which are deviated in the object plane, impinge directly on a screen. The shadowgraphy effect arises when the object bends rays towards each other, producing a lighter region, or spreads them out, producing a darker region. Consider a ray tube passing through the object plane with its top at  $y_1$  and its bottom at  $y_2$ . At the screen, distance  $d_3$  downstream, the top and bottom will be at  $y_1 + d_3\theta(y_1)$  and  $y_2 + d_3\theta(y_2)$ . The power of the light passing through the tube will be unchanged, so the intensity at the screen is:

$$\begin{aligned} I &= I_0 \frac{y_2 - y_1}{[y_2 + d_3\theta(y_2)] - [y_1 + d_3\theta(y_1)]} \\ &= I_0 \frac{\Delta y}{\Delta y + d_3\Delta\theta} \end{aligned}$$

As  $\Delta y \rightarrow 0$ , this becomes:

$$I(p) = I_0 \frac{1}{1 + d_3 d\theta/dy} \quad (\text{A.10})$$



**Figure A.3:** Paths of rays between the lens ( $x = -2$ ) and the screen ( $x = 8$ ). Note that caustics will eventually be formed, at which the ray model no longer applies



The intensity  $I(p)$  is observed at a position  $p$  corresponding to the ray tube intersection with the screen:

$$p = y + d_3\theta(y) \quad (\text{A.11})$$

In general, for given  $p(y, \theta)$ ,

$$I(p) = I_0 \left( \frac{dp}{dy} \right)^{-1} \quad (\text{A.12})$$

Thus, given the deflection profile  $\theta(y)$  for the flame, the intensity profile at a screen, at distance  $d_3$ , is calculated from the parametric equations (A.10) and (A.11). As  $d_3 \rightarrow 0$ ,  $p \rightarrow y$  and  $I \rightarrow I_0 \left( 1 - d_3 \frac{d\theta}{dy} \right)$  giving the result often quoted in the literature: intensity variation is proportional to  $-d\theta/dy$  and hence for some objects,  $d^2n/dy^2$ . As  $d_3$  increases, so does distortion of the shadowgraphy image.

It is possible to calculate the deflection profile,  $\theta(y)$ , of an object from the shadowgraphy image. Re-arranging (A.10) one finds:

$$\frac{d\theta}{dy} = \frac{1}{d_3} \left[ \frac{I_0}{I(p(y, \theta))} - 1 \right]$$

This expression may be cast in discrete form, where the intensity profile,  $I(p)$ , is taken from the image.

$$\theta_{i+1} = \theta_i + \frac{\Delta y}{d_3} \left[ \frac{I_0}{I(p(y, \theta))} - 1 \right] \quad (\text{A.13})$$

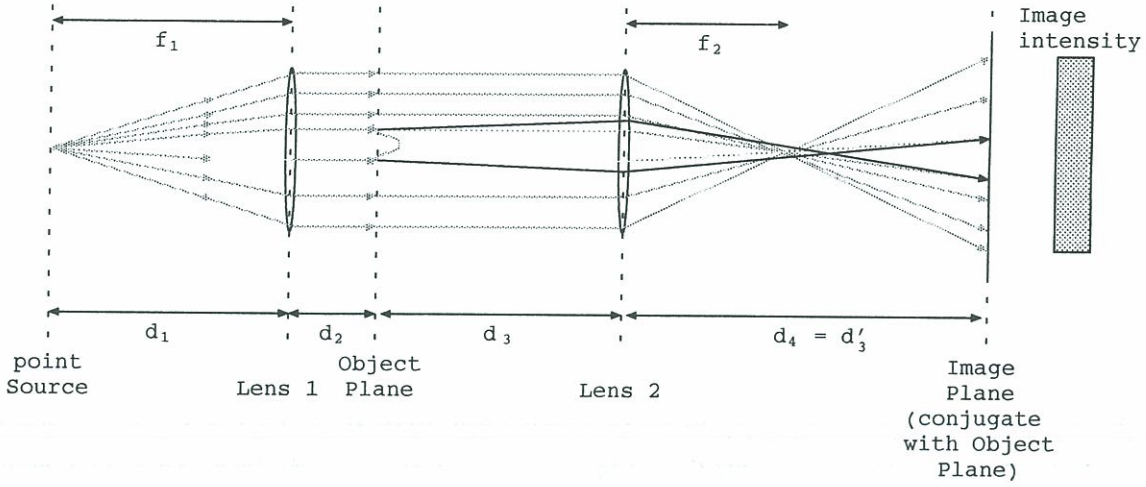
$$p = y_i + d_3\theta_i \quad (\text{A.14})$$

It is unlikely that experimental data will be sufficiently good to deduce the deflection profile  $\theta(y)$  from the intensity profile, which must then be considered as it is. In this case a rough way of quantifying the distortion of the image is useful, even if this distortion is not to be removed.

The difference  $\Delta \equiv (p(y) - y)$  is the parameter which quantifies the degree of distortion of the image. Physically, this is the  $y$ -deflection of a particular ray which travels between the object and the screen. The ratio of the maximum deflection to a characteristic thickness of the flame gives us a way to quantify distortion.

$$\eta = \frac{p_{max} - y}{t_{flame}} = \frac{\theta_{max}d_3}{t_{flame}} \quad (\text{A.15})$$

In order to obtain an intensity profile which resembles  $\partial\theta/\partial y$ , we find that  $\eta$  needs to be less than 0.1. For deflection angles profiles typical of any flame, the set-up described above is suitable only when the screen is very close. To resolve this problem, at least one lens is placed between the object plane and the screen. (Only the case of a single lens shall be described here because many lens systems behave in qualitatively the same way).



**Figure A.4:** Two-lens shadowgraphy set-up with point source, flame and screen. The image plane is conjugate with the object plane, making the shadowgraphy image disappear

Let us now consider figure A.4. If  $d_3 > f_3$ , the screen can be placed at the object's conjugate plane. All rays emitted in any direction from a point in the object plane converge at the corresponding point in the conjugate plane. With the screen at this position, there is no shadowgraphy effect. Either side of this position, the light and dark regions swap over.

Using the same notation as in equation (A.11), the screen intensity profile is given by the parametric equations (A.16) and (A.17). These can be inverted in the same way as described above.

$$p = y \left( 1 - \frac{d_4}{f} \right) + \theta \left( d_3 + d_4 - \frac{d_3 d_4}{f} \right) \quad (\text{A.16})$$

$$I(p) = I_0 \left[ \left( 1 - \frac{d_4}{f} \right) + \frac{d\theta}{dy} \left( d_3 + d_4 - \frac{d_3 d_4}{f} \right) \right]^{-1} \quad (\text{A.17})$$

Similarly, we can consider the ratio,  $\eta$ , of the  $y$ -deflection of the most deviated ray to the thickness of the flame in the image plane.

$$\text{image flame thickness} = t_{flame} \times \frac{f_2 - d_4}{f_2}$$

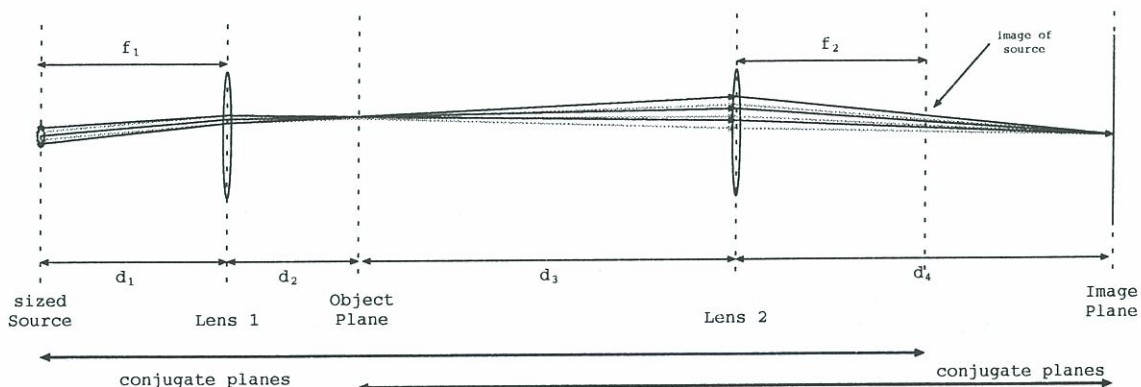
$$\text{image } y\text{-deflection} = y_{max \text{ at lens 2}} \times \frac{d'_3 - d_4}{d'_3} = d_3 \theta_{max} \times \frac{d'_3 - d_4}{d'_3}$$

$$\text{thus } \eta = \frac{d'_3 - d_4}{d'_3} \frac{f_2 - d_4}{f_2} \frac{d_3 \theta_{max}}{t_{flame}}$$

So far we have considered the position of the screen ( $d_4$ ) relative to the position of the object's conjugate plane ( $d'_3$ ). It is equally valid to consider the position of the object ( $d_3$ ) relative to the screen's conjugate plane ( $d'_4$ ). Making the relevant substitutions for  $d'_3$  and  $d_4$ ,  $\eta$  can be expressed as:

$$\eta = \frac{d_3 - d'_4}{d_3} \left( \frac{f_2}{d'_4 - f_2} \right)^2 \frac{d_3 \theta_{max}}{t_{flame}}$$





**Figure A.5:** *Shadowgraphy set-up with finite size source, lens 1, flame, lens 2 and screen. The same three rays of light are shown undeviated (grey) and deviated in the object plane (black). The focussed image of the source has changed position but the deviated rays converge to the same point on the screen.*

The factor  $\eta$  is very useful when designing a shadowgraphy set-up because it enables a rapid estimation of the type of image which will result. Large  $\eta$  means a strong but very deformed image. Small  $\eta$  means a weak but more accurate image. Best results are obtained at  $|\eta| < 0.1$ , where the screen is close to the object's conjugate plane. This process was used in order to design a shadowgraphy configuration for the cryogenic combustion facility.

If light is blocked at any point in the system, for instance by missing a lens or by impinging on the aperture of the camera lens or by non-perfect alignment of lenses, the image of that region will contain schlieren effects. These can easily pass unnoticed as they occur where the shadowgraphy effect is strongest. A sign of a schlieren effect is a dark region without an adjoining light region.

### A.3.3 Diffused ray shadowgraphy

Changing the vertical position of the light source in figure A.4 changes the angles of the parallel rays passing through the test section. A summation of these is a diffused ray set-up. Thus the simplest way to visualize the image produced by a diffused ray set-up is as the superposition of many identical but slightly displaced images from a parallel ray set-up. (In the object's conjugate plane, these images all converge). This set-up has the advantage of reducing inadvertent schlieren effects. The shadowgraphy effect is also reduced or even annihilated, which is sometimes desirable.

## A.4 Schlieren

A schlieren effect occurs when light is blocked. Let us consider figure A.5, which shows three rays (the gray lines) from a large source which happen to pass through the same point in the object plane. The rays are all deviated by the same angle (the dark lines), which corresponds to the same displacement in the focal plane of the second lens. They

then all converge at the same point in the object's conjugate plane, where the screen is placed so that shadowgraphy effects are eliminated. A mask placed at the focal point of the second lens blocks an amount of light which depends on the deviation angle, the source shape and the mask shape. For example, a rectangular source perpendicular to a straight razor blade gives an intensity proportional to the deviation angle. No further processing of the image is necessary to obtain  $\theta(y)$ . In certain situations this is equivalent to  $\partial n/\partial y$ . Increasing the size of the source reduces the contrast of the image and moving the blade changes its brightness.

## A.5 Three Dimensional Refractive Index Fields

Until this point we have assumed that all deflection takes place the object plane. In reality, the deflecting object is three dimensional. We know that the shadowgraphy effects disappear when the object plane coincides with the conjugate plane of the screen but what happens when the conjugate plane of the screen lies within the three-dimensional object?

For axisymmetric objects, the total ray deviation can be considered to be from the plane through the center of the object. The strength of a shadowgraphy image then depends on the distance from this plane to the screen's conjugate plane. In the schlieren set-up, the screen's conjugate plane should coincide with the center of the object. In both cases, the majority of the deflection comes from the central plane of the object, where refractive index gradients are perpendicular to the rays. However, the exact radial deflection profile, taking into account the rest of the object, can be deduced by a process similar to the Abel inversion described in Dunn-Rankin and Weinberg (1998).

For non-axisymmetric objects, there is not enough information to deduce the refractive index field. Weinberg (1963) shows that a good estimate can be obtained if the shape of the surface is known but this is rarely the case. Despite this, important qualitative information can be obtained if the apparatus is set up carefully. For shadowgraphy images, the screen's conjugate plane should be placed just outside the object. For schlieren images, the screen's conjugate plane should be placed at the center of the object. In both cases, areas of strong contrast indicate that at some point along the path of the ray there is a strong refractive index gradient perpendicular to the ray.

Now let us consider objects which are axisymmetric apart from small turbulent fluctuations, such as a jet or a flame surrounding a jet. Apart from the small fluctuations, the parts of the object perpendicular to the ray direction lie on the plane through the center of the object. Thus, to a first approximation, the shadowgraphy or schlieren image is that of a slice through the central plane of the object. Superimposed on this are the effects from behind or in front of this plane but these are usually less intense.



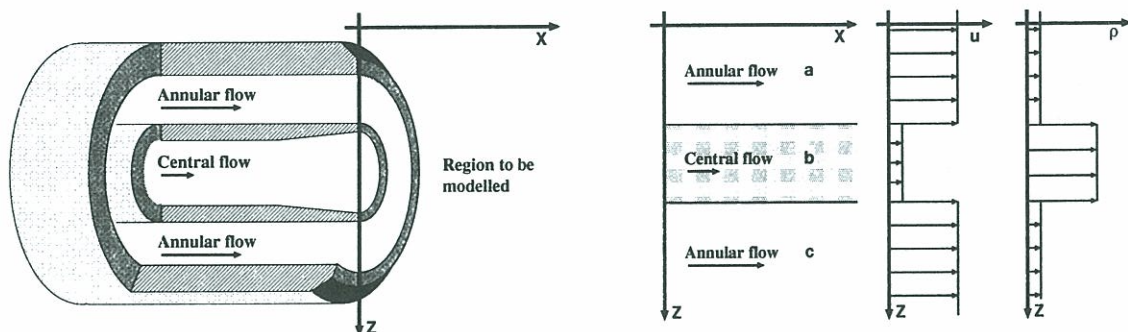
## Appendix B

# Dispersion relation of a two-dimensional bounded wake flow

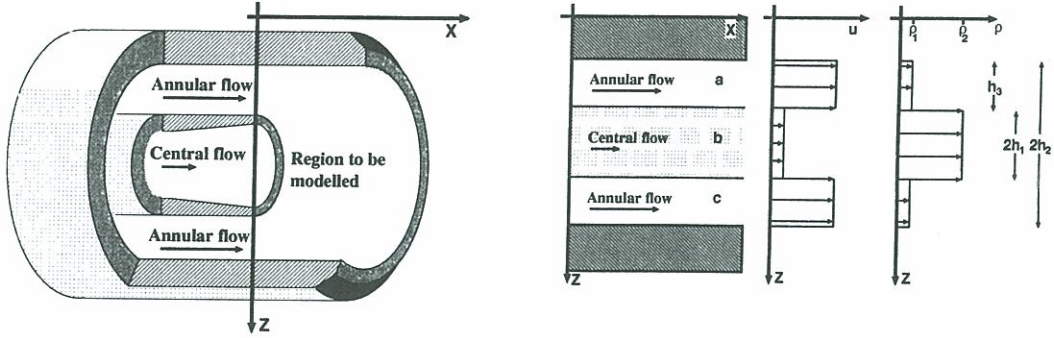
Yu and Monkewitz (1990) propose a simple model of an unbounded 2-D wake with infinite axial extent, shown in figure B.1. The wake and annular flows are both 2-D inviscid fluids with uniform velocity and density. The analysis is developed here such that the fluids are bounded above and below by solid walls, as shown in figure B.2. We consider finite surface tension and neglect gravity.

Three layers of fluid are sandwiched between two plates and are labelled  $a$ ,  $b$ , and  $c$  from top to bottom. All are assumed irrotational and inviscid so that their motion can be described by potential flow  $\phi_\alpha$ , where  $\alpha$  represents  $a$ ,  $b$  or  $c$ . At the two interfaces, which are described by functions  $\eta_{ab}$  and  $\eta_{bc}$ , full slip is allowed. The central flow's width is  $2h_1$ . The distance between the plates is  $2h_2$ , so the thickness of the outer flow is  $h_3 = h_2 - h_1$ .

In the three fluids,  $\nabla^2\phi_a = \nabla^2\phi_b = \nabla^2\phi_c = 0$ . For perturbations of the form  $\exp\{i(kx - \omega t)\}$  superimposed on fluids moving in the  $x$ -direction at velocity  $u$ , the general



**Figure B.1:** *Left: Cut-away diagram of a coaxial injector without recess. Right: The two-dimensional model which is used in this analysis for an un-recessed injector. It is an unbounded wake flow with infinite axial extent. Velocity and density profiles are shown.*



**Figure B.2:** Left: Cut-away diagram of a coaxial injector with recess. Right: The two-dimensional model which is used in this analysis for an recessed injector. It is a bounded wake flow with infinite axial extent. Velocity and density profiles are shown.

expressions of the potentials are given by equation (B.1).

$$\phi_\alpha \equiv u_\alpha x + \phi'_\alpha = u_\alpha x + (A_\alpha e^{kz} + B_\alpha e^{-kz}) \exp\{i(kx - \omega t)\} \quad \alpha = a, b, c \quad (\text{B.1})$$

where  $A_\alpha$  and  $B_\alpha$  are constants. Throughout this analysis we consider the same wavenumber and the same angular frequency in all three fluids, which is to assume that coupling between a wavenumber  $k_1$  in the middle jet and wavenumber  $k_2$  in the outer flow averages to zero when considered over the infinite  $x$ -extent of the model, for  $k_1 \neq k_2$ .

Fluid layer  $a$  has the constraint that the  $z$ -velocity is zero at  $z = -h_2$ :

$$\left. \frac{\partial \phi_a}{\partial z} \right|_{z=-h_2} = 0$$

thus

$$A_a e^{-kh_2} = B_a e^{kh_2}$$

and therefore

$$\phi_a = u_a x + C_a \cosh(kh_2 + kz) \exp\{i(kx - \omega t)\} \quad (\text{B.2})$$

Similarly for fluid  $c$ ,

$$\phi_c = u_c x + C_c \cosh(-kh_2 + kz) \exp\{i(kx - \omega t)\} \quad (\text{B.3})$$

As an aside,  $C_a$  and  $C_c$  are proportional to  $e^{-kh_2}$ , ensuring that as  $h_2 \rightarrow \infty$ ,  $\phi_a$  and  $\phi_c$  decay exponentially.

The interfaces also feature the common term  $\exp\{i(kx - \omega t)\}$ :

$$\eta_{ab} = H_{ab} \exp\{i(kx - \omega t)\} \quad (\text{B.4})$$

$$\eta_{bc} = H_{bc} \exp\{i(kx - \omega t)\} \quad (\text{B.5})$$

The linearized condition that the interface between the fluid layers is a material surface is given by equation (B.6), for fluid  $\alpha$ . This leads to one condition for fluid  $a$  (B.9), two for fluid  $b$  (B.10 and B.11) and one for fluid  $c$  (B.12). Note that the  $z$ -axis points down.

$$\left. \frac{\partial \phi_\alpha}{\partial z} \right|_{\text{interface}} = \frac{\partial \eta}{\partial t} + u_\alpha \frac{\partial \eta}{\partial x} \quad (\text{B.6})$$



Furthermore, the pressure difference across the interface must be equaled by the surface tension. Using a linearized expression of the curvature this equation writes:

$$p_\alpha - p_\beta = -\sigma \frac{\partial^2 \eta_{\alpha\beta}}{\partial x^2} \quad (\text{B.7})$$

If gravity is ignored, the pressure in fluid  $\alpha$  is given by Bernoulli's equation (B.8), where  $p_{ref,\alpha}$  is a reference pressure. Note that  $\phi_\alpha$  has been expressed in terms of  $u_\alpha x + \phi'_\alpha$ .

$$\frac{p_\alpha}{\rho_\alpha} = \frac{p_{ref,\alpha}}{\rho_\alpha} - \frac{\partial \phi'_\alpha}{\partial t} - \frac{1}{2} \left( u_\alpha + \frac{\partial \phi'_\alpha}{\partial x} \right)^2 - \frac{1}{2} \left( \frac{\partial \phi'_\alpha}{\partial z} \right)^2 \quad (\text{B.8})$$

We notice that, for the case at rest where  $\phi'_\alpha \equiv 0$  in all three fluids and  $\eta_{\alpha\beta} \equiv 0$ , the pressures must be equivalent, leading to  $p_{ref,\alpha}/\rho_\alpha - u_\alpha^2/2 = \text{constant}$ . Combining (B.7) and (B.8) and neglecting second order terms in derivatives of  $\phi'_\alpha$  leads to two equations (B.13 and B.14), one at each interface. Thus, in total, six equations must be satisfied at the interfaces:

$$\frac{\partial \phi_a}{\partial z} = \frac{\partial \eta_{ab}}{\partial t} + u_a \frac{\partial \eta_{ab}}{\partial x} \quad \text{at } z = -h_1 \quad (\text{B.9})$$

$$\frac{\partial \phi_b}{\partial z} = \frac{\partial \eta_{ab}}{\partial t} + u_b \frac{\partial \eta_{ab}}{\partial x} \quad \text{at } z = -h_1 \quad (\text{B.10})$$

$$\frac{\partial \phi_b}{\partial z} = \frac{\partial \eta_{bc}}{\partial t} + u_b \frac{\partial \eta_{bc}}{\partial x} \quad \text{at } z = h_1 \quad (\text{B.11})$$

$$\frac{\partial \phi_c}{\partial z} = \frac{\partial \eta_{bc}}{\partial t} + u_c \frac{\partial \eta_{bc}}{\partial x} \quad \text{at } z = h_1 \quad (\text{B.12})$$

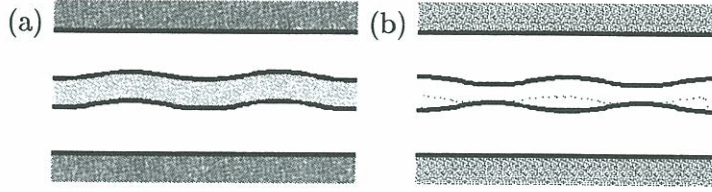
$$\rho_a \left( \frac{\partial \phi'_a}{\partial t} + u_a \frac{\partial \phi'_a}{\partial x} \right) - \rho_b \left( \frac{\partial \phi'_b}{\partial t} + u_b \frac{\partial \phi'_b}{\partial x} \right) = \sigma \frac{\partial^2 \eta_{ab}}{\partial x^2} \quad \text{at } z = -h_1 \quad (\text{B.13})$$

$$\rho_b \left( \frac{\partial \phi'_b}{\partial t} + u_b \frac{\partial \phi'_b}{\partial x} \right) - \rho_c \left( \frac{\partial \phi'_c}{\partial t} + u_c \frac{\partial \phi'_c}{\partial x} \right) = \sigma \frac{\partial^2 \eta_{bc}}{\partial x^2} \quad \text{at } z = h_1 \quad (\text{B.14})$$

Note that  $\partial \phi_\alpha / \partial z \equiv \partial \phi'_\alpha / \partial z$ . We now substitute equation (B.2) for  $\phi_a$ , (B.1) for  $\phi_b$ , (B.3) for  $\phi_c$ , (B.4) for  $\eta_{ab}$ , (B.5) for  $\eta_{bc}$ ,  $\rho_a$  for  $\rho_c$  and  $u_a$  for  $u_c$ . This leads to six equations in  $(x, z)$  space with six unknowns ( $C_a, C_c, A_b, B_b, H_{ab}, H_{bc}$ ) and a set of parameters ( $k, \omega, v_a, v_b, \rho_a, \rho_b, \sigma, h_2, h_1$ ). We wish to find the constraint on the parameters which leads to a non-trivial solution to this set of equations. This is most easily achieved by expressing the equations as a matrix multiplied by vector  $[C_a, C_c, A_b, B_b, H_{ab}, H_{bc}]^T$  equating to zero. For non-trivial solutions the determinant of the matrix must be zero, giving the desired constraint on the parameters in the form of a dispersion relation.

The six equations can be reduced to three if varicose and sinuous disturbances are considered separately (Figure B.3). In the varicose case, the interfaces move in opposite directions so that  $H_{ab} = -H_{bc}$ ,  $C_a = C_c$  and  $A_b = B_b$ . In the sinuous case, the interfaces move in the same direction and  $H_{ab} = H_{bc}$ ,  $C_a = -C_c$  and  $A_b = -B_b$ . At this point, subscripts  $a$  and  $c$ , which represent the outer fluid, are replaced with subscript 2 and subscript  $b$ , which represents the central fluid, is replaced with subscript 1. Substituting for the three equations at the top interface gives, in the sinuous case:

$$\begin{pmatrix} \sinh(kh_2 - kh_1) & 0 & i(u_2 - \omega/k) \\ 0 & \cosh(kh_1) & i(u_1 - \omega/k) \\ i(u_2 - \omega/k)(-\rho_2 \cosh(kh_2 - kh_1)) & i(u_1 - \omega/k)(-\rho_1 \sinh(kh_1)) & -\sigma k \end{pmatrix} \begin{pmatrix} C_2 \\ A_1 \\ H_{21} \end{pmatrix} = 0$$



**Figure B.3** : Sinuous (a) and varicose (b) instabilities.

and in the varicose case:

$$\begin{pmatrix} \sinh(kh_2 - kh_1) & 0 & i(u_2 - \omega/k) \\ 0 & -\sinh(kh_1) & i(u_1 - \omega/k) \\ i(u_2 - \omega/k)(-\rho_2 \cosh(kh_2 - kh_1)) & i(u_1 - \omega/k)(\rho_1 \cosh(kh_1)) & -\sigma k \end{pmatrix} \begin{pmatrix} C_2 \\ A_1 \\ H_{21} \end{pmatrix} = 0$$

Setting the determinant to zero gives the dispersion relation (B.15).

$$-k\sigma + (u_2 - c)^2 \rho_2 \coth(kh_3) + (u_1 - c)^2 \rho_1 \left\{ \begin{array}{l} \tanh(kh_1) \text{ (sinuous)} \\ \coth(kh_1) \text{ (varicose)} \end{array} \right\} = 0 \quad (\text{B.15})$$

As a reminder,  $h_3 = h_2 - h_1$ . Following Yu and Monkewitz (1990) it is convenient to define reference variables:  $u_{ref} = (u_2 + u_1)/2$ ,  $h_{ref} = h_1$  and  $\rho_{ref} = \rho_2$ . This leads to the following non-dimensional variables and parameters:  $k^* = kh_1$ ,  $c^* = c/u_{ref}$ ,  $\sigma^* = \sigma/(h_1 \rho_2 u_{ref}^2)$ ,  $h_3^* = h_3/h_1$ . We also define  $S = \rho_1/\rho_2$  and  $\Lambda = (u_1 - u_2)/(u_1 + u_2)$ . The dispersion relation can now be expressed as:

$$-k^* \sigma^* + (1 - \Lambda - c^*)^2 \coth(k^* h_3^*) + S(1 + \Lambda - c^*)^2 \left\{ \begin{array}{l} \tanh(k^*) \text{ (sinuous)} \\ \coth(k^*) \text{ (varicose)} \end{array} \right\} = 0 \quad (\text{B.16})$$



## Appendix C

# Conditions at a liquid/vapour interface

The conditions at a liquid oxygen/gaseous hydrogen interface are investigated above and below the critical pressure of oxygen. Particular attention is given to the application of these conditions to a numerical analysis, such as that used in chapter 4. We successively consider:

1. An interface within pure oxygen.
2. An interface within a binary mixture of hydrogen and oxygen.
3. An interface within a multi-species mixture corresponding to hydrogen and oxygen with combustion products.

This progression enables a clear explanation of the relevant issues.

### C.1 Single component system

In the first situation, hot oxygen is blown vertically down on a pool of dense cold oxygen.

#### C.1.1 Criteria for existence of a liquid/vapour interface.

The dynamic pressure variation is negligible, so the pressure can be taken to be uniform everywhere. The temperature profile descends monotonically from the hot to the cold side and the density  $\rho(p, T)$  can be calculated from the equation of state. In the supercritical case there is a continuous density variation. In the subcritical case there is a density discontinuity, which corresponds to the liquid/vapour interface. The existence of an interface is determined uniquely by the pressure. Its position is determined by the temperature profile.

In a numerical calculation, the position of this interface could be a free variable calculated from the temperature profile via the equation of state. However, the presence of a phase transition is extremely useful since good experimentally validated correlations exist to describe conditions at such an interface. These can be used as boundary conditions of a computational domain.

### C.1.2 Equilibrium at a liquid/vapour interface in a pure species.

At an interface, the liquid and vapour must be at the same temperature and pressure:

$$p^l = p^v, \quad \text{mechanical equilibrium} \quad (\text{C.1})$$

$$T^l = T^v, \quad \text{thermal equilibrium} \quad (\text{C.2})$$

The canonical variables of the Gibbs energy are  $p$ ,  $T$  and composition so  $G$  does not change during a phase change at equilibrium. If  $p$  and  $T$  are changed by incremental amounts such that equilibrium is maintained,  $dG^l = dG^v$ . Using  $dG = -SdT + Vdp$  and substituting  $\Delta S = \Delta h_v/T$ , one arrives at the Clapeyron equation (C.3). Here  $\Delta h_v$  is the latent heat of the phase change. By integration from any point of the phase transition line in the  $(p, T)$  diagram, the rest of the line can be obtained.

$$\frac{dp_s}{dT_s} = \frac{\Delta h_v}{T_s \Delta V} \quad (\text{C.3})$$

Considering the vapour phase as an ideal gas and assuming that the molar volume of the condensed phase is negligible compared with that of the vapour, one obtains  $\Delta V \approx V_{vap} \approx rT_s/p_s$ . By substitution into (C.3) the Clausius-Clapeyron equation is obtained:

$$\frac{dp_s}{dT_s} = \frac{\Delta h_v}{rT_s^2/p_s} \quad (\text{C.4})$$

This expression may be integrated by assuming that  $\Delta h_v$  is constant in the range investigated. One finds for the saturation pressure:

$$p_s(T_s) = p_0 \exp \left( \frac{\Delta h_v}{r} \left[ \frac{1}{T_0} - \frac{1}{T_s} \right] \right) \quad (\text{C.5})$$

where the point  $(p_0, T_0)$  lies on the liquid/vapour phase equilibrium line.

It is important to note that equation (C.5) is not applicable near the critical pressure, where the ideal gas equation of state is no longer valid and where  $\Delta h_v$  tends rapidly to zero. The heat flux is also related to the mass flux at the interface by equation (C.6).

$$\lambda_v \frac{dT}{dx} \Big|_v = \dot{m} \Delta h_v + \lambda_l \frac{dT}{dx} \Big|_l \quad (\text{C.6})$$

### C.1.3 Transport Properties and Heat Capacity.

The specific heat capacity exhibits a singularity and  $\lambda$  increases significantly at the critical point. However,  $\mu$ ,  $\lambda$ ,  $D$  and  $c_p$  can all be evaluated as functions of temperature and pressure for a single species using correlations described in the literature. (See for example Oefelein (1997) and Kee et al. (1986)).

## C.2 Binary mixture

If the gaseous oxygen in the counterflow configuration is replaced with gaseous hydrogen the equation of state also depends on composition. One can assume that the new equation



of state can be represented by a hypothetical pure fluid, regardless of composition. Oefelein (1997), for example, uses pure oxygen. Initially this does not seem to be a very realistic assumption. A large family of equations of state assume the law of corresponding states, in which the equation of state depends only on two parameters: the critical pressure and the critical temperature. For pure oxygen,  $p_{crit} = 50.4$  bar and  $T_{crit} = 155$  K. For pure hydrogen,  $p_{crit} = 13.0$  bar and  $T_{crit} = 33.2$  K. These values are sufficiently different that no equation of state with a single value of  $(p_{crit}, T_{crit})$  will satisfactorily describe an arbitrary mixture of  $H_2$  and  $O_2$ .

However, all equations of state are very close to the ideal gas equation of state at reduced temperatures  $(T/T_{crit})$  above approximately 2 and at pressures up to around 200 bar. Therefore in regions above roughly 300K the equation of state for pure oxygen will be a reasonable approximation to that of the mixture. From the simulations in chapter 4 it is found that the region below 300K contains over 98% oxygen so the equation of state for oxygen will be the best possible approximation over all regions. Nevertheless, around critical conditions even a small amount of impurity cannot be neglected. According to Delplanque and Sirignano (1993) neglecting dissolved hydrogen results in a significant underestimation of the critical mixing temperature. This is important in determining the existence of a liquid/vapour interface.

### C.2.1 Criteria for existence of a liquid/vapour interface.

At equilibrium an interface can exist even when the pressure exceeds the critical pressure of both pure substances. For example, if one assumes that no hydrogen can dissolve, the liquid oxygen will be in equilibrium with the partial pressure of oxygen vapour above it. Since the partial pressure is some fraction of the total pressure, an interface can exist when the total pressure exceeds the critical pressure of the pure substance. This is a rough argument because solubility of hydrogen in oxygen is neglected and an ideal gas is assumed. The following, more rigorous, argument requires consideration of chemical potentials or fugacities.

### C.2.2 Equilibrium at a liquid/vapour interface in a binary mixture.

A convenient relationship arises if a liquid/vapour interface exists. The pressure, temperature and concentrations can be determined, as well as a link between heat and mass fluxes across the surface. For a binary mixture, as for a pure species, the Gibbs energy does not change across a phase boundary at equilibrium. This leads to equations (C.7) and (C.8) as well as equations (C.1) and (C.2).

$$\mu_1^l = \mu_1^v, \quad \text{chemical equilibrium (species 1)} \quad (C.7)$$

$$\mu_2^l = \mu_2^v, \quad \text{chemical equilibrium (species 2)} \quad (C.8)$$

$\mu_i$  is the chemical potential of species  $i$ , defined as

$$\mu_i \equiv \left( \frac{\partial(nG)}{\partial n_i} \right)_{T,p,n_j}$$

where  $n_i$  is the number of moles of species  $i$  and  $n = \sum n_i$  is the total number of moles present.

The use of chemical potentials suffers from several practical problems. By its definition, there is no unequivocal absolute value of  $\mu_i$ . Also  $\mu_i \rightarrow \infty$  as the total pressure tends to zero or as the concentration of species  $i$  tends to zero. A more practical version of the chemical potential is the fugacity,  $\hat{f}_i$ , defined implicitly by the following equation together with the limiting condition (C.10).

$$d\mu_i \equiv rT d(\ln \hat{f}_i), \quad \text{constant } T \quad (\text{C.9})$$

$$\lim_{p \rightarrow 0} \left( \frac{\hat{f}_i}{X_i p} \right) \equiv 1 \quad (\text{C.10})$$

where  $X_i$  is the molar fraction of the species. Note that as  $p \rightarrow 0$ , where ideal gas behaviour is approached, fugacity is analogous to partial pressure. As a further demonstration of this, equation (C.9) can be compared with equation (C.11), which is an expression for the chemical potential of an ideal gas.

$$d\mu_i \equiv rT d(\ln X_i p) \quad \text{constant } T, \text{ ideal gas} \quad (\text{C.11})$$

The chemical potential equilibrium conditions (C.7) and (C.8) can now be replaced with (C.12) and (C.13).

$$\ln \hat{f}_1^l = \ln \hat{f}_1^v \quad (\text{C.12})$$

$$\ln \hat{f}_2^l = \ln \hat{f}_2^v \quad (\text{C.13})$$

Now the fugacity must be expressed in terms of temperature and pressure or temperature and volume. Delplanque and Sirignano (1993) use the temperature and volume expression given below and a compressibility factor,  $Z$ , of the mixture, derived from the equation of state.

$$rT \ln \left( \frac{\hat{f}_i}{X_i p} \right) = \int_V^\infty \left[ \left( \frac{\partial p}{\partial n_i} \right)_{T,V,n_j} - \frac{rT}{V} \right] dV - rT \ln Z \quad (\text{C.14})$$

At high pressures, the energy required to vaporize one mole of component  $i$  from the liquid mixture to the gaseous mixture at  $T$  and  $p$  differs from the latent heat of vaporization of  $i$ . The latter is defined as the energy required to vaporize one mole of pure liquid  $i$  in its own vapour at  $T$  and  $p$ . In a mixture the enthalpy of vaporization has to be calculated for each component via expression (C.15).

$$\Delta h_{vi} = \frac{h_i^v - h_i^l}{W_i} = \frac{rT^2}{W_i} \frac{\partial}{\partial T} \left[ \ln \left( \frac{\hat{f}_i}{X_i^v p} \right) - \ln \left( \frac{\hat{f}_i^l}{X_i^l p} \right) \right] \quad (\text{C.15})$$

The value of  $\hat{f}_i/(X_i p)$  can be calculated from equation (C.14). The heat flux remains related to the mass flux by equation (C.6).

### C.2.3 Transport properties and heat capacity of the mixture.

The transport and thermodynamic coefficients  $\mu$ ,  $\lambda$  and  $c_p$  can be evaluated relatively easily. However, evaluating the binary mass diffusivity coefficients becomes more difficult. The theory has been well developed in binary gases at low to moderate density. However, theories in the condensed phase are only partially developed.



### C.3 Multi Component Mixtures

When a flame is established between the hydrogen and oxygen many more species must be taken into account. Indeed, it is unlikely that any hydrogen will reach the liquid surface. The qualitative features are the same as for binary mixtures. Up to a certain temperature and pressure an interface will exist between the liquid and vapour phase. At equilibrium, the temperature, pressure and fugacities (or chemical potentials) must be equal for each component across the interface. The critical point is determined by the species concentrations at this interface. Above the critical point, the density change will be continuous, so the model becomes a single phase convection-diffusion configuration.

Estimating the mass diffusion coefficients in multicomponent, multiphase mixtures is a difficult task because there are no correlations that apply to both liquid and vapour phases. There are also no correlations in near-critical gases and liquids.

### C.4 Conclusion

Below the critical pressure of pure oxygen, a liquid/vapour interface will always exist. Conditions at this interface are well known and are given in section C.2. The liquid and vapour phases can be simulated separately with jump conditions at the interface linking the two simulations. This permits the use of an optimized equation of state and transport quantity correlations in each phase. At the expense of some accuracy, simulation of the liquid phase can be replaced by the assumption that it is pure oxygen. Thus only the gaseous phase needs to be simulated. It can be checked *a posteriori* that the concentrations of other species gathering at the interface are very small. If they are not, the assumption is not acceptable.

Above the critical pressure of pure oxygen, it cannot be assumed *a priori* that an interface will always exist. Consequently it is not possible to split the simulation up into liquid and vapour phases. It is necessary to simulate the entire domain, allowing an interface to form if this is dictated by the equation of state. This approach requires much care in the choice of equation of state, which has to be valid over a wide range of temperatures and compositions. The same is true of transport properties, particularly around the critical pressure. The steep gradients and discontinuities which occur could cause numerical problems and would necessitate the use of an adaptative grid.





## Appendix D

# Consumption rates in strained laminar diffusion flames

A counterflow diffusion flame is considered between two reactants, labelled 1 and 2. Following Darabiha (1992), let  $G_\alpha$  and  $\mathcal{D}_\alpha$  represent the consumption rate and diffusivity of reactant  $\alpha$ . The mass stoichiometric ratio  $s = G_2/G_1$ . An asymptotic analysis at constant strain rate,  $\epsilon_s$ , in the limit of infinitely fast chemistry and with  $\rho^2\mathcal{D}$  independent of temperature gives:

$$G_\alpha = \rho Y_{\alpha 0} \left( \frac{2\mathcal{D}_{\alpha 0}\epsilon_s}{\pi} \right)^{1/2} \frac{\exp^{-\eta_{\alpha f}^2}}{1 - \operatorname{erf}(\eta_{\alpha f})} \quad (\text{D.1})$$

where  $\eta$  is a transformed spatial coordinate and the subscript  $f$  denotes the flame position. The flame positions  $\eta_{\alpha f}$  are solutions of the transcendental equation:

$$e^{-\eta_{1f}^2}(\beta^2 - 1) \frac{1 - \operatorname{erf}(\eta_{1f})}{1 + \operatorname{erf}(\eta_{1f}\beta)} = \beta\phi \quad (\text{D.2})$$

where the global equivalence ratio,  $\phi$ , compares conditions prevailing at infinity to the mass stoichiometric ratio:

$$\phi = sY_{10}/Y_{20} \quad (\text{D.3})$$

$\beta$  designates the square root of the density ratio:  $\beta = (\mathcal{D}_{10}/\mathcal{D}_{20})^{1/2}$ , which means one can write  $\eta_{2f} = \beta\eta_{1f}$ . If  $\beta = 1$  then the consumption rates are given by:

$$G_1 = \rho Y_{10} \frac{1 + \phi}{\phi} \left( \frac{\mathcal{D}\epsilon_s}{2\pi} \right)^{1/2} e^{-\eta_f^2} \quad (\text{D.4})$$

$$G_2 = \rho Y_{20}(1 + \phi) \left( \frac{\mathcal{D}\epsilon_s}{2\pi} \right)^{1/2} e^{-\eta_f^2} \quad (\text{D.5})$$

with  $\eta_f$  defined implicitly by  $\operatorname{erf}(\eta_f) = (1 - \phi)/(1 + \phi)$ . (A crude approximation of the error function when  $\eta_f \approx 0$  is simply  $\operatorname{erf}(\eta_f) \sim 2\eta_f/\sqrt{\pi}$ ).

It is now necessary to evaluate  $\rho\mathcal{D}^{1/2}$  as a function of pressure.

$$\rho^2\mathcal{D}(p, T) = \rho^2(p, T) \mathcal{D}(p, T)$$

However,  $\rho^2\mathcal{D}$  is independent of temperature and can be evaluated at a reference temperature. Keeping the pressure constant one may write:

$$\rho^2\mathcal{D}(p, T) = \rho^2(p, T_{ref}) \mathcal{D}(p, T_{ref})$$

Now  $\mathcal{D}$  is inversely proportional to pressure:

$$\mathcal{D}(p, T_{ref}) = \frac{p_{ref}}{p} \mathcal{D}(p_{ref}, T_{ref})$$

Thus

$$\rho^2\mathcal{D}(p, T) = \rho^2(p, T_{ref}) \frac{p_{ref}}{p} \mathcal{D}(p_{ref}, T_{ref})$$

or

$$\begin{aligned} \rho^2\mathcal{D}(p, T) &= \left(\frac{p}{rT_{ref}}\right)^2 \frac{p_{ref}}{p} \mathcal{D}(p_{ref}, T_{ref}) \\ &= \left(\frac{p_{ref}}{rT_{ref}}\right)^2 \frac{p}{p_{ref}} \mathcal{D}(p_{ref}, T_{ref}) \end{aligned}$$

One may also write:

$$\rho^2\mathcal{D} = \frac{p}{p_{ref}} [\rho^2\mathcal{D}]_{ref}$$

The final result is:

$$G = \rho_{ref} Y_{20} (1 + \phi) \left(\frac{\mathcal{D}_{ref} \epsilon_s}{2\pi}\right)^{1/2} \left(\frac{p}{p_{ref}}\right)^{1/2} \exp^{-\eta_f^2} \quad (\text{D.6})$$

from which it can be seen that the consumption rate and the heat release rate are proportional to the product  $(\epsilon_s p)^{1/2}$ . This indicates that the consumption rate per unit flame surface increases with the square root of the pressure.



# Bibliography

- Abramovich, G. (1963). *The Theory of Turbulent Jets*. Cambridge, Mass: MIT Press.
- Aguerre, F. (1994). *Etude expérimentale et numérique des flammes laminaires étirées stationnaires et instationnaires*. Ph. D. thesis, Ecole Centrale de Paris.
- Barrère, M., A. Jaumotte, B. Fraeijs de Veubeke, and J. Vandekerckhove (1960). *Rocket Propulsion*. Elsevier.
- Baum, M., T. Poinsot, D. Haworth, and N. Darabiha (1994). Using Direct Numerical Simulations to study  $H_2/O_2/N_2$  flames with complex chemistry in turbulent flows . *Journal of Fluid Mechanics* 281, 1 – 32.
- Berger, E. Scholtz, D. and M. Schumm (1990). Coherent vortex structures in the wake of a sphere and a circular disk at rest and under forced vibrations. *Journal of Fluid Structures* 4, 231 – 257.
- Bernal, L. and A. Roshko (1986). Streamwise Vortex Structure in Plane Mixing Layers. *Journal of Fluid Mechanics* 170, 499 – 525.
- Blanchère, H. and S. Defoort (2001). Etude de l'influence du retrait sur les propriétés d'atomisation d'un jet coaxial. Rapport DEA, Ecole Centrale de Paris.
- Broadwell, J. and R. Breidenthal (1982). A Simple Model of Mixing and Chemical Reaction in a Turbulent Shear Layer. *Journal of Fluid Mechanics* 125, 397 – 410.
- Buckmaster, J. (1997). Edge-flames. *Journal of Engineering Mathematics* 31, 269 – 284.
- Buckmaster, J. and T. Jackson (2000). Holes in flames, flame-isolas, their edges. In *Proceedings of the Combustion Institute*, 28.
- Buckmaster, J. and R. Weber (1996). Edge flame holding. In *Proceedings of the Combustion Institute*, 26, pp. 1143 – 1149.
- Burluka, A. and R. Borghi (2000). Stretch effect on the vaporization rate in Fendell's problem. *Combustion and Flame* 122, 227 – 232.
- Candel, S., G. Herding, R. Snyder, P. Scouffaire, C. Rolon, L. Vingert, M. Habiballah, F. Grisch, M. Péalat, P. Bouchardy, D. Stepowski, A. Cessou, and P. Colin (1998). Experimental investigation of a shear-coaxial cryogenic jet-flame . *Journal of Propulsion and Power* 14, 826–834.
- Carreau, J.-L., A. Dunand, E. Prévost, D. Porcheron, G. LeVisage, G. Monoté, and F. Roger (2001). Paramètres et caractéristiques de l'atomisation d'un jet liquide rond par un jet de gaz annulaire et coaxial. In *Colloque de synthèse du groupe de recherche "Combustion dans les moteurs fusées"*, CNES, Toulouse, pp. 135 – 151.

- Carreau, J.-L., E. Porcheron, L. Prevost, and F. Roger (1997). Atomisation coaxiale d'un jet liquide cryogénique ou non: Effet de la masse volumique du gaz et de la géométrie de l'injecteur. In *Colloque de synthèse du groupe de recherche "Combustion dans les moteurs fusées"*, CNES, Toulouse.
- Cessou, A., R. Bazile, P. Colin, S. Guerre, F. Lebourg, O. Werquin, and D. Stépowski (2001). Fluorescence de la vapeur d'oxygène et diffusion Raman du LOX par plan laser sur le banc Mascotte. In *Colloque de synthèse du groupe de recherche "Combustion dans les moteurs fusées"*, CNES, Toulouse, pp. 393 – 406.
- Cessou, A., P. Colin, and D. Stépowski (1998). Statistical investigation of the turbulent flame geometrical structures in a liquid oxygen / gaseous hydrogen shear-coaxial jet. In *Proceedings of the Combustion Institute*, 27, pp. 1039 – 1046.
- Chomaz, J., P. Huerre, and L. Redekopp (1988). Bifurcations to local and global modes in spatially-developing flows. *Phys. Rev. Lett.* 60, 25 – 28.
- Coffee, T., A. Kotlar, and M. Miller (1983). The Overall Reaction Concept in Premixed, Laminar, Steady-State Flames. I. Stoichiometries. *Combustion and Flame* 54, 155 – 169.
- Dandy, D. and S. Vosen (1992). Numerical and Experimental Studies of Hydroxyl Radical Chemiluminescence in methane-air flames. *Combustion Science and Technology* 82, 131 – 151.
- Darabiha, N. (1992). Transient behaviour of laminar counterflow Hydrogen-Air diffusion flames with complex chemistry. *Combustion Science and Technology* 86, 163 – 181.
- Davidson, D., M. Roehrig, E. Petersen, M. Di Rosa, and R. Hanson (1996). Measurement of the OH A-X(0,0) 306nm absorption bandhead at 60 atm and 1735K. *Journal of Quantitative Spectroscopy and Radiative Transfer* 55(6).
- Davies, T. (1981). Schlieren photography - short bibliography and review. *Optics and laser technology February*, 37 – 42.
- de Ris, J. (1969). Spread of a laminar diffusion flame. In *Proceedings of the Combustion Institute*, 12, pp. 241 – 252.
- Decker, M., A. Schik, U. Meier, and W. Stricker (1998). Quantitative Raman imaging investigations of mixing phenomena in high-pressure cryogenic jets. *Applied Optics* 37(24), 5620 – 5627.
- Delhaye, B., D. Veynante, S. Candel, and H. Ha Minh (1994). Simulation and Modeling of Reactive Shear Layers. *Theoret. Comput. Fluid Dyn.* 6, 67–87.
- Delplanque, J.-P. and W. Sirignano (1993). Numerical study of the transient vaporization of an oxygen droplet at sub- and super-critical conditions. *Int J. Heat and Mass Transfer* 36(2), 303–314.
- Delplanque, J.-P. and W. Sirignano (1994). Boundary-layer Stripping Effects on Droplet Transcritical Convective Vaporization. *Atomization and Sprays* 4, 325–349.
- Delplanque, J.-P. and W. Sirignano (1995). Transcritical vaporization and combustion of LOx droplet arrays in a convective environment. *Combustion Science and Technology* 105, 327–344.



- Deshpande, M., S. Venkateswaran, M. Foust, and C. Merkle (1997). Finite splitter plate effects on flame holding in a confined hydrogen-oxygen shear layer. In *35th Aerospace Sciences Meeting and Exhibit*. AIAA. Paper 97-0258.
- Dunn-Rankin, D. and F. Weinberg (1998). Location of the Schlieren Image in Premixed Flames: Axially Symmetrical Refractive Index Fields. *Combustion and Flame* 113, 303 – 311.
- Emmons, H. (1956). The film combustion of liquid fuel. *Z. angew. Math. Mech* 36(1/2), 60 – 71.
- Eroglu, H., N. Chigier, and Z. Farago (1991). Coaxial atomizer liquid intact length. *Physics of Fluids* 3(2), 303 – 313.
- Esch, R. E. (1957). The Instability of a Shear Layer Between Two Parallel Streams. *Journal of Fluid Mechanics* 3, 289 – 303.
- Farago, Z. and N. Chigier (1991). Morphological classification of disintegration of a round liquid jet in a coaxial air stream. In *ICLASS-91*, Rouen, France. ICLASS.
- Fendell, F. (1965). Ignition and extinction in combustion of initially unmixed reactants. *Journal of Fluid Mechanics* 21, 281 – 303.
- Fernández, E., V. Kurdyumov, and A. Liñán (2000). Diffusion flame attachment and lift-off in the near wake of a fuel injector. In *Proceedings of the Combustion Institute*, 28, pp. 2125 – 2131.
- Frey, A. and J. T'ien (1979). A theory of flame spread over a solid fuel including finite-rate chemical kinetics. *Combustion and Flame* 36, 263 – 289.
- Gaydon, A. (1974). *The Spectroscopy of Flames* (2 ed.). London: Chapman and Hall.
- Gicquel, O. (1999). *Développement d'une nouvelle méthode de réduction des schémas cinétiques : application au méthane*. Ph. D. thesis, Ecole Centrale de Paris, Chatenay-Malabry, France.
- Gicquel, P. (2001). Etudes Expérimentales des Sprays Cryogéniques en Combustion dans des Conditions Sub et Supercritiques. In *Colloque de synthèse du groupe de recherche "Combustion dans les moteurs fusées"*, CNES, Toulouse, pp. 359 – 370.
- Gill, G. (1978). A qualitative technique for concentric tube element optimization, utilizing the factor (dynamic head ratio - 1). In *AIAA 16th Aerospace Sciences Meeting*. Paper 78-76.
- Gicquel, P. (1997). Experimental investigation of a lox spray under hot fire conditions. In *ICLASS 97*.
- Guerre, S., R. Bazile, and D. Stepowski (1996). Conditioned dissipation and average consumption maps in a turbulent nonpremixed flame using planar laser-induced fluorescence of O<sub>2</sub>. In *Proceedings of the Combustion Institute*, 26, pp. 105 – 133.
- Hamins, A. and K. Seshadri (1984). Structure of counterflow diffusion flames burning multicomponent fuels. In *Proceedings of the Combustion Institute*, 20, pp. 1905 – 1913.
- Hannemann, K. and H. Oertel (1989). Numerical simulation of the absolutely and convectively unstable wake. *Journal of Fluid Mechanics* 199, 55 – 88.

- Herding, G. (1997). *Analyse expérimentale de la combustion d'ergols cryotechniques*. Ph. D. thesis, École Centrale Paris.
- Herding, G., R. Snyder, P. Scouffaire, C. Rolon, and S. Candel (1996). Flame stabilization in cryogenic propellant combustion. In *Proceedings of the Combustion Institute*, 26, pp. 2041–2047.
- Herding, G., R. Snyder, J. Rolon, and S. Candel (1997). Investigation of Cryogenic Propellant Flames Using Computerised Tomography of OH Emission Images. *Journal of Propulsion and Power* 14, 146–151.
- Higuera, F. and A. Liñán (1996). Flow field of a diffusion flame attached to a thick-walled injector between two coflowing reactant streams. *Journal of Fluid Mechanics* 329, 389 – 411.
- Hirano, T. and Y. Kanno (1973). Aerodynamic and thermal structures of the laminar boundary layer over a flat plate with a diffusion flame. In *Proceedings of the Combustion Institute*, 14, pp. 391 – 398.
- Hirano, T. and M. Kinoshita (1975). Gas velocity and temperature profiles of a diffusion flame stabilized in the stream over liquid fuel. In *Proceedings of the Combustion Institute*, 15, pp. 369 – 387.
- Hopfinger, E. and J. Lasheras (1994). Break-up of a water jet in high velocity co-flowing air. In A.J.Yule and C.Dumanchel (Eds.), *6th International Conference on Liquid Atomisation, Spray Systems*, New York, pp. 110–117. ICLASS: Begell House.
- Huerre, P. (1987). Spatio-temporal instabilities in closed and open flows. In E. Tirapegui and D. Villarroel (Eds.), *Instabilities and Nonequilibrium Structures*, pp. 141–177. D. Reidel Publishing Company.
- Huerre, P. (2000). Open shear flow instabilities. In G. H.K.Moffatt and M.G.Worster (Eds.), *Developments in Fluid Mechanics: A Collection for the Millenium*. Cambridge University Press.
- Huerre, P. and P. Monkewitz (1990). Local and global instabilities in spatially developing flows. *Annual Review of Fluid Mechanics* 22, 473 – 537.
- Inoue, O. (1985). A new approach to flow problems past a porous plate. *AIAA Journal* 23, 1916 – 1921.
- Ivancic, B., W. Mayer, G. Krulle, and D. Bruggemann (1999). Experimental and numerical investigation of time and length scales in lox/gh<sub>2</sub>-rocket combustors. In *35th AIAA/ASME/SAE/ASEE Joint Propulsion Conference and Exhibit*, 1801 Alexander Bell Drive, Suite 500, Reston, VA, 20191-4344. AIAA: AIAA.
- Jones, J., L. Isaacson, and S. Vreeke (1971). A turbulent boundary layer with mass addition, combustion and pressure gradients. *AIAA Journal* 9(9), 1762 – 1768.
- Juniper, M., P. Scouffaire, and S. Candel (2000). Etude de la combustion cryotechnique à haute pression avec un injecteur générique. Effet de la température de l'hydrogène. Technical report, École Centrale Paris, ECP.
- Juniper, M., A. Tripathi, P. Scouffaire, J. Rolon, and S. Candel (2000). The structure of cryogenic flames at elevated pressures. In *Proceedings of the Combustion Institute*, 28.



- Katta, V. and W. Roquemore (2000). Response of a hydrogen-air opposing-jet diffusion flame to different types of perturbations. In *Proceedings of the Combustion Institute*, 28, pp. 2055 – 2062.
- Kee, R., G. Dixon-Lewis, J. Warnatz, M. Coltrin, and J. Miller (1986). A Fortran computer code package for the evaluation of gas phase multicomponent transport properties . Technical Report SAND86-8246 UC-401, Sandia National Laboratories.
- Kee, R., F. Rupley, and J. Miller (1989). A fortran chemical kinetics package for the analysis of gas phase chemical kinetics. Technical Report SAND89-8009B UC-706, Sandia National Laboratories.
- Kendrick, D., G. Herding, P. Scoufflaire, C. Rolon, and S. Candel (1999). Effects of recess on cryogenic flame stabilization. *Combustion and Flame* 118(3), 327–339.
- Kent, J. and A. Williams (1975). Extinction of laminar diffusion flames for liquid fuels. In *Proceedings of the Combustion Institute*, 15, pp. 315 – 325.
- Koch, W. (1985). Local instability characteristics and frequency determination of self-excited wake flows. *Journal of Sound and Vibration* 99, 53 – 83.
- Kuwana, K., S. Suzuki, R. Dobashi, and T. Hirano (1999). Effects of liquid distribution on flame spread over porous solid soaked with combustible liquid. In M. Curtat (Ed.), *Fire Safety Science - Proceedings of the 6th International Symposium*, pp. 637 – 648.
- Lasheras, J. and E. Hopfinger (2000). Liquid jet instability and atomisation in a coaxial gas stream. *Annu. Rev. Fluid Mech.* 32, 275.
- Lasheras, J., E. Villermaux, and E. Hopfinger (1998). Break-up and atomization of a round water jet by a high-speed annular air jet. *Journal of Fluid Mechanics* 357, 351–379.
- Le Visage, D. (1996). *Pulverisation d'un jet issu d'un injecteur coaxial assisté: Géométrie de l'injecteur, modélisation et approche cryogénique*. Ph. D. thesis, Université de Poitiers.
- Lee, J., C. Frouzakis, and K. Boulouchos (2000). Two-dimensional direct numerical simulation of opposed-jet hydrogen/air flames: Transition from a diffusion to an edge flame. In *Proceedings of the Combustion Institute*, 28, pp. 801 – 806.
- Leroux, B. (2001). *Etude expérimentale des flammes turbulentes oxygène / combustible liquide*. Ph. D. thesis, École Centrale Paris.
- Li, J., S. Zaleski, and R. Scardovelli (1995). Simulations Numériques 3D de l'arrachage des gouttes sur une couche liquide plane. In V. Duthoit (Ed.), *Cinquième colloque du Groupe De Recherche "Combustion dans les moteurs fusée"*, pp. B. Société Européenne de Propulsion.
- Liñán, A. (1974). The asymptotic structure of counterflow diffusion flames for large activation energies. *Acta Astronautica* 1, 1007 – 1039.
- Lide, D. (1991). *CRC Handbook of Chemistry and Physics* (72 ed.). CRC Press Inc.
- Lindstedt, P. (1998). Modeling of the chemical complexities of flames. In *Proceedings of the Combustion Institute*, 27, pp. 269 – 285.

- Loiseleux, T., J. Chomaz, and P. Huerre (1998). The effect of swirl on jets and wakes: Linear instability of the Rankine vortex with axial flow. *Physics of Fluids* 10(5), 1120 – 1134.
- Mahalingam, S., D. Thevenin, S. Candel, and D. Veynante (1999). Analysis and numerical simulation of a nonpremixed flame in a corner. *Combustion and Flame* 118, 221 – 232.
- Mahalingam, S. and P. Weidman (2002). Activation energy asymptotics analysis and numerical modeling of a strained laminar corner flame. *Combustion Theory Modelling - (Submitted)*.
- Marble, F. and T. Adamson (1954). Ignition and Combustion in a Laminar Mixing Zone. *Jet Propulsion*, 85 – 94.
- Mathis, C., M. Provansal, and L. Boyer (1984). The Bénard-von Kármán instability: an experimental study near the threshold. *Journal de Physique (Paris) Letters* 45, 483 – 491.
- Mayer, W., A. Shick, B. Vielle, C. Chauveau, I. Gokalp, D. Talley, and R. Woodward (1998). Atomization and Breakup of Cryogenic Propellants Under High-Pressure Subcritical and Supercritical Conditions. *Journal of Propulsion and Power* 14(5), 835 – 842.
- Mayer, W. and H. Tamura (1996). Propellant Injection in a Liquid Oxygen/Gaseous Hydrogen Rocket Engine. *Journal of Propulsion and Power* 12(6), 1137 – 1147.
- Monkewitz, P. (1988a). A note on vortex shedding from axisymmetric bluff bodies. *Journal of Fluid Mechanics* 192, 561 – 575.
- Monkewitz, P. (1988b). The absolute and convective nature of instability in two-dimensional wakes at low Reynolds numbers. *Phys. Fluids* 31, 999 – 1006.
- Monkewitz, P. and K. Sohn (1988). Absolute Instability in Hot Jets. *AIAA Journal* 26(8), 911 – 916.
- Niioka, T., S. Hasegawa, T. Tsukamoto, and J. Sato (1991). Diffusion-Flame Extinction of Liquid Fuel at Elevated Pressure. *Combustion and Flame* 86, 171 – 178.
- Oefelein, J. (1997). *Simulation and Analysis of Turbulent Multiphase Combustion Processes at High Pressures*. Ph. D. thesis, Pennsylvania State University.
- Oefelein, J. and V. Yang (1998). Modeling High-Pressure Mixing and Combustion Processes in Liquid Rocket Engines. *Journal of Propulsion and Power* 14(5), 843 – 857.
- Pearce, R. and A. Gaydon (1965). *The identification of molecular spectra* (3 ed.). London: Chapman and Hall.
- Preklik, D. and P. Spagna (1988). Low frequency and high frequency combustion oscillation phenomena inside a rocket combustion chamber fed by liquid or gaseous propellants. In *AGARD Conference Proceedings*, Volume 450, pp. 6-1 to 6-18.
- Rayleigh, J. (1896). *The Theory of Sound*, Volume 2. Dover.
- Raynal, L. (1997). *Instabilité et entrainement à l'interface d'une couche de mélange liquide-gaz*. Ph. D. thesis, Université Joseph Fourier - Grenoble I, Grenoble.



- Raynal, L., E. Villermaux, and E. Hopfinger (1997). Instabilité d'une interface de cisaillement liquide-gaz. In *Groupe De Recherche "Combustion dans les moteurs fusée" 1997*, pp. C. SEP.
- Rehab, H. (1997). *Structure de l'écoulement et mélange dans le champ proche des jets coaxiaux*. Ph. D. thesis, Université Joseph Fourier - Grenoble I, Grenoble.
- Rehab, H., E. Villermaux, and E. Hopfinger (1997). Flow regimes of large-velocity-ratio coaxial jets. *Journal of Fluid Mechanics* 345, 357 – 381.
- Rohmat, T., H. Katoh, T. Obara, T. Yoshihashi, and S. Ohyagi (1998). Diffusion flame stabilized on a porous plate in a parallel airstream. *AIAA Journal* 36(11), 1945 – 1952.
- Schreiber, D. (1991). *Quelques problèmes de combustion liés à l'allumage dans les moteurs fusée cryotechniques*. Ph. D. thesis, Ecole Centrale de Paris, Châtenay-Malabry, France.
- Snyder, R., G. Herding, J. Rolon, and S. Candel (1997). Analysis of Flame Patterns in Cryogenic Propellant Combustion. *Combustion Science and Technology* 124, 331–370.
- Sreenivasan, K., S. Raghu, and D. Kyle (1989). Absolute instability in variable density round jets. *Exp. Fluids* 7, 309 – 317.
- Strykowski, P. (1986). *The Control of Absolutely and Convectively Unstable Shear Flows*. Ph. D. thesis, Yale University, New Haven, Connecticut.
- Takahashi, F., W. Schmoll, and V. Katta (1998). Attachment mechanisms of diffusion flames. In *Proceedings of the Combustion Institute*, 27, pp. 675 – 684.
- Thévenin, D. and S. Candel (1994). Ignition Dynamics of a Diffusion Flame Rolled Up in a Vortex. *Phys. Fluids* 7(2), 434 – 445.
- Triantafyllou, G., M. Triantafyllou, and Chryssostomidis (1986). On the formation of vortex streets behind stationary cylinders. *Journal of Fluid Mechanics* 170, 461 – 477.
- Tripathi, A. (2001). *Structure des flammes cryotechniques à haute pression*. Ph. D. thesis, Ecole Centrale de Paris, Châtenay-Malabry, France.
- Tripathi, A., M. Juniper, P. Scouffaire, and S. Candel (1998). Etude de la combustion cryotechnique à haute pression (1ère partie). imagerie d'émission, spectroscopie et ombroscopie. Technical report, Ecole Centrale de Paris, Châtenay-Malabry, France.
- Tripathi, A., M. Juniper, P. Scouffaire, and S. Candel (1999). Etude de la combustion cryotechnique à haute pression (2eme partie). imagerie d'émission, spectroscopie et ombroscopie. Technical report, Ecole Centrale de Paris, Châtenay-Malabry, France.
- Tripathi, A., M. Juniper, P. Scouffaire, J. Rolon, D. Durox, and S. Candel (1999). Effect of LOx tube recess studied by OH and H<sub>2</sub>O natural emission. In *37th AIAA Conference*, Volume AIAA-99-2490, Los Angeles.
- Villermaux, E. (1998). Mixing and Spray Formation in Coaxial Jets. *Journal of Propulsion and Power* 14(5), 807 – 817.

- Vingert, L., M. Habiballah, P. Hervat, F. Dugué, and P. Vuillermoz (1997). Evolution of the Mascotte test bench to high pressure operation and related combustor technology issues. In *3ème Colloque Franco-Allemand sur la Combustion dans les Moteurs-Fusée*, Marseille, France.
- Vogel, A. (1994). Investigations on atomization of a coaxial injected h<sub>2</sub>/lox jet under hot fire conditions. In *ICLASS-94*, pp. 742 – 749. ICLASS.
- Weinberg, F. (1963). *Optics of Flames*. London: Butterworths.
- Williams, F. (1985). *Combustion Theory*. Benjamin/Cummings.
- Yecko, P. and S. Zaleski (2000). Two-phase shear instability: waves, fingers and drops. *Annals of the New York Academy of Sciences* 898, 127 – 143.
- Yu, M.-H. and P. Monkewitz (1990). The effect of nonuniform density on the absolute instability of two-dimensional inertial jets and wakes. *Physics of Fluids A* 2(7), 1175 – 1181.
- Zaleski, S. (1998). Etude numérique de la rupture des jets et des gouttes. In *Groupe De Recherche "Combustion dans les moteurs fusée" 1995-1998*, pp. 15 – 18. Technical report, SEP.
- Zaleski, S., J. Li, and S. Succi (1995). Two-dimensional Navier-Stokes simulation of deformation and break-up of liquid patches. *Phys. Rev. Lett.* 75, 244 – 247.
- Zitoun, R. and B. Deshaies (1997). Burning Velocities of Rich H<sub>2</sub>-O<sub>2</sub> Flames under Cryogenic Conditions. *Combustion and Flame* 109, 427 – 435.
- Zukoski, E. (1985). Afterburners. In G. Oates (Ed.), *The Aerothermodynamics of Aircraft Gas Turbine Engines*, pp. 47 – 144. AIAA, New York.
- Zukoski, E. and F. Marble (1955). The role of wake transition in the process of flame stabilization on bluff bodies. In *Combustion Researches and Reviews*, pp. 167 – 180. Butterworths, London.



Les moteurs à ergols cryotechniques sont alimentés en oxygène liquide et hydrogène gazeux. Le développement de méthodes de conception est fondée sur des simulations numériques fiables, qui doivent s'appuyer sur une connaissance détaillée des structures de flamme et des conditions d'entrée bien définies. Ce projet de recherche concerne la région proche des injecteurs d'ergols. On traite ici: (1) la structure de flamme et la géométrie de l'injecteur, (2) la stabilisation de la flamme.

Des essais ont été effectués sur un injecteur comparable à ceux des moteurs réels. Des modèles sont développés et leurs résultats comparés aux résultats expérimentaux afin d'étudier l'effet de la géométrie de l'injecteur. Un nouveau résultat d'intérêt scientifique est qu'un sillage est plus instable quand l'écoulement extérieur est confiné. Ce mécanisme pourrait expliquer l'effet du retrait sur la flamme cryotechnique.

La zone initiale de la flamme est divisée en deux parties et une analyse de flamme à contre-courant est appliquée à la première. La seconde partie est traitée d'abord comme une flamme dans un coin. La flamme au dessus d'une plaque poreuse avec injection de comburant est étudiée ensuite et on envisage dans un deuxième temps une flamme au dessus d'un comburant en cours de vaporisation. Finalement la flamme derrière une marche au dessus d'une nappe liquide est envisagée. Grâce à cette progression, les paramètres sans dimensions qui pilotent la stabilisation sont identifiés.

Cryogenic rocket motors are fueled by liquid oxygen and gaseous hydrogen. The development of design methods is based on reliable numerical simulations, which rely on detailed knowledge of the flame structure and well-defined entry conditions. This research project concerns the region near the fuel injectors. We examine here: (1) The flame structure and injector geometry, (2) The flame stabilization.

Tests have been performed on an injector which is similar to those in real motors. Models are developed and their results compared with experimental results in order to study the effect of the injector geometry. A new result of scientific interest is that a wake is more unstable when the outer flow is confined. This mechanism might explain the effect of recess on a cryogenic spray flame.

The base of the flame is divided into two parts and a counter-flow flame analysis is applied to the first part. The second part is considered first as a flame in a corner (cross-flow flame). The flame above a porous plate with fuel injection is considered next and we envisage then a flame above a vaporizing fuel. Finally, the flame behind a step over a vaporizing fuel is envisaged. With this progression, the dimensionless parameters which control flame stabilization are identified.





## **MODÈLE DE RÉSUMÉ ET MOTS CLÉS**

(verso de la page de couverture)

Réalisation d'un appareillage de Spectrométrie de Masse en Ionisation Résonnante : application à l'étude spectroscopique et analytique de terres rares.

---

L'analyse isotopique des lanthanides et des actinides est souvent perturbée par la présence d'interférences isobariques. La Spectrométrie de Masse à Ionisation Résonnante (RIMS) peut permettre de s'affranchir de ces problèmes grâce à la possibilité d'opérer une double sélectivité, élémentaire et isotopique.

### **Sélectivité élémentaire :**

L'irradiation d'un gaz d'atomes par un faisceau laser accordable provoque l'excitation, puis l'ionisation, des seuls atomes dont une transition électronique correspond à la longueur d'onde laser.

### **Sélectivité isotopique due au système dispersif en masse :**

Après un rappel des notions théoriques essentielles de la photoionisation résonnante et de l'atomisation thermique, nous décrivons l'appareillage réalisé. Nous présentons ensuite les résultats expérimentaux obtenus sur le Samarium, le Gadolinium et sur le mélange Samarium-Gadolinium :

- Sur le domaine spectral/429-448/nm, 27 longueurs d'onde de photoionisation du Samarium sont identifiées. Nos résultats montrent que le RIMS peut être envisagé comme technique complémentaire des techniques classiques d'identification des transitions électroniques.

- A forte énergie laser (3mJ/pulsé), deux processus différents conduisent à la photoionisation du Gadolinium :

- \* Photoionisation résonnante, à deux photons de même fréquence, à partir d'un niveau excité.
- \* Photoionisation résonnante assistée.

- A faible énergie laser (0,3 mJ/pulsé), le processus de photoionisation résonnante assistée est dominant. La sélectivité élémentaire est alors considérablement améliorée et le signal détecté indépendant des fluctuations énergétiques du faisceau laser.

- Les premiers résultats de l'étude du mélange Sm-Gd prouvent l'efficacité de la technique RIMS pour éliminer les interférences isobariques.

Nos conclusions suggèrent que des études spectroscopiques approfondies soient entreprises. Différentes orientations pour celles-ci, les modifications expérimentales qu'elles nécessitent sont envisagées dans le dernier chapitre.

---

### **Mots clés :**

Spectroscopie à Ionisation Résonnante-Spectrométrie de Masse à Ionisation Résonnante-Photoionisation laser-Samarium-Gadolinium.

### **Key words :**

Resonance ionization Spectroscopy-Resonance Ionization Mass Spectrometry-Laser photoionization-Samarium-Gadolinium.